Electro-Optic Sampling of Transient Electric Fields from Charged Particle Beams

by

Michael James Fitch

Submitted in Partial Fulfillment
of the
Requirements for the Degree
Doctor of Philosophy

Supervised by
Professor Adrian C. Melissinos

Department of Physics and Astronomy
The College
Arts and Sciences

University of Rochester
Rochester, New York

2000

dedicated to

my parents,
Janet M. Fitch and
the Rev. George W. Fitch
who instilled in me
the value of an education,

and to my fiancée,
Lindsay V. Alexander,
whose love and patience
carried me through my dissertation.

Curriculum Vitae

Michael James Fitch was born in Frederick, Maryland, USA, on June 10, 1970. He was the salutatorian of Susquehanna Township High School (Harrisburg, Pennsylvania) in 1988, and was awarded a National Merit Scholarship. He studied at Princeton University and received the degree *Artium Baccalaurei* in Physics *cum laude* in 1992. Following a year at Duke University, he enrolled in graduate school in the Department of Physics and Astronomy at the University of Rochester in 1993. He was supported in part by a fellowship from the U.S. Department of Education during his first two years of study. He received the Master of Arts degree in 1995. Under the supervision of Prof. Adrian C. Melissinos, he began research at Fermi National Accelerator Laboratory in 1995. He was supported by a Fermilab Beams Division Graduate Fellowship from 1996 to 2000. His fellowship mentors were Patrick L. Colestock and Helen T. Edwards.

Acknowledgments

I owe a debt of gratitude to many people. First and foremost, I would like to thank my thesis advisor, Professor Adrian C. Melissinos. I have grown tremendously under his tutelage, and I have been inspired by his boundless energy, enthusiasm, creativity, and by his remarkably quick and accurate physical intuition. I appreciate very much his efforts to keep in close touch with my progress over long distance by phone, fax, email, and videoconference, and with his frequent visits to Fermilab. I have really enjoyed working with him.

My mentors at Fermilab under the Fermilab Beams Division Graduate Fellowship program were Dr. Patrick L. Colestock and later, Dr. Helen T. Edwards. The advice of Dr. Colestock was very helpful, especially when the idea of electro-optic sampling was taking shape as a thesis project. Even after he left for Los Alamos National Laboratory, I could still count on him to help me decipher the jargon of accelerator physics. Dr. H. Edwards was a driving force behind the photoinjector project, and she was a powerful advocate. She pushed the project (and this thesis) forward in many ways. I thank also Professor Nicholas P. Bigelow, who encouraged me to join this project, and who also provided advice and helpful suggestions.

Experimental physics is a collaborative effort. It has been a pleasure to work with many colleagues, including Jean-Paul Carneiro, Walter H. Hartung, Nikolai Barov, James K. Santucci, Sergey Seletskiy, Wade Muranyi, Donald Edwards, Richard A. Carrigan, Jr. and Moyses Kuchnir. Past members of the photoinjector group include Kip Bishofberger, Sven Fritzler, Alan R. Fry, Eric R. Colby, Linda

Klamp Spentzouris, Brian D. Taylor, Karl P. Koepke, Frank A. Nezrick and Ilja Bohnet.

I would especially thank Jean-Paul, a fellow graduate student, for all his help teaching me to operate the photoinjector. He was generous with his time, his cheer, his emittance data, and his fine French coffee. Many thanks also to Walter Hartung for many late nights at the AØ control console, and for many useful discussions ranging from photoemission to beam impedance to LaTeX typesetting. His dry sense of humor will be missed. Thanks also to Kip Bishofberger who gave me many detailed comments on the draft of Chapter 2, and whose input greatly improved the appearance of the figures throughout. I extend my thanks to James Santucci who ably kept the laser running while I was writing up. Ralph Pasquinelli generously loaned many useful things from his treasure troves of equipment, including the long-term loan of the Optical Spectrum Analyzer. Special thanks also to Alan Hahn for the loan of the streak camera. I acknowledge many useful discussions with Frank Nezrick, and thank him for other equipment loans. Thanks also to Siegfried Schreiber (DESY) for helpful discussions.

I owe personal thanks to my friends and family who provided moral support and encouragement. I hope to have an opportunity to extend my gratitude in person to all of them.

I would also like to thank Dr. David A. Finley, Dr. Stephen D. Holmes, and Dr. John P. Marriner. In their capacities as Beams Division Head, they continually supported the ongoing research of graduate students in the AØ Photoinjector project even in times of tight budgets. Their concern for graduate students is most appreciated. The director of Fermilab, Dr. Michael S. Witherell, and the former director Dr. John Peoples, Jr. are offered my thanks for the same reason.

This work was supported in part by the U. S. Department of Energy under contract number DE-FG02-91ER40685. This work was also supported by Fermilab, which is operated by Universities Research Association for the U. S. Department of Energy under contract number DE-AC02-76CH03000. The author wishes to acknowledge the support of a Fermilab Beams Division Graduate Fellowship.

Abstract

The passage of a relativistic charged particle beam bunch through a structure is accompanied by transient electromagnetic fields. By causality, these fields must be behind the bunch, and are called “wakefields.” The wakefields act back on the beam, and cause instabilities such as the beam break-up instability, and the head-tail instability, which limit the luminosity of linear colliders. The wakefields are particularly important for short bunches with high charge. A great deal of effort is devoted to analytical and numerical calculations of wakefields, and wakefield effects. Experimental numbers are needed.

In this thesis, we present measurements of the transient electric fields induced by a short high-charge electron bunch passing through a 6-way vacuum cross. These measurements are performed in the time domain using electro-optic sampling with a time resolution of approximately 5 picoseconds. With different orientations of the electro-optic crystal, we have measured different vector components of the electric field. The Fourier transform of the time-domain data yields the product of the beam impedance with the excitation spectrum of the bunch. Since the bunch length is known from streak camera measurements, the k loss factor is directly obtained. There is reasonably good agreement between the experimental k loss factor with calculations from the code MAFIA. To our knowledge, this is the first direct measurement of the k loss factor for bunch lengths shorter than one millimeter (rms).

We also present results of magnetic bunch compression (using a dipole chicane) of a high-charge photoinjector beam for two different UV laser pulse lengths on the photocathode. At best compression, a 13.87 nC bunch was compressed to 0.66 mm (2.19 ps) rms, or a peak current of 3 kA. Other results from the photoinjector are given, and the laser system for photocathode excitation and electro-optic sampling is described.

Table of Contents

List of Tables

List of Figures

Chapter 1

Introduction

The desire to understand the physical world around us has motivated scientists, philosophers, and religious thinkers for centuries. In science, experimental and theoretical advances have gone hand in hand with the invention and development of more powerful instruments. The microscope and the telescope, which revolutionized science in the 16th century, are historical examples. The science of optics was revolutionized in the 1960s by the laser, with far-reaching applications.

The discovery of radioactivity in the 1890s gave birth to the field of nuclear physics. Advances in nuclear, and later, particle physics since then have been closely linked to developments in particle accelerators. Accelerators have furthered other fields as well. Synchrotron radiation from electron storage rings is a bright source of energetic photons for x-ray crystallography, with applications including materials science and structural molecular biology.

The physics of beams in accelerators (or accelerator physics) shows a remarkable richness of phenomena. As an example, the recent discovery of "beam echoes" [1, 2] is one of many coherent nonlinear phenomena similar to those observed in other fields. With the periodic boundary conditions of a circular machine, a countable basis set arises naturally, which is an interesting component of the theoretical and experimental investigation.

Lasers are finding wider use in accelerators. The laser photocathode RF gun, or the photoinjector, is a source of high quality electron bunches. The essential characteristic of "high quality" is that the charge occupies as small a volume in phase space as possible (high peak current, low emittance, and small energy spread). High quality electron bunches are needed both for the next generation of linear colliders for high-energy physics, and for short wavelength free-electron lasers (FEL's).

Laser cooling of heavy-ion particle beams has been demonstrated [3, 4]. The possibility of laser cooling [5], or optical stochastic cooling [6, 7], of electron beams has been suggested.

For particle beams of very high energy density, it is not possible to intercept the beam with any material. Intercepting the beam with a laser can be used as a monitor of nanometer beam sizes at the final focus of a linear collider [8] or for sub-picosecond characterization of the bunch [9]. Compact (sub)-picosecond x-ray sources based on laser photons that are Thomson backscattered[1] from an electron beam [10–14] are promising for time-resolved pump-probe x-ray experiments. Hard photons with 100% polarization [15] can also be produced. Applications to γ–γ colliders [16, 17] are constrained by critical-field quantum electrodynamics (QED) effects [18–22].

1.1 Electro-Optic Sampling

In this thesis we present results of a novel application of electro-optic sampling to measuring the transient fields (the wakefields) from the passage of a high-charge electron bunch. This measurement is all-optical, non-intercepting, and minimally invasive. Applications include wakefield characterization of structures, and bunch length measurement.

An electric field applied to an electro-optic crystal changes the polarization of

---

[1] A limiting case of Compton scattering.

the light passing through the crystal. By analyzing the polarization change, the electric field is measured. Because the electro-optic effect has a fundamentally fast response time of order femtoseconds, a short laser pulse and a thin crystal can be used to sample the electric field at a particular time. As the relative delay between the short laser pulse and the waveform is varied, the waveform is measured.

Developing new techniques of beam measurement is important for future machines. Bunch length measurements at the picosecond and sub-picosecond level have attracted a great deal of interest recently. The streak camera has achieved a resolution of 225 fs [23], though these devices are increasingly expensive and inefficient with faster time resolution, and the technology may be near its practical limits. Other recent progress has used the coherent transition radiation (CTR) [24] from the bunch, which is in the far-infrared (millimeter and sub-millimeter wavelengths), to get information about the bunch length. An autocorrelation of the far-infrared light with a Michelson or Martin-Puplett interferometer [25–27] gives a bunch length, assuming the *shape* of the bunch distribution. However, because the autocorrelation function is symmetric, $G(x) = \int_{-\infty}^{+\infty} f(t-x)\, f(t)\, dt = G(-x)$, a asymmetric bunch shape cannot be recovered. The spectrum of the CTR radiation alone is not enough to find the bunch shape by inverse Fourier transformation because of missing phase information. With the addition of Kramers-Kronig relations [28] applied to the CTR spectrum to recover some phase information, an asymmetric shape can be recovered, but the head/tail ambiguity remains.

A bunch length measurement based on the electro-optic sampling technique is attractive because the time resolution can be in principle as short as tens of femtoseconds. No assumptions about the bunch shape need to be made.

Our measurements also give an experimental estimation of the wakefunction and k loss factor for a 6-port vacuum cross. Although a lot of theoretical effort and computer modeling has been invested in calculating the wakefunctions, direct experimental numbers are needed. Wakefields lead to instabilities in linear colliders, (such as the beam break-up instability and the head-tail instability) which limit the luminosity.

The theory and description of the experiment is given in Chapter 5, and the results and discussion are given in Chapter 6. Independently of this work, a group from FOM-Institut voor Plasmafysica "Rijnhuizen" (Nieuwegein, The Netherlands) has done similar electro-optic sampling experiments; references are given in Section 5.1.

1.2 The AØ Photoinjector and TESLA

The project at Fermilab known as the AØ Photoinjector (or AØPI) is a collaboration of several institutions[2] to prototype the low-energy stages of a proposed next-generation electron-positron linear collider, known as the TeV Electron Superconducting Linear Accelerator, or TESLA (details may be found in the conceptual design report, [29]). A drawing of the AØ Photoinjector beamline is shown in Figure 1.1. An overview of the TESLA design is shown in Figure 1.2.

New accelerator facilities are costly, so it is desirable to have a broad user base. For this reason, the TESLA project has an integrated x-ray FEL based on self-amplified spontaneous emission (SASE) [30]. Another proposed short wavelength FEL is the linear coherent light source (LCLS) [31, 32]. The concept of the free electron laser was first described by Madey [33]. Named by analogy to the conventional quantum laser[3], the physical mechanism at work in the FEL is stimulated Bremsstrahlung radiation from electrons in a periodic magnetic field. Theory of FEL operation can be found in, for example, the 1989 review article by Roberson and Sprangle [35].

---

[2] Contributing institutions include FNAL, Univ. of Rochester, UCLA, INFN-Milano, and DESY.

[3] With an external narrow-band optical cavity for feedback, the degeneracy parameter of the FEL radiation could be as high as 10^{14} [34], which is within an order of magnitude of a conventional quantum laser in the visible.

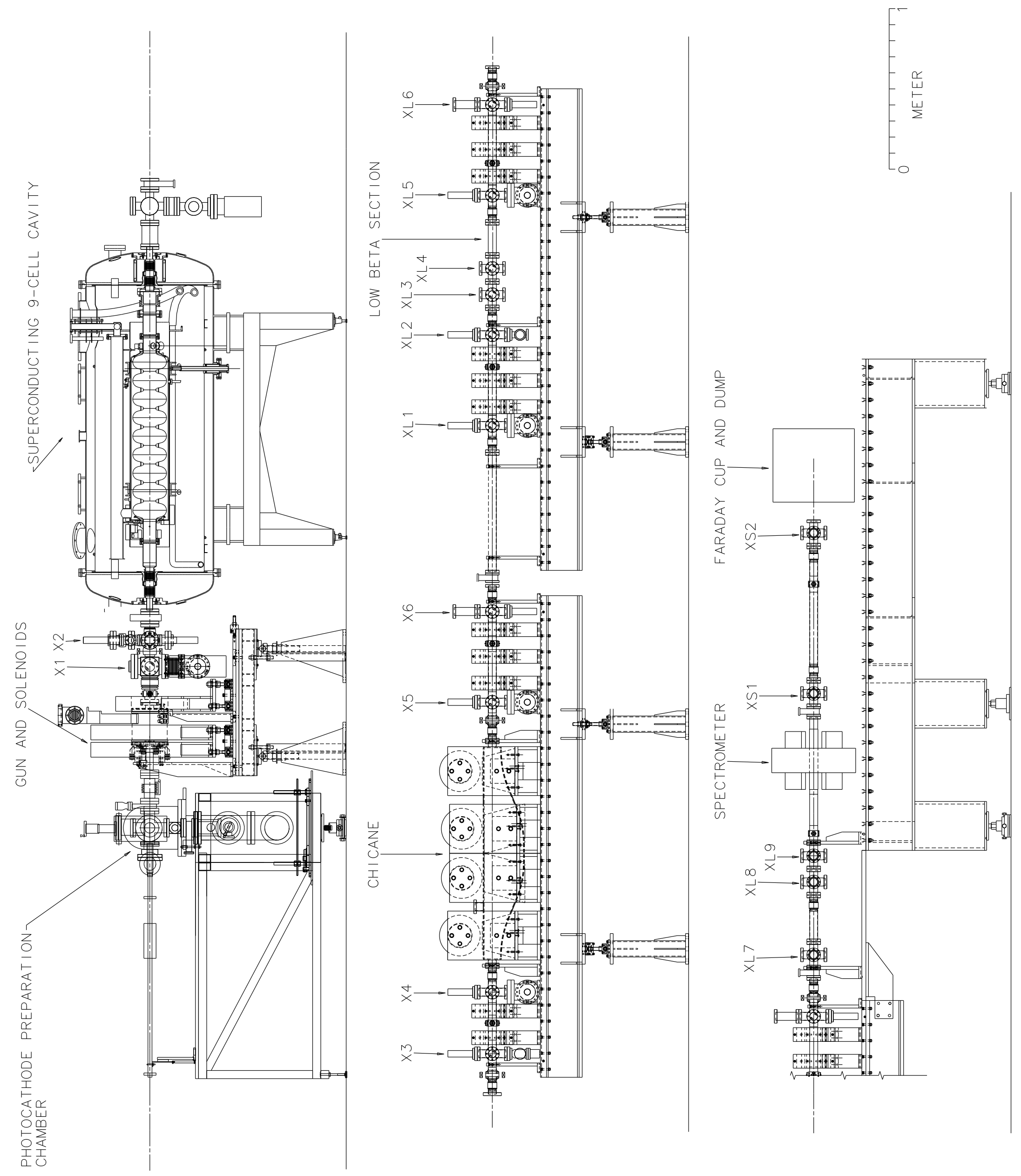

Figure 1.1: The Beamline of the AØ Photoinjector

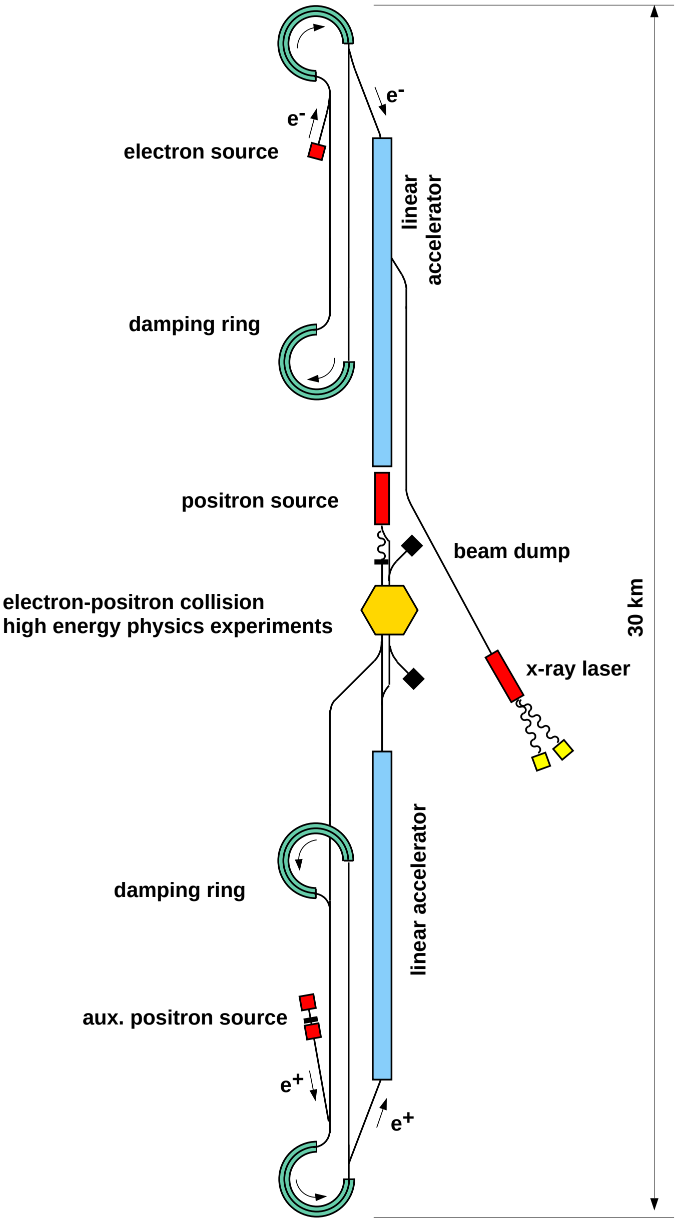

Figure 1.2: The linear collider design of TESLA. Figure courtesy of S. Schreiber.

Plans at the TESLA Test Facility for a test of a SASE FEL in the vacuum ultraviolet have recently achieved success with the recent report [36] of SASE at a record short wavelength of 109 nm. This milestone depends entirely on the high quality electron beam from the injector provided by Fermilab.

The requirements for the photoinjector are demanding. Because of the Coulomb repulsion of the electrons (the space charge force) the beam tends to blow itself up. As the electrons are accelerated relativistically, the space charge force is cancelled as γ^{-2} (where $\gamma = E/mc^2$). This can be thought of in the lab frame as a magnetic force from the beam current which pinches the beam and opposes the space charge, or it could be thought of as "freezing out" of the beam motion from time dilatation. Clearly, most of the emittance growth from space charge occurs in the low-energy portion of the accelerator. This is why the injector presents a challenge for maintaining high beam quality.

The design of the injector is described by Colby [37], and two copies were built—one was sent to DESY for use at the TESLA Test Facility, and one remained at Fermilab for dedicated experiments. Results of the photoinjector are given in Chapter 3. We include also in Chapter 3 photoemission studies using Cs_2Te. The photocathode preparation chamber was provided by INFN-Milano.

The photoinjector was tested with beam using a laser system contributed by our group (from the University of Rochester). A description of the laser system, including temporal pulse shaping, is described in Chapter 2.

Studies of magnetic bunch compression for two different laser pulse lengths are given in Chapter 4.

Chapter 2

The Laser System

2.1 Overview of the Laser System

The laser photoinjector can now be regarded as a mature technology for the production of high-quality electron beams. Numerous groups including those described in Refs. [38–42] have constructed suitable lasers. The system described here is different from most in the use of pulse trains. The laser is used for photocathode excitation as well as electro-optic sampling.

Our group designed and built the pulse train laser system for photocathode drive of the A0 Photoinjector [43]. A counterpart group from Max Born Institute [42, 44] contributed a laser to TTF at Deutches Elektronensynchrotron (DESY) Hamburg. Both groups had in common the goal of producing a laser pulse train with the 1 MHz micropulses making up the 800 pulse train (see Figure 2.1) specified in the TESLA design report [29].

We departed in several key respects from the Max Born Institute group. In particular, they use Nd:YLF throughout. Our group's experience with Nd:glass lasers for the SLAC E-144 experiment [18–22], and existing equipment from that effort led us to the choice of glass. In addition, we desired the shorter pulse widths available with glass for eventual experiments. The poorer thermal properties of glass meant accepting a lower (1 Hz) macropulse repetition rate.

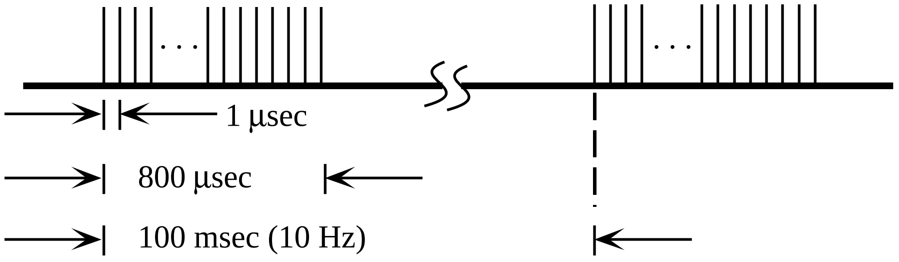

Figure 2.1: The TESLA pulse train requirement is a burst of 1 MHz pulses that is 800 pulses long. The burst is repeated at 10 Hz.

Another motivation for the choice of glass is that the cost is low compared to YLF and it allows scalability to higher pulse energies by adding successive glass amplifiers. A single giant pulse with energy of order 1 J in the IR could be used for experiments using picosecond X-ray pulses by Thomson scattering [8–14], or for a laser-plasma acceleration experiment [45]. An upgrade to 1 J pulses is possible for our laser system with the addition of a large aperture zigzag Nd:glass slab amplifier [46].

It is desired that each pulse in the long pulse train be of the same amplitude, that is, the pulse train has a rectangular envelope. The gain of the amplifiers, however, is not constant in time but depends on the pump profile, spontaneous emission, and gain depletion from amplification. A envelope-shaping scheme using electro-optic loss modulation before the amplifiers is discussed in the dissertation of A. R. Fry [47], previously from our group. Initially, the average envelope is used to generate a correction which is cut out of the envelope before amplification. The product of the shaped input envelope with the gain envelope is approximately rectangular. Slow iterations are made to the correction factor based on previous shots, so this is called “feed-forward”.

Pulse trains as long as 800 pulses have been demonstrated. In order to have

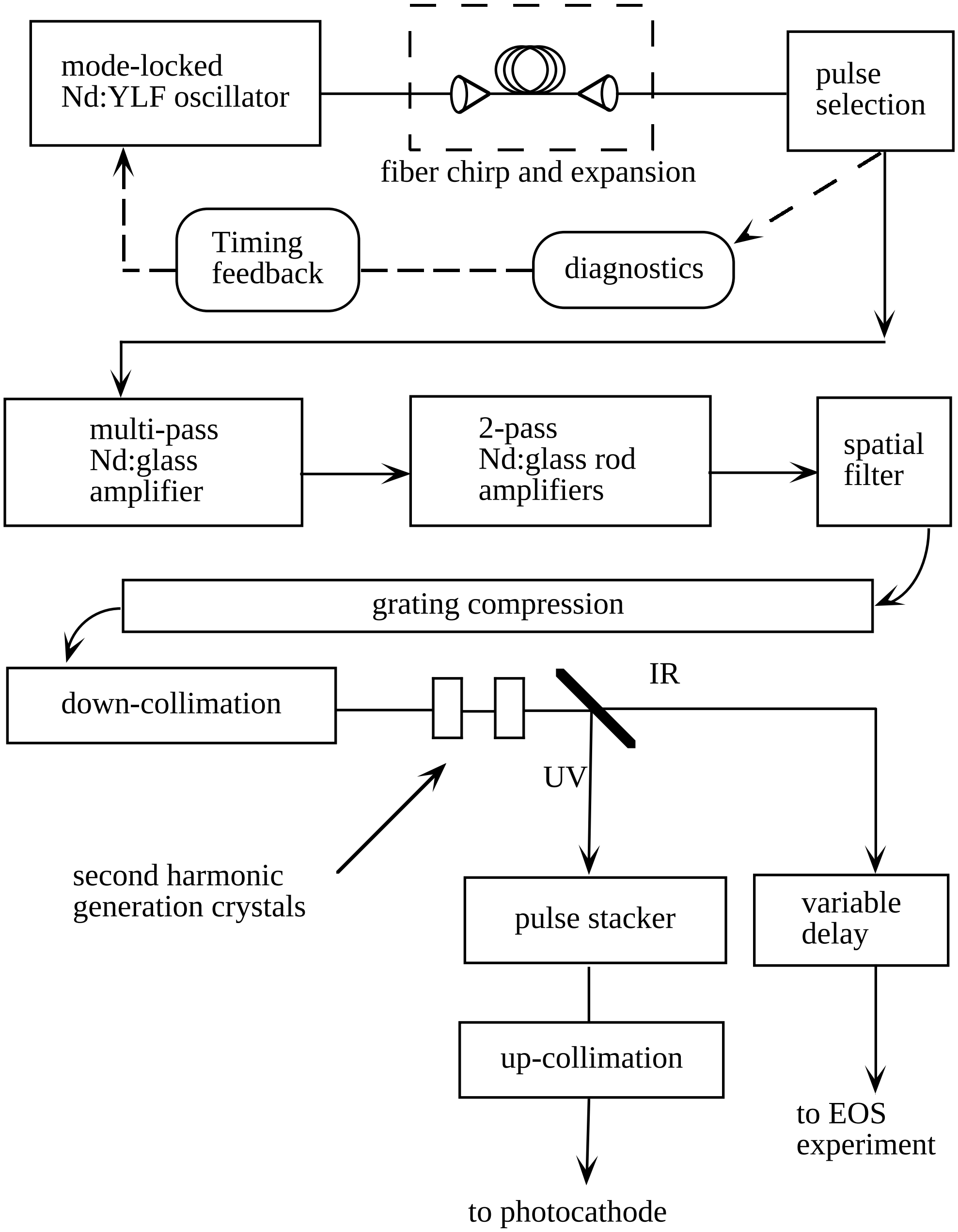

Figure 2.2: Block diagram of the laser system from the oscillator to the beam transport line.

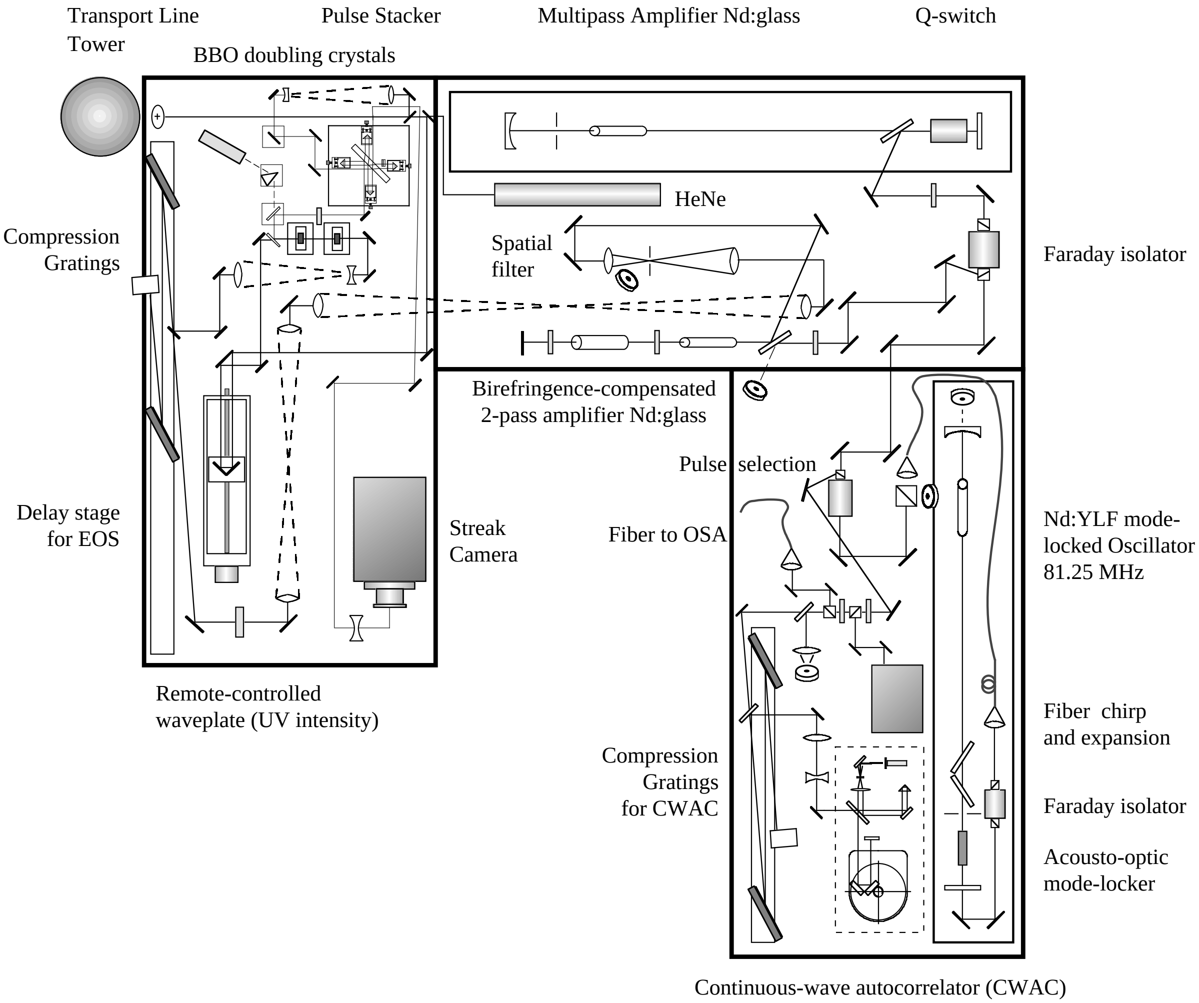

Figure 2.3: Layout of the Laser System on three 4' by 8' optical tables.

acceptable flatness of the pulse train envelope for more than 200 pulses, it is necessary to operate the "feed-forward" system (see discussion in Section 2.4), however the losses are high. *Without* envelope shaping, we achieved acceptably flat pulse trains of 50–200 pulses that delivered 3–5 μJ per pulse in the UV onto the cathode.

There were two pulse lengths available in the UV. The short laser pulse was 1.89 ps σ_t (from Gaussian fit to a streak camera image). This pulse was split into four copies and combined with appropriate delays (a pulse stacker) to make the long UV pulse. The long pulse is not Gaussian but is an approximately flat-top distribution with 10–12 ps FWHM. These results are discussed in Section 2.8.

A overview of the laser system is depicted in the block diagram of Figure 2.2. The physical component layout of the laser system on three optical tables (4' by 8') is shown in Figure 2.3.

2.2 Oscillator

The beginning of the laser system is an actively mode-locked oscillator. This laser generates the seed pulses which are to be amplified in the rest of the system. All of the timing stability and jitter suppression is enacted on this stage, as active mode-locking permits synchronizing the output to an external reference frequency. There are various schemes of passive mode-locking using physical mechanisms such as Kerr lens mode-locking (particularly important for Ti:sapphire), saturable absorbers, colliding pulse mode-locking (CPM) [48], etc.

The oscillator is a homebuilt design using commercial components mounted on an Invar plate (Invar-36, an alloy of 36% Ni and 64% Fe, is a material with a low thermal expansion coefficient $\alpha = +1.18 \times 10^{-6}\,^{\circ}\mathrm{C}^{-1}$). A Quantronix 116 pump chamber houses a 4 mm diameter by 79 mm Nd:YLF rod (1.1% doping). A Krypton arclamp (450 torr pressure) is continuously pumping the rod with

27 Amperes (typ.) passing through the lamp. Noise in the arclamp power supply is suppressed by a a feedback loop which employs a photodiode monitoring the lamp output light. We have measured the noise spectrum of the current both with and without the feedback, and have found a significant reduction (~10 dB) in 60 Hz and harmonics of the line voltage. The pump chamber employs a "flooded cavity" elliptical reflector surrounding the lamp and rod, with de-ionized water ($1\ \mathrm{M}\Omega \cdot \mathrm{cm}$ typ.) cooling the rod and the lamp.

A pair of Brewster-angle thin-film polarizers (TFP's) in the oscillator cavity insures linear polarization. In addition, the orientation of this polarizer (relative to the ordinary and extraordinary axes of the YLF rod) selects the lasing wavelength to be 1053 nm (σ) [49]. The gain is higher on the 1047 nm (π) line, but 1053 nm is a better match to the peak of the broad gain curve in phosphate Nd:glass. [50]

The resonator contains, in addition to the rod and the Brewster-angle thin film polarizers, a quartz mode-locker (see Section 2.2.2) and a circular iris. One end mirror is concave ($R_1 = 5$ m), and coated for high reflectance, while the second end mirror is a flat ($R_2 = \infty$) output coupler, coated for 88% reflectance. The total optical path length of the cavity is $L = 184.46$ cm. The condition for resonator stability, neglecting the thermal lens of the rod, is [49]

$$0 < g_1 g_2 < 1 \qquad \text{with} \qquad g_i = (1 - \frac{L}{R_i}) \tag{2.1}$$

and we have $g_1 g_2 = 0.63$ which is well within the stable region. The mode diameter is largest at the curved mirror, so the rod is positioned as close as practical to the curved mirror. More details about the design and modeling of this resonator can be found in Ref. [47].

An iris is used to select the transverse (spatial) mode of the oscillator to be TEM_{00} which is Gaussian. The intensity distribution of the $\mathrm{TEM}_{p\ell}$ mode in cylindrical coordinates is given [49] by:

$$I_{p\ell}(r,\phi,z) = I_o \rho^{\ell} [L_p^{\ell}(\rho)]^2 (\cos^2 \ell\phi) \exp(-\rho) \tag{2.2}$$

with $\rho = 2r^2/w^2(z)$. The only dependence on the axial position z is through the spot size $w(z)$. The lowest Laguerre polynomials are:

$$L_0^{\ell}(\rho) = 1, \qquad L_1^0(\rho) = 1-\rho, \qquad L_2^0(\rho) = 1 - 2\rho + \frac{1}{2}\rho^2 \tag{2.3}$$

Diffraction losses on a circular iris of radius a depend on the Fresnel number $N = a^2/\lambda L$ and are more severe for higher modes (plots of losses are given by Koechner [49]). Therefore, the TEM$_{00}$ has the lowest losses and is the selected spatial mode.

2.2.1 Active Mode-locking: Theory

A linear laser resonator, which we will consider to be a length L bounded by two curved mirrors, has a countable set of frequency modes analogous to acoustic modes in an organ pipe. For each transverse (spatial) mode there will be a countable set of these longitudinal (frequency) modes. If we assume that only one spatial mode is present, then the frequencies of allowed modes will depend only on the length of the resonator, and is determined by the boundary condition $L = m\lambda/2$, for m an integer. The frequency spacing between adjacent modes is $\Delta\nu = c/2L$. For $\Delta\nu = 81.25$ MHz, the required resonator length is $L = 184.46$ cm. Free oscillation of laser modes will occur for those modes whose gain exceeds the cavity losses. The 1053 nm transition in Nd:YLF has a width of 1.35 nm FWHM.

Since

$$\Delta\nu = \frac{c\,\Delta\lambda}{\lambda^2} = \frac{c}{2L} \qquad \text{and} \tag{2.4}$$

$$\Delta\lambda = \frac{\lambda^2}{2L} = 3 \times 10^{-4}\ \text{nm}, \tag{2.5}$$

approximately 4×10^3 modes exist inside the gain bandwidth. Each mode will oscillate with a random phase with respect to the other modes, so the laser output will be characterized by large intensity fluctuations.

If a sinusoidal amplitude modulation ($\sin \Omega t$) is imposed on a frequency mode ω, then the resulting frequency spectrum will have the original spike at ω as well as the sidebands at $(\omega + \Omega)$ and $(\omega - \Omega)$. For the case where many frequency modes ω_i are oscillating at once, each mode will have sidebands $\omega_i \pm \Omega$. If the modulation frequency corresponds to the spacing between adjacent resonator modes:

$$\omega_{i+1} - \omega_i = 2\pi\,\Delta\nu = \Omega \tag{2.6}$$

then the sidebands of the i-th mode will interfere with the neighboring $(i \pm 1)$-th modes. These will compete for gain in the laser medium with the result that the modes ω_i, $(\omega_{i-1} + \Omega)$, and $(\omega_{i+1} - \Omega)$ will be coupled together with the same phase, leading to a stable phase relationship among all the modes. Note that Equation 2.6 is a resonance condition between the modulation frequency Ω and the cavity length L (because L determines $\Delta\nu$).

A more detailed treatment of mode-locking is given in many texts on lasers, for example Refs. [49, 51]. The main results are that (a) the output of the laser, which is a superposition of all the modes will be periodic in time with period $1/\Delta\nu$, (b) the particular periodic function that results is a narrow spiked function, and (c) the minimum width of the spike is Fourier-transform-limited by the available bandwidth.

2.2.2 Mode-locking: Implementation

Active mode-locking is commonly implemented by acousto-optic modulators. In the acousto-optic, or photoelastic effect, the index of refraction in a medium is modified by the stress field of sound pressure waves. A standing sound wave in a quartz block will have a periodic array of pressure nodes and antinodes, and acts as a transmission grating with a sinusoidal time dependence. The laser light diffracted away from the zero-order peak is deflected from the cavity axis and lost. A sinusoidal loss-modulation of amplitude δ_{AM} is imposed on the oscillating modes. For an acousto-optic amplitude modulator in the Bragg regime (where only the zeroth and first diffraction orders are important) the transmission is [49]

$$T(t) \approx \cos\left(\delta_{AM}\ \sin \omega_m t\right). \tag{2.7}$$

Therefore the cavity loss modulation of Eq. 2.6 is at a frequency $\Omega = 2\,\omega_m$ twice that applied to the mode-locker.

A commercial acousto-optic modulator[1] is used for mode-locking. Transducers attached to a quartz block convert RF power into a standing sound wave. The quartz crystal has a comb of acoustic resonances, and the system is temperature tuned at 29.1°C to a resonance at 40.625 MHz (exactly half the 81.25 MHz). Thermal detuning of the resonance has a slope of +4.5 kHz/°C, and the resonance width is 8.5 kHz FWHM). To maintain resonance, two temperature control baths are used. Peltier heater/coolers (thermo-electric effect) in contact with the quartz crystal and a thermistor are connected to a fast feedback loop. The Peltier coolers require a good heat sink, so the acousto-optic modulator was fastened to a copper block machined with a water channel. A constant-temperature bath circulated water through the block at 29.1°C and acted as a slow feedback loop keeping the fast feedback loop of the Peltier coolers quiescent.

---

[1] IntraAction Corp., model ML-40.623B1-3

9.027775	MHz	f_o	master oscillator
1299.9996	MHz	$144f_o$	RF (1.3 GHz) for gun and 9-cell
81.249975	MHz	$9f_o$	laser oscillator frequency
1.003086	MHz	$f_o/9$	pulse train frequency
0.250772	MHz	$f_o/36$	mixing, synch 1 Hz triggers
1300.250	MHz	$144f_o + f_o/36$	mixing with transmitted RF

Table 2.1: Low-level radiofrequencies in use and the relation to the master oscillator.

2.2.3 Timing Stabilization

Active mode-locking makes possible the synchronization of the laser output with an external reference signal. Drive lasers for photoinjectors must be synchronized to the radiofrequency (RF) drive of the accelerating cavities. The requirement for TESLA is a phase jitter less than one degree of the RF. The RF frequency of 1.3 GHz has a cycle period of 760 ps, so a timing jitter of one degree rms corresponds to 2.1 ps rms.

The low-level radiofrequency (LLRF) sources for the accelerating cavities and the laser and all other needs of the system are derived from a single master oscillator. Table 2.1 contains a list of the frequencies, their use, and their harmonic relation to the master oscillator. Note that in the text, numbers are often rounded to fewer digits. Typical thermal stability of the precision quartz oscillators used is $\delta f/f = 2 \times 10^{-10}$ per °C.

The laser relies on two frequencies from the LLRF: an 81.25 MHz (sinusoid) for the mode-locked oscillator, and a 1.003 MHz (TTL pulses) signal for pulse-train selection.

A commercial feedback loop[2] shown in Figure 2.4 is employed to suppress the timing jitter of the oscillator. The reference signal (81.25 MHz) is divided by

---

[2] Series 1000 Timing Stabilizer, Lightwave Electronics Corporation, Mountain View CA.

2 and applied as the drive signal to the acousto-optic mode-locker. The actual phase of the 81.25 MHz on the laser output is picked up from a photodiode and a phase detector compares the actual 81.25 MHz with the reference. The phase error signal from the phase detector is applied to a phase shifter which modifies the drive signal.

A simple phase detector is an RF mixer. Suppose the reference and signal frequencies are identical, but 90 degrees out of phase (in quadrature). Then the output voltage of an ideal mixer would vary linearly with small changes in phase about this point. However, a real mixer has a small offset voltage even if the signals are perfectly in quadrature. The timing stabilizer circuit corrects for this error using a "chopper-stabilized" phase detector which periodically flips the polarity of the reference signal and takes the difference to arrive at a corrected phase error signal [53, 54].

2.2.4 Estimating the Timing Jitter

Because of the importance of timing jitter to the performance of the system, we discuss two methods used to measure it.

In the time domain, the oscillator is a periodic series of pulses 12.3 ns apart. In the frequency domain, this is a comb of peaks at harmonics of the fundamental 81.25 MHz, and each peak has noise sidebands. As discussed by Rodwell and Weingarten [52, 54] the noise sidebands on the fundamental are dominated by intensity fluctuations, while at higher harmonics, the sidebands are dominated by phase noise. The area of the phase noise sidebands can be used to estimate the timing jitter.

Following the derivation in [54], if a single pulse from a mode-locked laser is Gaussian with width σ_t, then a pulse train with pulse repetition period T_ℓ can be

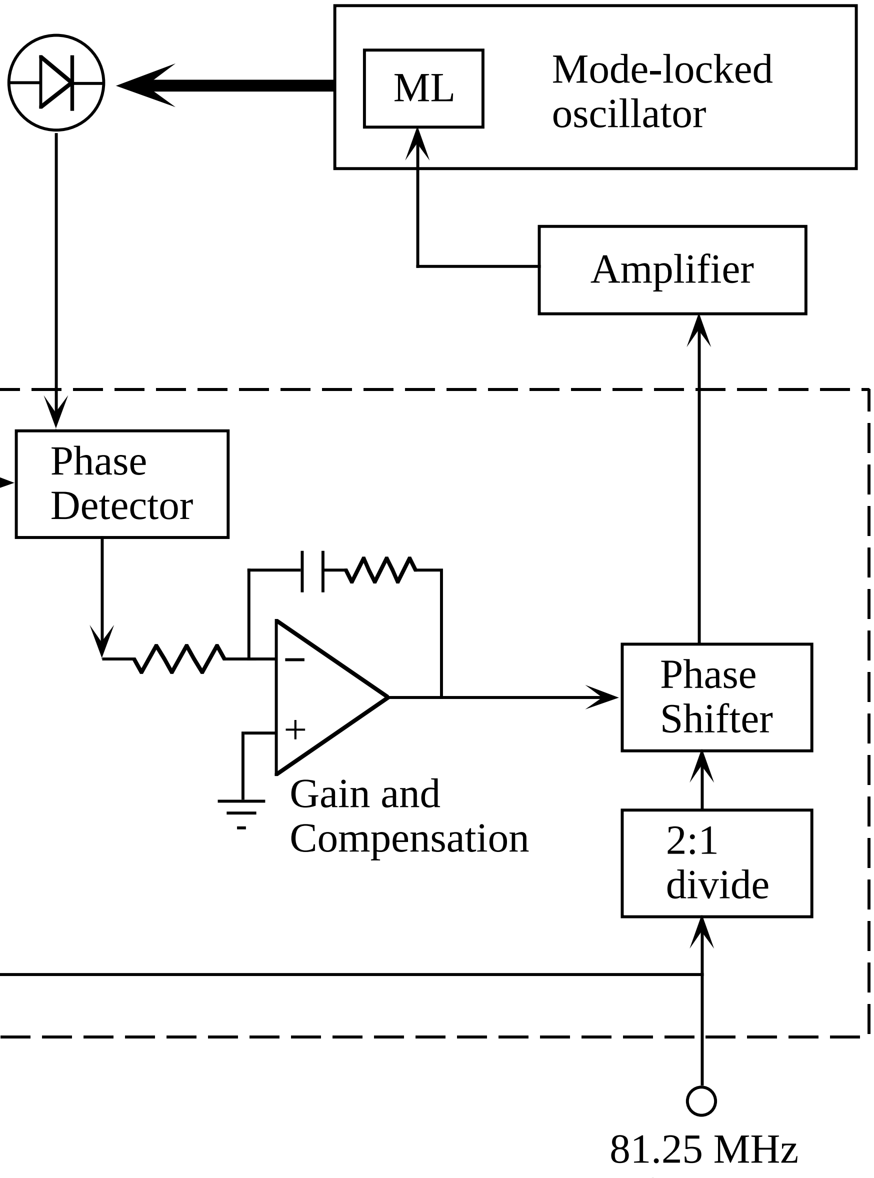

Figure 2.4: Timing Jitter Suppression. A commercial phase-lock feedback loop (in dashed box) compares the phase of the laser oscillator pulses to the reference and shifts the drive accordingly. After Ref. [52].

written as:

$$P(t) = A(t) \times \sum_{n=-\infty}^{n=+\infty} \frac{1}{\sqrt{2\pi}\,\sigma_t} \exp\left(-(t - T_0 - nT_\ell - J(t))^2/2\sigma_t^2\right) \tag{2.8}$$

where the jitter function $J(t)$ is the timing fluctuation of the pulse train. The rms deviation of this function from zero, σ_J is the timing jitter that we seek. Also, T_0 is a constant, and $A(t) = \bar{P}T_\ell(1 + N(t))$ is a slowly-varying amplitude factor which includes the normalized intensity fluctuations $N(t)$. Taking a Fourier transform of Eq. 2.8 and keeping terms to second order in $n\omega_\ell\sigma_J$, (calling $\omega_\ell = 2\pi/T_\ell$) the power spectral density $S_P(\omega)$ is:

$$\begin{aligned} S_P(\omega) \simeq \bar{P}^2 e^{-\omega^2\sigma_t^2} \sum_{n=-\infty}^{n=+\infty} \Big\{ &(1 - n^2\omega_\ell^2\sigma_J^2)\,[2\pi\,\delta(\omega - n\omega_\ell) + S_N(\omega - n\omega_\ell)] \\ &+ n^2\omega_\ell^2\, S_J(\omega - n\omega_\ell) \Big\} \end{aligned} \tag{2.9}$$

where $S_J(\omega)$ is the power spectral density of $J(t)$ (phase noise sidebands), and similarly $S_N(\omega)$ is the power spectral density of $N(t)$ (amplitude noise sidebands). From Equation 2.9 it can be seen that the phase noise sidebands at harmonic n have power proportional to n^2 and so will predominate at sufficiently high harmonics, while the amplitude noise sidebands dominate the low harmonics.

This method was used to estimate the timing jitter of the 81.25 MHz mode-locked oscillator. Using a 6 GHz photodiode[3] and a microwave spectrum analyzer[4] we measured the spectrum near 2843.75 MHz ($n = 35$). The trace shown in Figure 2.5 was a video average of 128 sweeps (70 ms sweep time) which takes > 10 sec to acquire. The ratio of the peak amplitude at $n\omega_\ell$ to the sideband amplitude at $n\omega_\ell + \Delta\omega$ is the ratio $1 : n^2\omega_\ell^2 S_J(\Delta\omega)$. From this, the jitter can be estimated [54]

---

[3] Ortel RLW-50s

[4] Hewlett-Packard 8560A

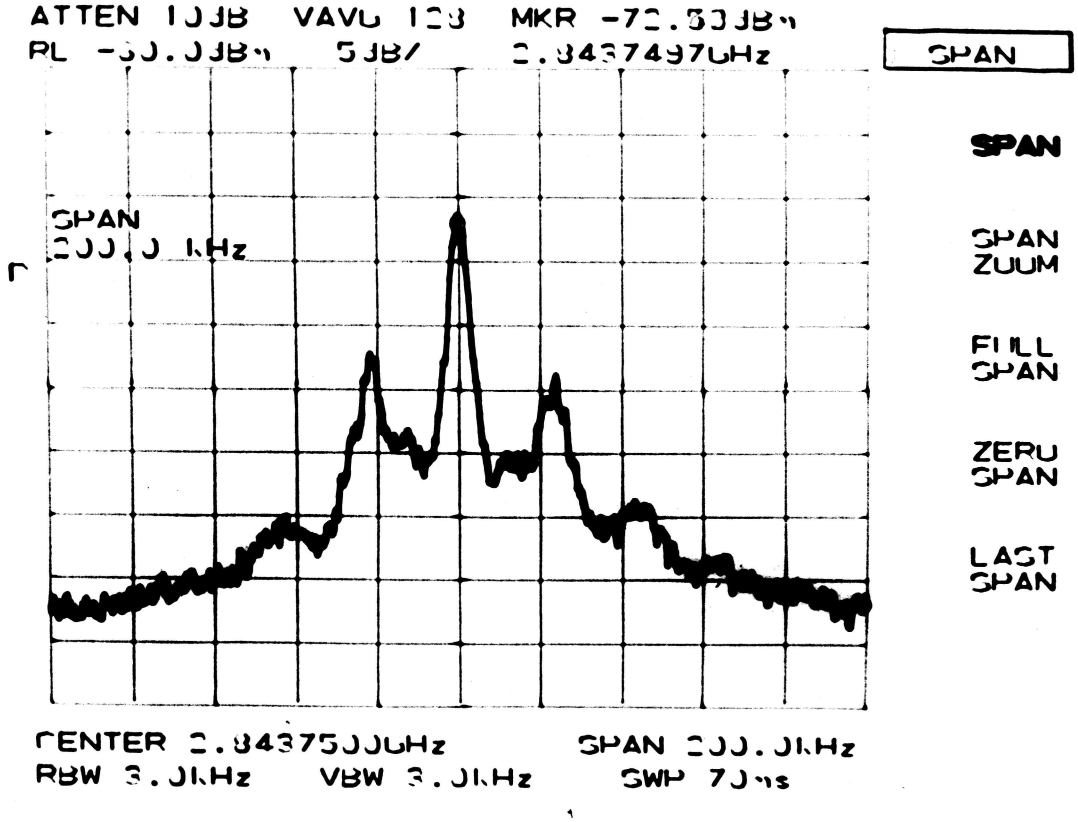

Figure 2.5: Phase noise sidebands of the laser oscillator near 2843.75 MHz (n=35). The horizontal scale is 20 kHz per division; the vertical scale is 5 dB per division.

according to:

$$\sigma_J = \sqrt{\frac{1}{\pi}\int_{\omega_{low}}^{\omega_{high}} S_J(\omega)\, d\omega} = 1.78 \pm 0.14 \text{ ps.} \tag{2.10}$$

The resolution bandwidth of the spectrum analyzer used for this measurement was 3 kHz. The low frequency integration limit should be chosen so that the harmonic peak itself is excluded from the sideband area. The value given above is the result of integrating from 5 kHz to 100 kHz. The upper and lower error bars are estimated by by repeating the integration with low frequency cutoffs at 4 kHz and 6 kHz. The high frequency cutoff is taken where the sideband amplitude is consistent with the noise floor of the spectrum analyzer.

In Section 3.4 below, we give a measurement of the total jitter of the laser with respect to the 1300 MHz RF in the gun. (The jitter measurement just given compares the laser pulses to the 81.25 MHz reference frequency.) Near the zero-crossing of the RF in the gun, small changes in timing give large changes in the charge. A statistical estimation of the jitter discussed in Section 3.4 gives the result $\sigma_J = 2.8 \pm 0.2$ ps.

2.2.5 Pulse Chirp and Expansion

Ever since the application of the chirped pulse amplification (CPA) technique [50, 55–57] to generating ultrashort optical pulses, the use of single-mode optical fibers for pulse chirp and expansion [58] has been common. The principle of CPA is to expand (stretch) the pulse in time through the frequency chirp, which greatly reduces the peak intensity of the pulse in the amplifiers without requiring large-aperture amplifiers.

There are two physical effects in the fiber: self-phase modulation (SPM), and group-velocity dispersion (GVD). Self-phase modulation arises from the intensity-dependent refractive index ($\boldsymbol{\chi}^{(3)}$), and symmetrically increases the spectral bandwidth of the pulses about the center wavelength. A simple but illustrative derivation of SPM is given by C. Hirlimann [51]. Consider a light pulse with intensity $I(t)$ passing through a material. The nonlinear index of a material which depends on the intensity can be written as $n = n_o + n_2 I(t)/2$. For simplicity, consider only a plane wave: $E(t, x) = E_o e^{i(\omega_o t - kx)}$, with $k = \omega_o n(t)/c$. Defining the instantaneous frequency as the time derivative of the phase,

$$\omega(t) = \frac{\partial}{\partial t}\Phi(t) = \omega_o - \frac{\omega_o}{c}\frac{\partial n(t)}{\partial t}x = \omega_o - \frac{\omega_o n_2}{2c}x\frac{\partial I(t)}{\partial t}. \tag{2.11}$$

So the plane wave which was initially at a pure frequency ω_o now contains a spread of new high and low frequencies.

Group velocity dispersion in the fiber is the frequency dependence of v_g, and in standard notation [59]:

$$\beta_2 = \frac{d}{d\omega}\left(\frac{1}{v_g}\right) \cong \frac{\lambda^3}{2\pi c^2}\frac{d^2 n}{d\lambda^2}. \tag{2.12}$$

The GVD is said to be normal if $\beta_2 > 0$ and anomalous if $\beta_2 < 0$. (In this notation, $\beta_1 = 1/v_g$.) A narrow optical pulse containing many frequencies that propagates through a medium with GVD will spread out in time and develop a frequency chirp as the red and blue frequencies travel at different group velocities.

Nonlinear dispersion limits the usefulness of the fiber expansion, since distortion of the linear chirp is difficult to compensate, and leads to wings in the compressed pulse. Martinez [60] showed that a positive group velocity dispersion could be obtained with an anti-parallel grating pair with the addition of an inverting telescope. This could be used as an additional pulse stretcher, or with a high-bandwidth oscillator (Nd:glass or Ti:sapphire), could eliminate the fiber altogether.

However, a fiber offers a few advantages over a grating pair stretcher [61]. One is ease of alignment, since coupling light into a fiber is much simpler than aligning the multiple elements of a grating pair stretcher. There are no finite-beam-size effects, because the pulse is uniformly stretched and has no spatial chirp. Also, the spatial mode is cleaned to a perfect TEM_{00} (Gaussian) mode.

The output pulses from the mode-locked Nd:YLF oscillator are of order 100 ps, with a spectral bandwidth of 0.6–0.9 nm. After the single-mode fiber (9 μm core diameter, 2.2 km length), the pulse spectral bandwidth has increased to 2.3 nm (typ.), and the pulse length has been stretched to 300–360 ps FWHM as measured with a 6 GHz photodiode[5] and a fast digital sampling oscilloscope.[6] The most useful diagnostic of the oscillator is the spectrum after the fiber to monitor the increased spectral bandwidth from self-phase modulation.

2.2.6 Diagnostics

Because of the critical function of the oscillator within the overall system, there are several dedicated diagnostics to monitor and optimize the oscillator.

A photodiode at the end of the oscillator cavity monitors the light leaking through the high reflectance coated curved end mirror. The standard photodiode is a silicon p-i-n diode [62]) mounted in a disk-like aluminum housing designed to optimize the speed of the rising edge [63]. Risetimes of 1 ns were typical, even for 1 V signals into a 50 Ω load (a current risetime on the order of 2×10^7 Amp/sec). A second photodiode after the optical fiber was dedicated to the timing jitter suppression feedback system described in Section 2.2.3. Additional photodiodes are used for Pockels cell timing.

After the pulse selection Pockels cell, the rejected light was available to diagnostics of the oscillator spectrum. A grating spectrometer consisted of a fixed slit, a lens which imaged the slit onto a grating, and a second lens which imaged the diffracted light onto a pixel array (EG&G Reticon). The video trace from

---

[5] Ortel RLW-50s, 6 GHz, 75 ps FWHM

[6] Tektronix 11801 with SD-24 plug-in (20 GHz)

the array was displayed on an oscilloscope, see Figure 2.6(B). The resolution of the grating spectrometer was measured by turning off the RF power to the acousto-optic mode-locker so that the oscillator was free-lasing. Since the continuous lasing of Nd:YLF has a spectral width much narrower than the resolution of the instrument, the resulting spectrum is just the instrument resolution. The full-width at half maximum (FWHM) was approximately 0.40 nm, with a wider pedestal, probably from aberrations in the lenses. (see Figure 2.6(A).)

A commercial Optical Spectrum Analyzer (OSA) was also used to monitor the spectrum of the oscillator[7]. This device is a scanning grating monochromator, designed for a resolution of 0.08 to 0.1 nm, which agrees with the spectral width measured for the free lasing oscillator (Figure 2.6(C) linear scale, and (E) logarithmic scale). The spectrum of the mode-locked oscillator after the fiber is shown in Figure 2.6(D) linear scale and (F) log scale. Waveforms and measurements can be read over GPIB, such as the oscillator bandwidth FWHM (full width at the -3 dB point). The noise floor is approximately -70 dBm (0.1 nWatt).

The stretched, chirped oscillator pulses out of the fiber were compressed by a pair of gratings. A rotating-arm continuous-wave autocorrelator (CWAC) measured the autocorrelation of the compressed oscillator pulses [64]. The CWAC trace is a good diagnostic of the quality of the chirp and expansion from the fiber, since a nonlinear chirp gives large uncompressed wings, or pedestals, in the compressed pulse. However this is not necessarily an accurate representation of the amplified compressed pulse, because of gain narrowing. In Figure 2.8 we see a CWAC trace for which the infrared pulse is 1.8 ps FWHM (assuming a Gaussian pulse shape, the measured green width of 2.56 ps FWHM is divided by $\sqrt{2}$). Note there is also a broad pedestal. Similar autocorrelation widths have been obtained

---

[7] We acknowledge the loan of the Hewlett-Packard HP70951A Optical Spectrum Analyzer from R. Pasquinelli (FNAL).

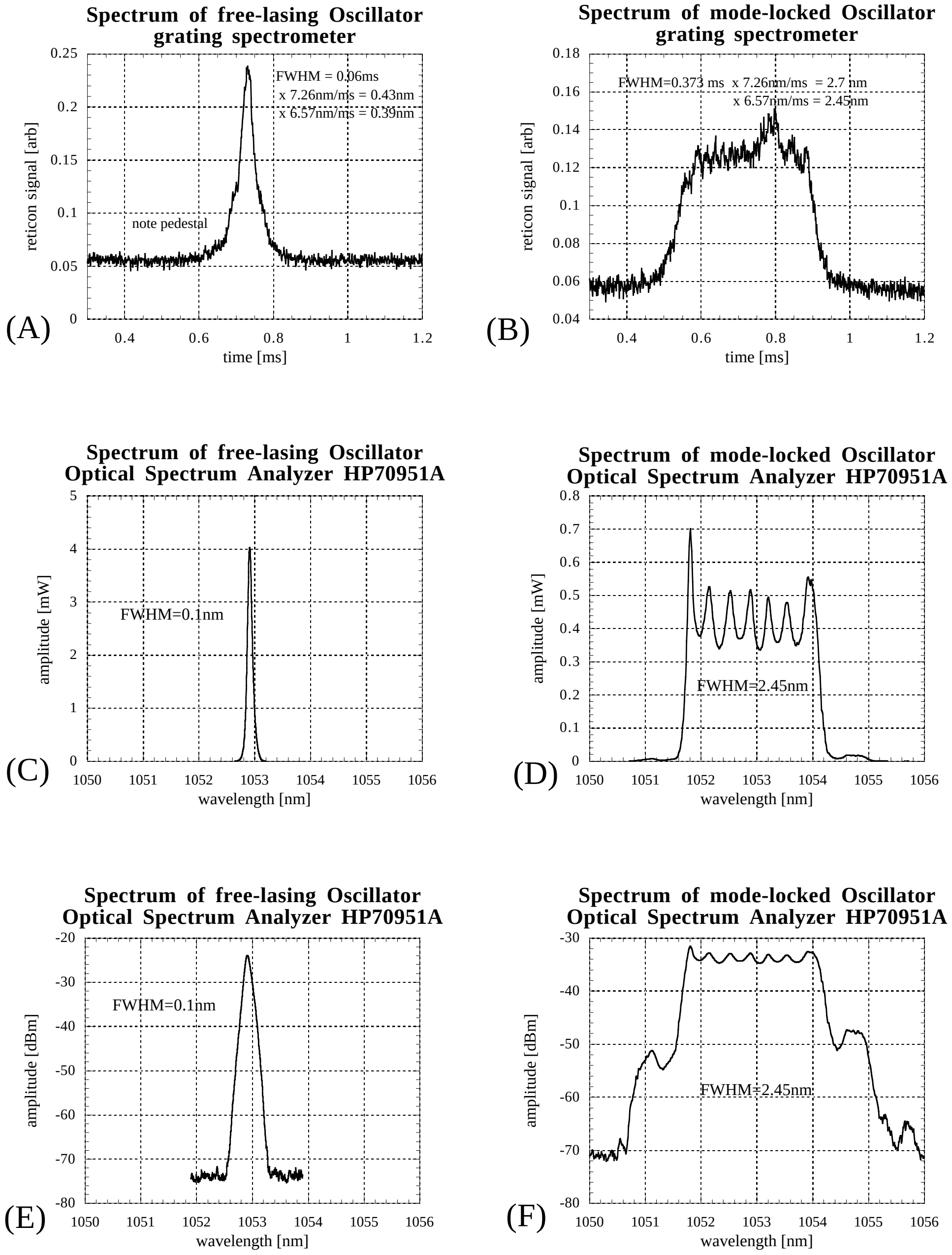

Figure 2.6: Comparison of the oscillator spectrum as measured by the grating spectrometer (A,B) and with the optical spectrum analyzer on a linear scale (C,D), and logarithmic scale (E,F). The oscillator is mode-locked on the right column (B,D,F) and free-lasing on the left column (A,C,E).

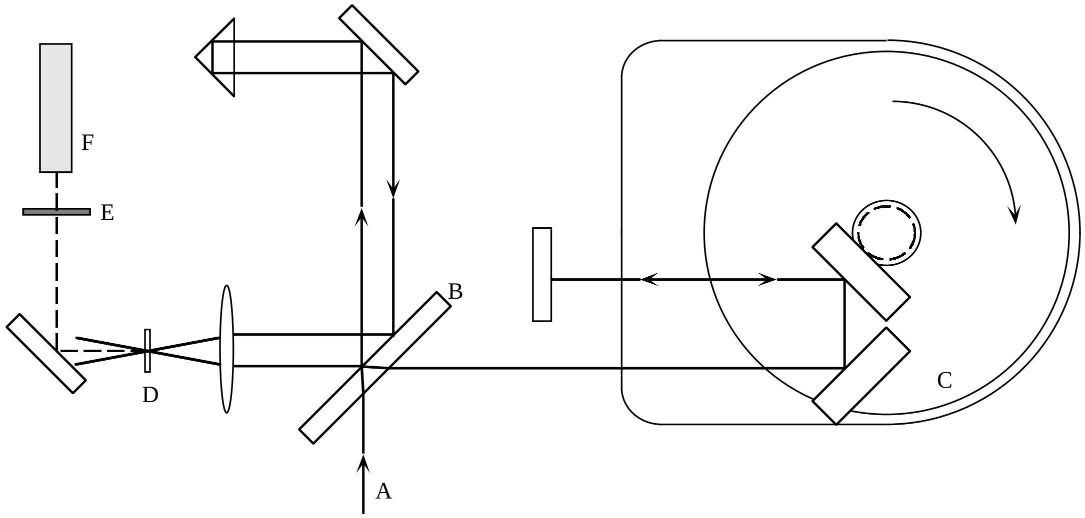

Figure 2.7: Schematic drawing of the continuous-wave autocorrelator (CWAC). The input beam (A) is divided by a beamsplitter (B) into a fixed arm and a variable delay arm on a rotating platform (C). The beams are crossed at a focus in a $LiIO_3$ crystal (D), and the green light is detected by a photomultiplier tube (F) after an infrared-blocking filter (E).

for the amplified pulse using a stepping autocorrelation measurement. (Figures 2.16 and 2.17)

A diagram of the CWAC is shown in Figure 2.7 A 50/50 beamsplitter sends light to a fixed delay arm and a variable delay arm, which is a mirror pair on a turntable spinning at 13.5 Hz. The two beams enter off axis in a focussing lens, and cross each other at a focus in a thin lithium iodate ($LiIO_3$) crystal. The crossing angle of the two beams allows phase matched non-collinear second harmonic generation ($\vec{k}_1 + \vec{k}_2 = \vec{k}_3$). The resultant green signal is background-free and is detected with a photomultiplier tube (PMT) and displayed on an oscilloscope. A trigger for the scope is from a photodiode (not shown) that detects a stray light beam at one particular angle of the rotating stage. The fixed delay arm is mounted on a short linear stage with a micrometer. It is used for calibration and to center the pulse overlap in the linear travel portion of the rotating stage.

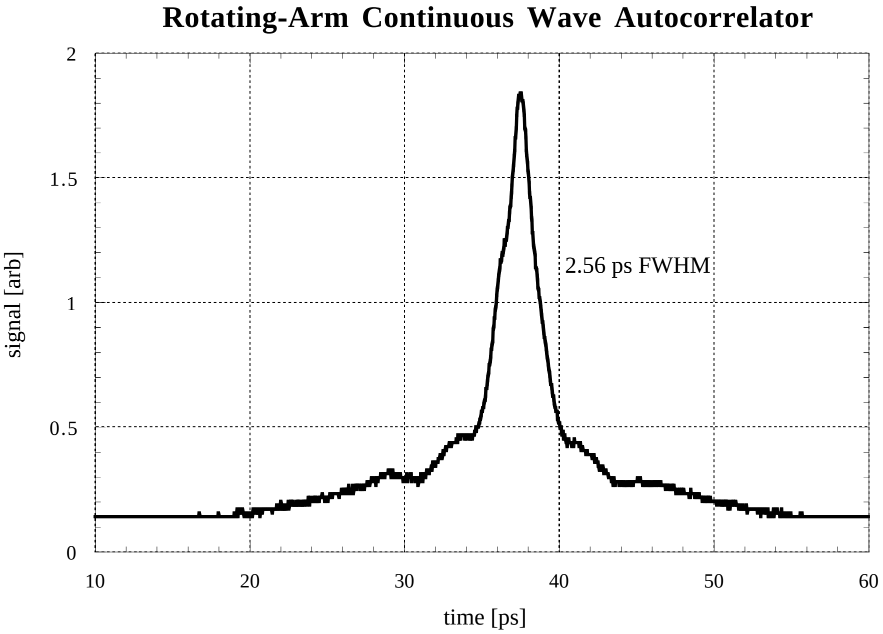

Figure 2.8: The compressed oscillator pulse length is measured by a continuous-wave autocorrelator (CWAC). The central spike has FWHM of 2.56 ps which implies for a Gaussian pulse shape that the infrared FWHM is 1.8 ps.

2.3 Pulse Selection

In order to select pulses from the oscillator for amplification, a fast optical switching element would have to discriminate between adjacent pulses 12.3 ns apart. A second fast optical switch is required for the multipass amplifier. Its function is to trap injected pulses into the cavity for amplification by N round trips and then to eject those pulses cleanly. In addition, the TESLA design of bursts of 1 MHz pulses would require that these switches and driver electronics be retriggerable in less than 1 μsec. An electro-optic modulator (EOM) or Pockels cell seemed the most promising approach.

Common commercial Pockels cells require driver electronics that switch several kilovolts to achieve the desired polarization retardation. High voltage electronic switches based on microwave triode tubes, for example, have long recovery times, and are limited to pulse repetition rates of the order of 1-10 kHz. For Pockels cells with transverse voltage applied, there is a trade-off that can be made, namely to decrease the voltage by reducing the aperture and lengthening the crystal.

With low-voltage Pockels cells, it is possible to use solid-state drive electronics, which are capable of MHz repetition rates. The pulse selection modulator[8] uses two crystals of lithium tantalate ($LiTaO_3$) with total length 80 mm, with a square aperture of 2.1 mm × 2.1 mm. The half-wave voltage (at 1053 nm) is merely 175 V. The driver uses high voltage bipolar transistors in a push-pull arrangement driving a 100 Ω transmission line.

The modulator in the multipass amplifier, the "Q-switch," must have a high threshold for optical damage. It is a cell of two KDP crystals[9] of total length 110 mm, and 175 V is sufficient for quarter wave retardation.

These devices use two crystal arrangements to provide cancellation of thermal drifts and static birefringence. Even so, the static birefringence is a sensitive function of the tip/tilt alignment angles, and a DC voltage is applied to the crystal to set the static operation point.

The pulse selection cell can make a narrow gate: a risetime of 8 ns, a 2 ns flat-top, and an 8 ns fall. The contrast between the selected pulse and the rejected pulses has been measured as high as 100:1 (20 dB). Typically the contrast was slightly less at 50:1 (17 dB). See Figure 2.9 for a photodiode waveform of the selected pulse.

Difficulties in using these cells arise primarily from the small aperture, and alignment problems. A square-aperture diffraction pattern is visible in the beam after the pulse selection. The single-pass transmission of the 110 mm long KDP cell was measured to be 90%. Including aperture losses, we measured between 70% and 78% on different days, depending on the mode-matching of the input

---

[8] M360-80, Conoptics, Inc.

[9] M350-105, Conoptics, Inc.

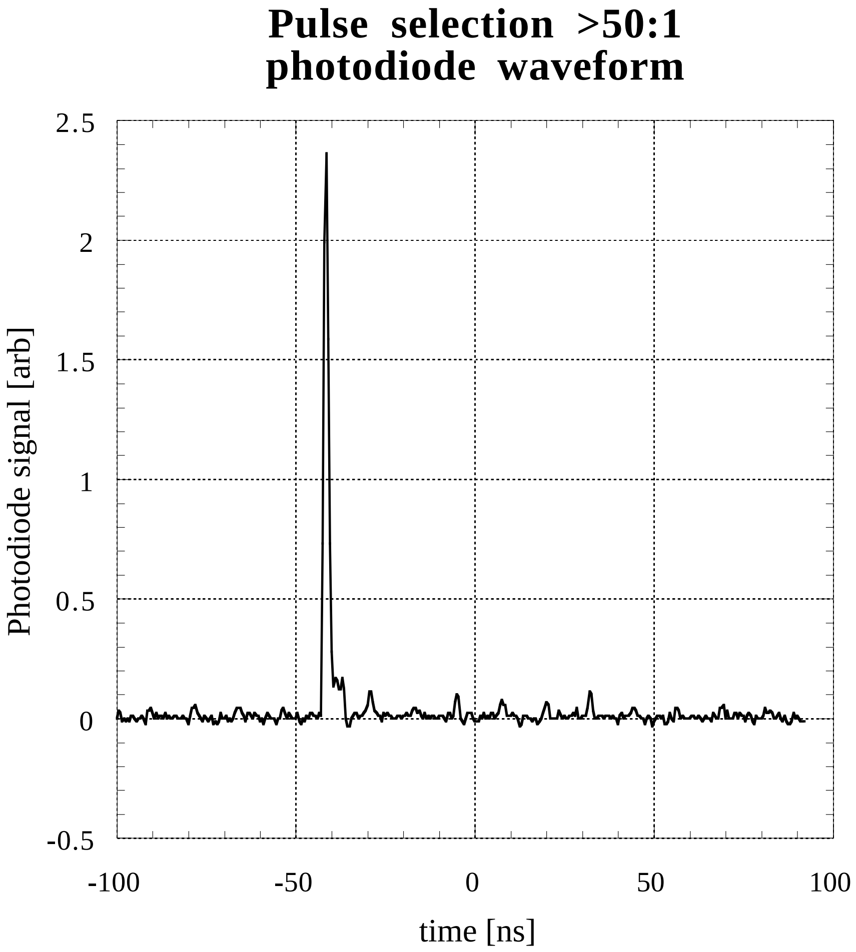

Figure 2.9: Pulse selection waveform with a FND-100 photodiode. The contrast is typically 50:1 to 100:1 when optimized.

beam. Implications of these losses to the multipass amplifier will be discussed in the next section.

2.4 Multipass Amplifier

A regenerative amplifier [65] is a laser resonator into which a small seed pulse is injected and amplified up to saturation. The output pulse energy in saturation is stable since all of the stored energy in the laser medium is depleted. Two additional characteristics of regenerative amplification are that the spatial profile of the output is independent of the input profile, and the pointing of the output ray is insensitive to small pointing perturbations of the input ray.

The last two characteristics can be explained simply. The input seed pulse can be represented as a linear combination of spatial modes of the resonator. The lowest order spatial mode is a Gaussian (TEM_{00}), and higher order modes have a larger spatial extent. With a limiting aperture in the cavity, usually an iris, the higher order modes will experience greater diffractive losses and will be suppressed. Provided there is some overlap of the injected seed pulse with the TEM_{00} mode, this component will experience the greatest exponential gain and, after a large number of round trips in the cavity, will dominate the output.

A multipass amplifier resembles a regenerative amplifier, except that the amplified pulse is ejected after a *fixed* number of round trips in the cavity, as required for fixed external timing. Because of the pulse train operation, the number of round trips is much less than that necessary for saturation. We found that for 14 round trips, the spatial profile on the output and the pointing on the output are not sensitive to the input.

Figure 2.10 shows how the pulses are switched into and out of the multipass cavity. The KDP electro-optic modulator (Q-switch) is statically biased for quarter wave. When the Q-switch is not fired, every laser pulse that enters by reflection

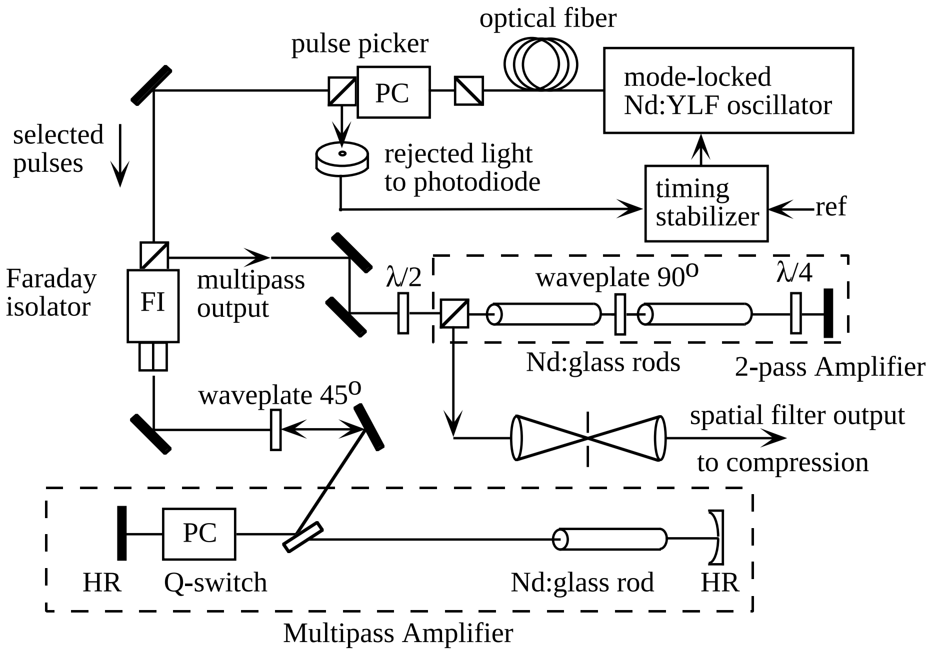

Figure 2.10: Schematic of the laser amplifiers.

off the Brewster-angle thin film polarizer (TFP) is vertically polarized. Then the pulse passes through the Q-switch, acquires a quarter-wave retardation (to circular polarization), is reflected from the end mirror, and passes again through the Q-switch acquiring a further quarter wave retardation to horizontal linear polarization. The pulse will then pass through the TFP and continue through the cavity, and after two passes through the rod, it passes through the TFP and back through the Q-switch. It acquires two more quarter-wave retardations returning to vertical polarization and exits the cavity by reflection from the TFP.

The Q-switch electro-optic modulator is fired to trap the selected pulse inside the cavity. After acquiring two quarter-wave retardations and passing through the TFP, the selected pulse takes about 8 ns to return to the Q-switch (total round trip time in the cavity is 10.4 ns). During this time, the voltage on the modulator is raised so that the retardation is zero-wave, and the pulse is trapped in the cavity. The voltage is held high for the length of time necessary for the desired number of round trips (typically 128.4 ns for 14 round trips). There is another 8 ns window to lower the voltage, and the amplified voltage is then ejected. A Faraday isolator[10] using permanent magnets [66] is used to separate the input and output beams. The measured isolation ratio of the Faraday isolator is 43 dB.

The risetime of the modulator is 8 ns, which is adequate. However, the falltime is slightly worse, and this results in incomplete switch-out of the amplified pulse, with small satellite pulses 10.4 ns before and after the main pulse. It is desired to suppress these satellite pulses as much as possible. The vendor rebuilt one modulator and achieved moderate improvement. The falltime degradation may be caused by leakage current.

In principle, the cavity length of the multipass could be lengthened to accommodate a longer fall time. With longer L, the mode volume increases, which gives better filling of the rod, but higher diffraction losses on the very small (2.1 mm

---

[10] Optics for Research, model IO-5-YAG-HP

× 2.1 mm) aperture of the Q-switch modulator. Longer resonators, in general, also suffer higher sensitivity to mechanical vibration and misalignment. The retriggering deadtime of the electronics[11] favors a shorter round trip time (shorter resonator) for the same number of gain passes. The choice of the resonator length L for a 10.4 ns round trip time is a compromise, and we have further chosen this time to be incommensurate with the period of the RF, so that the satellite pulses are not accelerated at the same RF phase for which the main pulse is accelerated.

There are two regimes for operation of the multipass amplifier. The first is long pulse trains, up to 800 μsec, and the other is short pulse trains, typically 10 to 100 μsec. For constant beam-loading in the superconducting cavities, the TESLA design needs every pulse to be the same intensity.

For long pulse trains, the primary interest is in a flat envelope, that is, each pulse has equal intensity, or the envelope has an exactly rectangular profile. We have observed that fluctuations from micropulse to micropulse are correlated with intensity fluctuations from the oscillator. A curved envelope on the output of the amplifiers is a direct result of the gain dynamics, and is influenced mainly by the flashlamp pump profile, but also by fluorescence (spontaneous emission) and by gain depletion from the presence of laser radiation. Amplified spontaneous emission (ASE) is not an important parasitic loss [67] for the laser system described here.

The gain dynamics can be modeled using a Frantz-Nodvick type solution to the rate equations [68]. When the lifetime of the lower laser level is too long to be treated as instantaneous, the Frantz-Nodvick approach is inappropriate. For Nd:YLF, the lifetime of the terminal $^4I_{11/2}$ level is 21.6 ns [69], while published values for Nd:glass of the same level vary from 10 to 100 ns [49]. Numerical solutions to the full rate equations including the lower level lifetime have been

---

[11] DG-535, Stanford Research Systems, Sunnyvale CA

used by Skeldon *et al.* [70] to model gain dynamics in a regenerative amplifier. Shot-to-shot variations in the total pulse train energy must also be minimized.

Will *et al.* [42] present analytic and numerical modeling of the gain dynamics of an idealized four-level laser system for uniform pumping. They show that the timing of the beginning of the flashlamp discharge relative to the laser pulse train has a large effect. For the lamps firing too late, the upper laser level (and the gain) is still increasing, and early pulses are amplified less than following ones, with an exponential relaxation to a steady-state: the envelope is curved with an upward increasing profile. Similarly, for the lamps firing too early, the gain has been pumped higher than can be maintained in the steady state. At a critical matching point, the energy taken out by laser amplification (and spontaneous emission) is exactly balanced by the pumping, and a flat pulse train is achieved.

Will *et al.* implemented a feedback system onto the flashlamp power supplies to correct for the inevitable departures from this idealized model. The “droop,” or tilt, of the flashlamp current at late times in the flashlamp discharge must be compensated. Will *et al.* used power supplies with integrated-gate bipolar transistors (IGBT’s) as the high-current switch. Using these switches in a linear (rather than binary) regime allowed feedback control with an arbitrary waveform generator and a learning algorithm. Because the next shot is corrected based on the previous n shot(s), this scheme is sometimes called “feedforward.” A similar system could be added to the power supplies used in the laser system described here, since IGBT switches are used as well.

A group at ELSA (Etude d’un LaSer Accordable) [41] used loss-modulation with a transverse-field electro-optic modulator at the output of their laser system to achieve a pulse train with a rectangular envelope. A photodetector upstream of the modulator picks up information about a particular pulse in the envelope, and this information is used to correct the next few pulses. This system is limited by optical damage to the modulator, and also suffers from low transmission (50% or worse).

The envelope flattening system used here is similarly based on electro-optic loss-modulation, but *before* the amplifiers. Results are given in Ref. [43]). A transverse-field electro-optic modulator is placed after the pulse selection cell, and is driven by a DAC card used as an arbitrary waveform generator (200 kHz bandwidth). The cell pre-shapes the input pulse-train to recover a flattened pulse train on the amplifier output. By placing the cell in a low-intensity laser beam, the limitation of optical damage disappears. However, the energy losses remain high for flattened outputs of the full 800 μsec pulse trains.

For machine protection reasons, the photoinjector often operated with much shorter pulse trains of 10 to 50 μsec. In this case, we have found it unnecessary to use the envelope shaping system, since acceptably flat envelopes can be made by simply adjusting the flashlamp timing. We have also achieved good results without the envelope-shaping cell for pulse trains as long as 100 to 200 μsec. Figure 2.11 shows a typical photodiode waveform for 200 UV pulses. There is some loss of resolution on the scope display and screen capture. Digital aliasing in the display and real amplitude noise both contribute about equally to the apparent fluctuations. This data was taken without the flattening system running (cell removed).

Typically, the multipass amplifier produces output energies of 120 μJ per pulse for an input pulse energy of approximately 2 nJ. This is a net gain of 6×10^5 in 14 round trips, or 1.48 for the net single pass gain. The net gain includes the cavity losses, and if the aperture losses from the Pockels cell are the dominant loss (described in Section 2.3) which we measured to have 78% transmission in single-pass, then the gross single pass gain could be $\sim$2.4, which is similar to the performance of the two-pass rod amplifiers and also agrees with the expectations based on the lamp input power and tabulated pumping efficiencies. The square

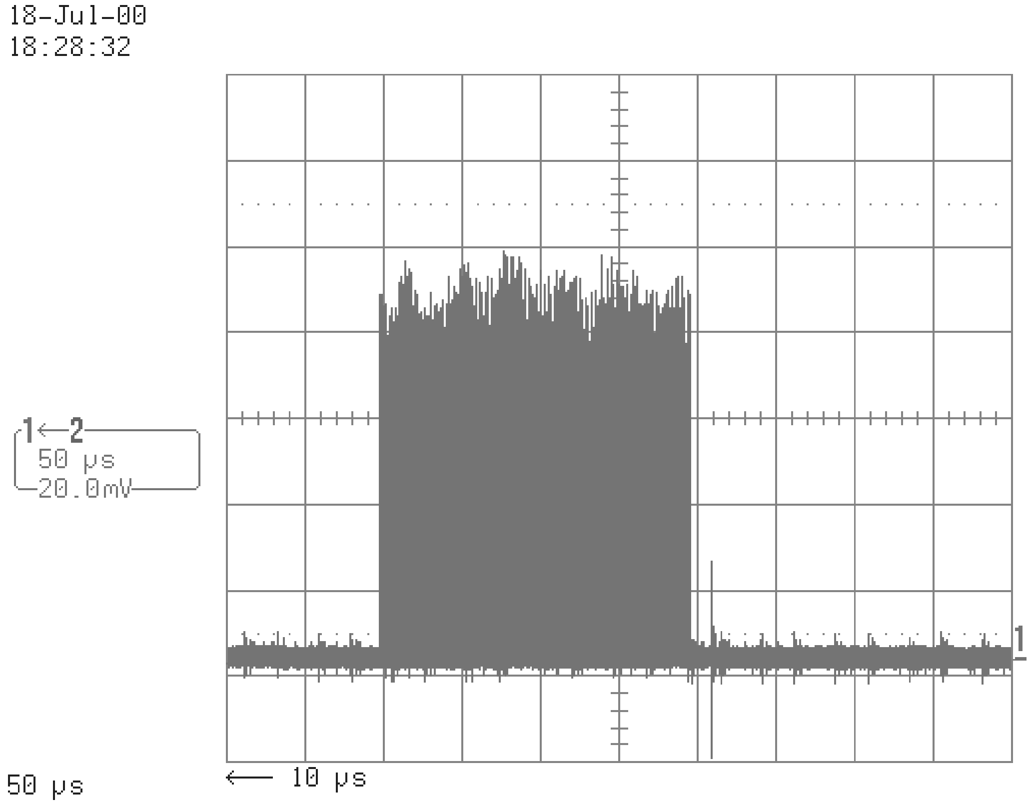

Figure 2.11: Screen capture of UV pulse train waveform from a photodiode, 200 pulses long (Horizontal axis: 50 μsec per division).

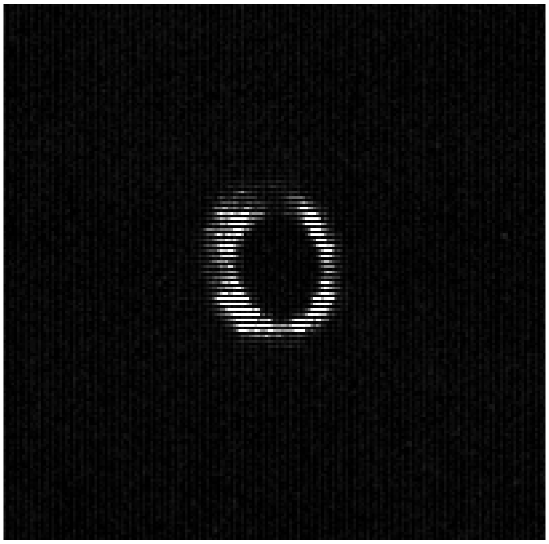

Figure 2.12: Effect of square Pockels Cell Aperture. The multipass beam as viewed on an alignment pinhole shows square corners.

aperture of the Pockels cell is likely the limiting aperture of the cavity. In support of this claim, we note that the radius of the circular iris in the cavity intended for mode selection can be adjusted over a reasonable range with little effect on the output. Also, if the bright central portion of the beam is passed through an alignment iris, square corners in the beam profile are barely discernible as the iris diameter is reduced so it clips the edges of the beam, shown in Figure 2.12.

2.5 Two-pass amplifier

The final gain stage after the multipass amplifier is a birefringence-compensated two-pass amplifier. The two-pass does not require any active optical switching. Light from the multipass amplifier is sent through a Brewster-angle thin-film polarizer (TFP), then through two Nd:glass rods. A quarter-wave plate and a mirror retroreflects the laser a second time through the rods, where it is now ejected by the polarizer. A depiction of the layout is shown in Figure 2.10.

In this scheme the thermal birefringence of the rods causes some power to be coupled into the orthogonal polarization state, which is lost on the polarizer. The beam shape is also distorted by this loss, giving the well-known "Maltese cross" pattern. We have characterized the depolarization in the 10 mm diameter glass rod at different average pumping powers by passing an expanded HeNe laser through the rod with crossed polarizers on either side. The beam was viewed on a white card with a CCD camera. Images were digitized with a frame grabber card and saved to disk (shown in Figures 2.13 and 2.14). Note that some speckle from the HeNe laser can be seen in these images.

The lamps were turned on, and images taken after reaching thermal steady-state. After stopping the lamps, the beam distortion was observed to take approximately 2 minutes to become very faint and disappear. The thermal relaxation time constant for a rod of radius r_o is $\tau = r_o^2 C_p \rho / K$ [49, 71]. With the specific heat of LG-760 glass $C_p = 0.57$ J/(g °C), the density $\rho = 2.60$ g/cm^3, and the thermal conductivity $K = 0.67$ W/m °C, we find $\tau = 55$ sec for the 10 mm diameter rod and $\tau = 20$ sec for the 6 mm diameter rod.

The Maltese cross pattern arises from the thermal stress-induced birefringence (the photoelastic effect) of the glass. Neglecting the variation with the rod length z, the isothermal contours are concentric circles. The local optical indicatrix will adopt the same symmetry, and for light propagating along the z-axis, the changes in refractive index for polarization along the $\hat{\mathbf{r}}$ and $\hat{\boldsymbol{\phi}}$ directions is given by [49]:

$$\Delta n_r(r) = -\frac{1}{2} n_0^3 \frac{\alpha Q}{K} C_r r^2 \tag{2.13}$$

$$\Delta n_\phi(r) = -\frac{1}{2} n_0^3 \frac{\alpha Q}{K} C_\phi r^2 \tag{2.14}$$

with α the thermal expansion coefficient, Q the thermal loading in W/cm^3 and C_r

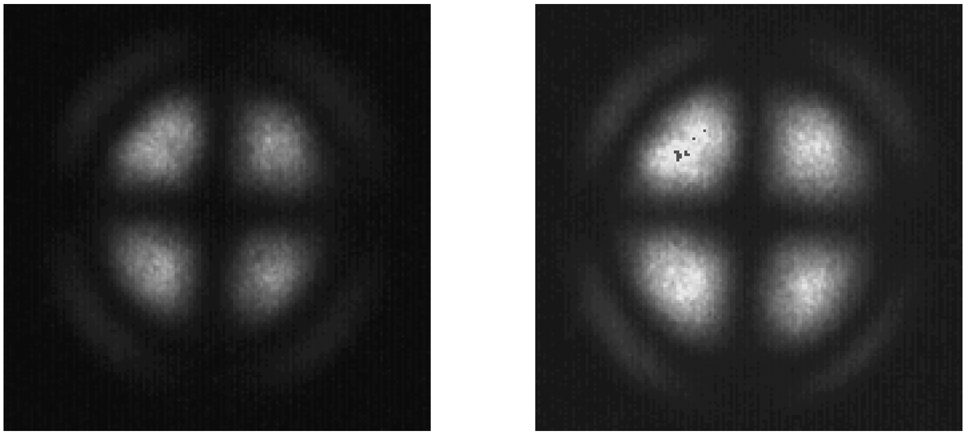

2-pass 511V 130J 1.1ms

2-pass 599V 100J 0.55ms

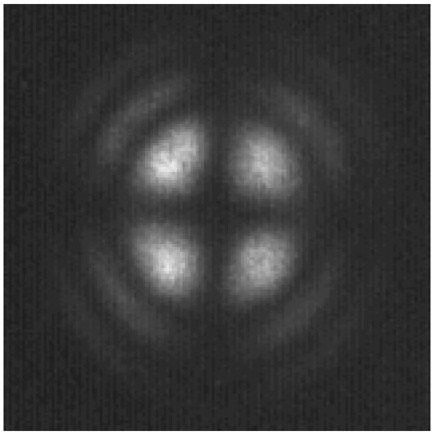

2-pass 599V 200J 1.1ms Birefringence

Figure 2.13: Thermal birefringence in the 10 mm rod

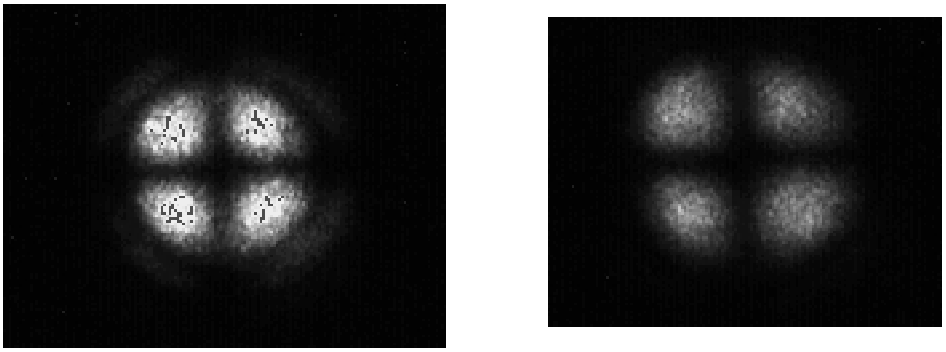

MP 599V, 1.1ms birefringence

MP 511V 1.1ms biref

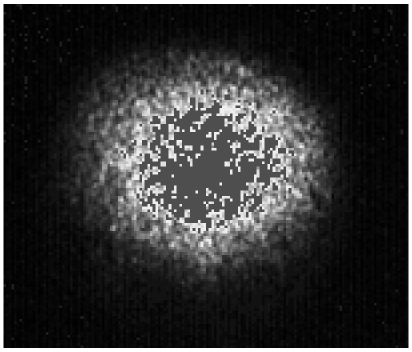

MP cold

Figure 2.14: Thermal birefringence in the 6 mm rod

and C_ϕ are functions of the elasto-optical coefficients, and can be found in Uppal *et al.* [72] for glass.

When the birefringent rod is viewed between a polarizer/analyzer pair, the transmitted intensity is [73]

$$I_{\text{out}}(r,\phi) = I_0\left[1 - \sin^2(2\phi)\,\sin^2(\delta/2)\right] \tag{2.15}$$

where the angular coordinate of the rod ϕ is now referenced to the polarizer, and the polarization phase shift δ is

$$\delta(r) = \frac{2\pi}{\lambda} L\left(\Delta n_\phi(r) - \Delta n_r(r)\right). \tag{2.16}$$

It is seen that the dependence on $\sin^2(2\phi)$ gives the four-lobed pattern, while the r^2 dependence of δ is the origin of radial nodes.

This birefringence can be partially compensated for a system of two identical rods by inserting a 90° polarization rotator between the two rods. This interchanges the $\hat{\mathbf{r}}$ and $\hat{\boldsymbol{\phi}}$ directions so that the birefringence of one rod cancels that of the other [49] Further improvements are possible, such as to incorporate a phase conjugate mirror to correct phase-wavefront distortions.

The improvement from birefringence compensation is found by measuring the energy throughput of the spatial filter immediately after the two-pass amplifier both with and without the 90° rotator. Note that reduced energy losses from depolarization as well as reduced spatial filter losses from the improved spatial profile both contribute. We found the energy after the spatial filter was typically 20–25% higher with the 90° rotator than without. The two rods used in the birefringence-compensated amplifier are not identical, so the larger diameter rod is operated at a lower pump power for better cancellation of the smaller rod.

2.6 Pulse Compression

As discussed in Section 2.2.5, the laser pulses after the fiber have an increased bandwidth from self-phase modulation and this bandwidth is linearly swept in time, or chirped, over the pulse length due to group velocity dispersion in the fiber.

Treacy [74] showed that the group velocity dispersion of a pair of parallel diffraction gratings is negative and linear, and it is opposite in sign to the positive group velocity dispersion (GVD) introduced by the fiber. Therefore, the parallel gratings in the Treacy geometry act as an optical pulse compressor, correcting to first order (compensation to third order is described by, for example, Refs. [61, 75] and references therein).

In the parallel configuration of Treacy, shown in Figure 2.15, the dispersion for a double pass is given by

$$\frac{dt}{d\lambda} = \frac{2}{c}\frac{(\lambda/d)(L/d)}{\cos^3\theta_{out}} = \frac{2}{c}\frac{(\lambda/d)(L/d)}{[1-(\sin\theta_{in}-\lambda/d)]^{3/2}} \tag{2.17}$$

where the grating spacing d is given by $d^{-1} = 1700$ lines/mm. Clearly, the grating spacing L and the angle of incidence are the critical parameters.

We measured the duration of the compressed IR pulse by autocorrelation [76] with non-collinear second harmonic generation. The autocorrelation of a function $f(t)$ is

$$G(x) = \int_{-\infty}^{+\infty} f(t)\, f(t-x)\, dt \tag{2.18}$$

Since the autocorrelation function is necessarily symmetric, $G(-x) = G(x)$, the limitations of this technique include the inability to interrogate pulses that are asymmetric in time, nor can the pulse shape be found. Modern methods utilizing time-frequency distributions [77, 78] for pulse reconstruction (such as FROG [79]

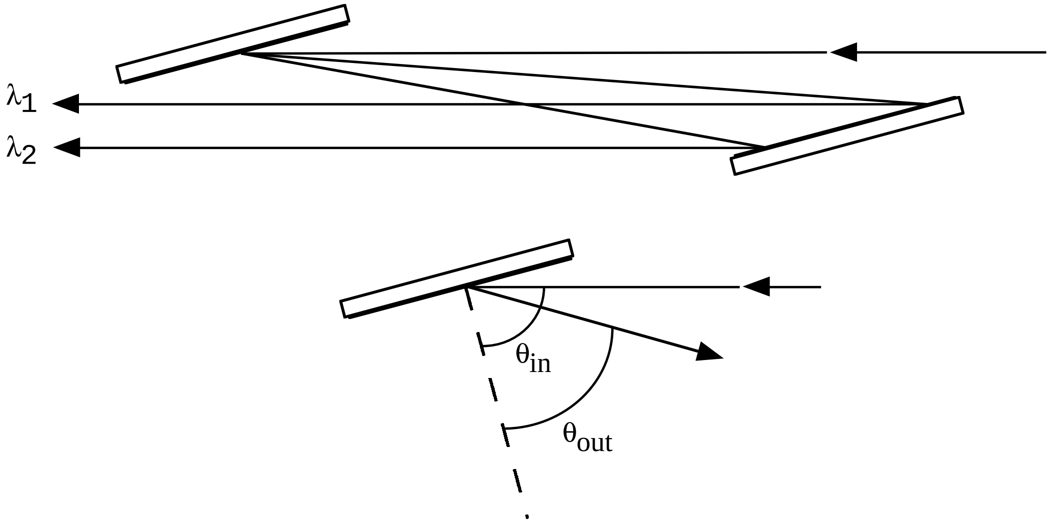

Figure 2.15: First-order grating compression in the geometry of Treacy [74].

and the self-referencing interferometric technique SPIDER [80, 81]) have become important for femtosecond pulses. These methods allow pulse reconstruction with amplitude and phase information. Autocorrelation with SHG allows an estimation of the pulse length (assuming the pulse *shape*).

In Figure 2.16 is a typical stepping autocorrelation of the compressed IR pulse. The green pulse is fitted to $\sigma = 1.32$ ps. Assuming a Gaussian pulse shape, the autocorrelation width is $\sqrt{2}$ times the actual width, so the IR is 0.93 ps σ_t or 2.2 ps FWHM. In Figure 2.17 is shown the autocorrelation versus the oscillator spectral bandwidth.

2.7 Harmonic Generation

The work function of Cs_2Te photocathodes is 3.5 eV, so the cutoff wavelength is well into the ultraviolet. Using two stages of second harmonic generation we

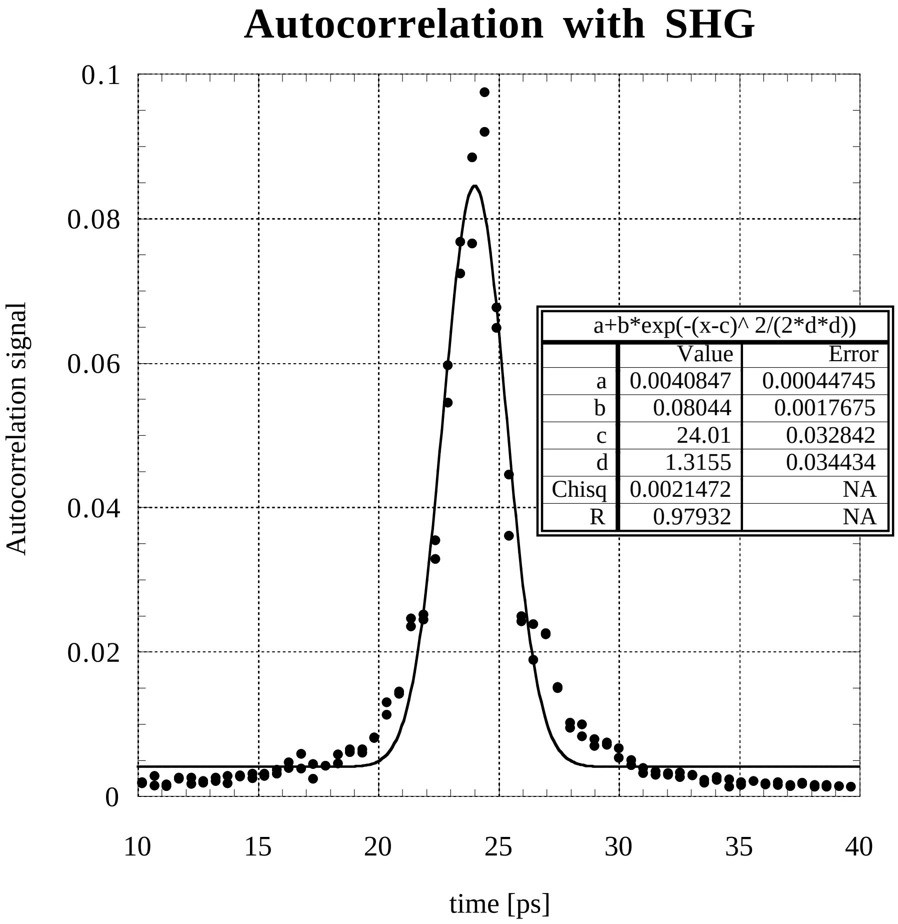

Figure 2.16: Stepping autocorrelation by SHG. Assuming a Gaussian pulse shape, the amplified IR is 2.2 ps FWHM.

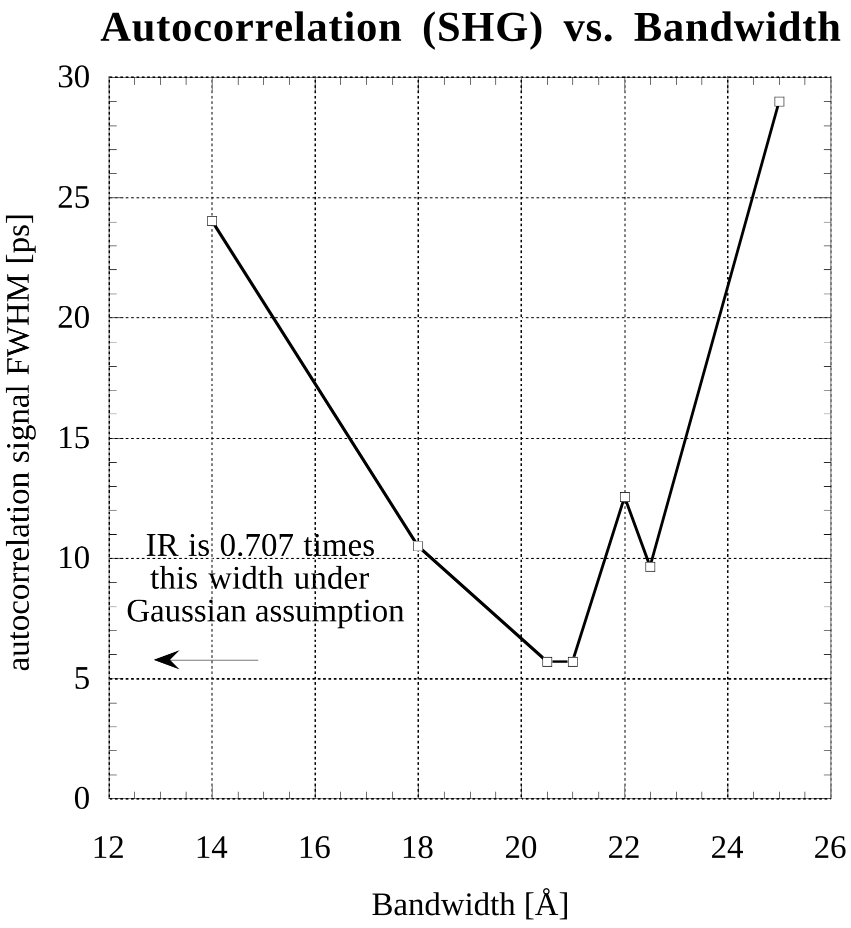

Figure 2.17: Autocorrelation vs. Bandwidth

convert the compressed infrared pulses at $\lambda = 1053$ nm to the fourth harmonic at 263.5 nm. The typical overall conversion efficiency is $\eta_{41} = 5$ %.

Second harmonic generation (SHG) is the degenerate case of nonlinear optical three wave mixing. A full theoretical treatment is given in many standard texts, for example, Yariv [82]. (See also Section 5.2 on page 133.)

The first stage of conversion is a type II BBO crystal (β-barium borate, or β-$BaBO_3$) of dimensions $5 \times 5 \times 10$ mm. BBO is a good choice because of the high nonlinear coefficient, and the large frequency acceptance for phase-matching. However, the angular acceptance is small, and we have found that the collimation of the infrared is critical to achieving good efficiency. For a compressed infrared pulse of mean energy 590 μJ on the input, the mean energy of the green pulse ($\lambda = 532$ nm) was 200 μJ, giving a conversion efficiency of $\eta_{21} = 33\%$.

The green light is converted to ultraviolet (UV) in a type I BBO crystal of dimensions $5 \times 5 \times 10$ mm. There are very few other choices of crystals for harmonic conversion into the ultraviolet, but again, BBO is a good choice for the same reasons of a high nonlinear coefficient, and a large frequency acceptance for phase matching. Again, we have found that the small angular acceptance means that careful collimation of the input beam is crucial for high efficiency SHG. For 200 μJ of green incident on the crystal, the UV mean energy is 40 μJ, so the efficiency from green to UV is $\eta_{42} = 20$ % and the efficiency from IR to UV is $\eta_{41} = \eta_{42}\eta_{21} = 6.7$ %.

More typical values for short pulse trains would be 200–250 μJ of IR and 10–15 μJ of UV per pulse, and $\eta_{41} = 4$–6 %.

Immediately after the compression gratings, (section 2.6) the beam is down-collimated in a 2.5:1 telescope (+500mm, -200mm). Then two turning mirrors steer the beam through both crystals which are mounted as close together as possible. The distance between the last lens of the telescope and the first crystal was made as short as possible, because diffraction increases the spot size. The optimal collimation is that for which the waist is between the two crystals, and the lens spacing was varied to find the best setting, based on measurements of the conversion efficiency. This measurement requires iterative alignment of the input angle to the telescope, beam steering out of the telescope and adjustment of the tip/tilt angles of the crystals, mostly to correct small centration errors in the lenses.

2.8 UV temporal pulse shaping

The optimal UV laser pulse length on the cathode depends on the required emittance and bunch length. A longer laser pulse will reduce the charge density at the cathode. Since the space-charge induced emittance growth of the beam from the Coulomb force is canceled like $1/\gamma^2$ (by the self-magnetic field of the beam), reducing the charge density of the beam where γ is small should reduce the emittance.

However, if the pulse-length is too long compared to the RF period, then effects of RF curvature also cause deleterious effects such as a nonlinear energy-phase correlation (which is difficult to compensate), as well as emittance dilution (RF-curvature induced emittance growth).

Pulse shaping in the UV is done by interferometrically combining four copies of the short laser pulse (with appropriate delays) in a “pulse stacker.”

2.8.1 Pulse Stacker

The pulse stacker is adapted from a design used by D. Reis [83] and is similar to that reported by Siders *et al.* [84] and Park *et al.* [85]. The input pulse is split into several copies (2^p copies, in this case) which are separately delayed and recombined.

Our version is a compact arrangement of small (0.5”) right-angle prisms on translation stages about a single large (4") beamsplitter. There is space to mount up to eight prisms, (four pairs of delay lines), which can stack $2^4 = 16$ pulses, although we found adequate results with four prisms (two pairs of delay lines and four stacked pulses). See Figure 2.18 for a drawing of the pulse stacker. The assembly is compact, fitting on a mounting plate that is 12" square.

There are two output beams from the pulse stacker, only one of which is used, so the throughput is < 50 % (typ. 46%). The two output beams could be re-combined with orthogonal polarization in order to achieve high throughput.

There are two main issues that must be addressed in using the pulse stacker. The first is the presence of interference fringes in the time domain, and the second is pointing of each of the stacked pulses.

We wish to show the validity of the envelope approximation for photocathode excitation with stacked pulses. If the input pulse (to the pulse stacker) is described by the analytic signal $s(t)$, the total energy of this pulse is the integral of the energy density $u(t)$.

$$U = \int_{-\infty}^{+\infty} u(t)\, dt = \int_{-\infty}^{+\infty} |s(t)|^2 \, dt \tag{2.19}$$

In this case the analytic signal is proportional to the electric field. For a pulse with a Gaussian envelope, we choose the signal following the notation of L. Cohen [77, 78],

$$s(t) = \left(\frac{\alpha}{\pi}\right)^{1/4} \exp(-\alpha t^2/2 + i\omega_o t). \tag{2.20}$$

The output pulse is a sum of delayed copies of $s(t)$ summed interferometrically. For p pairs of delay arms (with delay d_n), there are $N = 2^p$ pulses:

$$u_{\text{out}}(t) = \frac{1}{2}\left(\frac{1}{\sqrt{2}}\right)^{2p} \left|\sum_{n=1}^{N} s(t + d_n)\right|^2 \tag{2.21}$$

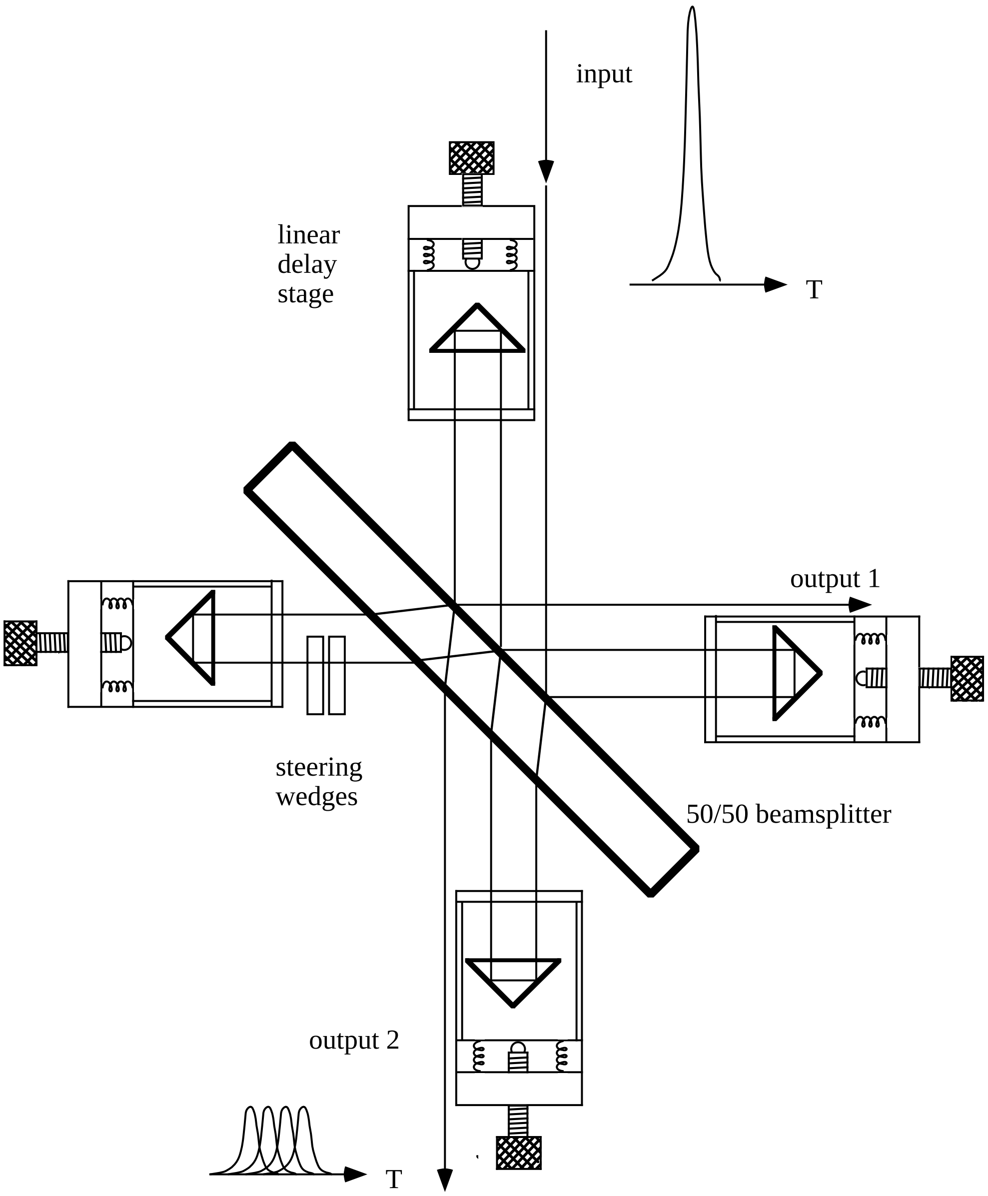

Figure 2.18: Pulse stacker with two pairs of arms. The steering wedges are used to correct for small variations in the apex angle of the prisms.

We can expand this sum into diagonal elements and cross-terms:

$$\left|\sum_{n=1}^{N} s(t+d_n)\right|^2 = \sum_{n=1}^{N} |s(t+d_n)|^2 + \sum_{n=1}^{N} \sum_{m<n}^{N} 2\,\Re[s(t+d_n)\,s^*(t+d_m)] \qquad (2.22)$$

where $\Re$ denotes the real part. The first term is just the individual pulse envelopes at the delayed times, while the second term contains the interferences. For $s(t)$ of the form of Equation 2.20 the interference terms cannot be neglected, and will contain a $[\cos\omega_o(d_m - d_n)]$ term. In general, we see that the pulse structure depends on the relative phase shift between overlapping pulses. Siders *et al.* [84] give cross-correlation data that shows addition of in-phase pulses to create a flat top or super-Gaussian pulse, and addition of pulses π out of phase to create a dark pulse. D. Reis [83] used a pulse stacker to create a pair of infrared pulses before a regenerative amplifier, and after compression and fourth harmonic generation, interference effects were observed using a streak camera.

Siders *et al.* [84] mention that the phase difference between pulses reflected and transmitted from a dielectric beam splitter is approximately π. For the geometry we have chosen, the adjacent pulses always suffer a relative phase shift of 0 or 2π, and so are always in phase, and give a flat top or super-Gaussian profile. The phase differences between the stacked pulses is still sensitive to the relative delay through the $\cos\omega_o(d_m - d_n)$ term.

We did not observe any interference effects using a streak camera. It may be that any interference fringes are "fast beats" and are averaged out to zero by the limited ($\sim$ 1 ps) time resolution of the streak camera. We should also note that the "prompt" photoemission response time of the Cs_2Te photocathode in the gun is estimated to be of order $\tau_{\mathrm{pe}} \sim 100$ fs. This estimate is made as follows. Take the laser absorption depth to be $d = 30$ nm. Then electrons liberated at rest throughout this depth are accelerated ballistically by a field $|E| \sim 35$ MV/m, which takes a time to exit the surface of $\tau_{\mathrm{pe}} \sim \sqrt{2md/qE} \sim 100$ fs. The optical period at 263.5 nm is $T_{opt} = 0.88$ fs, so that fast beats at the optical period or as slow as 50 T_{opt} will be averaged out to zero.

To make this argument more concrete, consider the effect of an averaging time δt on the interference terms. The energy density $u(t)$ of Equation 2.19 is replaced by

$$u_{\delta t}(t) = \frac{1}{\delta t}\int_t^{t+\delta t} u(t')\,dt' = \frac{1}{\delta t}\int_t^{t+\delta t} |s(t')|^2\,dt' \ . \tag{2.23}$$

We then re-calculate the off-diagonal terms in Equation 2.22 which are

$$g_{nm,\,\delta t}(t) = \frac{1}{\delta t}\int_t^{t+\delta t} 2\,\Re\left[s(t'+d_n)\,s^*(t'+d_m)\right]\,dt' \ . \tag{2.24}$$

One way to represent the beating of stacked pulses is to give each pulse a frequency chirp, so that the overlapping region is the intersection of different ends of the frequency chirp. Then we write

$$s(t) = \left(\frac{\alpha}{\pi}\right)^{1/4} \exp(-\alpha t^2/2 + i\beta t^2/2 + i\omega_o t) \tag{2.25}$$

Where β represents the residual chirp from imperfect compression or from material dispersion (in the prisms and beamsplitter, for example). The crossterms are negligible for a condition on β. We find:

$$g_{nm,\,\delta t}(t) \sim 0 \qquad \text{if} \qquad \frac{1}{\sqrt{\alpha}} \gg \delta t > \frac{2\pi}{\beta(d_n - d_m)} \tag{2.26}$$

In order to put in the numbers, we make some estimations of a reasonable chirp β for the UV pulse, assuming that the ratio $(\delta\omega/\omega_o)$ for the IR pulse is the same as for the UV, and assuming that the bandwidth $\delta\omega$ is chirped linearly over the

UV pulse length. Then the condition (Eq. 2.26) for the cross-terms to vanish is:

$$1.9 \text{ ps} \gg \delta t > 370 \text{ fs} \tag{2.27}$$

The estimate we made earlier of the photoemission time ($\tau_{\rm pe} \sim 100$ fs) is not far off from that which is required of δt for no beats to be resolved.

2.8.2 Measurements of the Laser Temporal Profile

The laser temporal profile was measured using a Hamamatsu C5680-21S streak camera with M5676 fast sweep module and a Pulnix progressive scan CCD camera.[12] The principle of streak camera operation is depicted in Figure 2.19. Light enters a slit and is focussed onto a photocathode. Photoelectrons are accelerated out of the cathode, and an extremely fast voltage sweep is applied to deflecting electrodes, giving a time-dependent deflection. The electrons strike a microchannel plate (MCP) which is an electron multiplier [86–88]. The MCP consists of many thin glass tubes or channels with internal diameters typically 10–20 μm. The inside walls of these tubes are coated with a material with high secondary electron yield. Initial electrons collide with the walls, liberating several electrons, which in turn liberate even more. The avalanche of electrons strikes a phosphor, converting to visible light and the phosphor image is digitized with a CCD camera.

Because of the high gain in the MCP, great care must be taken to prevent damage with too much incident light. The limiting time resolution in a streak camera has several contributions: wavelength dispersion of the light in the input optics, spatial spread (slit width), the limited spatial resolution and deflection speed, and space-charge broadening inside the streak tube. The space-charge broadening, also called the intensity dependence of the time resolution can be quite dramatic for measurements of the UV laser pulses, and the laser must be

---

[12] We thank A. Hahn, FNAL Beams Division, for the loan of the streak camera

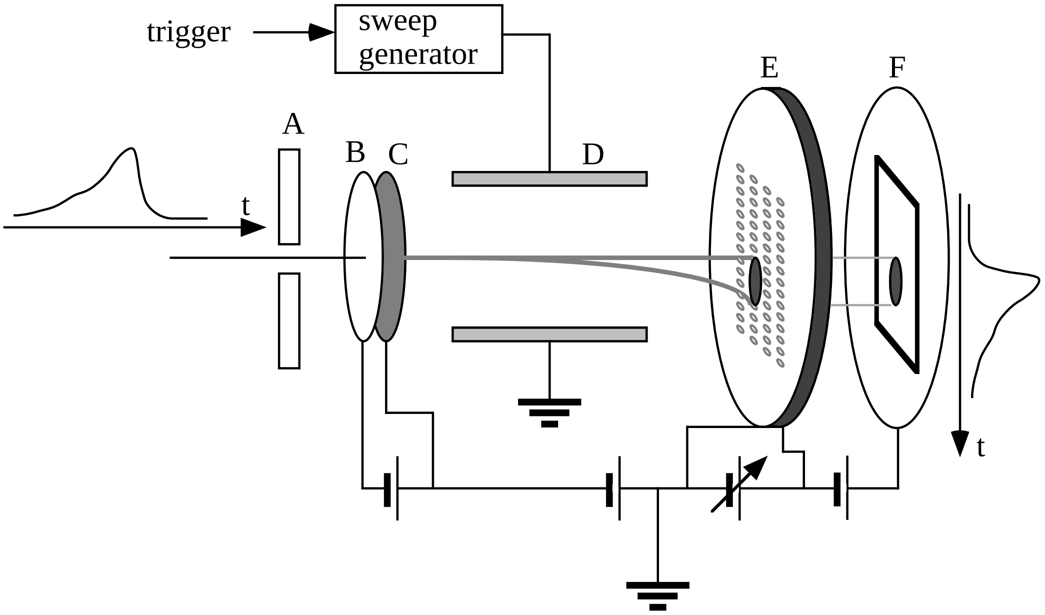

Figure 2.19: Principle of operation of a streak camera. A: slit, B: photocathode, C: accelerating mesh, D: deflecting sweep electrode, E: micro-channel plate (MCP), F: phosphor screen. After [89].

attenuated. A filter stack is not desired, because material dispersion lengthens the pulse. We attenuated the laser by turning off one or both two-pass rods, rotating a waveplate, and by expanding the laser spot on the slit. We also used the smallest slit width (10 μm) on the streak camera with which we achieved a time resolution of approximately 1 picosecond, as implied by the width of the image in focus mode.

We obtained a calibration of the streak camera in a simple and straightforward manner. A thick block of fused silica was placed over half of the slit, so that the laser spot was split in two portions, one of which passed through the delay block, and the other did not. From the known thickness (L = 6.20 mm) and index of refraction (n = 1.501 for λ = 263 nm) the delay difference is $\tau = (n-1)L/c =$ 10.4 ps. Fitting the centroids for the two halves of the beam spot, one obtains an average pixel difference over several images, yielding a calibration of 3.9 pixels per picosecond. This procedure was repeated one year later using light from the electron beam with the streak camera in the cave and the time resolution had degraded slightly to 3.6 pix/ps, probably from variation in the voltage risetime of the deflectors. We therefore report that, at most, a 10% systematic error could be ascribed to all of the streak camera measurements reported in this work.

A streak camera trace (projected image) of the unstacked pulse is shown in Figure 2.20 (top) and is Gaussian with $\sigma_t = 1.8$ ps. In figure 2.20 (bottom) we show a a streak trace of 4 stacked pulses which is a flat top or super-Gaussian profile with 10.7 ps FWHM. This result shows that the pulse stacker can be successfully used to form a flat top temporal profile.

2.8.3 Alignment of the Pulse Stacker

The compactness of our pulse stacker results from the use of small right-angle prisms as retroreflectors arranged around a single large-aperture beamsplitter. However, a disadvantage of the reduced number of optical elements is the loss of alignment knobs. The 4.0 inch diameter dielectric-coated beamsplitter was mounted with adjustment knobs on the tip and tilt. Each prisms was mounted to an adapter plate which was attached to a small translation stage. Machined slots in the adapter plate allowed translation of the prism perpendicular to the stage motion. This adjustment was needed to keep the horizontal beam separation at the desired displacement of 0.40 inch.

The pulse stacker produced four spots (2^p for $p = 2$) which had to be aligned to overlap on the cathode. The distance from the pulse stacker to the cathode through the transport line (see Section 2.10) is approximately 20 meters.

When only two pulses are stacked, it is relatively easy to get the two laser spots to overlap by adjusting the input ray and tilting the beamsplitter slightly if needed. For the second pair of spots, the alignment problem is more difficult. The

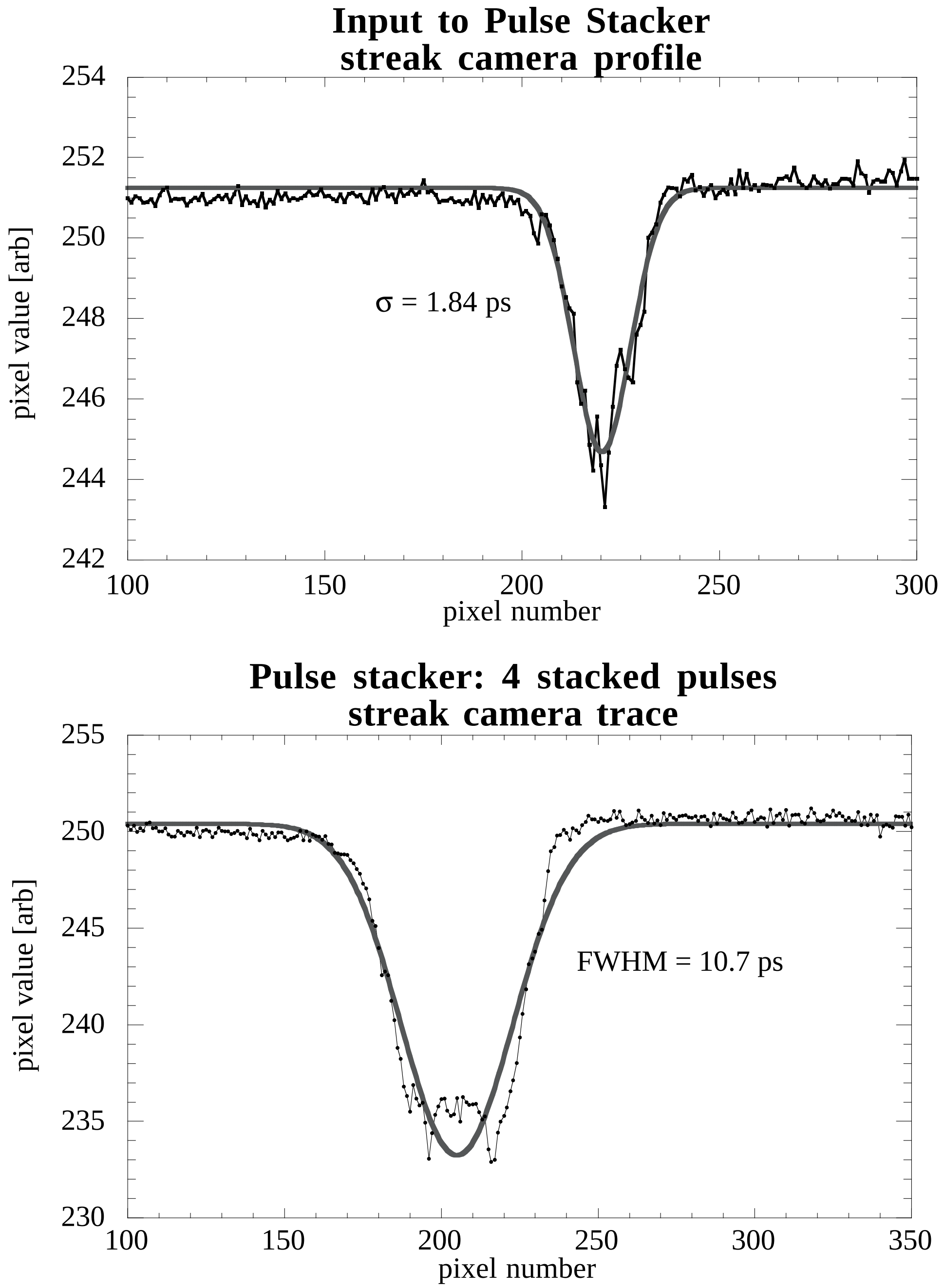

Figure 2.20: Top: Streak camera measurement of the laser pulse length before the pulse stacker. A Gaussian fit gives $\sigma_t = 1.8$ ps. Bottom: Streak camera measurement of the laser pulse length out of the pulse stacker, with four stacked pulses. A Gaussian fit gives 10.7 ps FWHM, but note that the profile is a non-Gaussian flat top.

essential problem is that we must correct for small variations in the apex angle of the prisms. For a right-angle prism with apex angle $\alpha = \frac{\pi}{2} + \epsilon$, the angular deviation is 2ϵ (neglecting refraction at the hypotenuse). The prisms have a standard tolerance of $2\epsilon < \pm 3$ minutes of arc, or ± 0.87 mrad. If uncorrected, this would give rise to a 1.7 cm spread in spots over 20 m, which is clearly unacceptable.

We found it necessary to add a pair of steering wedges to one arm (and to readjust the delay in this arm). A single wedge whose faces deviate from parallel by some small angle ϵ will deflect a normal ray by a fixed angle θ:

$$\sin\theta = n \sin\epsilon \quad \text{or} \quad \theta \approx n\epsilon. \tag{2.28}$$

The locus of all rays upon rotation of the wedge is a cone of apex angle θ. By combining two such wedges, the output ray can be steered to any angle within the cone of apex angle 2θ. After some effort, we overlapped all four spots on the virtual cathode with maximum horizontal (vertical) error of 0.2 mm (0.23mm), or within an angle of 10 (11.5) μrad. After a small adjustment to a waveplate, all four spots had equal laser energy to within 2% of the total. For the total energy normalized to unity, the four beams have respectively energy 0.238 (earliest), 0.248 (second), 0.245 (third), and 0.270 (last).

2.9 UV spatial profile shaping

The spatial profile of the laser on the cathode is a critical parameter to control in a photoinjector. The initial charge density distribution of the electron beam $\rho(x, y)$ is determined by both the laser energy density $U(x, y)$ and the uniformity of the quantum efficiency $\eta(x, y)$:

$$\rho(x, y)\, dx\, dy \propto U(x, y)\, \eta(x, y)\, dx\, dy. \tag{2.29}$$

If the quantum efficiency (the ratio of the number of electrons removed to the number of incident photons) is expressed in engineering units, such as nC/μJ, then the proportionality is an equality. For very low emittance photoinjector designs [32], arbitrary shaping of the laser profile is used to compensate for spatial nonuniformities in the quantum efficiency of the cathode. (See Section 3.3.4 for a measurement of the cathode uniformity.)

Simulations by E. Colby [37] showed that for a Gaussian spatial profile of the laser, the outlying tails of the Gaussian distribution contributed significantly to the emittance of the beam. A collimation of the beam itself by scraping away charge with a dense absorber generally does more damage than good through wakefield kicks. Also, pointing jitter of the beam couples to charge jitter. Instead, it is better to clip the edges of the laser spot. For this effort, the desired laser spot profile was a truncated Gaussian, which is an approximation to a uniform distribution.

It is possible to create a laser spatial profile which is a uniform disk by means of an apodizer, such as a serrated edge aperture. It is necessary to image this beam profile throughout the system to avoid diffraction effects. A truncated Gaussian distribution can be simply created by a passing a clean Gaussian beam through a circular aperture. For an aperture size which is very much larger than the wavelength, the effects of diffraction can be treated to good approximation as (one-dimensional) diffraction from a knife edge.

We investigated imaging of a circular aperture using an expanded, collimated Helium-Neon (HeNe) laser (632.8 nm). After the iris, the laser was imaged with a 3:1 telescope onto a target. Using a CCD camera and a frame grabber card, images were written to disk, and analyzed by taking projections of a narrow horizontal stripe with 20 pixels vertical spread (1.15mm using the calibration 17.5 pixels/mm). Analysis using an even narrower stripe of 8 pixels (0.46 mm) vertical spread was also performed but laser speckle makes this data appear very noisy. We repeated the experiment using a 1:1 telescope as well as with no imaging. In Figure 2.21 we present a series of profiles of the HeNe laser for different iris diameters with the 3:1 telescope. We found good approximations to a uniform distribution with 80% energy transmission.

We used this scheme to shape the spatial profile of the UV laser spot on the cathode. It is easy to implement, and with it we achieved good results. We placed the iris in the cave approximately 1 m from the cathode. Because of the high radiation fields during operation of the photoinjector, it was desirable to have remote control over the size of the iris. An inexpensive servo motor connected by a ball-in-socket linkage[13] could control the iris diameter from 0.5 mm to 20 mm. The UV beam size on the iris could be adjusted with the final telescope in the laser room, so the transmission was a function of both the iris diameter and the beam focussing. Typical settings had $\sim$ 20% loss on the iris.

A typical UV spot is shown in Figure 2.22 which was taken with a CCD camera on the virtual cathode target. The oblong structure visible in the upper left quadrant was traced to a bulk defect in the quartz vacuum window in cross X1 by the RF gun. In a narrow cut (Figure 2.23, top row) on the laser spot image, there are evidently departures from a perfectly uniform disc. However, the total projections (Figure 2.23, bottom row) are not far from the semi-elliptical shape of the projection of a perfect disc.

2.10 Beam Transport

The UV laser must be transported a distance $\sim$20 m from the laser room to the photocathode in the cave. It is desirable to do this with as little attenuation of the UV as possible. Also, pointing jitter from sources such as vibration must be

---

[13] We acknowledge with thanks the efforts of Todd Johnson (FNAL) and James Santucci (FNAL).

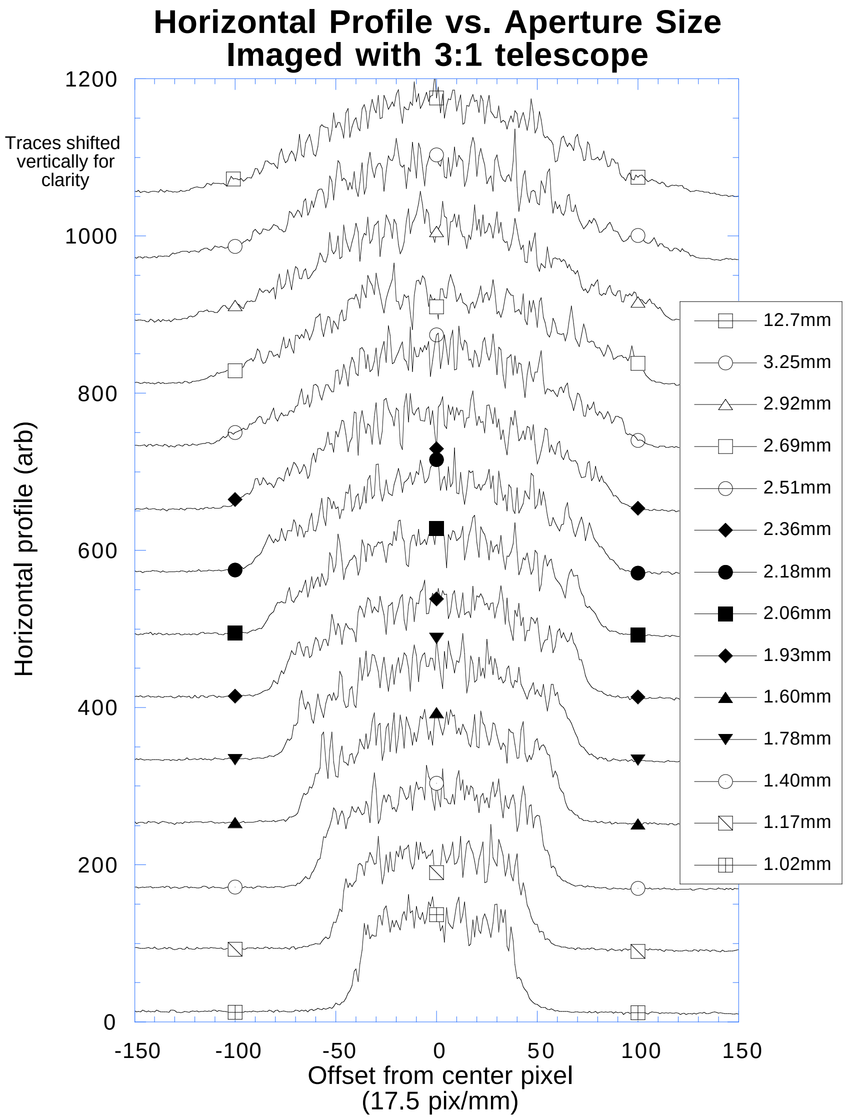

Figure 2.21: The spatial profile of a HeNe laser is clipped by a circular aperture and imaged (3:1) to a target. The truncated Gaussian distribution is a good approximation to a uniform distribution with 80% energy transmission. The legend gives the iris diameter in mm.

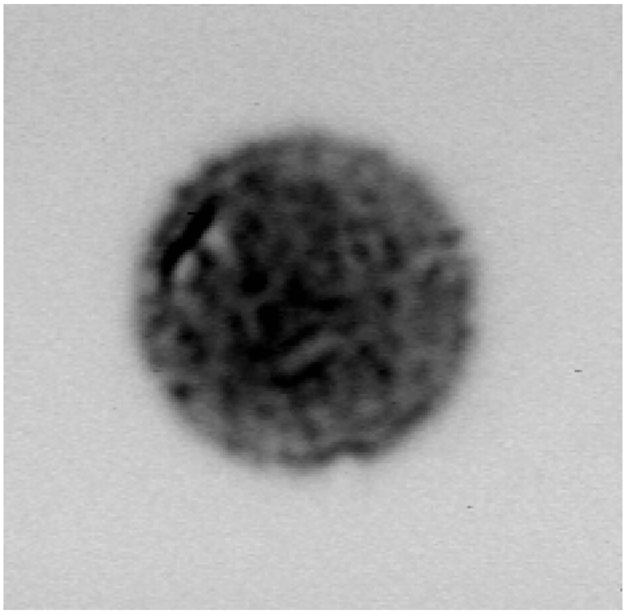

Figure 2.22: UV laser spatial profile on cathode as measured at the virtual cathode target.

minimized. Finally, there must be remote control over the laser alignment inside the beam enclosure and in the evacuated laser transport lines.

2.10.1 Vacuum and Mechanical

High vacuum is not needed in the transport system. There are two justifications for at least a good roughing vacuum. Firstly, air absorbs and scatters UV laser light at 263.5 nm causing attenuation. The contribution of Rayleigh scattering, a well-known textbook example [90], has a cross-section which scales as $\sigma \propto \omega^4$. Secondly, timing and pointing variations due to propagation in turbulent or convective gases must be minimized.

There are three mirrors mounted in welded vacuum boxes (see Figures 2.24 and 2.25), all with remotely controlled actuators on the mirror mounts. Also, each box is monitored by a video camera, so that the laser spot on each mirror can be monitored and adjusted if necessary. The vacuum boxes are linked by 4 inch diameter vacuum pipe, and the laser enters and exits through AR-coated UV

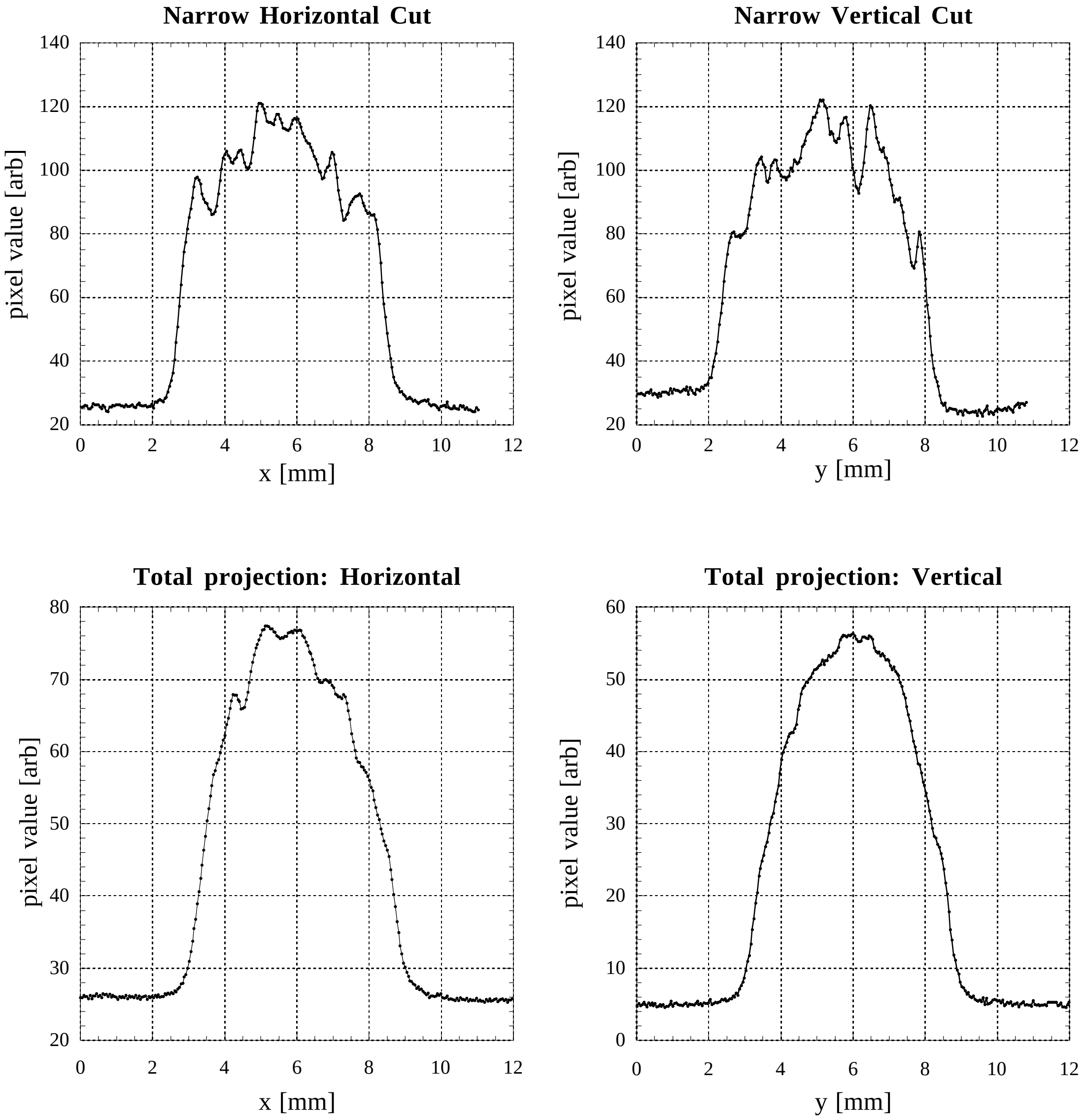

Figure 2.23: UV laser profile on cathode, from the image shown in Figure 2.22. Narrow cuts (top row) in the horizontal (L) and vertical (R) directions, and total projections (bottom row) in horizontal (L) and vertical (R)

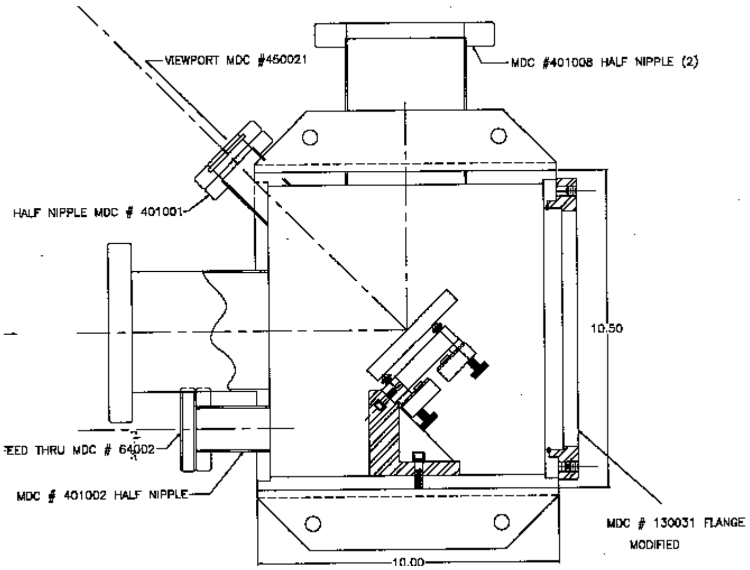

Figure 2.24: Vacuum mirror box: side view

quartz vacuum windows. For uncoated windows, the measured transmission was 88%, so including the 4% Fresnel reflection per side, the absorption is estimated to be 4%.

The mirror boxes must be mounted in such a way that vibration and motion is minimized. We investigated mounting the mirror boxes to the structural steel I-beam girders of the building. However, it was found that the girders suffer from both high-frequency vibration noise, and large low-frequency deflections with long damping times.

We chose instead to mount two of the three mirror boxes on pillars rigidly attached to the floor. For the height needed (~2.5 m) from the floor, the pillar should have a large cross-sectional area for greatest rigidity. We chose 12 inch diameter hollow steel pipe with flat plates welded on the ends. The column was filled with clean silica sand for vibration damping and mass loading. The estimated mass of the column is 90 kg with about 360 kg of sand. The columns were bolted to the concrete floor and grouted in place after final positioning.

The third mirror box is mounted to a concrete roof block of the cave (the

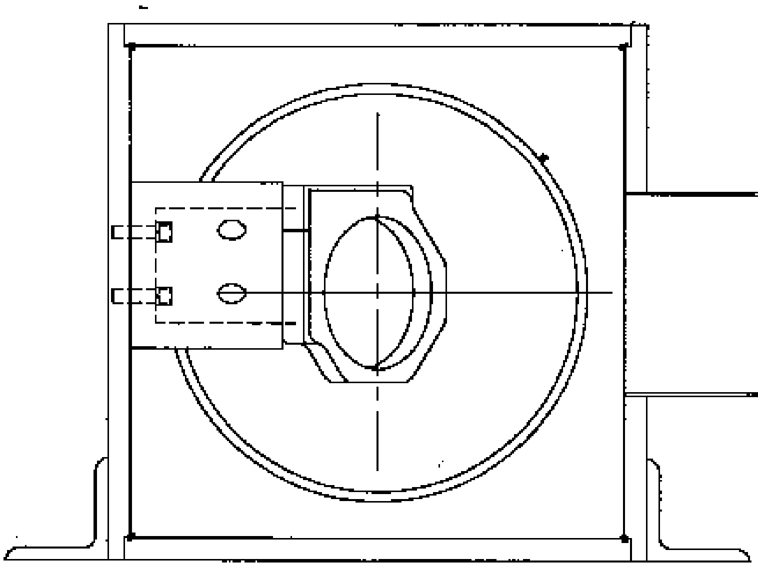

Figure 2.25: Vacuum mirror box: axial view

radiation enclosure). This block ($0.46 \times 0.91 \times 5.49$ m) was supported only at the ends by other concrete blocks, which allows a bending eigenmode. However the large mass of this block (5.4×10^3 kg) shifts the resonances to low frequencies, since generally $\omega \propto \sqrt{1/m}$. We found this mounting to be as good as or better than the pillar.

The mirrors at the bends require adjustment while under vacuum, and so must have remotely controlled actuators. The compact commercial actuator[14] used is a piezoelectric transducer that turns a screw by slip-stick motion. A slow motion of the piezo causes a screw rotation because of friction, while a fast motion, by inertia, produces no rotation. Electrical pulses of approximately 150 V (peak) with a fast rising edge and a slow falling edge cause rotation in one direction; swapping fast and slow edges is the reverse rotation. The speed of rotation is proportional to the number of pulses per second (1 kHz max). It was necessary to splice in low resistance (RG-59) cable in place of the standard phone cable

---

[14] Picomotor™ New Focus, Inc. (408-980-8088)

used by the manufacturer, since resistive losses in phone cable (26 AWG) prevent operation with a cable run greater than 10 m.

The vacuum system has a single pump-out port, and a spare 20 liter/sec ion pump maintained a stable pressure of 1×10^{-6} torr for many months. When this pump failed, the pressure was allowed to drift upwards, and was pumped down again occasionally as needed.

2.10.2 Optics

The mirrors used in the transport should have as high a reflectivity as possible for the ultraviolet (UV) laser pulses. It was desirable to align the invisible UV onto the cathode with a visible red HeNe (632.8 nm) which is collinearly propagated. For the electro-optic sampling experiment, an infrared beam was also required. Consequently the mirrors in the transport line needed to have highest possible reflectivity for the UV, and adequate reflectivity for the other wavelengths. A hybrid dielectric-metal coated mirror known as "UV-enhanced aluminum" was used in the early stages. However, the reflectivity at UV is only $R = 85\%$ which gives considerable losses over 4 reflections. These were upgraded to a triple-coated dielectric mirror which was $R \geq 98\%$ at 263 nm (UV), $R \geq 90\%$ at 1053 nm (IR), and $R \geq 65\%$ at 632.8 nm (HeNe). There are 4 such mirrors, and two quartz windows AR coated on both sides (4% absorption) and one quartz window AR coated on the air side only (for diagnostics). So the theoretical transport efficiency is $0.98^4 \cdot 0.96^2 \cdot 0.92 \sim 78\%$, which does not include losses on the remote-controlled iris (Section 2.9). The quartz vacuum windows dominate the losses. Taking 80% for the iris tranmission, we expect to deliver about 62% of the UV entering the transport line onto the cathode, and depending on the iris setting, we measure typically 50–70% overall.

Since the total transport distance is approximately 20 m, some thought must be given to the propagation of the beam size. The effects of diffractive spreading

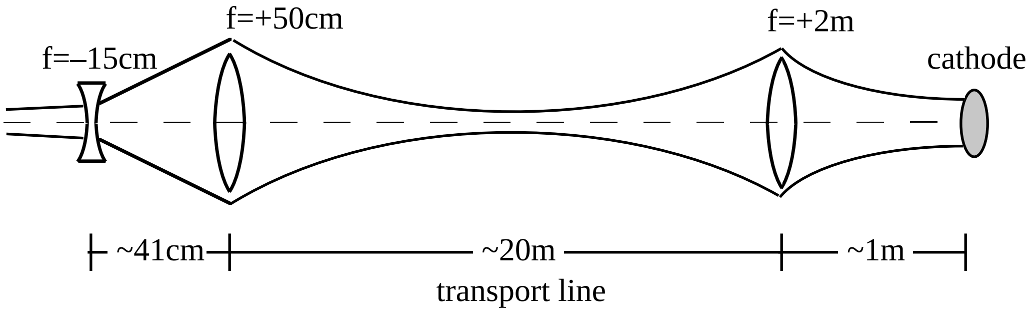

Figure 2.26: Sketch of the image relaying for the UV through the transport line.

for a large UV beam are not severe. The Rayleigh length Z_r for a 3 mm waist Gaussian beam at 263 nm is

$$Z_r = \frac{\pi w_0^2}{\lambda} \approx 100\text{m} \tag{2.30}$$

A 5:1.5 expansion telescope before the transport enlarged the small UV beam. It was desired to exploit the improved pointing stability by image relaying. The telescope was adjusted not for collimation, but for a waist at half the length of the transport line (see sketch in Figure 2.26), making the beam again large in the cave. A $f = +2$ m lens in the cave located 1 m from the cathode was used to reduce the beam size by a factor of two on the cathode. By adjusting the telescope in the laser room, the beam size in the cave could be adjusted over some range while still retaining the characteristics of image relaying.

To achieve delicate control over the laser size, as well as to clip the edges of the laser (which can contribute strongly to the emittance of the electron beam), a remote-controlled iris was installed in the cave, as was previously discussed in Section 2.9.

In Figure 2.27 we show the position of the remote-controlled iris, and the diagnostics of the UV on the cathode. Since the beamline enclosure is a high

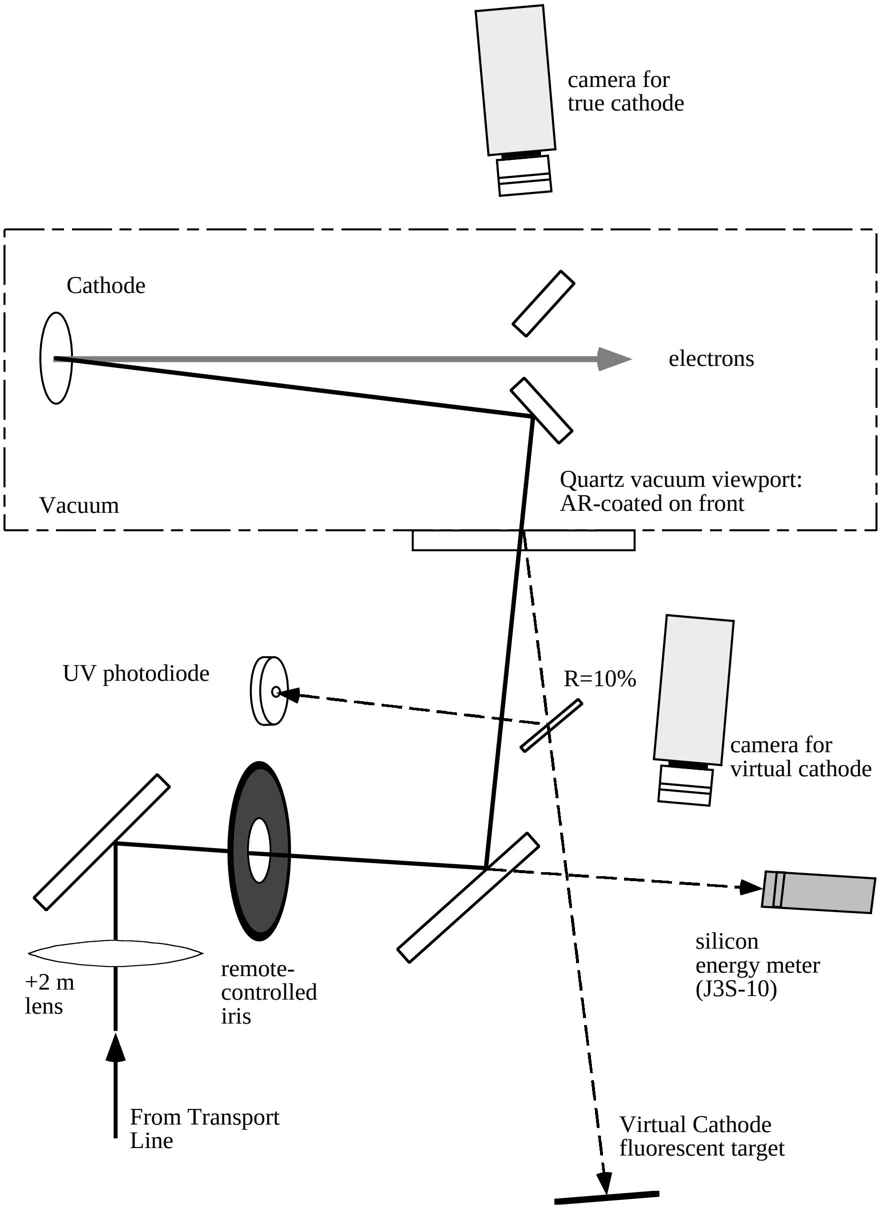

Figure 2.27: Optics and diagnostics for UV onto the cathode. Note the "Virtual Cathode" target, which fluoresces visible light for a CCD camera.

radiation area during operation, it is desirable to be able to make all necessary adjustments to the laser delivery without shutting off the accelerator to make an access. The virtual cathode is a target placed at an equivalent distance to the real cathode, so that the spot size and pointing of the laser are mapped 1:1 to the virtual cathode. The target material is white film stock (for black and white prints) painted with a fluorescent yellow ink. A visible light CCD camera is used to monitor the laser spot. The energy of the UV pulses is monitored in the cave by a photodiode and by a silicon energy meter. Cross calibration of the UV pickoff is done with a pyroelectric energy meter. Also shown in Figure 2.27 are two turning mirrors which have remote controlled actuators.

The spot profiles obtained from the virtual cathode are not useful if the fluorescing dyes are saturated. To test the linearity, the online data acquisition program (Section 3.1) logged the laser energy together with the pixel sum from the camera image. The pixel sum was calculated over a region of interest larger than the spot image but smaller than the entire frame. The fluorescence of the virtual cathode was shown to be linear up to our maximum UV illuminations.

The two mirrors inside the vacuum chamber (in cross X1) are fixed. Before assembly in the class 10 clean room, the alignment was done with a mock-up on the bench, and fiducial marks were lightly scribed on the mounting flange. After cleaning, the mirrors and mounts were reassembled with reference to the scribe marks and installed. (The input ray can, of course, be changed to correct for errors so long as a solution exists.) The fused silica mirror substrates (6 mm thick by 25.4 mm diameter) are coated with a multilayer dielectric stack with reflectivity $R > 99\%$ at 263 nm and $R > 50\%$ for 633 nm (HeNe red). Dielectric material close to the electron beam can become charged. We observed under some running conditions a slow drift in the position of the electron beam spot with occasional sudden jumps in position. This was attributed to slow charging of the mirror substrates and sudden discharging (sparking).

We made a vacuum break in the gun to replace the dielectric coated mirrors. The new mirrors used a "UV-enhanced aluminum" coating on a BK7 substrate (1 mm thick by 25.4 mm diameter) and were backed by a metal disc. The reflectivity is lower, $R > 88\%$ at 263 nm. Thus far, we have not observed any charging effects. However, these same mirrors have been used elsewhere in the beam line as OTR screens (see Section 4.2 on page 114), and several of them were damaged by dielectric breakdown—jagged cracking and crazing of the coating. Polishing a bulk metal surface to the degree necessary for a laser and at the same time obtaining a high enough reflectivity in the UV remains a technical challenge.

2.10.3 Pointing jitter

The pointing jitter of the laser spot onto the cathode was measured with the virtual cathode target. Over many shots, the image acquired is analyzed to find the centroid in both x and y using the statistical definition of centroid,

$$\mu_x = \frac{\sum_A x f(x,y)}{\sum_A f(x,y)} \tag{2.31}$$

where A is the [rectangular] region of interest and $f(x,y)$ is the pixel value at the coordinate (x,y) inside A. The ensemble of centroid values is used to find the rms position error.

The virtual cathode target, as described above (Figure 2.27), is a UV fluorescing material mounted on centimeter-ruled graph paper. A CCD camera looking at the target had sufficient field of view to see the graph paper lines, so a separate distance calibration image was not needed. We found that the rms position error was 140 μm (2.5 pixels) in x and slightly less at 130 μm (2.3 pixels) in y. The y data shown in Figure 2.28 has rms error 2.2 pixels. For a transport distance of $\sim$ 20 m this is equivalent to an rms angular pointing jitter of 7 μrad. In a measurement of this sort it is not possible to distinguish between fluctuations in

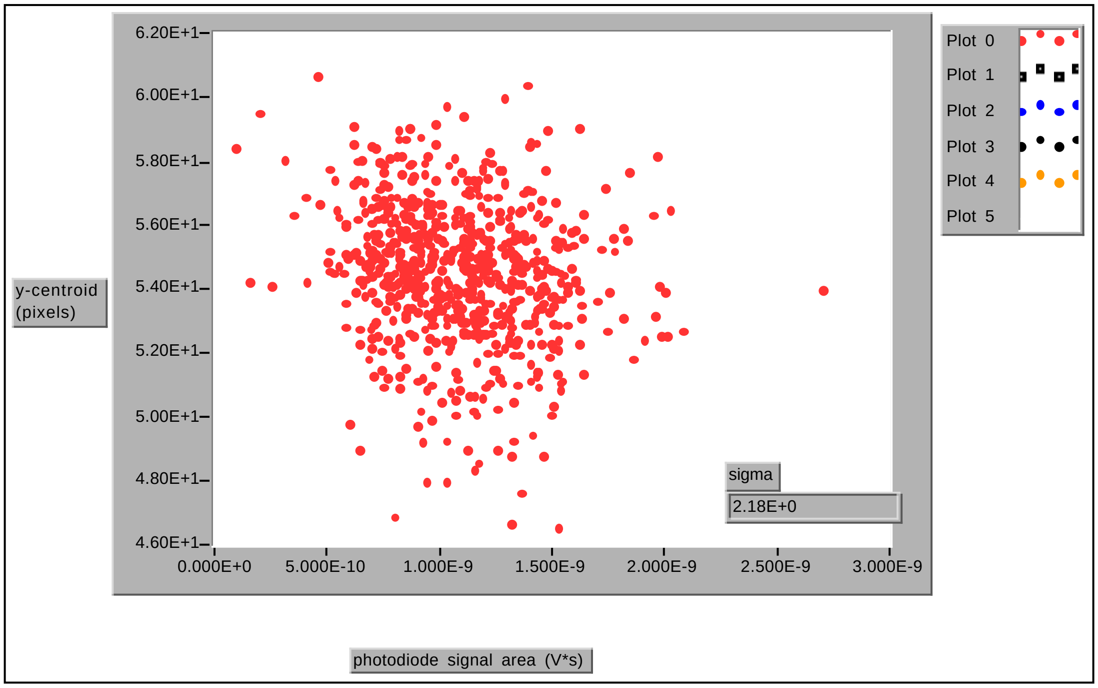

Figure 2.28: Laser pointing jitter in the vertical direction. The vertical axis is the y-centroid in pixels, and the horizontal axis is a measure of the laser energy from a photodiode. The distribution of centroids has a rms deviation of 2.3 pixels, or 130 μm. Converting to an angle, this is a pointing jitter of 7 μrad.

the spatial profile (hot spots) and spot motion, since both will contribute to the statistical centroid (equation 2.31). The horizontal axis of the plot in Figure 2.28 is proportional to the laser energy, and there is no significant correlation between the laser energy and the laser pointing.

Chapter 3

Performance of the Photoinjector

In this Chapter we describe the elements and performance achieved by the AØ Photoinjector. A drawing of the beamline was given in Figure 1.1 on page 5. In particular, we report on photoemission results from the high-quantum efficiency Cs_2Te photocathodes. We also discuss a measurement of the overall timing jitter between the UV laser pulse and the RF of the gun.

3.1 Beamline Elements and Optics

The design of the photoinjector is described by E. R. Colby [37]. Some recent results are reported in the conference literature [91–93].

The gun is a 1.625-cell π-mode normal conducting copper structure at 1.3 GHz. The full cell is side-coupled to the waveguide, and the half cell is iris-coupled to the full cell. Water cooling channels inside the structure are engineered to remove 36 kW average heat load at the full TESLA duty cycle (1%). With 3 MW (peak) of available RF power, the typical accelerating gradient is 35 MV/m (40 MV/m max).

The back plane of the gun accepts a molybdenum cathode plug on which the tellurium and cesium layers have been evaporatively coated. The photocathode preparation chamber with manipulator arms is mounted directly behind the gun.

The chamber, built by INFN Milano, is designed to keep the cathode under ultra-high vacuum (UHV) conditions as it is transferred from the preparation chamber into the gun [94].

Focusing solenoids around the gun are the critical beam optics elements for the Carlsten emittance compensation scheme (see Section 3.5). As described in [37], the injector uses a novel split-focussing solenoid: a primary solenoid, a bucking solenoid (which is the mirror image of the primary *behind* the cathode to ensure that the axial magnetic field vanishes at the cathode) and a secondary solenoid.

One unusual aspect of this system is the use of superconducting RF technology. The capture cavity is a 9-cell niobium structure which is operated at 1.8 K in a cryostat designed by Orsay, and built by industry. The cavity, constructed at DESY, is from a batch with low quench field (13 MV/m at cw), attributed to contamination at an equatorial weld. With 200 kW (peak) of available RF power, we routinely achieve gradients of 12 MV/m. In vertical tests at DESY, the Q of the cavity exceeded 10^{10} below quench. This agrees with that inferred from cryo losses (once the coupler is installed, the Q cannot be measured with RF because of the strong coupling) [95]. The cavity is equipped with a cold tuner which has a tuning range of ± 400 kHz.

The magnetic bunch compressor is a chicane of 4 dipoles. It is analogous to an optical compressor of four gratings (see Figure 3.1). The chicane is designed for a positive temporal dispersion $R_{56} = 9.2$ cm (maximum) [37, 96], which is the variation in the energy dependence of the path length:

$$R_{56} = \frac{dz}{(dE/E)}. \tag{3.1}$$

For positive R_{56} the bunch is given a negative energy-phase correlation, with the head having a lower energy than the tail. In the bends of the chicane, the more energetic particles are bent by a smaller angle, and so take the inside path and catch up to the particles at the head of the bunch which took the longer outside

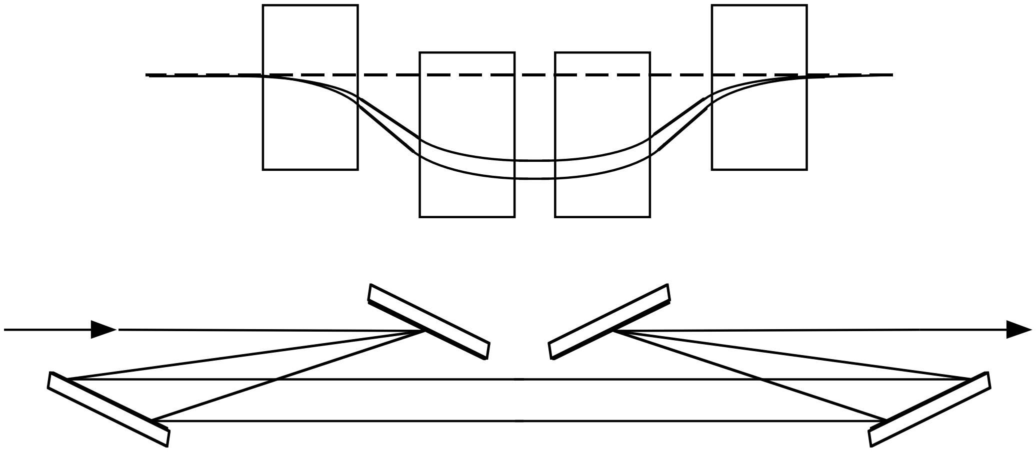

Figure 3.1: The magnetic compressor (top) is analogous to the optical compressor with four gratings. The optical compressor is often folded around the centerline with a roof mirror.

path. The pole faces of the dipoles are trapezoidal (not shown in Figure 3.1) so that the edges are perpendicular to the trajectory. This is to make the fringe field focussing [97] equal in both x and y planes. It is necessary to adjust the quadrupole doublet upstream of the chicane to compensate for this strong focussing.

A spectrometer magnet (bending in the horizontal plane) is used for momentum analysis. From the image of the beam onto an OTR screen in the 45° line the beam energy and energy spread are measured. (See Section 4.6, page 129). There are of course also quadrupole focussing magnets and steering trim coils.

All the beam flags are OTR screens (Optical Transition Radiation, see Section 4.2 on page 114) except two. The screen before the 9-cell cavity is a a Chromox scintillator, since OTR is weak (and divergent) for the low energy (4 MeV) beam out of the gun. Also there is one YAG scintillator (25 mm diameter by 1 mm). The OTR screens used include metal foils, Kapton coated by an evaporated layer of Al (typ. 100 nm thick), and commercial Al-based laser mirrors (UV-enhanced Al coating, on 25 mm diameter by 1 mm thick BK7 glass substrate). The foils suffered from poor surface quality, and it was difficult to stretch the kapton flat. The mirrors provided superior surface quality and flatness, but (as with the kapton) could be damaged by dielectric breakdown. The beamline also has several slit assemblies controlled by stepping motors for emittance measurement [98].

Image capture is accomplished by a series of digital CCD cameras and a frame grabber card in a MacIntosh. The cameras used are of two types, a high-grade scientific CCD camera from Cohu, Inc. (4910 Series), and a utility-grade CCD camera from Elmo Corporation. The Elmo cameras have been modified by jumper settings (automatic gain control (AGC) at minimum, gamma=1) for better linearity. The synchronization of the cameras is an important issue for data acquisition. N. Barov and W. Hartung have implemented a scheme in which all cameras are slaved to a master camera in the control area. The master camera is adjusted so that all the slave cameras are correctly synchronized with respect to the AC line. In this way uninterlaced images were captured. A LabVIEW program developed by N. Barov interfaced with the frame grabber card as well as the LeCroy digital oscilloscope over GPIB. It was used for online (1 Hz) image analysis, image acquisition with same-trigger scope measurements, and offline analysis of files.

3.2 Charge Measurement

Charge measurement is made using both integrating current transformers (ICT's) and Faraday cups. An integrating current transformer works by the principle of induction: a time varying current $I(t)$ passing through a loop of n turns will induce in the loop the same current divided by n. This current pulse is converted to a voltage pulse at the 50Ω oscilloscope termination. Using the built-in area function on a digital sampling oscilloscope (LeCroy LC534AL), the pulse integral is measured. The calibration is then simply obtained from Ohm's law.

$$Q = \int I\,dt = \frac{n}{R}\int V\,dt \tag{3.2}$$

For the Bergoz ICT, the number of turns is 40, and for $R = 50\Omega$ we have in practical units:

$$Q\ [\mathrm{nC}] = 0.8\int V\,dt\ [\mathrm{nV\,s}]. \tag{3.3}$$

This number was cross-checked with a pulse generator.

The advantage of measuring the ICT integral (area) rather than the peak value is clear if one attempts to include the effects of the long cable connecting the ICT with the oscilloscope. Generally speaking, the transfer function of the cable is far from flat and lossless, and dispersion in the cable will spread out the duration of the current pulse and distort its shape. By measuring the time integral, only the zero-frequency component of the transfer function has any importance. But this is merely the DC problem which is trivial to solve, and easy to calibrate. Only the DC resistance of the cable R_c must be measured, and from the voltage divider formed by the cable and the scope $R = 50\Omega$, the voltage measured on the scope is reduced by $R/(R + R_c)$. With a long cable run of RG-59, typical measured values of R_c were 3Ω, which is a 6% correction to the charge. A cable run of Heliax and RG-8 was installed which made this correction negligible.

A technical detail about measuring integrals of pulses using the built-in area function of a digital oscilloscope is the inclusion of background from small DC offsets. We observed this background to change from shot to shot. The sources of this small background may include the dark current signal, contact potential differences, or other noise, including pickup and ground loops. We used an on-line background subtraction by programming the math functions of the LeCroy LC354AL scope. A signal region for the ICT was defined using cursors, and an equal-width background region of the same waveform was chosen typically 50 ns after the pulse. The areas of the two were measured by the scope and subtracted. The calibration factor of 0.8 from Equation 3.3 was also programmed into the scope so that the measured charges were displayed in the correct units.

If the ICT is placed outside the beampipe, then the image current flowing in the walls of the pipe cancels that of the beam. Therefore, the ICT is placed over a ceramic break in the vacuum pipe. The image currents in the walls also must have a path, so a copper foil shield in the form of a double cone is placed over the ICT and clamped to the beampipe on either side of the ceramic break.

The ICT locations used most often are at cross X2 between the gun and the 9-cell cavity, cross X3 right after the 9-cell, and at cross X5 immediately after the dipole chicane (which is also the location of the electro-optic crystal).

A Faraday cup can be made from any electrically isolated beam dump. It should be thick enough to stop all primary electrons, and deep enough to retain the secondary electrons. Allowing the cup to discharge through a known resistance (at the scope 50Ω), one can integrate the voltage pulse in the same manner as the ICT to obtain a charge measurement. However, the capacitance of these structures is often unfortunately small, and voltages high enough to damage the scope can easily be generated (*e.g.* 10 nC into 100 pF is a voltage of 100 V). For this reason, 20–40 dB of attenuation is used to protect the scope.

3.3 Photoemission

In photoinjectors, the choice of the photocathode material is a major design consideration (see the review paper [99]). Alkali photocathodes have a demonstrated high quantum efficiency but suffer from extreme sensitivity to contamination or "poisoning" from trace gases. The quantum efficiency is ratio of the number of electrons extracted to the number of incident photons (see Section 3.3.1 below).

Metal photocathodes have the advantage of ruggedness to vacuum conditions but in general have poor quantum efficiency. Copper (Cu) cathodes are often used for simplicity, as normal conducting RF cavities are typically machined from Cu. The quantum efficiency of Cu has been reported in the range 3.5×10^{-5} [83] to 1.4×10^{-4} [100], and can vary with surface preparation. Sputtered magnesium (Mg) has been shown to have a quantum efficiency as high as 0.2–0.5% under DC fields, and can be exposed to air [101].

The gun uses a high quantum efficiency photocathode of cesium telluride (Cs_2Te) [102, 103]. Cesium telluride is less sensitive to trace gas poisoning than, for example, K_2CsSb or Cs_3Sb, and it has been shown that the quantum efficiency can be rejuvenated by heating along with UV illumination. The experience of cesium telluride photocathodes at the DESY TTF is described in [104].

We have also observed mutability in the quantum efficiency (QE) of these cathodes—the QE improves under running conditions both during a run day, and over several days of running. Figures 3.2 and 3.3 give the QE over time as measured at low charge (1 nC). To account for possible drifts in the phase of the gun, the QE reported is taken from the peak value of a gun phase scan.[1] When the 9-cell cavity is cooled to liquid helium temperatures, cryo-pumping improves the vacuum in the cathode region. Liquid nitrogen is always flowing into the 80 K shield, but because of the expense of liquid helium, an automated cryo start-up and shutdown is done at the beginning and end of each run day. Day zero of Figure 3.2 (22 August 1999) is the end of a week-long cryo shutdown in which the cavity was allowed to warm to 80 K. The filled squares are taken from the first phase scan of the day. On day 1, the QE was low (0.2 %) but increased to better than 1 % over the next four days. Increases of a factor of two are seen in days 8–12 and days 15–19. In Figure 3.3 are several QE points at successive times on

---

[1] We thank and acknowledge W. H. Hartung for compiling this data from the logbooks.

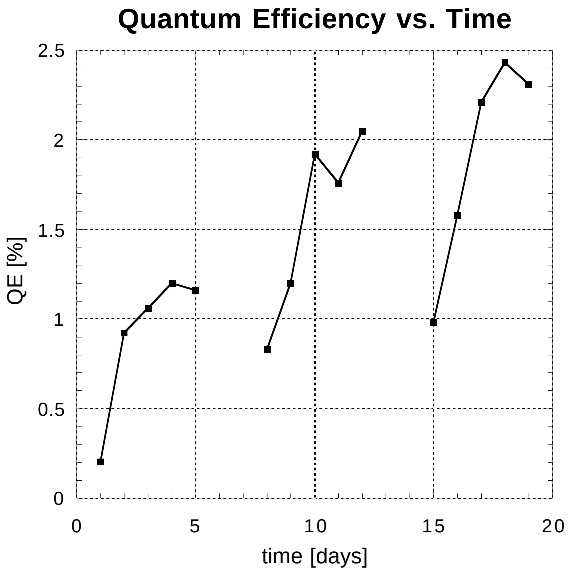

Figure 3.2: Quantum Efficiency vs. Time over three weeks of running. Day 0 is 22 August 1999.

1 September 1999 (day 10 of figure 3.2). The improvement on this day was more than a factor of two, from 1.92 % initially to 4.16 % after 10 hours.

The mutability of the cathode can be attributed to the adsorption and desorption of trace contaminants on the cathode surface. From Auger and x-ray photoemission spectroscopy, di Bona *et al.* showed that oxygen was the main contaminant [105] that desensitizes Cs_2Te cathodes.

3.3.1 Charge Extraction vs. Laser Energy

One wants to know what quantity of laser energy U is required to extract a given charge Q. At low charge, the quantum efficiency η is the desired number. By definition, the quantum efficiency is the ratio of the number of electrons extracted

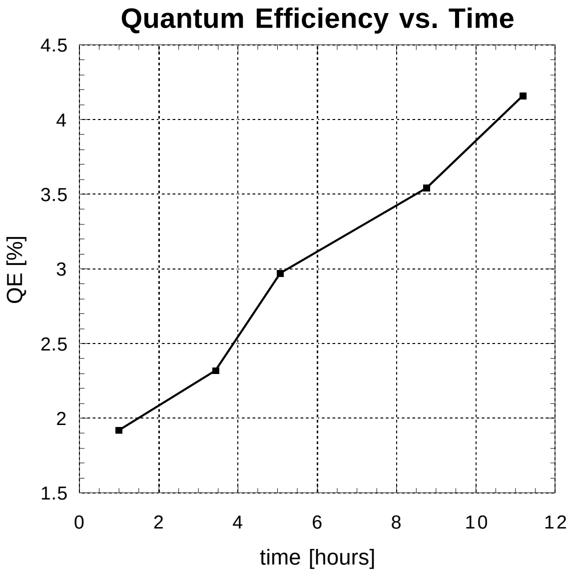

Figure 3.3: Quantum Efficiency vs. Time over one run day shows a typical improvement of a factor of two. Data taken 1 September 1999 (day 10 of figure 3.2).

to the number of incident photons:

$$N_e \equiv \eta N_{photons} \tag{3.4}$$

$$Q = \frac{\eta U \lambda}{hc} \tag{3.5}$$

$$Q\,[\mathrm{nC}] = 2.125\ \eta[\%]\,U[\mu\mathrm{J}]\left(\frac{\lambda}{263\ \mathrm{nm}}\right) \tag{3.6}$$

where the relation $hc = 1240$ eV·nm is convenient for unit conversion. However, implicit in Equation 3.4 is the assumption that sufficient electric field is present to remove from the cathode all the electrons liberated. When the attractive Coulomb force of the electrons to the oppositely-charge cathode becomes comparable to the accelerating electric field, then the charge extraction will be reduced. We refer to this effect as “saturation due to space charge.”

The saturation from space charge depends on the size of the laser spot. In

Figure 3.4 are plotted the measured charge versus laser energy on the cathode for three different laser spot sizes. All other parameters are kept the same, the gun phase and gun gradient are held constant. The laser spot size is adjusted by a combination of changing the aperture of the remote controlled iris and of the focussing that alters the laser spot size at the iris. The resulting laser spot profile is a truncated Gaussian, and for the smallest spot is nearly uniform in radius.

We will take a simple model[2] of the space charge force from Gauss's law of electrostatics. Similar arguments are given by Hartman *et al.* [106]. The Schottky effect will be discussed in Section 3.3.3 on page 90. We treat here only the force between the bunch and the oppositely-charged cathode in comparison to the force from the accelerating gradient. The key point is that the different regions of the laser spot reach saturation at different laser energies.

Consider a cathode of area A with both the quantum efficiency η and electric field $|\vec{E}_{cath}|$ constant over A.

$$q(x,y)\,dx\,dy = \begin{cases} \eta\, u(x,y)\,dx\,dy & \text{if } \eta u(x,y) < \epsilon_o|\vec{E}_{cath}| \\ \epsilon_o|\vec{E}_{cath}|\,dA & \text{if } \eta u(x,y) > \epsilon_o|\vec{E}_{cath}| \end{cases} \tag{3.7}$$

We have the normalizations for the total charge and total laser energy (which are the two experimentally measured quantities):

$$Q_t = \int_A q(x,y)\,dA \qquad \text{and} \qquad U_t = \int_A u(x,y)\,dA. \tag{3.8}$$

Clearly for a uniform laser spot [$u(x,y) = u_o$ for $\sqrt{x^2+y^2} < r$ and zero otherwise], the charge extraction will saturate abruptly.

---

[2] We thank W. H. Hartung for many useful discussions on this topic.

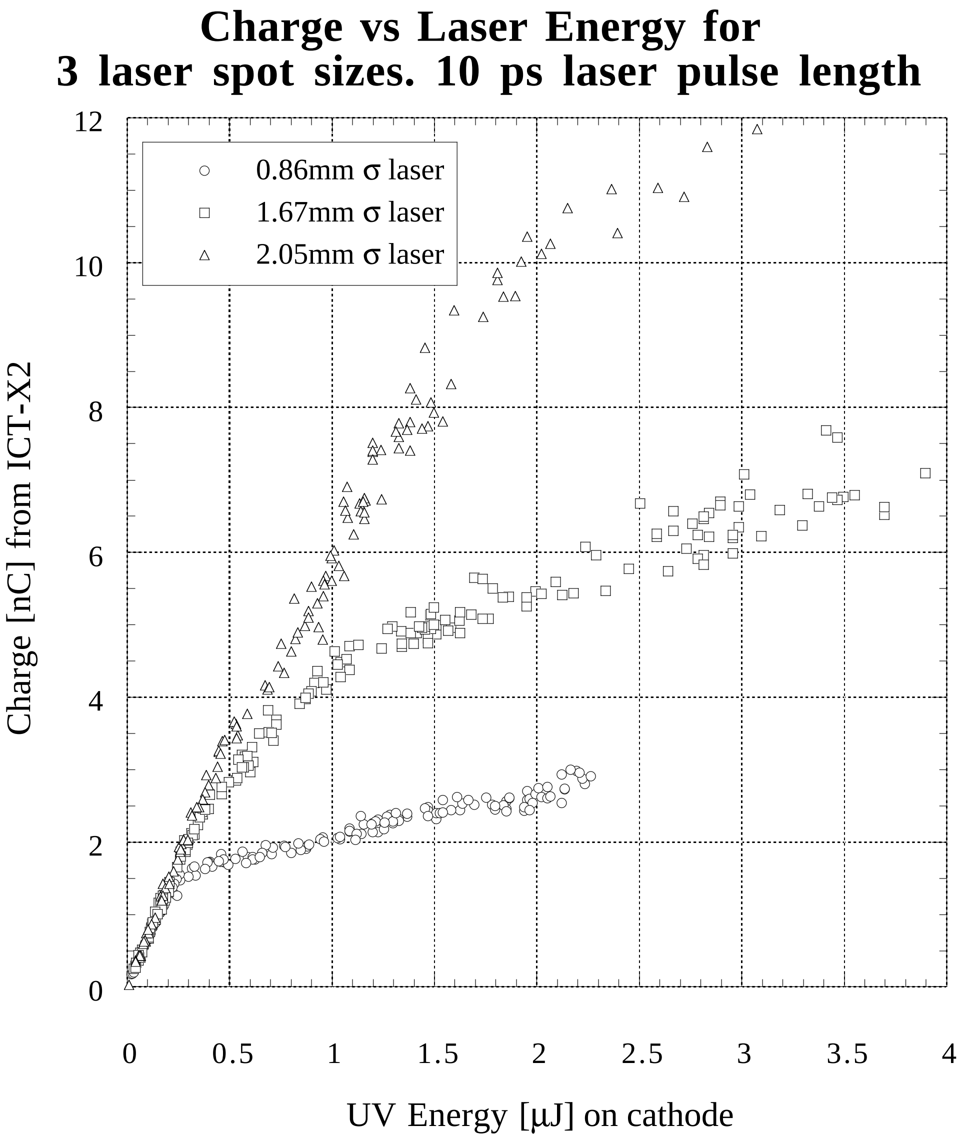

Figure 3.4: Charge versus laser energy for three different laser spot sizes. The effect of saturation from the space charge force is clearly seen as the laser spot size is reduced. All data were taken with the long (stacked) laser pulse which is 10 ps FWHM.

Gaussian Laser Spot

Consider a Gaussian spot on the cathode. The 2-vector $\vec{x}$ can be expressed in cartesian (x, y) or cylindrical polar (r, ϕ) coordinates. The laser distribution is

$$u(\vec{x}) = u(r, \phi) = \frac{U_t}{2\pi\sigma_r^2} \exp\left(\frac{-r^2}{2\sigma_r^2}\right). \tag{3.9}$$

We can divide the region A into two regions, $A = A_u + A_s$, the unsaturated and saturated regions, such that

$$\eta u(\vec{x}) < \epsilon_o |\vec{E}_{cath}|, \text{ for } \vec{x} \in A_u, \tag{3.10}$$

$$\eta u(\vec{x}) > \epsilon_o |\vec{E}_{cath}|, \text{ for } \vec{x} \in A_s. \tag{3.11}$$

The total extracted charge is found by combining equations 3.7 with 3.10 and 3.11.

$$Q_t = \int_{A_u} \eta\, u(\vec{x})\, dA + \int_{A_s} \epsilon_o |\vec{E}_{cath}|\, dA. \tag{3.12}$$

For the Gaussian laser spot of Equation 3.9, there are two cases to be considered. If the peak value satisfies

$$\eta \frac{U_t}{2\pi\sigma_r^2} < \epsilon_o |\vec{E}_{cath}|, \tag{3.13}$$

we have $A_s = 0$ and $A_u = A$ and therefore:

$$Q_t = \eta U_t \qquad \text{for } U_t < \frac{\epsilon_o |\vec{E}_{cath}|}{\eta}. \tag{3.14}$$

If the peak value is large enough that the inequality 3.13 is not satisfied, then

A_s is the circular region $r < s$. We find that s is given by:

$$s^2 = 2\sigma_r^2 \ln \frac{\eta U_t}{2\pi\sigma_r^2 \epsilon_o |\vec{E}_{cath}|}. \tag{3.15}$$

The integration over A_s is simply the area πs^2 multiplied by $\epsilon_o|\vec{E}_{cath}|$. The region A_u is then $r > s$, and the integration over A_u is elementary, and the two terms can be combined to yield

$$Q_t = 2\pi\sigma_r^2 \epsilon_o |\vec{E}_{cath}| \left[1 + \ln\left(\frac{\eta U_t}{2\pi\sigma_r^2 \epsilon_o |\vec{E}_{cath}|} \right) \right]. \tag{3.16}$$

Finally, we write together both cases for the Gaussian laser spot, which gives the charge extraction versus laser energy including saturation from space charge as

$$Q_t = \begin{cases} \eta U_t & \text{for } U_t < \frac{\epsilon_o |\vec{E}_{cath}|}{\eta}, \\ a\left\{1 + \ln \frac{\eta U_t}{a}\right\} & \text{otherwise.} \end{cases} \tag{3.17}$$

We have collected constants into

$$a = 2\pi\sigma_r^2 \epsilon_o |\vec{E}_{cath}| \tag{3.18}$$

We give the calculation for a truncated Gaussian laser spot in an appendix to this Chapter, Section 3.6.

Comparison with Experiment

Using equations 3.17 the measured extracted charge versus laser energy can be fit with two parameters a and b, and a third parameter (the decision point c) is

	σ_r	a	b	QE=b/2.12	σ_r^2/a
10 ps	2.05 mm	5.45	6.12	2.88 %	0.771
	1.67 mm	1.93	6.53	3.07 %	1.45
	0.86 mm	0.63	7.18	3.38 %	1.16
2 ps	0.86 mm	0.76	4.22	1.99 %	0.97

Table 3.1: Fitted parameters from charge extraction data. The fit parameter b is the electron yield [nC/μJ] which we convert to QE [%] using equation 3.6. The model discussed in the text predicts that the fit parameter a will scale with σ_r^2, which is in fair agreement with the data.

adjusted by hand.

$$Q_t = \begin{cases} bU_t & \text{for } U_t < c \\ a\left\{1 + \ln \frac{bU_t}{a}\right\} & \text{otherwise.} \end{cases} \tag{3.19}$$

Fits of the data shown in Figure 3.4 are given in Figure 3.5, and the fit is good since Pearson's R is greater than 99% in all cases.

We have collected in table 3.1 the parameters from the fits shown in Figure 3.5. As shown above, the simple model of space charge saturation predicts a dependence on the area of the laser spot (3.17 and 3.18). The measured ratios of σ_r^2/a are not constant, but vary within a factor of 2.

One interesting feature of the data is that the quantum efficiency is around 3% for the (stacked) 10 ps FWHM flat-top laser pulse but significantly lower, around 2%, for the 2 ps σ_t Gaussian laser pulse. The difference is seen when the 2 ps and 10 ps laser are plotted together, as in Figure 3.6. There is no systematic error dependent on bunch length (in either the charge measurement or the laser energy measurement) which could bias this observation. This is just space charge, and we will consider in the next section (Section 3.3.2) a physical picture in which the current density J (in Amps/cm^2) is the relevant quantity rather than the charge per unit area.

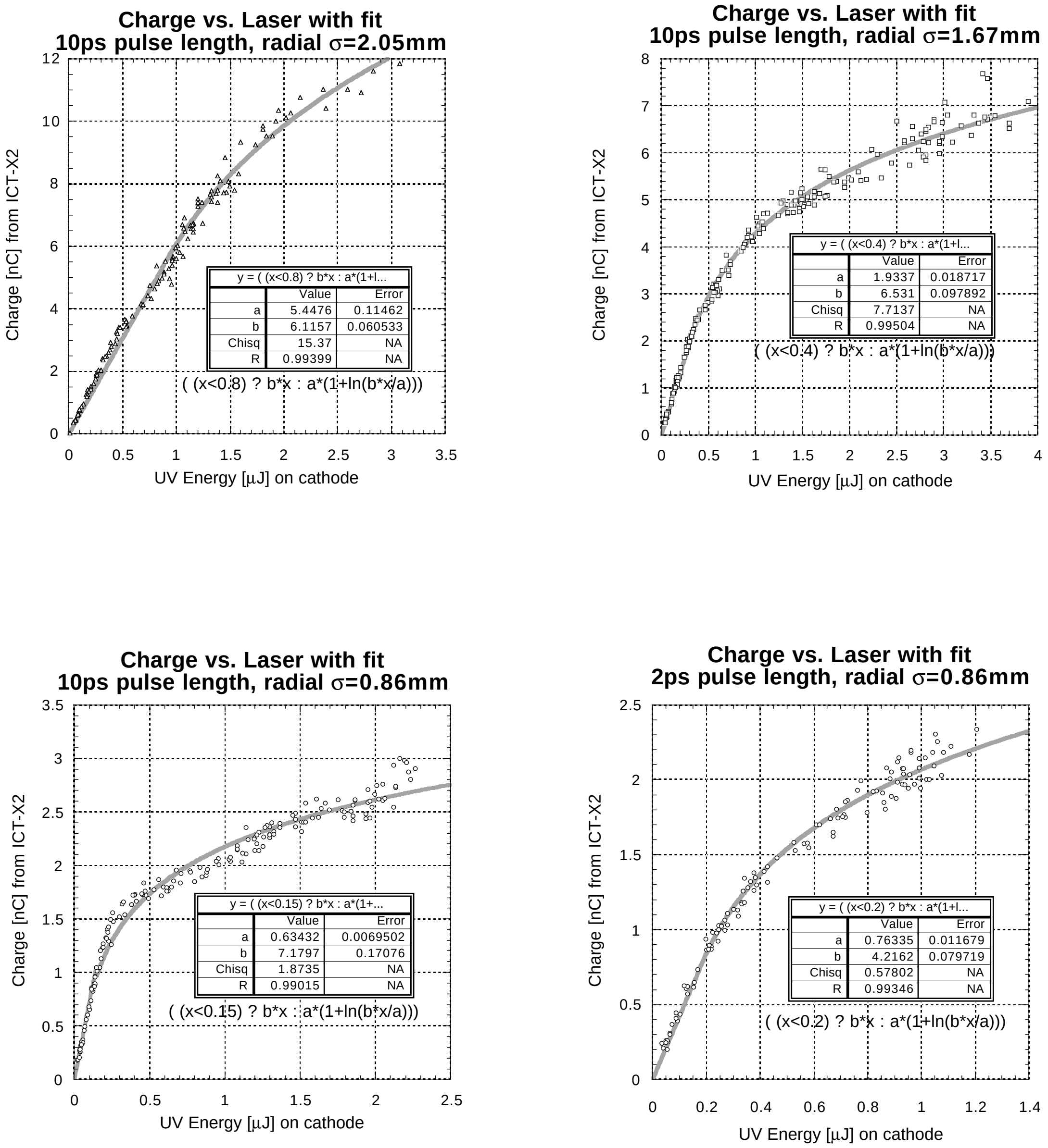

Figure 3.5: Charge extraction versus laser energy with a 2-parameter fit from a simple model of space charge balanced with the cathode gradient. See text for discussion.

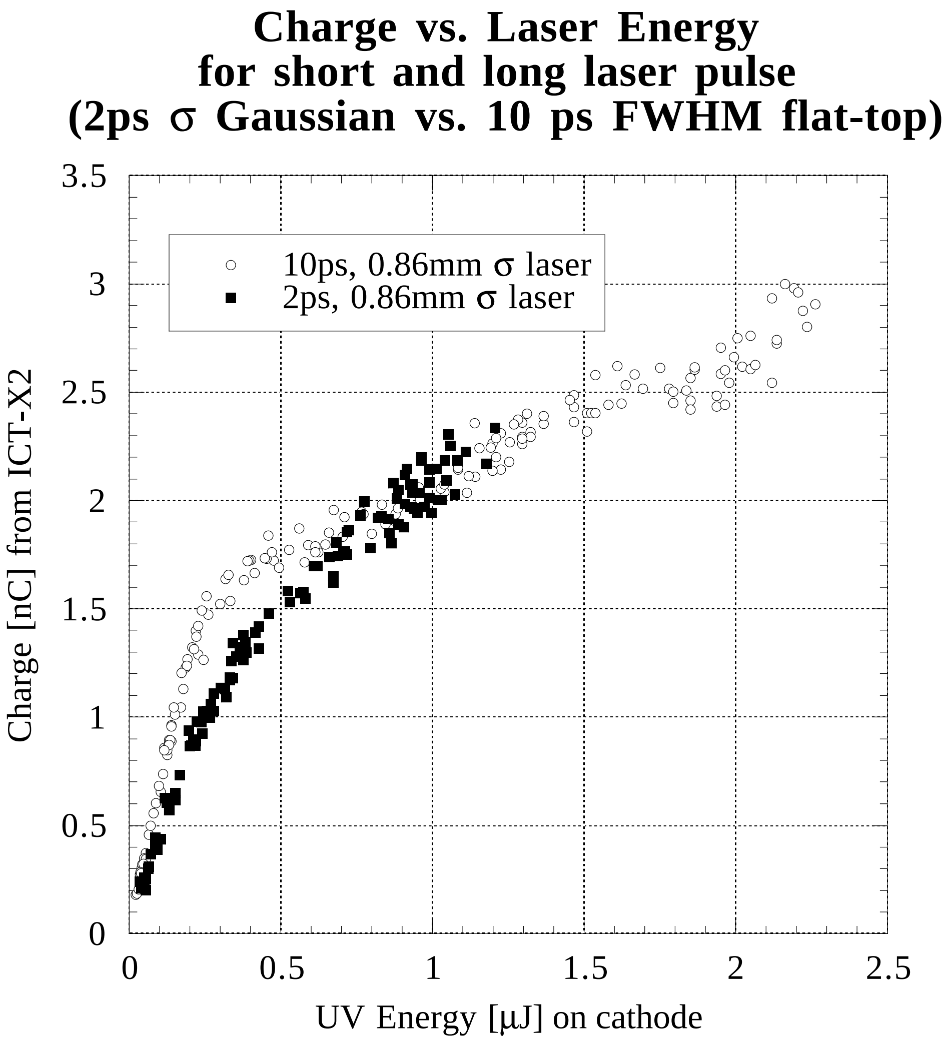

Figure 3.6: Charge extraction versus laser pulse length. The short pulse is Gaussian with $\sigma_t = 2$ ps while the long (stacked) is flat-top with FWHM= 10 ps. Both are for the radial $\sigma_r = 0.86$ mm beam size. The linear region clearly shows a significant difference in quantum efficiency.

3.3.2 Charge Extraction: Saturation Current

The model presented in the previous section was essentially a 2-dimensional model that treated the electron bunch as a thin sheet of charge. In the limit in which the bunch may be considered a steady current density J (that is, neglecting the magnetic terms from $\frac{\partial J}{\partial t}$), the Child-Langmuir law [107] predicts a saturation current density:

$$J_s = \frac{4\epsilon_o}{9}\sqrt{\frac{2e}{md}}E^{3/2} \tag{3.20}$$

which is derived for a plane diode of gap d. We take instead d to be the laser pulse length (see also Travier [108]).

Re-plotting the data of Figures 3.4 and 3.6 in terms of current density is the plot of Figure 3.7. For the current density, we use

$$J = \frac{Q}{2\pi\sigma_r^2\sqrt{2\pi}\sigma_t}. \tag{3.21}$$

However, the truncation of the laser profile by the iris makes this expression inaccurate for the smallest spot size. For the non-Gaussian stacked pulse, which has a FWHM bunch length τ, we use $\tau/2\sqrt{2\ln 2}$ in place of σ_t. Figure 3.7 shows that for the long (10 ps FWHM) stacked laser pulse, the saturation current is about 4 kA/cm^2. The deviation for the smallest laser spot size is probably from inaccuracy in estimating the effective area of the truncated Gaussian spot. If we take d to be the laser pulse length in the Child-Langmuir law, then the factor of $d^{-1/2}$ predicts the saturation current for the short laser pulse will be a factor of 1.6 higher than the long laser pulse. This is in reasonable agreement with Figure 3.7, which shows a ratio of of about 2.

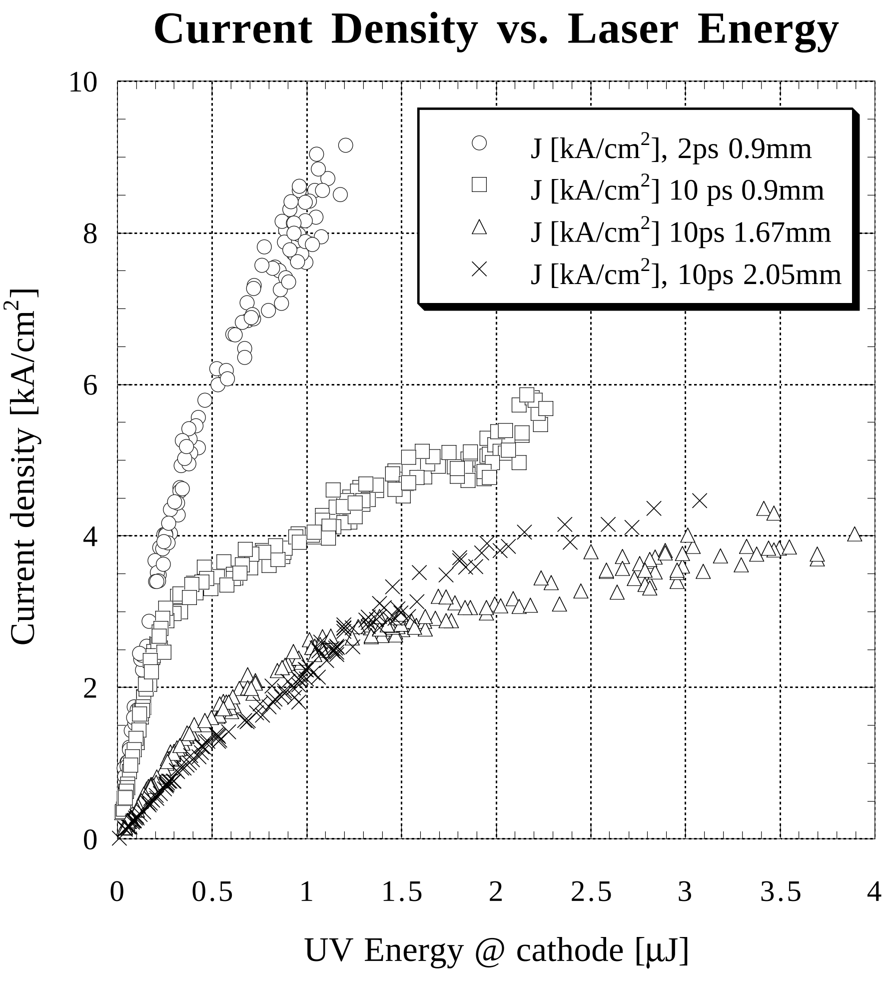

Figure 3.7: Current Density vs. Laser Energy. For the long stacked (10 ps FWHM) laser pulse, the saturation current density is approaching the same value. The deviation for the smallest laser spot size is probably from inaccuracy in estimating the effective area of the truncated Gaussian spot. The Child-Langmuir law predicts the saturation current of the short (2 ps σ Gaussian) laser pulse will be 1.6 times higher than the long laser pulse.

3.3.3 Phase scan vs. Gradient: Schottky effect

In the previous sections, there was no inclusion of the Schottky effect, which is an enhancement of the photoemission from lowering of the work function by the electric field.

For a surface electric field E, the work function $(\phi_o - \phi)$ lowering was given by Schottky [109] (a modern reference is, for example, [110]):

$$\phi_o - \phi = \left(\frac{eE}{4\pi\epsilon_o}\right)^{1/2} \tag{3.22}$$

and the quantum efficiency η is:

$$\eta = A\left[\hbar\omega - \phi_o + \left(\frac{eE}{4\pi\epsilon_o}\right)^{1/2}\right]^2 \tag{3.23}$$

so that for small lowerings

$$\Delta\eta \sim 2A(\hbar\omega - \phi)\,\Delta\phi \propto E^{1/2} \tag{3.24}$$

The Schottky effect is most clearly seen experimentally in charge extraction versus accelerating gradient in the gun. For the nominal gradient of 35 MV/m and for roughly half that at 17 MV/m we show a phase scan at low charge (1 nC max) in Figure 3.8. The shift in phase is an artifact. [Changing the amplitude also changes the phase, because of non-ideal behavior of the i–q vector modulator (Section 3.4, page 94).]

The experiment shown in Figure 3.8 was carefully repeated[3] for several settings of the accelerating gradient, keeping the laser energy constant, and adjusting the solenoids to the theoretical values (for charge collection). At each setting, a phase scan was performed. For each gradient, we take only a single data point at a

---

[3] We thank W. H. Hartung for generously making this data available to us.

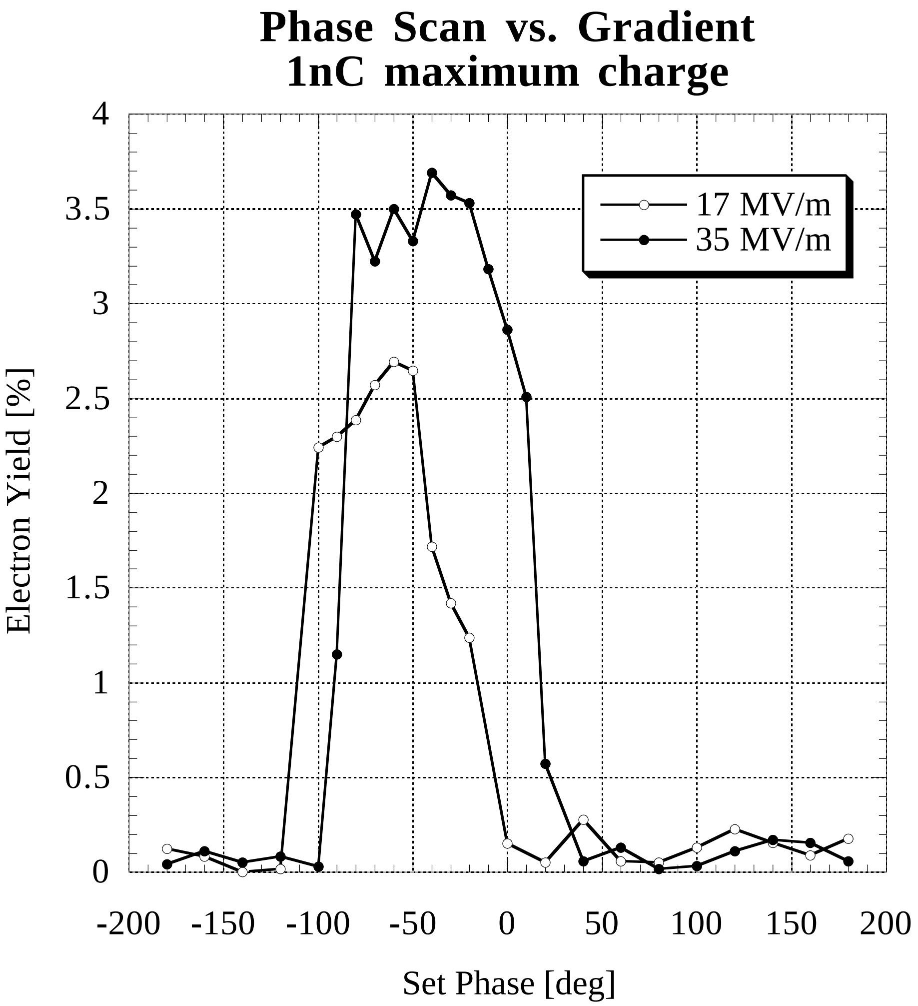

Figure 3.8: Phase scan for two gradients. The laser was kept constant at 0.18 μJ in a large spot (2 mm σ_r). The shift in phase is an artifact.

standard position in the phase scan curve which is at or near the peak value. In Figure 3.9, the current density J (defined in Eqn. 3.21) in kA/cm^2 versus gradient in MV/m is plotted on a log-log scale. We used a laser spot size of 2 mm radius and laser pulse length of 10.7 ps FWHM to calculate J from the measured charge Q. The low field region clearly shows the influence of space charge limitation, and the dependence on $E^{3/2}$ is very good. The two data points at the lowest field have less current density than the Child-Langmuir limit, but this may be a problem with charge collection. Above 20 MV/m, there is sufficient field to extract all the charge at this particular laser energy, and further increases in the field show the slow rise proportional to $E^{1/2}$ from the Schottky effect.

The data in Figure 3.9 shows a change in slope around 20 MV/m. From Eq. 3.20, we calculate the saturation current for a 20 MV/m field to be $J_s = 0.38$kA/cm^2 which agrees very well with the data ($J_s = 0.383$ kA/cm^2 at 20.6 MV/m).

3.3.4 Cathode Spatial Uniformity

Great effort is made to prepare photocathodes as uniform as possible over their useful area. This is important for high quality beams since the quantum efficiency (considered as a function of position on the cathode) multiplies the laser spatial profile to give the initial charge distribution. For future photoinjectors, it may be necessary to implement arbitrary control over the spatial profile of the laser pulses in order to compensate for the cathode nonuniformities. The first step is to measure the cathode uniformity.

By closing the remote-controlled iris, the laser spot could be made very small, and we prepared a laser spot which was a nearly uniform disk with a 0.79 mm diameter. Because the effects of space charge saturation are severe for small laser spots (see Section 3.3.1), we measured the charge versus laser energy, and set the laser energy well within the linear regime. This was quite low charge, 300-500 pC,

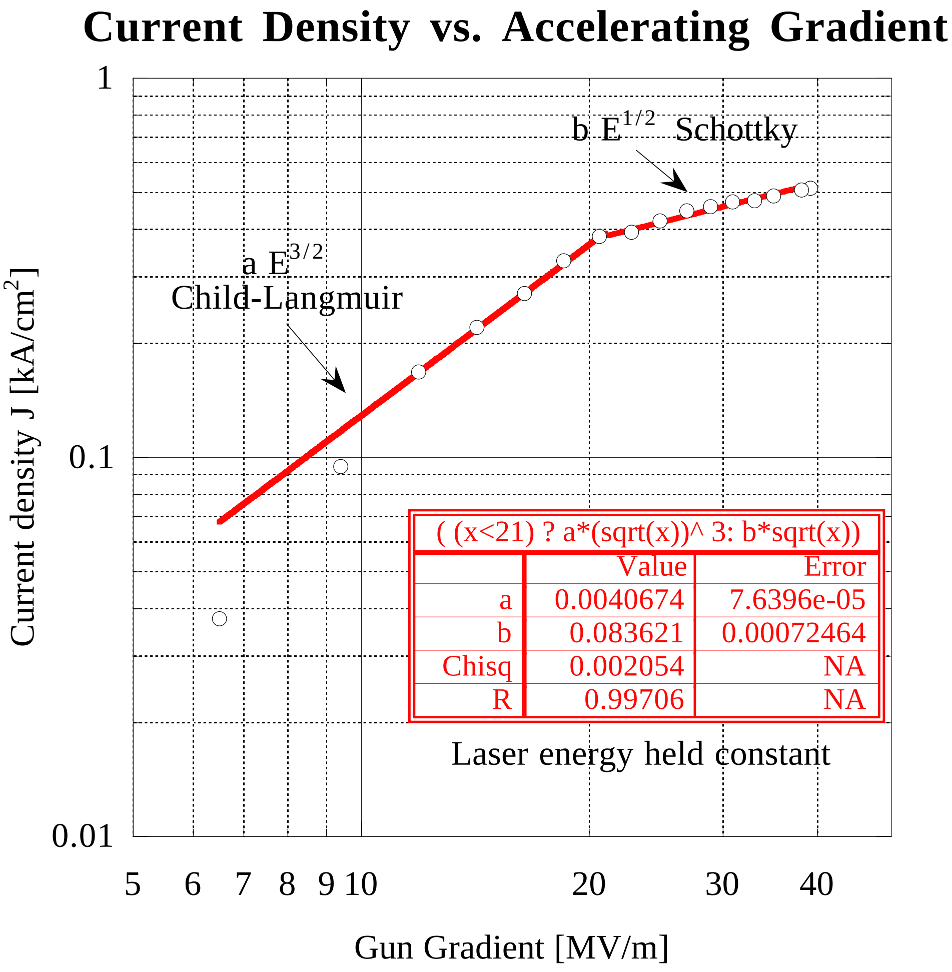

	Value	Error
a	0.0040674	7.6396e-05
b	0.083621	0.00072464
Chisq	0.002054	NA
R	0.99706	NA

Figure 3.9: Current Density vs. Gradient: Child-Langmuir and Schottky regions. The laser energy is held constant. The low field region shows the $E^{3/2}$ dependence from space charge predicted by the Child-Langmuir law. After the field is high enough to extract all the charge, there is in the high field region the $E^{1/2}$ dependence of the Schottky enhancement.

and at this point the noise in the charge measurement of ~ 50 pC contributed a lot of scatter to the data. The small spot was scanned over the cathode in 1 mm steps in a full (x, y) grid covering the cathode. At each position, N measurements were taken of the charge and the laser energy using a LabVIEW/GPIB program. Ignoring positions at the edges of the cathode for which no measurable charge was seen, there remained 153 positions. The median number of charge/laser points per position was $\langle N \rangle = 14$, so the statistical quality of the data was adequate, but could be improved. The data analysis was tedious, as separate files were created for each position, and each file was processed separately to extract the mean quantum efficiency. The rms (root-mean-square deviation from the mean, or σ) of the distribution was used as the error bar.

Mapping the mean quantum efficiency to a grayscale value[4], a density plot is shown in Figure 3.10. Forming a radius from the (x, y) pairs (the geometric center of the cathode is chosen as the origin), we plot the quantum efficiency points with error bars in Figure 3.11. It is evident from this plot that the quantum efficiency is constant in the region of the laser spot (3 mm radius at most).

3.4 Timing Synchronization and Stability

Earlier in Table 2.1 on page 17 we listed the phase-locked low-level RF frequencies and their use in the photoinjector. One of the main issues is the synchronization of the system and suppression of the jitter of the laser arrival time on the cathode with respect to the phase of the RF. Each of these low-level frequencies in Table 2.1 is generated by a phase-locked oscillator[5] that is slaved to the master oscillator[6]. The exception to this is a 250 kHz signal which is derived from division of the 1.003 MHz.

---

[4] We thank W. Hartung for his assistance in generating this plot.

[5] Communication Techniques, Inc., Whippany, NJ.

[6] MTI Milliren Technologies, Inc., Newburyport, MA.

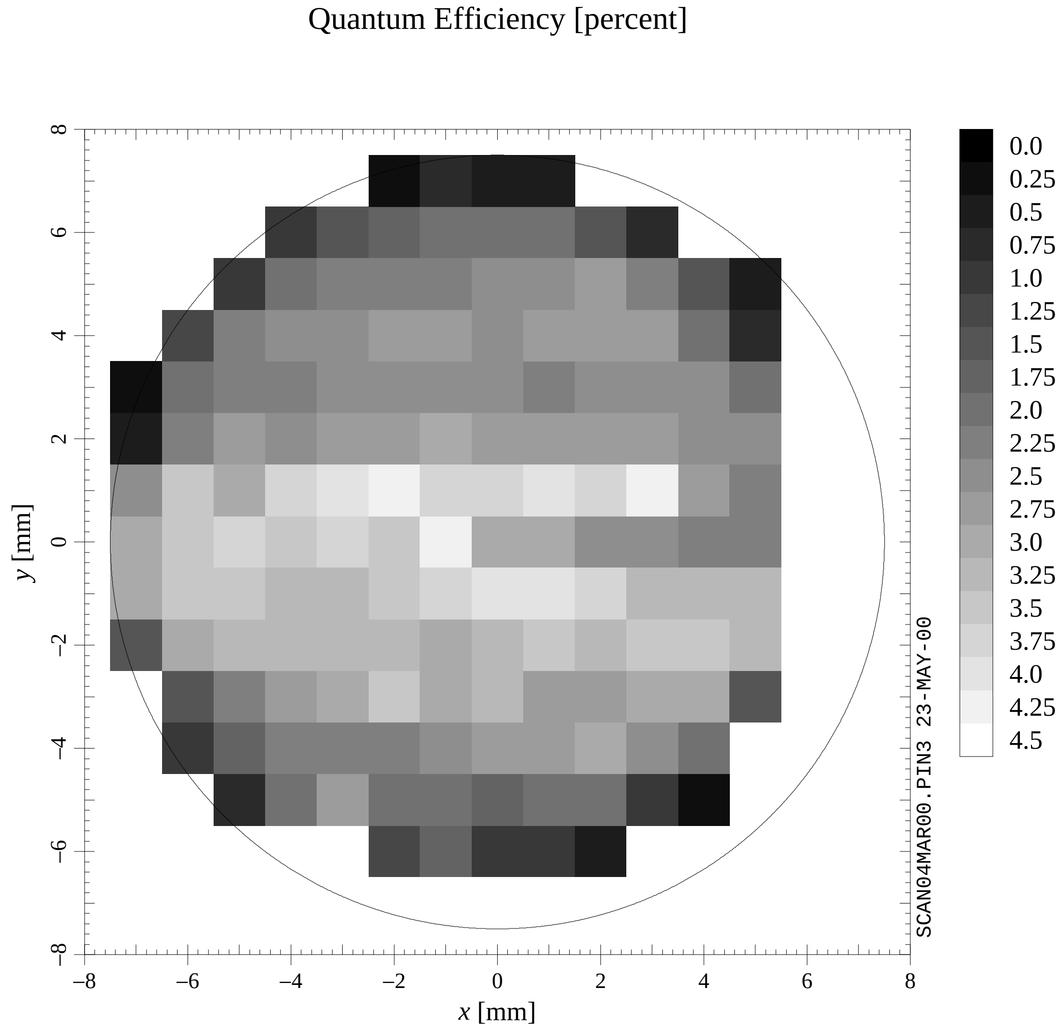

Figure 3.10: Photocathode Uniformity. The mean quantum efficiency over an ensemble of measurements at each position is mapped to a grayscale.

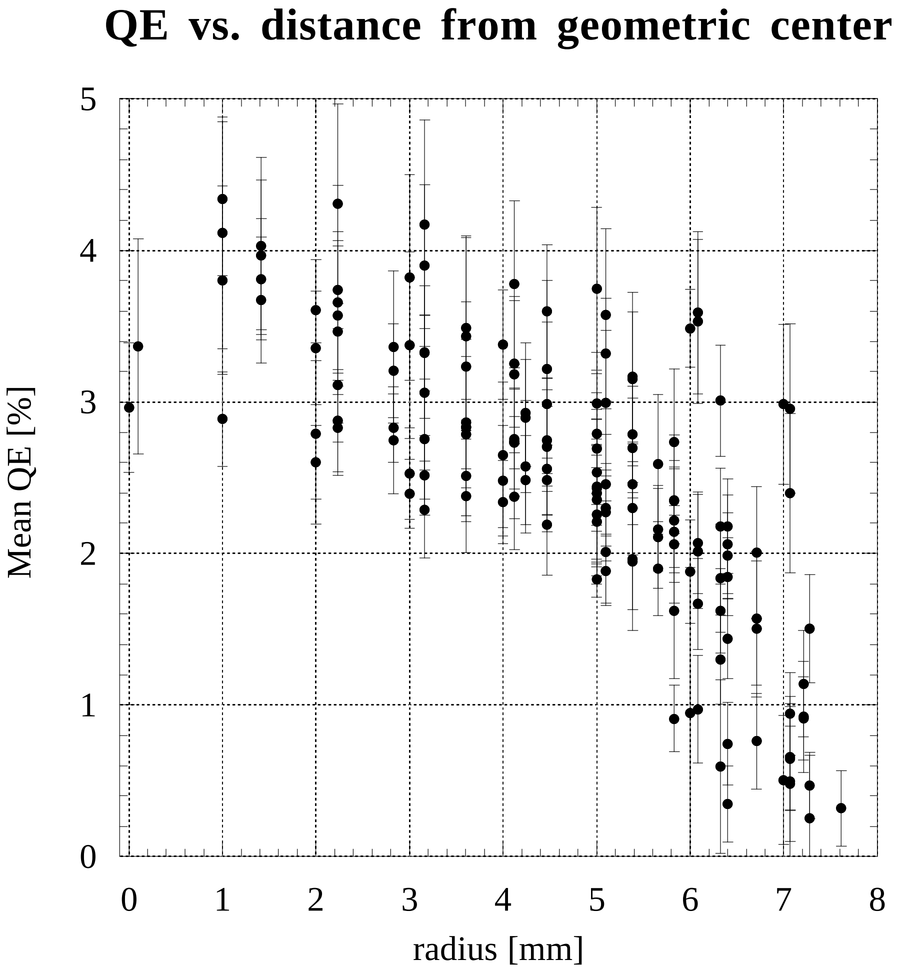

Figure 3.11: Photocathode Uniformity. The geometric center of the cathode is the origin, and a radius is formed from the (x, y) coordinate pairs. The error bar is the rms of the ensemble of measurements at each position. This is the same data as Figure 3.10.

The laser oscillator uses conventional phase-locking techniques for timing jitter suppression as described previously in Section 2.2.3.

The RF system for the superconducting 9-cell accelerating cavity has a feedback system which is necessary to fill the high Q structure and to maintain the desired phase. A schematic of this system is shown in Figure 3.12. The vector modulator controls the amplitude and phase of the low-level RF signal. After amplification in a solid state amplifier, traveling wave amplifier and Klystron, the RF is coupled into the 9-cell cavity. The transmitted power at 1300 MHz is mixed with a reference signal of 1300.250 MHz, and the resulting 250 kHz signal carries the amplitude and phase information. It is digitized and analyzed by a digital signal processor (DSP) interfaced with a Unix computer. Then control signals to the vector modulator are corrected until the output of the cavity matches the desired amplitude waveform and desired phase commanded by the user at the Unix console.

The RF for the gun is controlled in the same way. However, it was usually operated open-loop. That is, without dynamic corrections to the commanded amplitude and phase. In order to close the loop, the RF pulse on the gun must be more than 100 μsec long. In order to reduce the dark current from the gun, we usually preferred to operate with an RF pulse as short as possible. For 10 pulses, a 22 μsec RF pulse was the standard operating condition. We measured the phase jitter for the gun with and without feedback and found no conclusive difference.

The phase jitter measurement is inferred from the charge transmission near the zero crossing of the RF in the gun. Consider an axial electric field pointing *into* the cathode. We will choose this direction to have a positive sign, since the force on photoelectrons is $F = qE$ pointed *out* of the cathode. When the electric field is negative at the time of the arrival of the laser pulse, there will be no charge transmission. As the zero crossing of the electric field (which varies sinusoidally in time) sweeps over the duration of the laser pulse, the charge transmission will

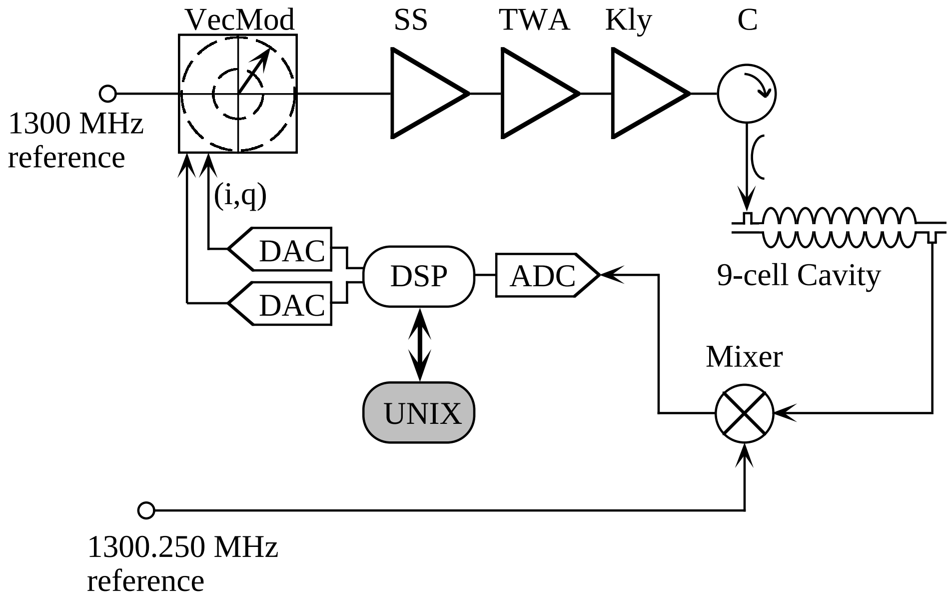

Figure 3.12: RF feedback system for the 9-cell cavity. See text for explanation. VecMod: vector modulator. SS: solid state amplifier. TWA: traveling wave amplifier. Kly: klystron. C: circulator. ADC: analog-to-digital converter. DSP: digital signal processor. DAC: digital-to-analog converter.

suddenly increase. In the absence of jitter between the laser and the RF, the charge transmission curve will rise like the cumulative integral of the laser pulse temporal profile, which for a Gaussian pulse is the error function. The slope of the transmission curve at half maximum is directly related to the width of the laser pulse. (This provides an independent check on the laser pulse length measurements with the streak camera.)

In the presence of jitter between the laser pulse arrival time on the cathode and the time of zero-crossing of the RF field, the rising curve of charge transmission becomes a band. The rms width of this band is a measure of the phase jitter. It is necessary to make the laser pulse as short as possible (we use the 2 ps σ Gaussian laser pulse by blocking arms of the pulse stacker) and to reduce the charge, so that space charge has little effect. We then log many points as the phase is varied near the zero crossing. We have recorded both the set phase as commanded at the Unix console, and the detected phase. The transmitted RF power from the gun at 1300 MHz is mixed with a stabilized reference frequency of 1300.25 MHz, and the phase of the transmitted RF is encoded onto the phase of the 250 kHz signal. Let the transmitted RF power from the gun at $(\Omega)/2\pi = 1300$ MHz and the local reference oscillator at $(\Omega+\omega)/2\pi = 1300.25$ MHz be written as

$$V_{RF}(t) = A_1 \cos(\Omega t + \varphi) \tag{3.25}$$

$$V_{LO}(t) = A_0 \cos[(\Omega + \omega)t]. \tag{3.26}$$

An ideal mixer gives the product

$$V_{mix} = V_{LO}(t)\, V_{RF}(t) = A_0 A_1 \cos[(\Omega+\omega)t] \cos[\Omega t + \varphi]. \tag{3.27}$$

Using the trigonometric identity $\cos\alpha \cdot \cos\beta = \frac{1}{2}[\cos(\alpha+\beta) + \cos(\alpha-\beta)]$

$$V_{mix} = \frac{A_0 A_1}{2} \left\{ \cos[(2\Omega + \omega)t + \varphi] + \cos(\omega t + \varphi) \right\}. \tag{3.28}$$

The high frequency term $(2\Omega + \omega)$ near 2600 MHz is filtered out, leaving only

$$V_{mix} = \frac{A_0 A_1}{2} \cos(\omega t + \varphi). \tag{3.29}$$

The 250 kHz signal is analyzed by the digital signal processor (DSP) to give the phase φ relative to an arbitrary phase constant, which has no physical significance and is ignored.

The data for the set phase (commanded) and the detected phase (readback) are analyzed separately. We show in Figure 3.13 the partial phase scan versus the detected phase. The analysis, shown in Fig. 3.14 is done by first subtracting off the best-fit slope to the rising region. Then statistics are applied to the points on the rising band (the boxed region of Figure 3.14) which gives the result:

$$\sigma_J = 3.6 \pm 0.2 \ \text{ps} \qquad \text{from detected phase} \tag{3.30}$$

Similarly, we analyze the same data set using the set phase. The partial phase scan is shown in Figure 3.15, and the analysis is shown in Figure 3.16. The rms jitter result is:

$$\sigma_J = 2.8 \pm 0.2 \ \text{ps} \qquad \text{from set phase} \tag{3.31}$$

We expected that using the detected phase would be an improvement over the set phase, however, the effect of measurement error in the detected phase adds in quadrature. These measurements are consistent if the measurement error is 2.26 ps, or about 1 degree of phase at 1300 MHz.

Previously in Section 2.2.4 on page 18 we discussed the jitter measurement of the mode-locked Nd:YLF laser with respect to its 81.25 MHz reference and found $\sigma_J = 1.78 \pm 0.14$ ps.

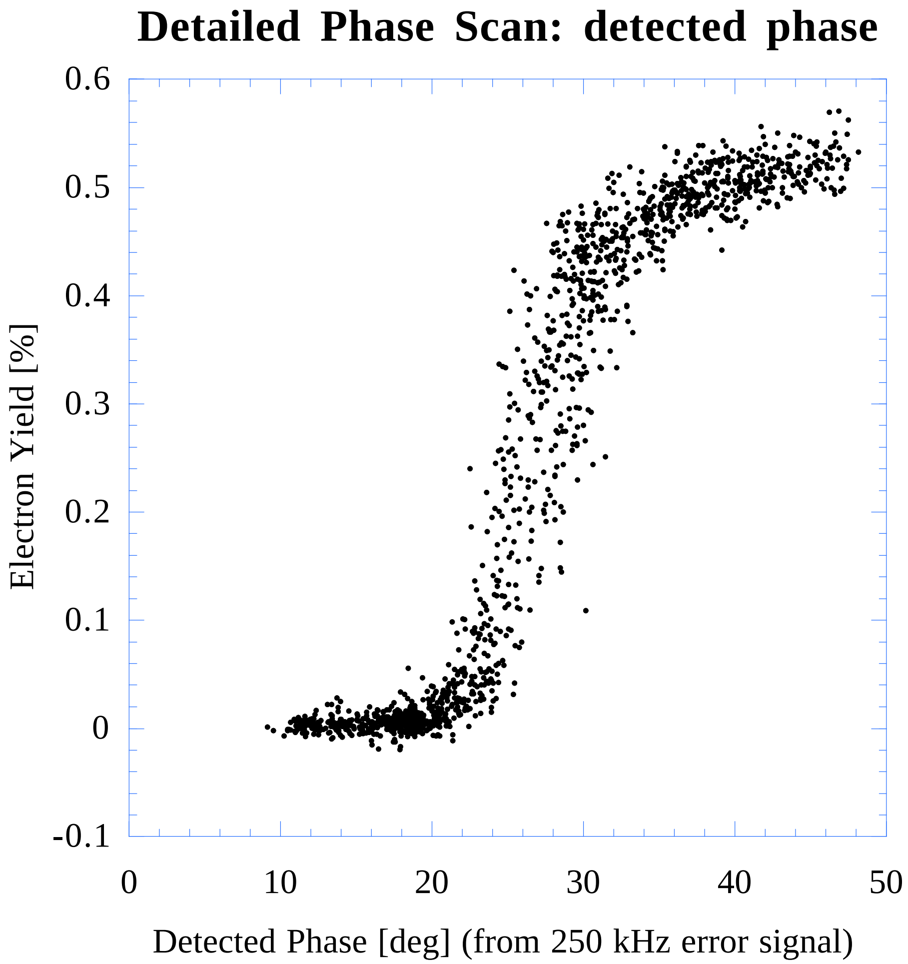

Figure 3.13: Detailed phase scan using the detected phase. The electron yield is the normalized charge extraction (number of electrons per photon) and has the same units as the quantum efficiency.

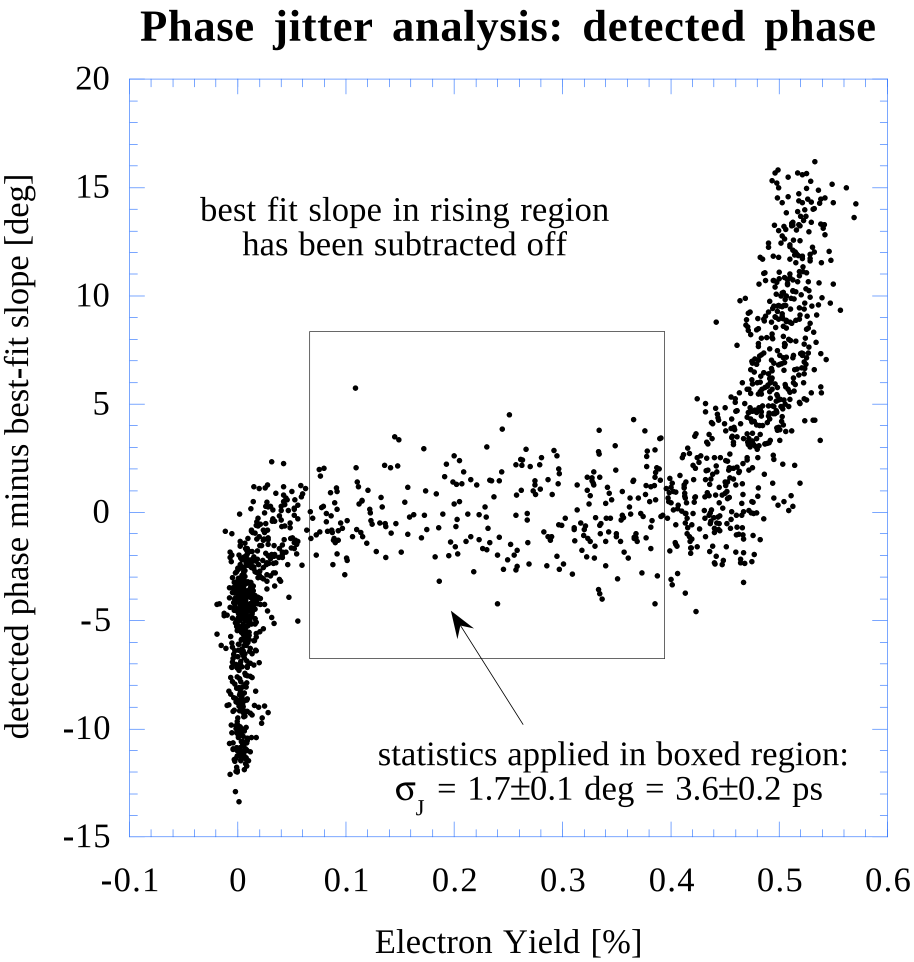

Figure 3.14: Phase Jitter Analysis: detected phase. First the best-fit slope in the rising region is subtracted off, and then statistics are applied to the rising band (boxed). The result is 3.6±0.2 ps rms jitter.

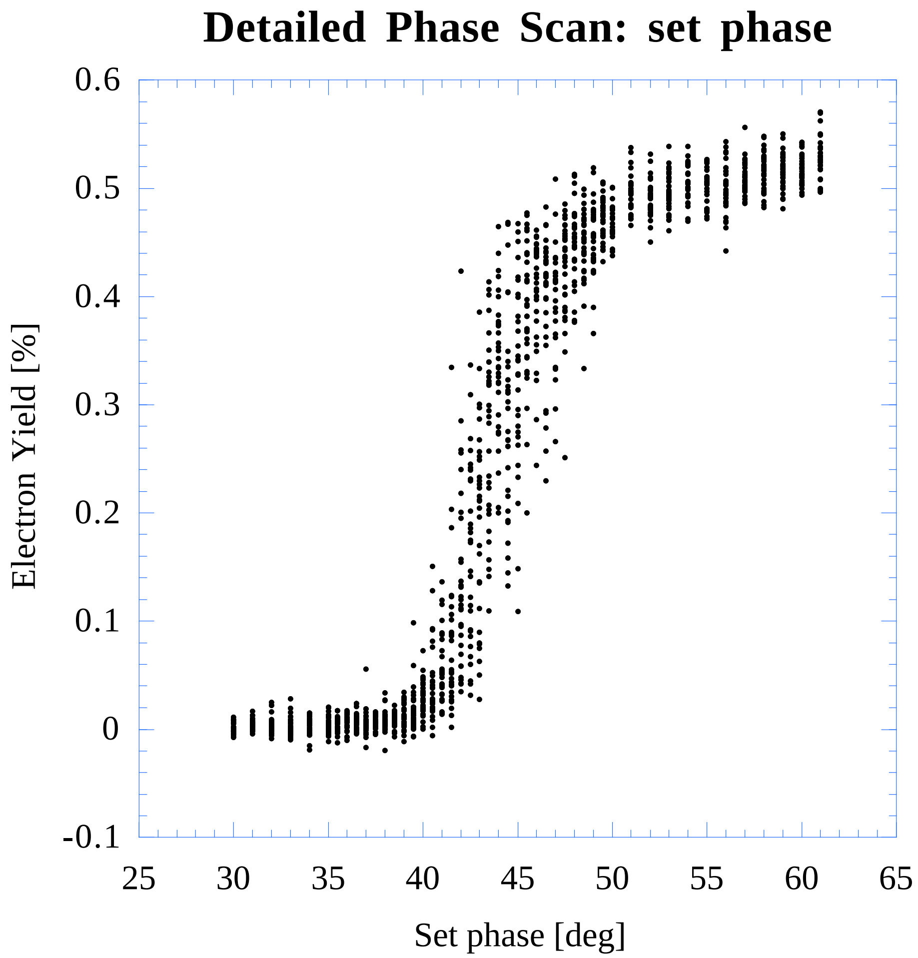

Figure 3.15: Detailed phase scan using the set phase. The electron yield is the normalized charge extraction (number of electrons per photon) and has the same units as the quantum efficiency.

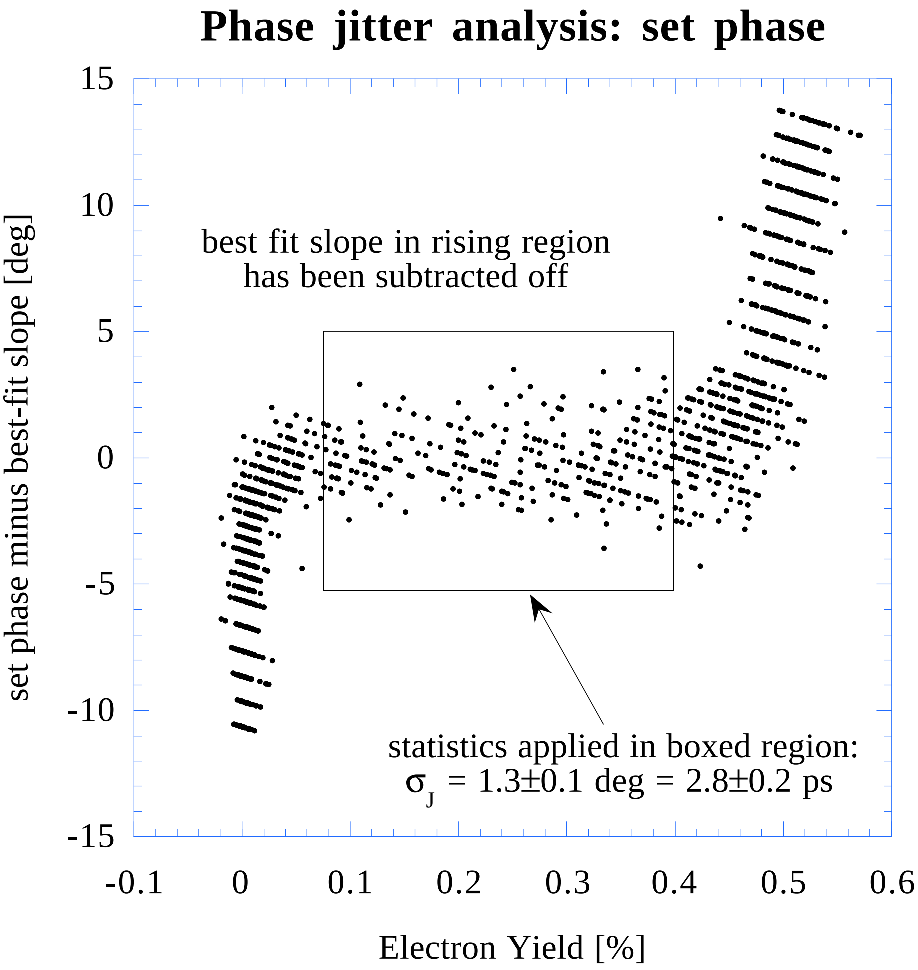

Figure 3.16: Phase Jitter Analysis: set phase. First the best-fit slope in the rising region is subtracted off, and then statistics are applied to the rising band (boxed). The result is 3.6 ± 0.2 ps rms jitter.

3.5 Emittance

The emittance of a photoinjector is a very important parameter to characterize, as it is a measure of the phase space occupied by the beam. In order to focus the beam to a small spot, clearly there must be an angular spread at the focus. A smaller spot is a trade-off with a larger angular spread, since the product of the two is a constant. Consider the beam particle distribution in the (x, p_x) plane, or by convention, the (x, θ_x) plane (the transverse momentum is related to $\theta_x \approx \frac{dx}{dz} \equiv x'$). The area occupied by the beam is the phase space, in this case, a two-dimensional phase space. The emittance corresponds to the area of the smallest ellipse in this plane which encloses all particles. The statistical definition of the normalized emittance is [37, 111]:

$$\epsilon_{n,x} = \pi\beta\gamma\sqrt{\langle x^2\rangle\langle\theta_x^2\rangle - \langle x\theta_x\rangle^2} \tag{3.32}$$

where the angle brackets imply averaging over the ensemble of beam particles. The factor of π is included by convention, and is carried with the units (π mm $\cdot$ mrad).

Liouville's Theorem, that the phase space volume of a system of particles is a constant of the motion (see Ref. [112]), is rigorously true only for the full 6-dimensional phase space. It is approximately valid for the 2-dimensional phase volumes $\epsilon_{n,x}$ and $\epsilon_{n,y}$ in the limit of weak coupling between the planes.

Nearly all methods of emittance measurement are time-integrated, with exceptions including the slice emittance measurement demonstrated at Brookhaven by X. Qiu *et al.* [113] and the time-resolved emittance using a streak camera proposed by E. Colby [37]. It is important to keep in mind that the measured emittance is usually a projected emittance. The space charge force causes a misalignment of the ellipses of the head, center, and tail of the bunch (like a twisted ribbon). If uncorrected, this misalignment causes an apparent increase in the (projected) emittance.

The Carlsten emittance compensation[7] scheme [114] uses a solenoid lens to realign the ellipses. A description of the theory of emittance compensation would take us too far afield.

In the quadrupole scan technique, the emittance is estimated by the focussing properties of the beam, *i.e.* by fitting the beam size versus quadrupole strength to a hyperbola. However, this is useful only if the beam envelope is emittance dominated. For space-charge dominated beams, it is better to use the emittance mask method. In our case, the beam is strongly space-charge dominated.

A slit mask is made of a material thick enough to stop the beam, with narrow, evenly spaced slits. The beam is brought to a parallel waist at the slit location. The individual beamlets that pass through the slits retain the transverse angular spread of the original beam, but now have a low enough charge that their evolution is to a good approximation, unaffected by space charge. After a drift length, the width of the slit images combined with the beam size on the slit mask gives the emittance in one plane.

The AØ photoinjector is equipped with 5 sets of emittance slits with stepper-motor actuators on two axes (in-out and rotation). A pair in x and y are located in cross X6 and cross XL6 (see beamline drawing, Figure 1.1, page 5) and a single slit and motor assembly in x is located in cross X3.

The characterization of the emittance is one of the results of the dissertation of J.-P. Carneiro [98], and details of the slit measurement technique and data analysis can be found there. We thank J.-P. Carneiro for providing us with a few of his results. Figure 3.17 shows measured emittance at 8 nC compared with the code HOMDYN. The solenoids were varied keeping equal currents in the primary (I_p), bucking (I_b), and secondary (I_s) coils. Experiments of this type were repeated for charge settings from 1 nC up to 12 nC, and at each setting, the conditions were varied (laser spot size, the gun gradient and phase, the solenoid

---

[7] A better term than "compensation" would be "correlation removal."

settings) to find the optimum emittance. The summary plot shown in Figure 3.18, which represents the analysis of thousands of images, gives a linear dependence of emittance on the charge.

3.6 Appendix: Truncated Gaussian Laser Spot

We repeat the calculation of Section 3.3.1 for a Gaussian laser spot which has been truncated at a radius t. The laser energy density is:

$$u(r,\phi) = \begin{cases} u_0 \exp \frac{-r^2}{2\sigma_r^2} & \text{for } r < t, \\ 0 & \text{for } r > t. \end{cases} \tag{3.33}$$

And defining $B = 1 - \exp(-t^2/2\sigma_r^2)$, the normalization is $u_0 = \frac{U_t}{2\pi\sigma_r^2 B}$. There are now three cases to be considered. Case (i), the peak value is below saturation, and we have $A_s = 0$ and $Q_t = \eta U_t$. In case (ii), there is some s in $0 < s < t$ where

$$\eta u(r = s, \phi) = \epsilon_o |\vec{E}_{cath}| \tag{3.34}$$

Then we have A_s is the circular region $r < s$, and A_u is the annular region $s < r < t$. Finally in case (iii) there is no s in $0 < s < t$ such that Equation 3.34 can be satisfied, (the entire spot is saturated) and $A_u = 0$, and $Q_t = \pi t^2 \epsilon_o |\vec{E}_{cath}|$. After simplification, the result for a truncated Gaussian laser spot is:

$$Q_t = \begin{cases} \eta U_t, & \eta U_t < aB \\ a\left[1 + \frac{(B-1)}{aB}\eta U_t + \ln \frac{\eta U_t}{aB}\right], & aB < \eta U_t < \frac{C}{1-B} \\ \pi t^2 \epsilon_o |\vec{E}_{cath}|, & \eta U_t > \frac{C}{1-B}. \end{cases} \tag{3.35}$$

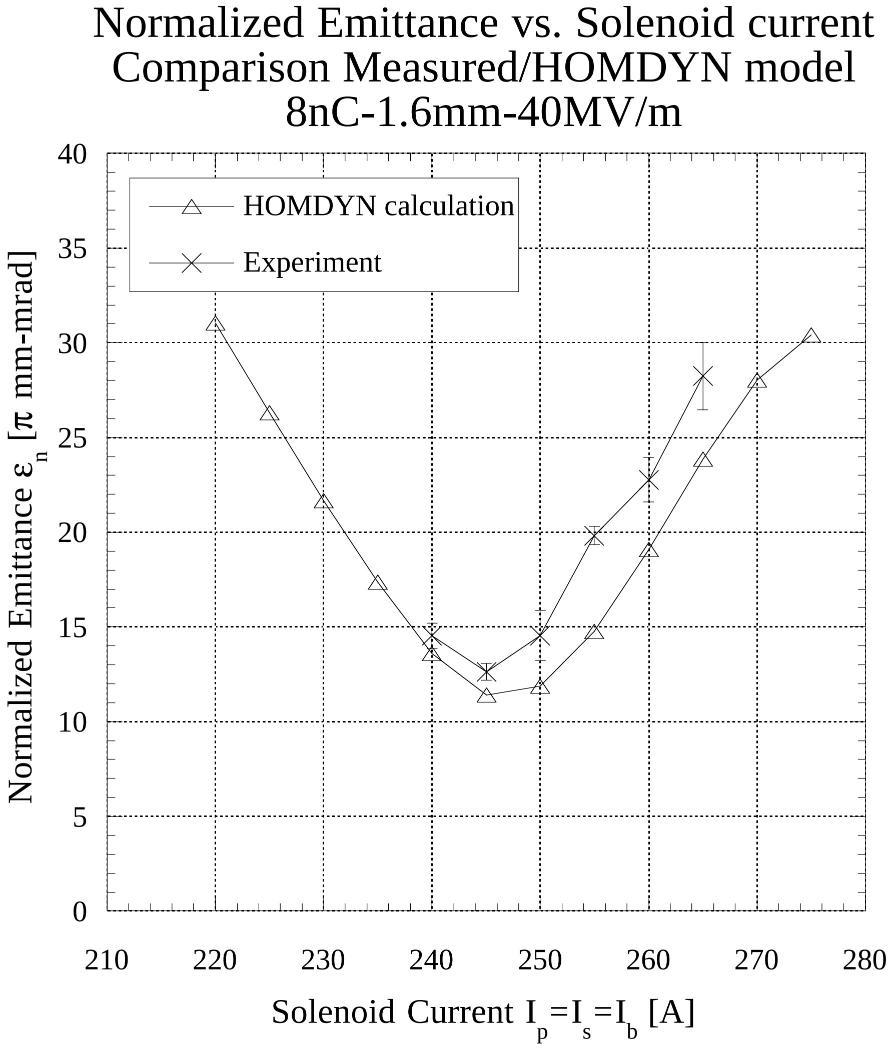

Figure 3.17: Measured Emittance compared with HOMDYN, for 8nC, laser spot is 1.6 mm σ_r. Figure courtesy of J.-P. Carneiro.

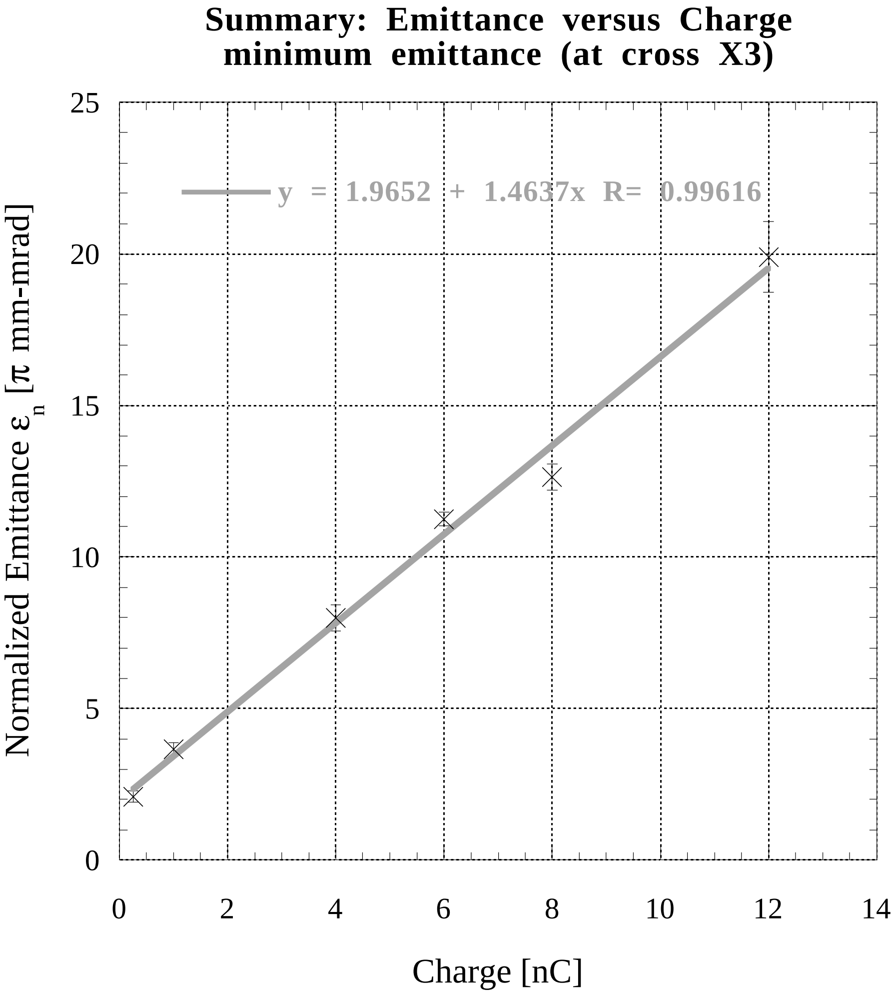

Figure 3.18: Emittance versus charge: grand summary of the optimum emittance at each charge setting. Figure courtesy of J.-P. Carneiro.

with a defined as in Eqn. 3.18 on page 84, and $C = 2\pi\sigma_r^2\epsilon_o|\vec{E}_{cath}|$. The new features are a term linear in the laser energy for the middle case, and a hard saturation of the charge for the highest laser energies.

Chapter 4

Temporal characterization of the Beam

Electron beams with short bunch lengths are desirable for high energy physics, free-electron lasers (FEL's) and other applications. For example, in colliders for high energy physics, the luminosity scales as the inverse bunch length (for fixed charge). Generally speaking, the cross-section for high-energy scattering events scales kinematically as $1/E$ as the energy E of the particles increases. High luminosity is necessary for observation of rare events. Free-electron lasers at short wavelengths also require a short bunch length in the undulator.

One of the advantages of the photoinjector is the ability to control the initial bunch length with the UV laser pulse length. The photoemission response time must be fast, or "prompt". Metal cathodes have the fastest response times (<100 fs), and semiconductors generally much slower (several picoseconds) emission times. Cs_2Te is probably intermediate (<1 ps). Space charge expansion of the bunch length at low energy is a problem. Space charge also increases the emittance. For this reason, it is better to lengthen the UV laser pulse, and compress the electron beam to a shorter bunch length after acceleration.

In this Chapter, we present measurements of the bunch length using a picosecond streak camera. Space charge expansion of the beam can be seen by the variation of the bunch length versus charge for both a short (2 ps σ_t) and a long (10.7 ps FWHM) laser pulse.

We also present measurements of magnetic bunch compression using a chicane of 4 dipole magnets. The compression experiments were performed at different charges, and also for both the long and the short bunch length. Our best compression at high charge is a peak current of 2.8 kA.

As we mentioned previously in Section 3.1 (page 72), magnetic compression is a rotation of the bunch distribution in the (z, p_z) plane, or equivalently, the $(z, \Delta E)$ plane. An intuitive picture of compression is depicted in Figure 4.1 (after [115]). The top ellipse is the distribution out of the gun, with a small energy spread but long bunch length. Second from top is after off-crest acceleration in the 9-cell cavity giving a time-energy correlation. The dispersion in the chicane rotates the distribution (third from top) resulting in a compressed beam (bottom).

The issue of emittance growth during bunch compression is a subject of current research in the field [116–120]. We have not made a careful study of this effect, but first indications for our bunch compressor are that the emittance is increased by a factor of ~ 2 when the beam is compressed [121].

4.1 Peak Current

One figure of merit for (sub)picosecond electron bunches is the peak current, which depends on both the charge and the bunch length. If the beam is Gaussian in time,

$$I(t) = \frac{Q}{\sqrt{2\pi}\sigma_t} \exp(-t^2/(2\sigma_t^2)) \tag{4.1}$$

Then the peak current is by definition the peak value of the current profile:

$$I_p = \frac{Q}{\sqrt{2\pi}\sigma_t} \tag{4.2}$$

$$I_p[\mathrm{kA}] = (0.398942\ldots) \, \frac{Q\,[\mathrm{nC}]}{\sigma_t\,[\mathrm{ps}]}. \tag{4.3}$$

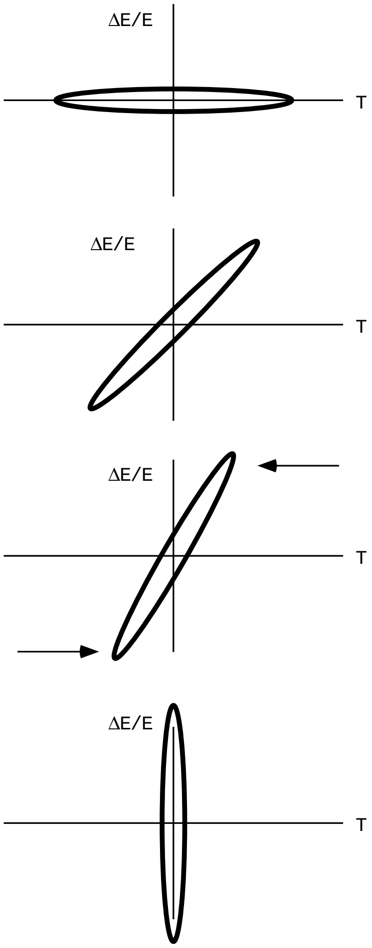

Figure 4.1: Phase space under bunch compression. (After [115].)

When the bunch length is reported as full width at half maximum (FWHM) τ, then

$$I_p = \frac{2\sqrt{2\ln 2}\,Q}{\sqrt{2\pi}\tau} \tag{4.4}$$

$$I_p[\mathrm{kA}] = (0.93944\ldots)\,\frac{Q\,[\mathrm{nC}]}{\tau\,[\mathrm{ps}]}. \tag{4.5}$$

We have compiled in Table 4.1 a list of the peak current achieved at selected facilities. A more complete list (together with other parameters) has been compiled by Travier [108] using 1993 numbers. We have attempted to summarize developments since then, which include bunch length measurements at or below the 100 fs level at the thermionic machines SUNSHINE [26, 27] and CEBAF [122], and nearly that short at the NERL (U. Tokyo) photoinjector [23, 123]. The three machines with the highest reported peak current are the Argonne Wakefield Accelerator (AWA) [124] with 1.97 kA, the CLIC Test Facility (CTF-II) at CERN [120] with 2.3 kA, and the AØ Photoinjector at Fermilab [this work] with 2.8 kA. The pulse train structure of the TESLA design at the full 1% duty cycle (with 800–1000 pulses in a macropulse repeated at 10 Hz) has both a high peak current and a high average current. Pulse structure and repetition rates for other machines listed in Table 4.1 is given by Travier [108].

Also of note is the emittance of high peak current beams. The estimated emittance in this work is 40 to 50 π mm·mrad for a compressed beam at 12 nC. This is a factor of 2 to 3 lower than the CTF-II compressed beam at similar charge, and much lower than the high charge AWA beam.

4.2 Streak camera set-up

The streak camera is a mature technology for measuring short pulses of light on the picosecond time scale. The present limit for time resolution is 370 fs FWHM

Facility	Q [nC]	σ_z [ps]	I_p [kA]
SUNSHINE, Stanford U. [26]	0.074	0.050	0.3
SUNSHINE, Stanford U. [27]	0.0056	0.142	0.016
Jefferson Lab CEBAF [122]	4.8×10^{-5}	0.084	2.3×10^{-4}
CANDELA, LAL-Orsay, France [125]	1.22	12	0.04
ELSA, Bruyères-le-Châtel, France [126]	2	9.4^c	0.085
Brookhaven ATF [127]	0.9	1.12^c	0.32
Brookhaven ATF [128]	0.4	1.4	0.11
NERL, U. Tokyo, Japan [23]	0.5	0.7	0.29
NERL, U. Tokyo, Japan [123]	0.35	0.187^a	0.74
ISIR, Osaka U., Japan [24]	26	$12^{a,b}$	0.87
Los Alamos National Lab [129]	4.5	6.8^c	0.28
Los Alamos National Lab [118]	1.1	0.3^a	1.4
Stanford Linear Collider [130]	2.4	2.6	0.37
Argonne Wakefield Accelerator [124]	93	22	1.69
Argonne Wakefield Accelerator [124]	42	8.51	1.97
CERN CTF-II (CLIC Test Facility) [120]	16	6.5	2.3
Fermilab A0 Photoinjector^d	13.2	1.89	2.8

Table 4.1: The peak current achieved at selected facilities from measured bunch length and charge. A more comprehensive list from 1993 parameters is compiled by Travier [108]. Notes: (a) authors report FWHM, and we convert assuming a Gaussian (FWHM $\tau = 2.35\,\sigma_t$), (b) authors report a non-Gaussian profile, (c) inferred from reported charge and peak current, (d) this work.

[23] using a Hamamatsu FESCA-200 streak camera. Below 1 ps, the streak camera is increasingly inefficient and expensive.

Optical transition radiation (OTR) [24, 28, 131] light from the bunch passing through a metal foil is a standard technique for generating a short pulse of light which carries the bunch information of the beam. (The discontinuity of the dielectric constant at the vacuum-metal boundary causes a charged particle passing through the boundary to radiate. See the references for a detailed theory.) OTR is prompt, and has a characteristic opening angle of $1/\gamma$, and in our case $E = \gamma mc^2 \sim 16$ MeV, so $1/\gamma \sim 32$ mrad or 1.8°. If the metal foil is mounted at 45° to the beam, there is OTR radiation in both the forward direction, and 90° to the side, as depicted in Figure 4.2.

Other choices of prompt radiators include Čerenkov radiation and synchrotron light from a bend. Obtaining useful Čerenkov light with our low beam energy requires an aerogel radiator as described in [37] at the AWA. Though an aerogel Čerenkov radiator was shown to be efficient in generating visible photons, the thickness of the radiator contributes to degraded time resolution. The aerogel is housed in a cell with thin vacuum windows and presents a high risk of contaminating the superconducting RF cavity.

The synchrotron radiation from a chicane dipole is far infrared. The critical frequency [90] is $\omega_c = 3\gamma^3 c/\rho$, and for a chicane dipole magnet of 680 Gauss and electron momentum of 18 MeV/c (or $\gamma \sim 36$) we have a bend radius $\rho = 88$ cm, which gives $\omega_c = 5 \times 10^{-13}$ rad/sec or $\lambda_c = 40$ μm). The photocathode of the streak camera is insensitive to these wavelengths. There is, of course a tail at shorter wavelengths, but the large angular spread of radiation in the bend arc (like a “searchlight”) would make collecting sufficient light with dispersionless optics problematic.

The streak camera is a Hamamatsu C5680-21S streak camera with M5676 fast sweep module and a Pulnix progressive scan digital CCD camera.[1] We described in Section 2.8.2 on page 53 the principles of operation and calibration of the streak camera. It is mounted more than one meter to the side of the beamline and shielded with 4-6 inches of Pb to protect the electronics from radiation damage.

The optics used to transport the light from the OTR screen to the streak camera, as shown in Figure 4.2, are chosen to be all-reflective to avoid dispersive effects, and as broadband as possible to optimize light collection[2]. We chose to use mirrors with a UV-enhanced Aluminum coating. A pair of parabolic mirrors provide imaging of the spot on the OTR screen to the slit of the streak camera, and an out-of-plane bend (periscope) rotates the image so that the vertical beam profile falls onto the (horizontal) slit of the streak camera. Consequently, the video images have the time axis advancing from top to bottom, and the vertical direction is left-right.

4.3 Data reduction

There are artifacts in the streak images from the CCD camera (Pulnix progressive scan digital CCD). When correctly triggered, the camera broadcasts an uninterlaced frame acquired from the last trigger. Using a digital frame grabber, instead of the analog frame grabber we used, would eliminate these artifacts. An example of an image is shown in Figure 4.3; horizontal lines and a lighter central band are seen. Time goes from top to bottom (early to late).

A four-frame average with the streak camera shutter closed was used as a background image. A rectangular region of interest (ROI) was chosen that spans the entire vertical range, and the central horizontal range. The vertical projection of the data in the ROI forms a one-dimensional histogram (or speaking loosely, a trace) that is saved to disk. The identical ROI on the average background

---

[1] We thank A. Hahn, FNAL Beams Division, for the loan of the streak camera.

[2] We acknowledge the design of N. Barov.

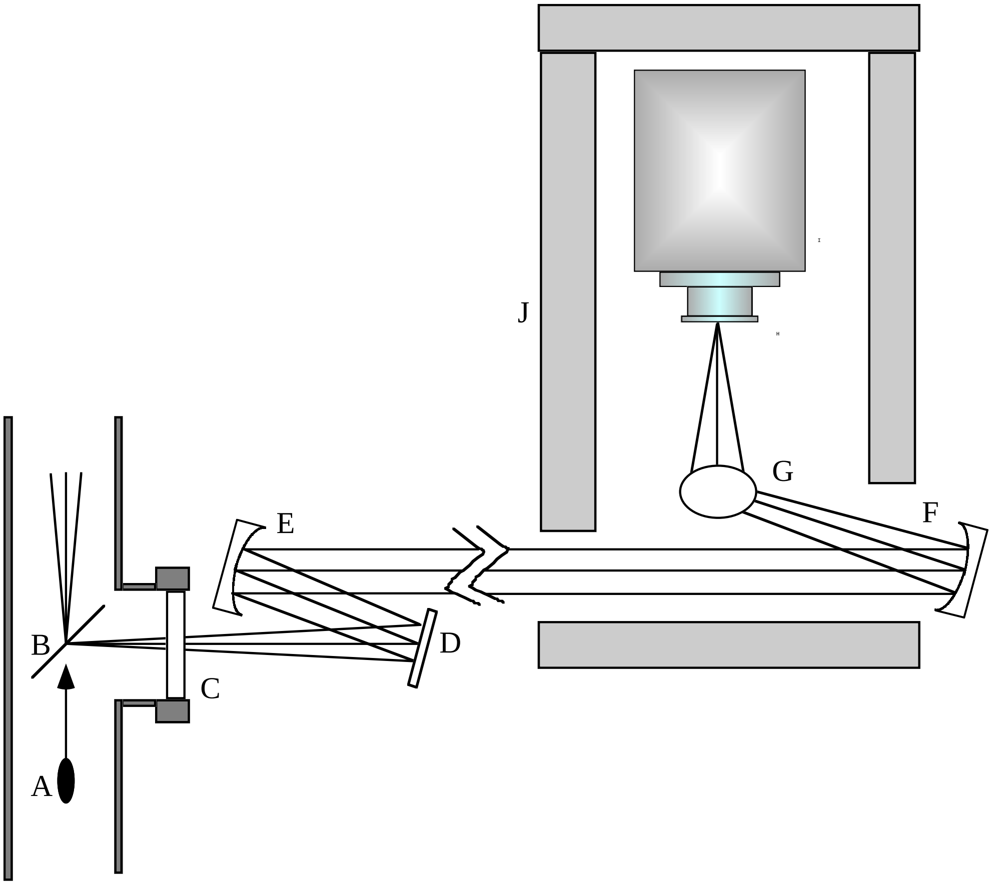

Figure 4.2: Input optics to the streak camera for bunch length measurement. A: electron bunch, B: optical transition radiation metal foil, C: vacuum viewport, D: plane mirror, E,F: off-axis parabolic mirrors, G: periscope (out-of-plane bend), H: horizontal slit assembly, I: streak camera, J: lead (Pb) shielding. The actual distance between E and F is greater than depicted.

image projects a background trace used for all images (more efficient than image math). There remained an unsubtracted noise varying from image to image within ± 0.5 count. The noise is only a problem for faint images.

Each background-subtracted trace is fitted to a Gaussian of the form

$$y = a + b\exp(-(x-c)^2/2d^2) \tag{4.6}$$

where b is the peak height, c the centroid, and d is the rms width, or σ. It is generally necessary to give the fit routine a good initial guess for these parameters, especially for the centroid c. For the streak images of high charge bunches far from optimal compression, the trace was not well fit to a Gaussian, being somewhat rectangular with a long trailing edge. Very faint images (low charge) were also difficult to fit. With these exceptions, the Gaussian generally gave a good fit, but even in bad cases it gives a reasonable estimation of the width. From the ensemble of images taken at each setting, we give a mean value with error bars estimated from the observed spread in the data. The error assigned to the fit (always smaller than the spread in the ensemble) is used when we are correlating each image to the charge on that shot.

To continue with the example image shown in Figure 4.3, a portion of the projected trace with a Gaussian fit is plotted in Figure 4.4. This is one of the points in the ensemble plotted in Figure 4.6 for $\phi_{\mathrm{gun}} = -30°$ and $\phi_{9-\mathrm{cell}} = -115°$ at the point of best compression, and the charge on this shot was 13.87 nC. The fitted σ is 7.87 pixels. Using the recent (and more conservative) calibration of 3.6 pixels per picosecond (see Section 2.8.2, on page 53) rather than 3.9 pix/ps, this is a bunch length of $\sigma_t = 2.19$ ps. It is necessary to include the finite time resolution of the streak camera, which is estimated by the width of the image in focus mode, 1.2 ps σ. Broadening due to the slit width (40 μm) is one contribution to the resolution. Assuming this adds in quadrature, we find the corrected bunch length of 1.83 ps σ_t. The peak current for this shot is 3.02 kA.

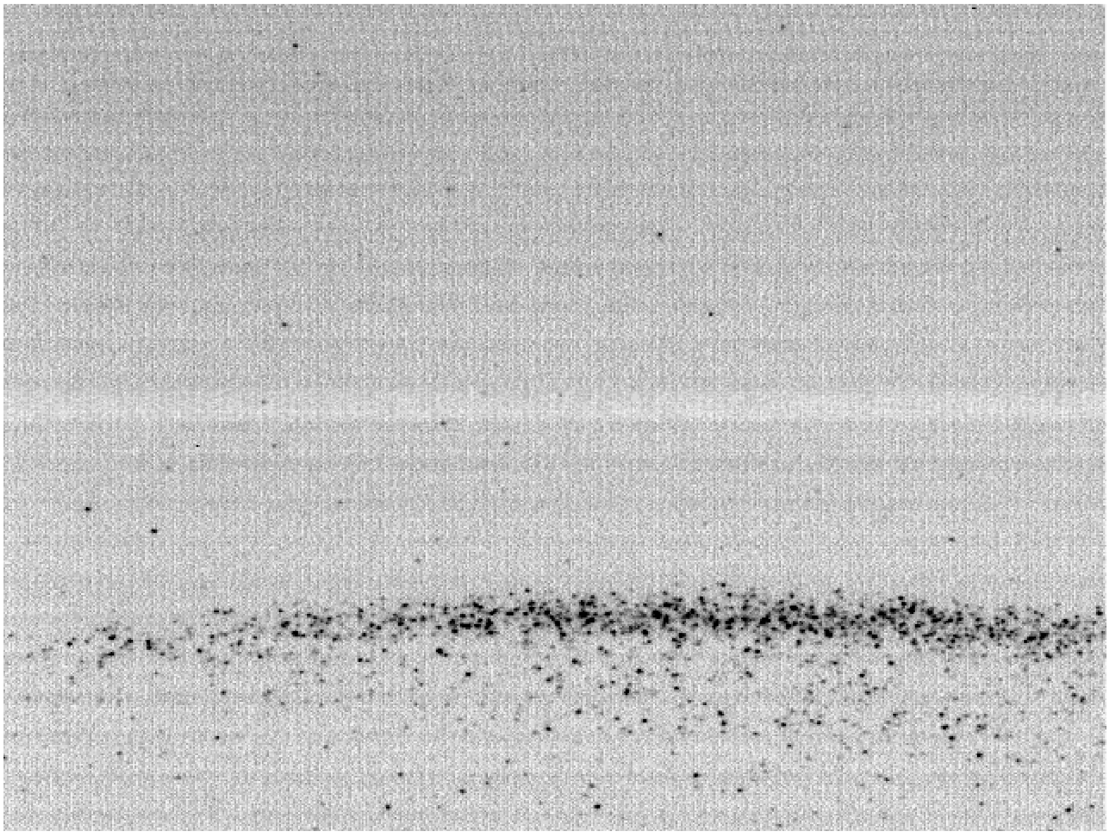

Figure 4.3: Streak Image: 13.87 nC compressed.

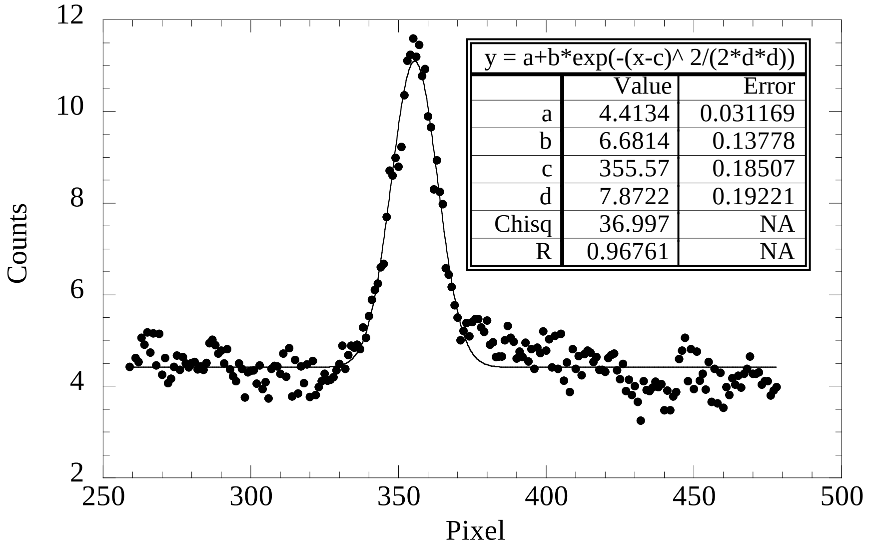

y = a+b*exp(-(x-c)^ 2/(2*d*d))

	Value	Error
a	4.4134	0.031169
b	6.6814	0.13778
c	355.57	0.18507
d	7.8722	0.19221
Chisq	36.997	NA
R	0.96761	NA

Figure 4.4: Fit to Profile of Streak Image above.

4.4 Results for the Long Laser Pulse

4.4.1 Uncompressed Bunch Length vs. Charge

We first present a series of measurements of the uncompressed bunch length as a function of charge. We have made this measurement for both the short laser pulse (Gaussian with 2 ps σ_t) and with the long laser pulse (quasi-flat top with 10.7 ps FWHM).

The expectation for no compression is that at low charge, the bunch length will be the same as the length of the laser pulse, but at higher charges, the space-charge force will have expanded the beam in time.

We also observed that the temporal profile of the beam at high charge is somewhat non-Gaussian, with a flatter top than a Gaussian and a slower falling tail. However we fitted all profiles to a Gaussian. The LabVIEW data acquisition program also recorded measurements from the LeCroy scope synchronized with the frame grabber. In this way, the charge could be measured for every image, and allowed us to study the correlations between charge and bunch length.

In Figure 4.5 we show the uncompressed bunch length versus charge. We have plotted each fitted point against the charge measured on each shot. The error bars on the bunch length are assigned from the error of the fit. The increase in the bunch length with higher charge is caused by space-charge expansion. At low charge, the bunch length is roughly the same as the UV laser pulse length on the cathode. At high charge, the bunch length has expanded by a factor of 3 by the time the beam arrives at cross X6.

4.4.2 Compressed Bunch length vs. Phase

Our approach in finding the optimal compression conditions has been to fix the current in the dipole chicane at the theoretical values for the central pair at 2.00 Amps (680 Gauss), and to reduce the current in the outer pair slightly for

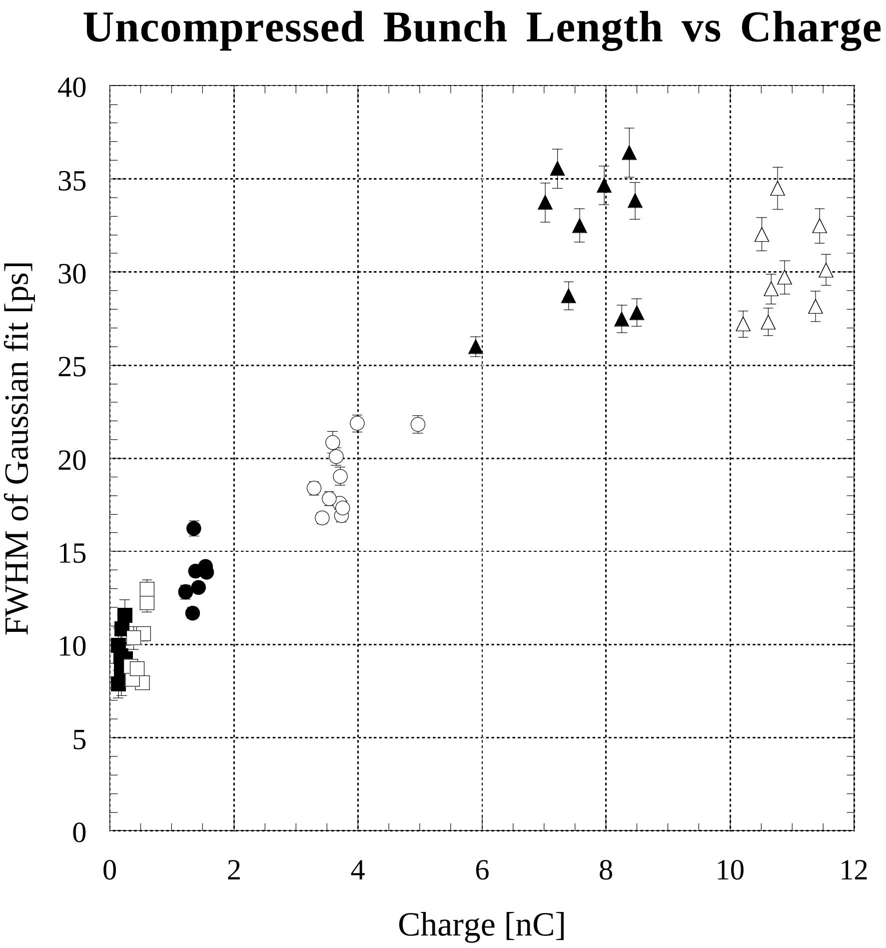

Figure 4.5: Uncompressed bunch length vs. Charge for the long (10 ps FWHM) laser pulse length. At low charge, the bunch length is the same as the laser, but increases with charge under space charge expansion. Error bars are from error in Gaussian fit.

vertical steering, typically 1.9 to 1.95 Amp. Then after finding light in the streak camera in focus mode, and making small steering changes to optimize the light, we put the camera into streak mode.

The critical parameter for the compression is the phase of the 9-cell capture cavity. The phases of the gun RF and 9-cell cavity RF are recorded as the "set phase" of the control system (Unix). To relate to the physically meaningful phase, we reference the 9-cell phase of maximum energy (crest). The physical gun phase is estimated by comparison of the charge transmission versus phase (the phase scan) to PARMELA. At a PARMELA phase of +0 degrees, the RF has a positive-going zero-crossing at exactly the center of the laser pulse.

When measuring the bunch length as a function of the 9-cell phase, we also repeated the measurement for a few values of the gun phase. We found that the gun phase had some effect on the shortest bunch length attainable, but it did not shift the position of the minimum bunch length (see Figure 4.6). The charge was as high as was obtainable for this experiment, with a mean charge of 12 nC. The shortest mean bunch length achieved of 4.4 ps FWHM (or 1.9 ps σ_t or 0.63 mm σ_z) therefore corresponds to a peak current of 2.8±0.1 kA, an impressive number.

For a fixed gun phase, we have repeated this experiment for several different values of the charge (see Figure 4.7). The expectation is that higher charge bunches will have experienced more space-charge self-forces, which increases the size of the energy-time phase space ellipse and distorts the ellipse through non-linear space-charge forces. Consequently the expectation is that the minimum bunch length at high charge will be longer than that at low charge. Indeed, this is observed, and we also observe that the point of minimum bunch length is weakly dependent on the charge, and occurs at a phase closer to crest for low charge.

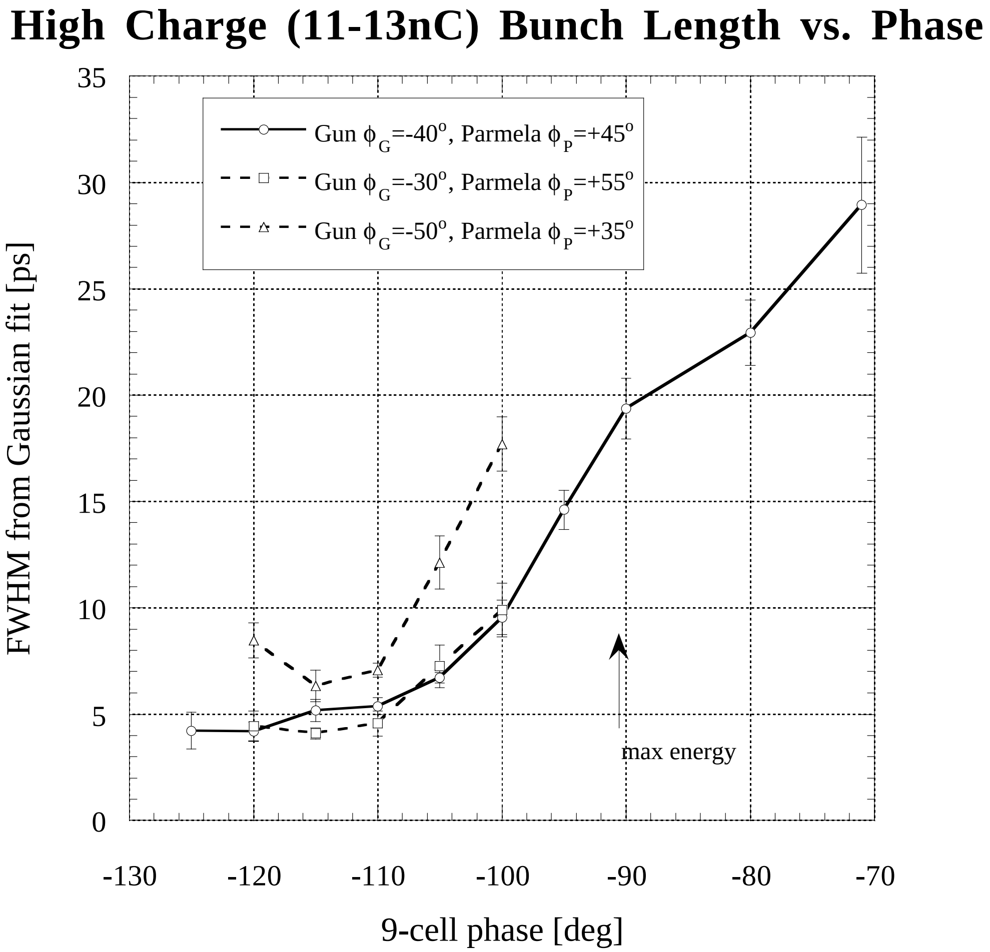

Figure 4.6: Compression vs. Phases of the 9-cell cavity and gun for the 10 ps laser pulse length. The width of the focus mode image was 2.77 ps FWHM, and the data were corrected assuming this broadening adds in quadrature to the real width.

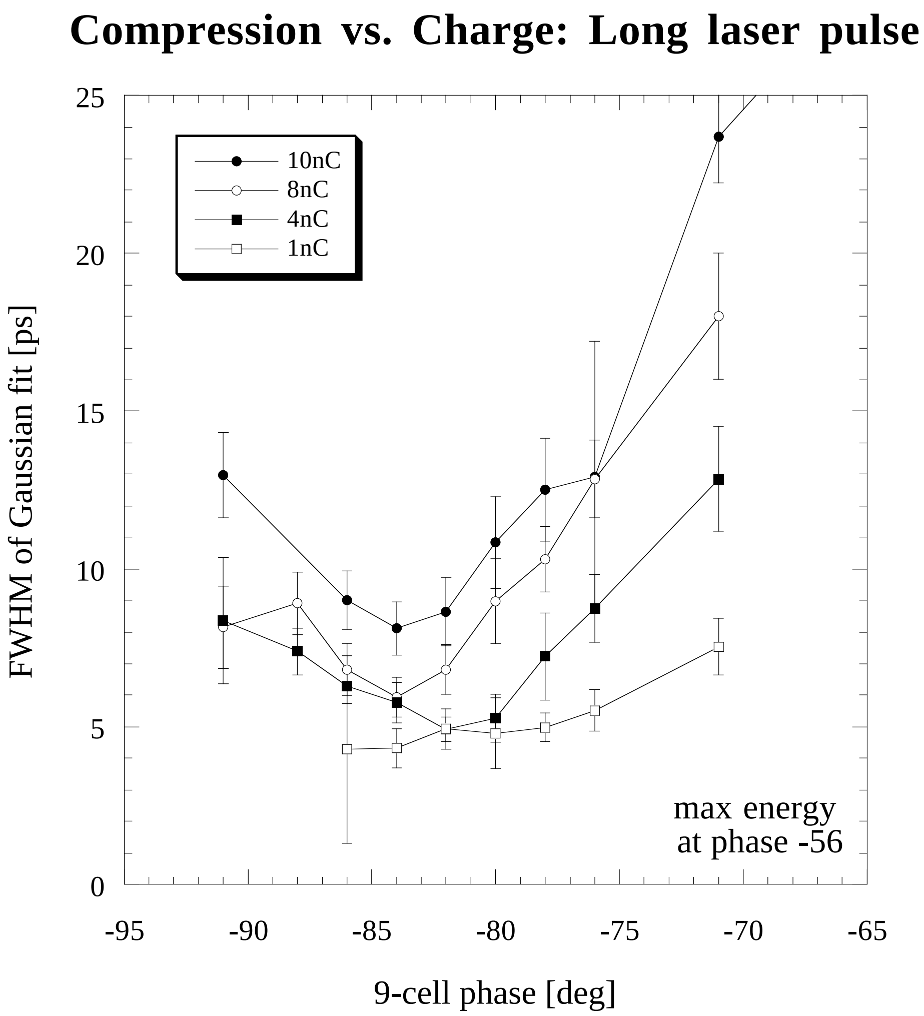

Figure 4.7: Compression vs. charge for the 10 ps laser pulse length.

4.5 Results for the Short Laser Pulse

4.5.1 Uncompressed Bunch Length vs. Charge

For the short laser pulse (2 ps σ_t Gaussian) on the cathode, we performed the same compression experiments as the 10 ps FWHM (non-Gaussian) laser pulse. Since the beam current density is higher, one might expect the space charge growth of the bunch length would be more severe.

With the chicane dipole magnets off and de-Gaussed, we measured the uncompressed bunch length with a streak camera looking at OTR radiation as before. In Figure 4.8 we plot the results for charge settings from 1 nC to 5 nC, reporting mean values for an ensemble of measurements at each setting with error bars from the rms deviation. It is clear that even at low charge, the bunch length has increased more than a factor of two above the initial laser pulse length on the cathode. By comparison, for the long (10 ps FWHM non-Gaussian) laser pulse (Figure 4.5 on page 122) the bunch length at low charge is the same as the initial laser pulse on the cathode. Note also that the bunch length increases linearly with charge.

4.5.2 Compressed Bunch Length vs. Phase

Following the same protocol as before, we compressed the beam for a fixed setting of the chicane dipole magnets (2.0 Amp in the central pair, and reducing the outer pair slightly for vertical steering) by varying the phase of the 9-cell cavity away from crest (on crest is at a set phase of -40 degrees). It is seen in Figure 4.9 that the minimum bunch length is insensitive to the charge and occurs at nearly the same dephasing for all charges (35 degrees off-crest). All of these measurements are for a large laser spot size on the cathode with the remote-controlled iris open. Fits to the spatial profile give a radial $\sigma_r = 2.1$ mm. The gun phase was set corresponding to a PARMELA phase of approximately +50 degrees.

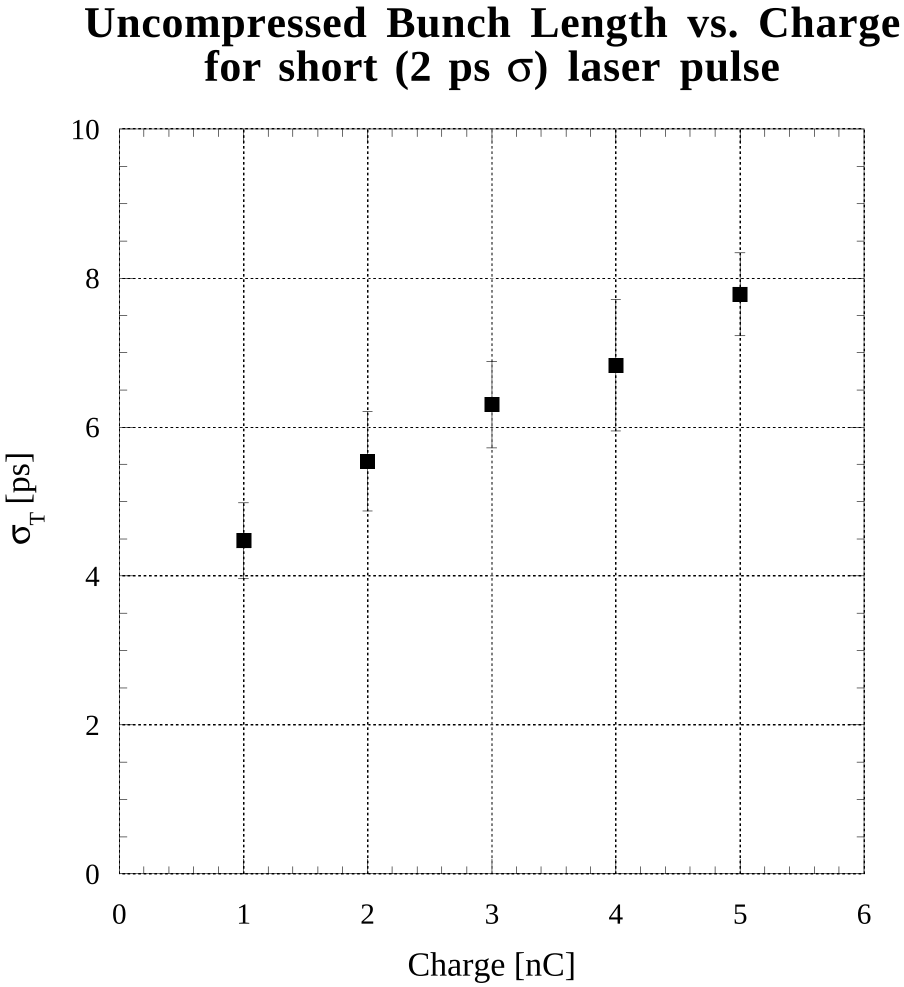

Figure 4.8: Uncompressed σ_t vs. Q for short laser pulse. At each charge setting, an ensemble of measurements was taken, and we report the mean bunch length with the error bar from the rms deviation of the data.

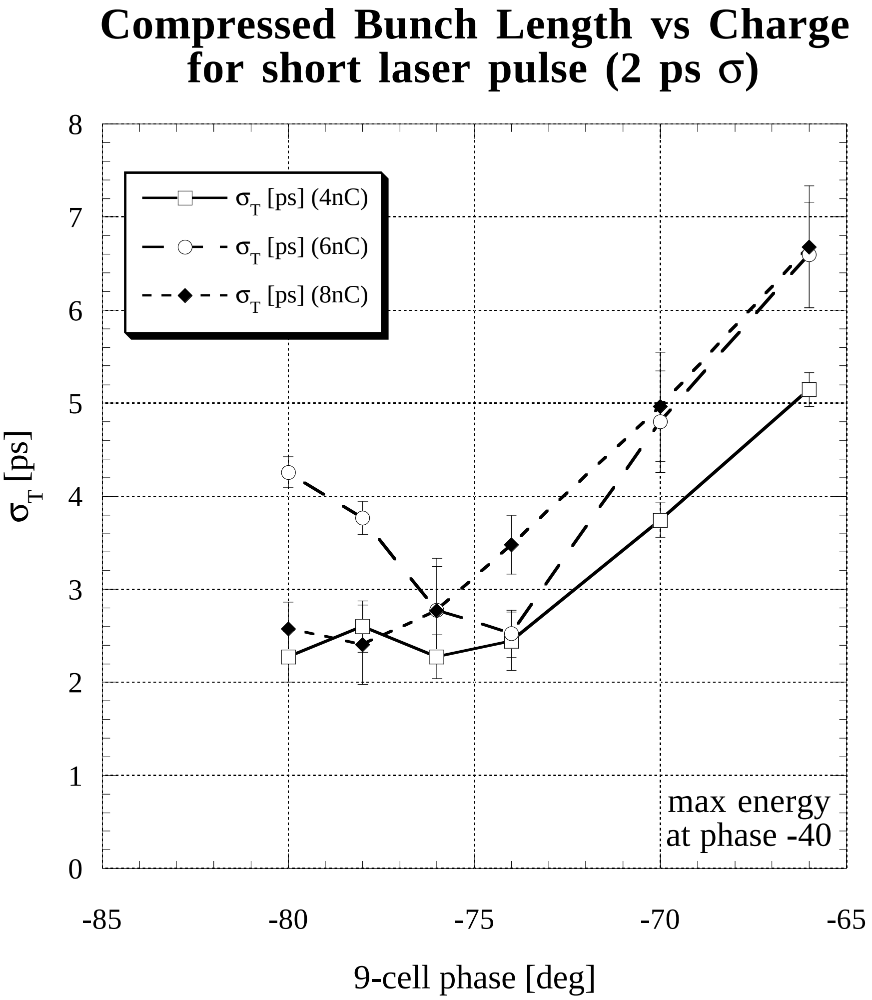

Figure 4.9: Compressed bunch length vs. charge for the short (2 ps σ Gaussian) laser pulse on the cathode. The minimum bunch length is insensitive to charge and occurs at nearly the same dephasing of the 9-cell cavity for all charges. A set phase of -40 degrees is on-crest.

The short laser pulse provides no advantage to compression. We see that generally a larger dephasing is required to compress the beam to the same level as with the long laser pulse, so the beam energy is lower. Also, the emittance is larger for the short laser pulse than the long. These effects are a consequence of the space charge force expanding the beam in all dimensions. Most of this expansion occurs in the gun, where β is rapidly changing from $\beta = 0$ to $\beta \to 1$.

4.6 Energy Spread

Compressing the beam requires an off-crest acceleration in the 9-cell superconducting RF cavity. This reduces the total energy and increases the energy spread. At the end of the beamline is a dipole spectrometer for momentum analysis of the beam. In Figure 4.10 we show the total energy and momentum spread of the beam as a function of the (set) phase of the cavity. Note that the region utilized for bunch compression is 20–30° off crest, which corresponds to a reduction in the total energy of about 2 MeV, and an increased momentum spread up to 3–4 %. The emittance growth effects of coherent synchrotron radiation and the non-inertial space charge force [116, 117, 120] from the bunch compressor need to be addressed. Preliminary indications are that the emittance is increased by a factor of ~ 2 [121]. The strong focussing in both planes (from the fringe fields of the dipoles) requires carefully setting the quadrupoles downstream to recover the beam envelope.

4.7 Summary

We have measured the electron bunch length using a picosecond streak camera for both a short laser pulse and a long laser pulse on the cathode. The uncom-

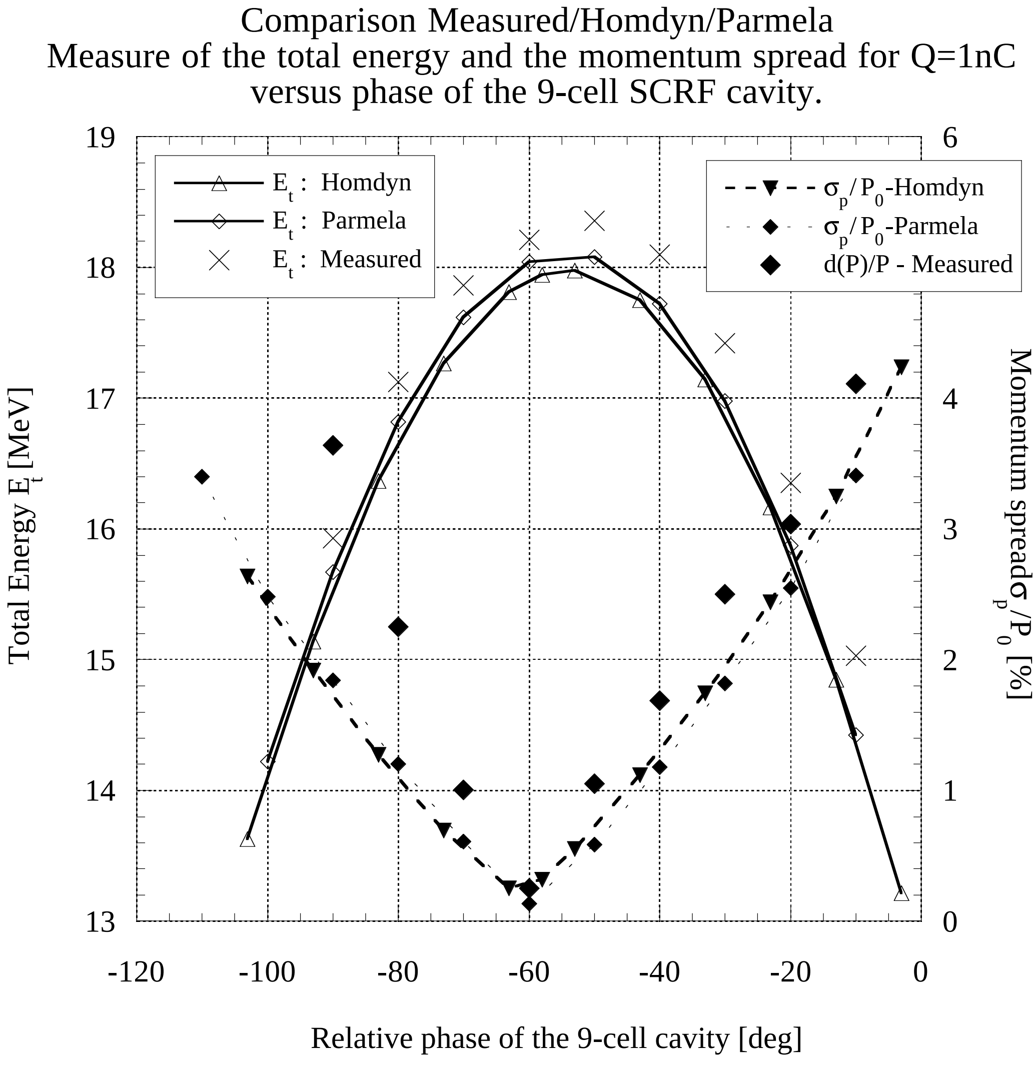

Figure 4.10: Total energy E_t and momentum spread (σ_p/P_o) versus accelerating phase of the 9-cell superconducting RF cavity. Comparison with predictions of PARMELA and HOMDYN. Figure courtesy J.-P. Carneiro.

pressed bunch length increases with higher charge, indicating that space charge is expanding the beam.

With the short laser pulse, the bunch expands in length by more than a factor of two even at low charge. It was possible to compress the bunch from the 2 ps laser pulse, but this required a large de-phasing of the 9-cell cavity away from crest.

With the long laser pulse, compression of high charge bunches was demonstrated. For a mean charge of 12 nC, the shortest mean bunch length achieved of 4.4 ps FWHM (or 1.9 ps σ_t or 0.63 mm σ_z). This corresponds to a peak current of 2.8±0.1 kA, an impressive result. The highest peak current in a single shot was 3.02 kA.

Note added: Recent developments in bunch compression have been rapid. Our reported peak current was a record for about 6 months. We have just been made aware of work from the CLIC Test Facility (CTF-II) at CERN, which was presented at a recent conference [132]. Braun *et al.* report compression of 10 nC bunches to 0.35 mm σ_z, a peak current of 3.4 kA. The emittance reported is $\epsilon_{n,x} \sim 100$ mm·mrad and $\epsilon_{n,y} \sim 250$ mm·mrad. Although a careful measurement of the emittance of the compressed beam at high charge has not yet been done at the AØ Photoinjector, preliminary indications are an increase in the emittance by a factor of approximately 2. If the compressed emittance is indeed shown to be in the range of 45–50 π mm · mrad, then this is a factor of 2 to 5 below the CTF-II beam.

Both our result and the CTF-II result are an important demonstration of the production of high charge, high peak current electron bunches with reasonably low emittance. These high quality beams are needed for future accelerators.

Chapter 5

Electro-Optic Sampling: Theory

5.1 Overview of Electro-Optic Sampling

Since the pioneering experiments of Auston [133,134] and Valdmanis [135,136] the technique of electro-optic sampling (EOS) has been shown to be a powerful technique for fast time-domain measurements of electric fields.

Notable recent achievements include free-space electro-optic sampling measurements with a bandwidth of 37 THz into the mid-infrared [137]. The record bandwidth is now 70 THz [138]. High detection sensitivity of <200 μV with temporal resolution <200 fs has been reported in investigations of crosstalk in low-temperature microwave circuits. [139].

Sources of radiation in the millimeter wave (or tera-Hertz, THz) region and methods of detection in this frequency band have motivated some of the work in this field. Applications include molecular spectroscopy, defect sensing in semiconductor wafers, manipulation of wavepackets in Rydberg atoms, etc.

The use of electro-optic sampling for accelerator applications has been previously suggested by Refs. [140–142] and others. Detection of the beam current by magneto-optic effects has been demonstrated by Ref. [141] with a time resolution that is subnanosecond. (For magneto-optic sampling, see Ref. [143].)

Recently, at Brookhaven, electro-optic detection of a charged particle beam was reported by detecting a faint light pulse through crossed polarizers as the beam passed by an electro-optic crystal [144]. The time resolution possible here is limited by the speed of the photodetectors and amplifiers, which is similar to that available with capacitive beam pickups. Earlier at Brookhaven, an RF phase measurement using the electro-optic effect and phase stabilization by feedback was demonstrated [145].

We have used electro-optic sampling to measure the electric field waveforms in vacuum induced by the passage of electron bunches with an estimated time resolution of $\sim$ 5 ps, limited by the laser pulse length [146, 147]. In this Chapter, we begin with some brief theoretical background, and discuss in detail the experimental setup. In the following Chapter we present experimental results and interpretation.

Independently of our work, a group at FOM-Institut voor Plasmafysica "Rijnhuizen" (Nieuwegein, The Netherlands) has used electro-optic sampling in ZnTe to resolve the sinusoidal electric field of the free electron laser FELIX at the optical frequency ($\lambda = 150$ μm) [148]. Of note is the rapid-scanning cross-correlation technique. The same group has sampled the electric field of the transition radiation from the electron beam exiting a beryllium window [149] and the electric field in vacuum [150] from which the bunch length is measured.

5.2 Electro-Optic Effect

The electro-optic effect is one of many nonlinear optical phenomena arising in the interaction of electromagnetic radiation with matter, and a complete theoretical treatment is given in many standard texts on nonlinear optical physics, such as Refs. [82, 151–153]. We give some background so that our presentation is more self-contained.

5.2.1 Nonlinear Susceptibility

The *response* of a medium to an applied electric field can be described by the induced polarization $\mathbf{P}$. For weak electric fields, the polarization is linearly proportional to the applied field:

$$\mathbf{P} = \epsilon_o \boldsymbol{\chi}^{(1)} \mathbf{E}. \tag{5.1}$$

A better approximation to the full *constitutive relation*[1] is an expansion in powers of the electric field.

$$\mathbf{P} = \epsilon_o [\boldsymbol{\chi}^{(1)} + \boldsymbol{\chi}^{(2)} \mathbf{E} + \boldsymbol{\chi}^{(3)} \mathbf{E}^2 + \cdots] \mathbf{E} \tag{5.2}$$

where, in addition to the linear optical susceptibility tensor $\boldsymbol{\chi}^{(1)}$, there is the second-order nonlinear susceptibility tensor $\boldsymbol{\chi}^{(2)}$, and third-order $\boldsymbol{\chi}^{(3)}$. Effects arising from $\boldsymbol{\chi}^{(2)}$ include second harmonic generation (see Section 2.7 on page 44), DC rectification, the linear electro-optic (or Pockels) effect, parametric oscillation, and three wave mixing (sum frequency and difference frequency generation). The third-order susceptibility gives rise to the quadratic electro-optic (or Kerr) effect, self-phase modulation, four-wave mixing, and other effects as well.

A simple example will illustrate (following [153]) the effects of $\boldsymbol{\chi}^{(2)}$. Consider an applied field with two frequencies:

$$\mathbf{E} = \mathbf{E}_1 \cos(k_1 x - \omega_1 t) + \mathbf{E}_2 \cos(k_2 x - \omega_2 t). \tag{5.3}$$

In the product form $\boldsymbol{\chi}^{(2)} \mathbf{E}^2$ there will be a term

$$\frac{1}{2} \boldsymbol{\chi}^{(2)} \mathbf{E}_1^2 [1 + \cos(2k_1 x - 2\omega_1 t)] \tag{5.4}$$

---

[1] Discussion of constitutive relations can be found in, *e.g.*, [90, 154].

which describes DC rectification and second harmonic generation of ω_1 (and a similar term for ω_2). There are also mixing terms of the form

$$\boldsymbol{\chi}^{(2)}\mathbf{E}_1\mathbf{E}_2[\cos\{(k_1+k_2)x-(\omega_1+\omega_2)t\}+\cos\{(k_1-k_2)x-(\omega_1-\omega_2)t\}] \quad (5.5)$$

which describe sum-frequency and difference-frequency generation. Whether these processes are efficient or inefficient is determined by the phase-matching conditions (momentum conservation).

Note that the susceptibility tensors possess certain symmetries. The crystal medium has symmetries described by the various crystallographic point groups, (see, Kittel [155], or Ashcroft & Mermin [156].) and the susceptibility tensor evidently must possess the same symmetries of the medium. If the crystal has inversion symmetry, then $\boldsymbol{\chi}^{(2)} = 0$, and further $\boldsymbol{\chi}^{(n)} = 0$ for n even. In general, for lossless media there is $\boldsymbol{\chi}^{(2)}_{ijk} = \boldsymbol{\chi}^{(2)}_{ikj}$ (the Kleinman symmetry [157]), reducing the number of independent elements of the tensor from 27 to 18. Using the crystal symmetries, the number of independent components of the tensor can be further reduced.

5.2.2 Parametrization of Electro-Optic Effect

The index of refraction n in a medium is related to the linear susceptibility by $\chi^{(1)} = n^2 - 1$, and for historical reasons, the electro-optic effect is often parametrized [82] by the changes in $(1/n^2)$ with an applied electric field. We caution that notations vary in the literature. The advantage of this parametrization is that it offers an intuitive picture of the index ellipsoid. This ellipsoid elongates and/or rotates in response to an applied field.

It is always possible to find principal axes $(\hat{\xi}_1, \hat{\xi}_2, \hat{\xi}_3)$ such that the index ellipsoid can be written:

$$\frac{\xi_1^2}{n_1^2}+\frac{\xi_2^2}{n_2^2}+\frac{\xi_3^2}{n_3^2}=1. \tag{5.6}$$

For biaxial crystals, $n_1 \neq n_2 \neq n_3$, while for uniaxial crystals[2] there is an extraordinary $n_e = n_3 = n_z$ direction, which by strict convention is chosen to be the z-axis, and an ordinary $n_o = n_1(\equiv n_x) = n_2(\equiv n_y)$ direction. For isotropic media, the ellipsoid degenerates to a sphere: $n_o = n_1 = n_2 = n_3$.

Choosing our coordinate system (x, y, z) to be the principal axes, the ellipsoid will be modified by the linear electro-optic effect in the presence of an electric field to be:

$$\left(\frac{1}{n^2}\right)_1 x^2+\left(\frac{1}{n^2}\right)_2 y^2+\left(\frac{1}{n^2}\right)_3 z^2+2\left(\frac{1}{n^2}\right)_4 yz+2\left(\frac{1}{n^2}\right)_5 xz+2\left(\frac{1}{n^2}\right)_6 xy=1 \tag{5.7}$$

where we have followed the notation of Yariv [82]. The change in the coefficients proportional to the applied electric field is written:

$$\Delta\left(\frac{1}{n^2}\right)_\ell=\sum_{j=1}^{3} r_{\ell j}E_j \qquad \text{for} \quad \ell=(1,\dots,6) \tag{5.8}$$

This is the definition of the electro-optic tensor $r_{\ell j}$, which is a 6×3 matrix. The index j which runs $(1, 2, 3)$ is shorthand for (x, y, z).

We make a connection back to the elements of the susceptibility tensor using relations found in Zernike and Midwinter [151]. A notation common to experimentalists is to absorb a factor of 2

$$d_{ijk}=\frac{1}{2}\chi_{ijk}^{(2)} \tag{5.9}$$

---

[2] The highest degree of rotational symmetry applies to only one axis.

and since $d_{ijk} = d_{ikj}$ the last two indices are contracted into $d_{i\ell}$ for $\ell = (1, \ldots, 6)$ with the convention:

$$\ell = \begin{cases} 1 & \text{for} \quad j = k = 1, \\ 2 & \text{for} \quad j = k = 2, \\ 3 & \text{for} \quad j = k = 3, \\ 4 & \text{for} \quad j = 2, \quad k = 3, \\ 5 & \text{for} \quad j = 1, \quad k = 3, \\ 6 & \text{for} \quad j = 1, \quad k = 2, \end{cases} \tag{5.10}$$

The connection is then

$$r_{\ell j} = -\frac{4\pi}{n^4} d_{j\ell} \tag{5.11}$$

The question of *which* index n to use is a subtle issue. Since the index n is related to the dielectric permeability tensor by $\mathbf{n}^2 = \boldsymbol{\epsilon}$, it is appropriate to use [158] $n^4 \Rightarrow \epsilon_\ell \epsilon_j \Rightarrow \epsilon_{jk}\epsilon_{j'k'}$

We next consider the specific case of lithium tantalate ($LiTaO_3$).

5.2.3 Case: $LiTaO_3$

The form of the electro-optic tensor for $LiTaO_3$ is [82]:

$$r_{ij} = \begin{pmatrix} 0 & -r_{22} & r_{13} \\ 0 & r_{22} & r_{13} \\ 0 & 0 & r_{33} \\ 0 & r_{51} & 0 \\ r_{51} & 0 & 0 \\ -r_{22} & 0 & 0 \end{pmatrix} \tag{5.12}$$

For an applied electric field along the 3-direction (E_z), the equation of the indicatrix is

$$\left(\frac{1}{n_o^2} + r_{13}E_3\right)x^2 + \left(\frac{1}{n_o^2} + r_{13}E_3\right)y^2 + \left(\frac{1}{n_e^2} + r_{33}E_3\right)z^2 = 1. \tag{5.13}$$

The maximum electro-optic effect is for light traveling in the y direction with linear polarization 45° between the x and z axes. Then the electro-optic coefficient is:

$$\Gamma = \frac{1}{2}\frac{\omega}{c}(n_o^3 r_{13} - n_e^3 r_{33})E_z \tag{5.14}$$

For electric fields along x or along y, there is also an electro-optic effect in $\mathrm{LiTaO_3}$, but with a smaller coefficient.

5.3 Time Resolution

The time resolution attainable with electro-optic sampling (EOS) is influenced mainly by three factors: the laser pulse length, the thickness of the crystal, and the group velocity mismatch of the optical field with the (lower frequency) sampled field.

Wu and Zhang [137] used a very thin (30 μm) crystal of $\langle 110 \rangle$ ZnTe (to minimize the group velocity mismatch) together with a 12 fs Ti:sapphire laser for free-space electro-optic sampling. The shortest oscillation period they found was 31 fs, and the amplitude spectrum contained frequencies out to 37 THz.

Leitenstorfer *et al.* [138] used ZnTe and GaP crystals with thickness between 6 and 20 μm (contacted to inactive substrates). They show it is necessary to correct for the response function of the crystal, and that the inclusion of the dispersion of the second-order nonlinear coefficient is essential. They observe frequency components up to 70 THz ($\lambda = 4$ μm).

Of course the time resolution we achieve is more modest, being dominated by

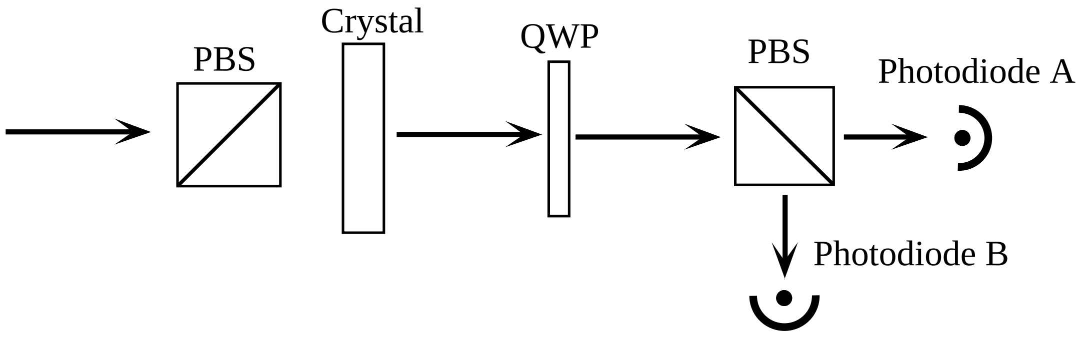

Figure 5.1: Simplified EOS setup. PBS: polarizing beam splitter, QWP: quarter wave plate.

the probe laser pulse length ($\sim$ 4 ps FWHM). Our point is that the technique is in principle capable of time domain measurements well below 100 fs. As future electron accelerators for free electron lasers and high-energy physics push bunch lengths to 100 fs and below, the longitudinal bunch charge distribution $\rho(z)$ could be measured by the electro-optic sampling when other techniques, such as the streak camera, have insufficient resolution.

5.4 Experimental setup

We have taken data using several different configurations. The elements common to all of the setups (see Figure 5.1) are a polarizer, the crystal, the compensator, and another polarizer (analyzer). The compensator is in this case a quarter wave plate. For two detectors A and B after the analyzer, the intensity measured at A is (using the shorthand $I_A \equiv A$):

$$A = I_o \sin^2(\frac{\Gamma}{2} + \phi) \tag{5.15}$$

with the electro-optic term Γ is small ($\sin\Gamma \sim \Gamma$), and ϕ is a constant. The intensity incident on the analyzer is I_o is conserved so the other detector B must measure an intensity:

$$B = I_o \cos^2(\frac{\Gamma}{2} + \phi) \tag{5.16}$$

If the static biasing is chosen such that $\phi = 0$, then for small signals, $A \propto I_o\Gamma^2$. Better is to choose $\phi = \pi/4$, and then the difference between the detectors divided by the sum of the detectors

$$\frac{A - B}{A + B} = \Gamma \tag{5.17}$$

independent of I_o. The electric field and Γ are related by the appropriate electro-optic coefficient, such as in Eq. 5.14. A more detailed analysis including the static birefringence of the crystal is given in the next Section (5.5).

The infrared probe beam is unconverted light after the doubling crystals. See Figure 5.2. The UV is separated using a dichroic beamsplitter, and the UV goes to the pulse stacker before being upcollimated for the transport line. The delay stage for the infrared is a linear stage with a stepping motor. The retroreflector is a hollow corner cube[3] with 1 arc sec angular deviation. The two colors are combined with a dichroic before the transport line, and separated with a final dichroic in the cave. In the design of the optics, the UV was given special attention to have as little loss as possible. The last dichroic however, was a "short wave pass" and there is a visible loss (~ 10%) of UV on it.

The infrared is sent to the experimental cross (X5) via optics mounted on the ceiling of the cave. The absorption and attenuation of IR in air are not a problem, so there is no need for an evacuated transport line. To protect the beam path

---

[3] Melles Griot 02 CCH 005

from accidental blockage from the many cables and other utilities, the IR was sent down a plastic pipe open at both ends.

On either side of the cross are mounted small breadboards for the polarizer, waveplate, analyzer and photodiodes. The light is focussed onto the crystal to minimize the interaction volume. The lenses are glass which has no birefringence and a null electro-optic tensor, so the polarization is not affected. The vacuum viewports are glass, and similarly do not change the polarization. A sketch of the optics and crystal (geometry A) is shown in Figure 5.3.

The data acquisition was handled by LabVIEW[4] on a MacIntosh. The program handled the stage motion, the opening and closing of the shutter (for background subtraction), and reading measurements from the Tektronix TDS640 digital oscilloscope over GPIB. A functional block diagram of the data acquisition is shown in Figure 5.4. After initialization, the UV shutter is opened (beam on) and n points are taken, then the UV shutter is closed (beam off) and m points are taken. Then the delay stage is moved by the desired time step, and the loop repeats.

In addition to the measurements of the photodiodes from the TDS scope, the oscillator bandwidth is also recorded, giving some indication of the stability of the IR pulse length. The shutter state is also recorded. Analysis is done offline with a series of macros in Kaleidagraph.

The crystal orientation known as geometry A is shown in Figures 5.3, and 5.5 (a mechanical drawing). In geometry A, the 3-axis of the $LiTaO_3$ crystal is 45° between the vertical and horizontal directions, so in beam coordinates the sensitivity is greatest to $2^{-1/2}(E_z + E_\theta)$. Geometry B is depicted in Figure 5.6, and the crystal 3-axis is oriented for maximum sensitivity to E_r. In both cases the crystal holder is machined from MACOR, an insulating ceramic.

---

[4] National Instruments, Inc.

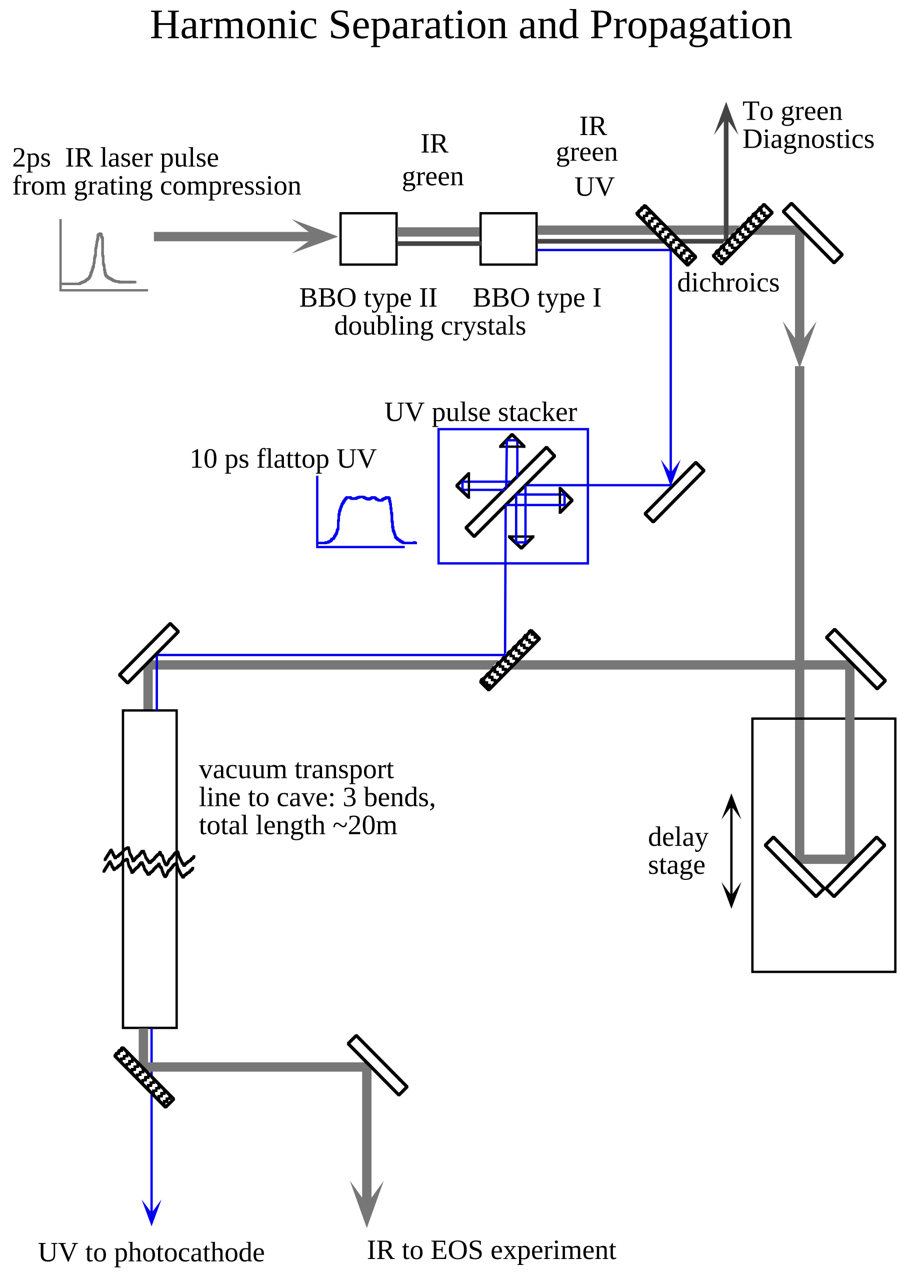

Figure 5.2: Harmonic Separation and Propagation. The IR and UV share the same transport line, and are split and recombined using dichroic beamsplitters.

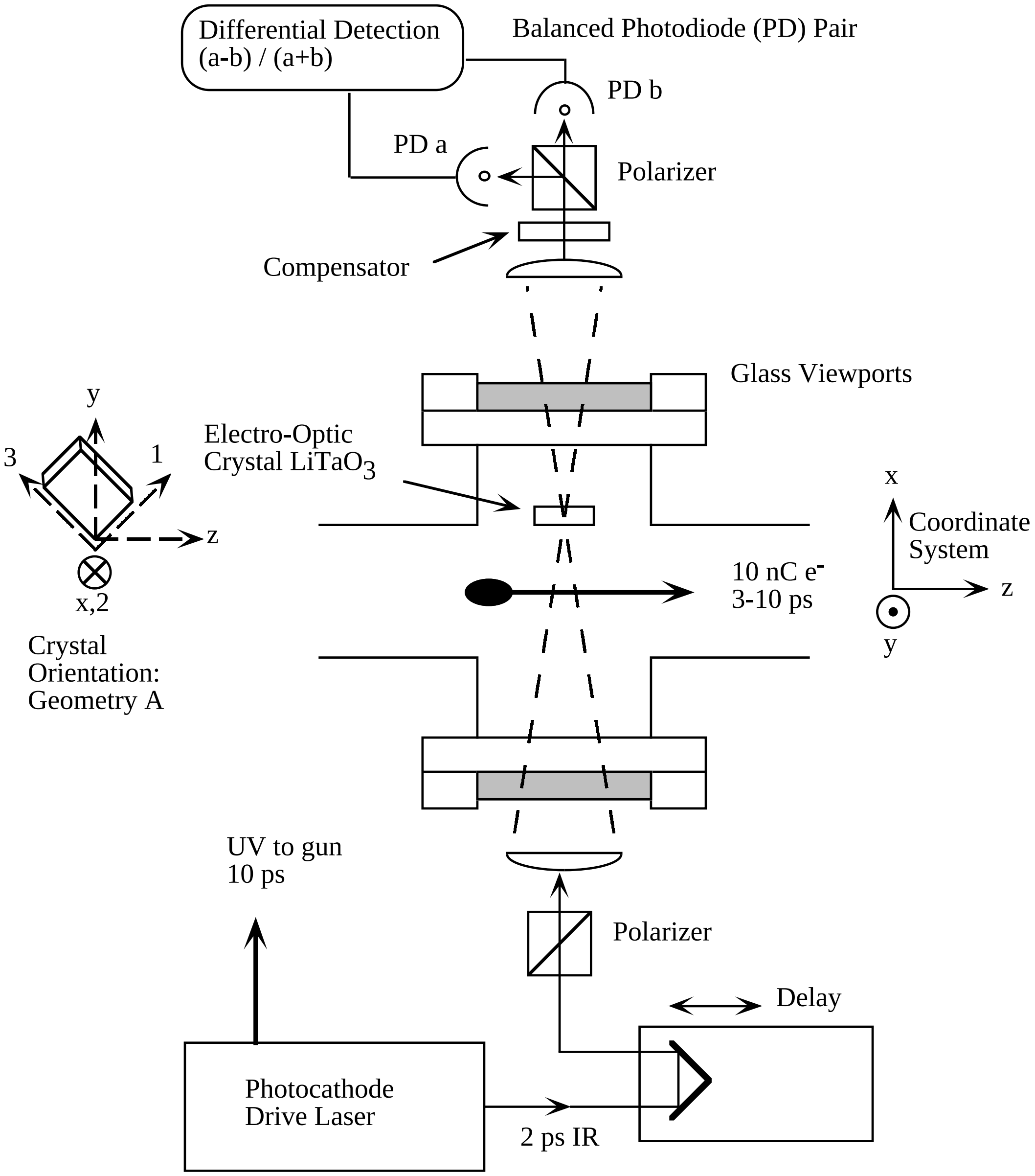

Figure 5.3: Optics for EOS. Note the coordinate system. Geometry A.

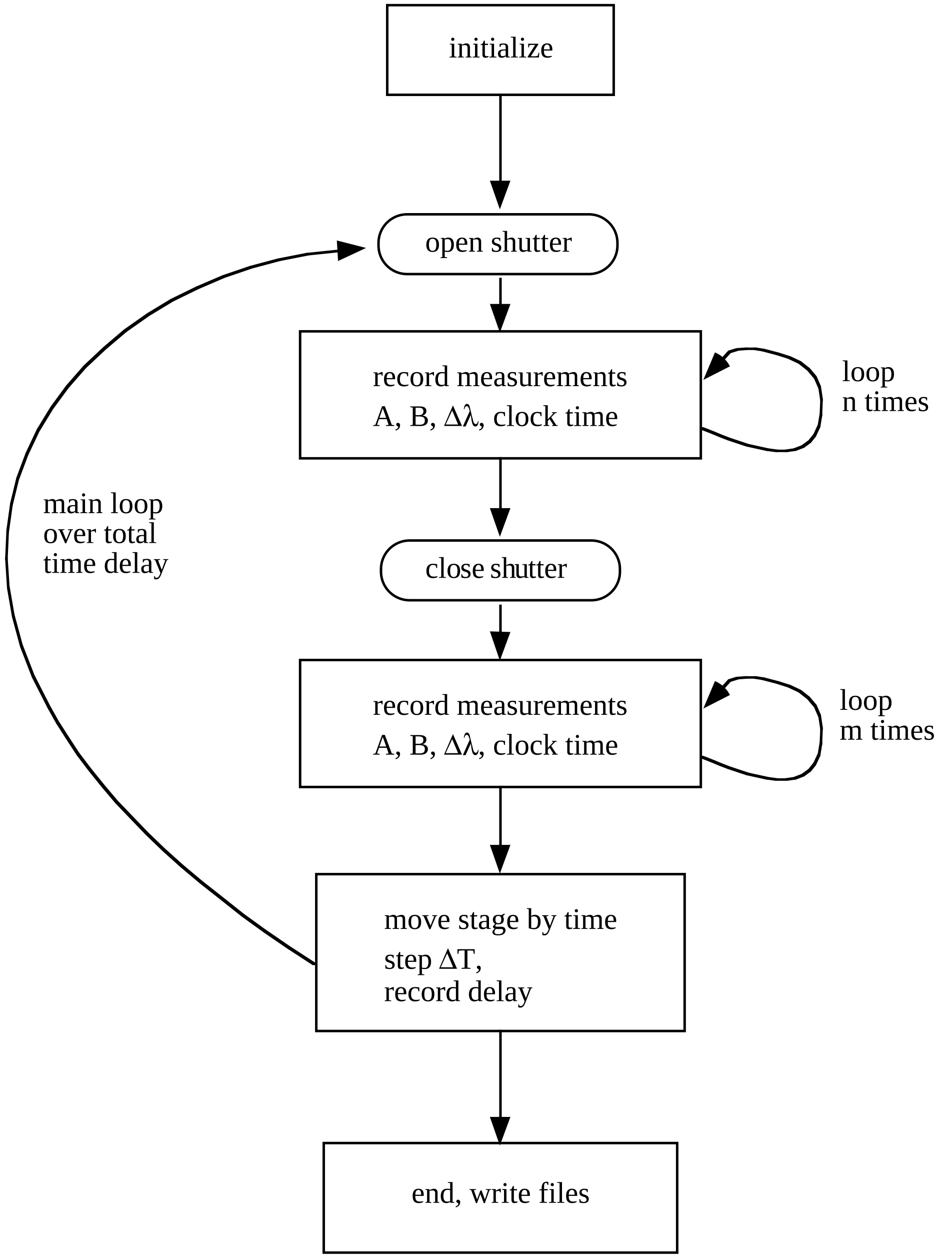

Figure 5.4: Functional diagram of data acquisition. See text.

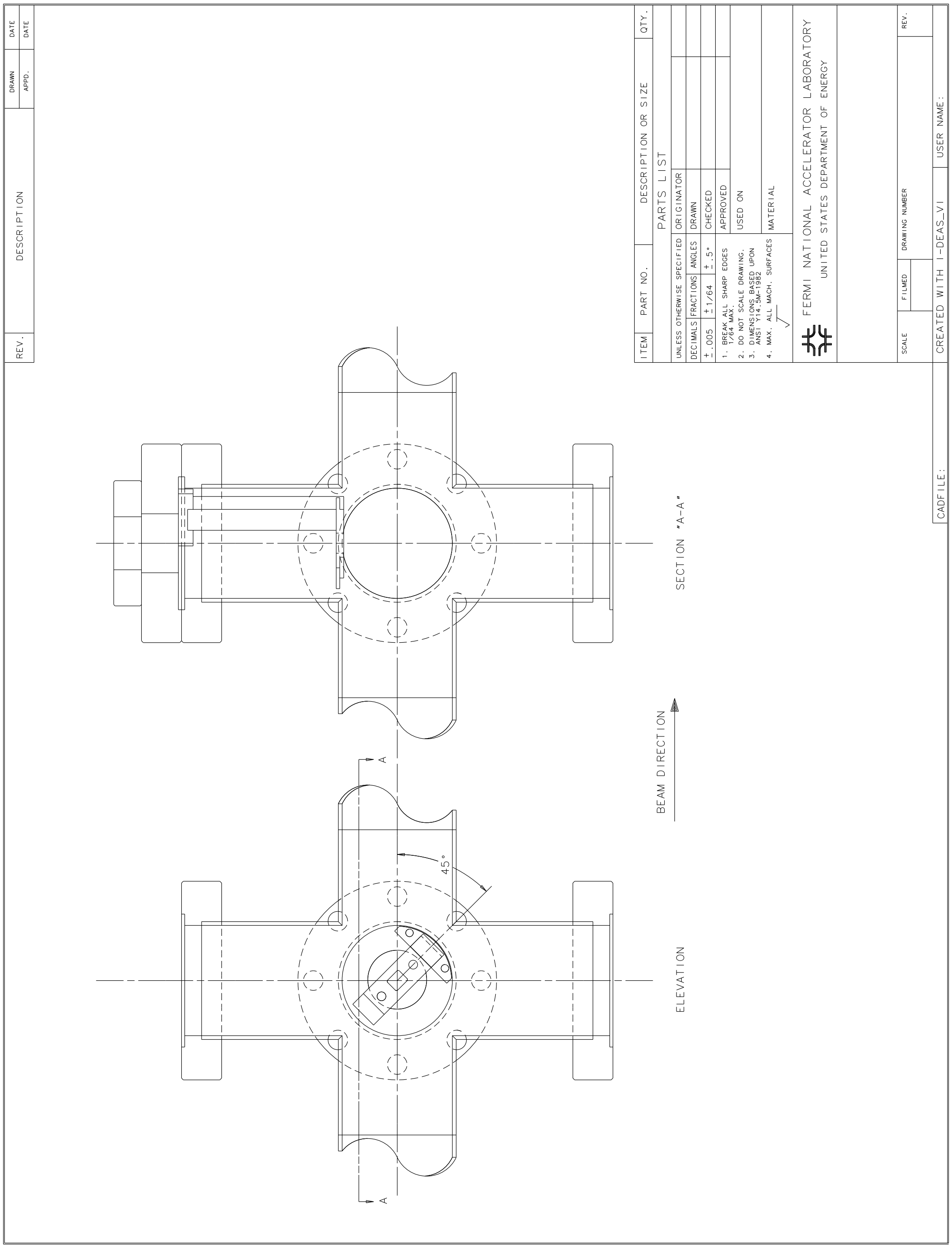

Figure 5.5: Crystal holder in cross X5. Geometry A.

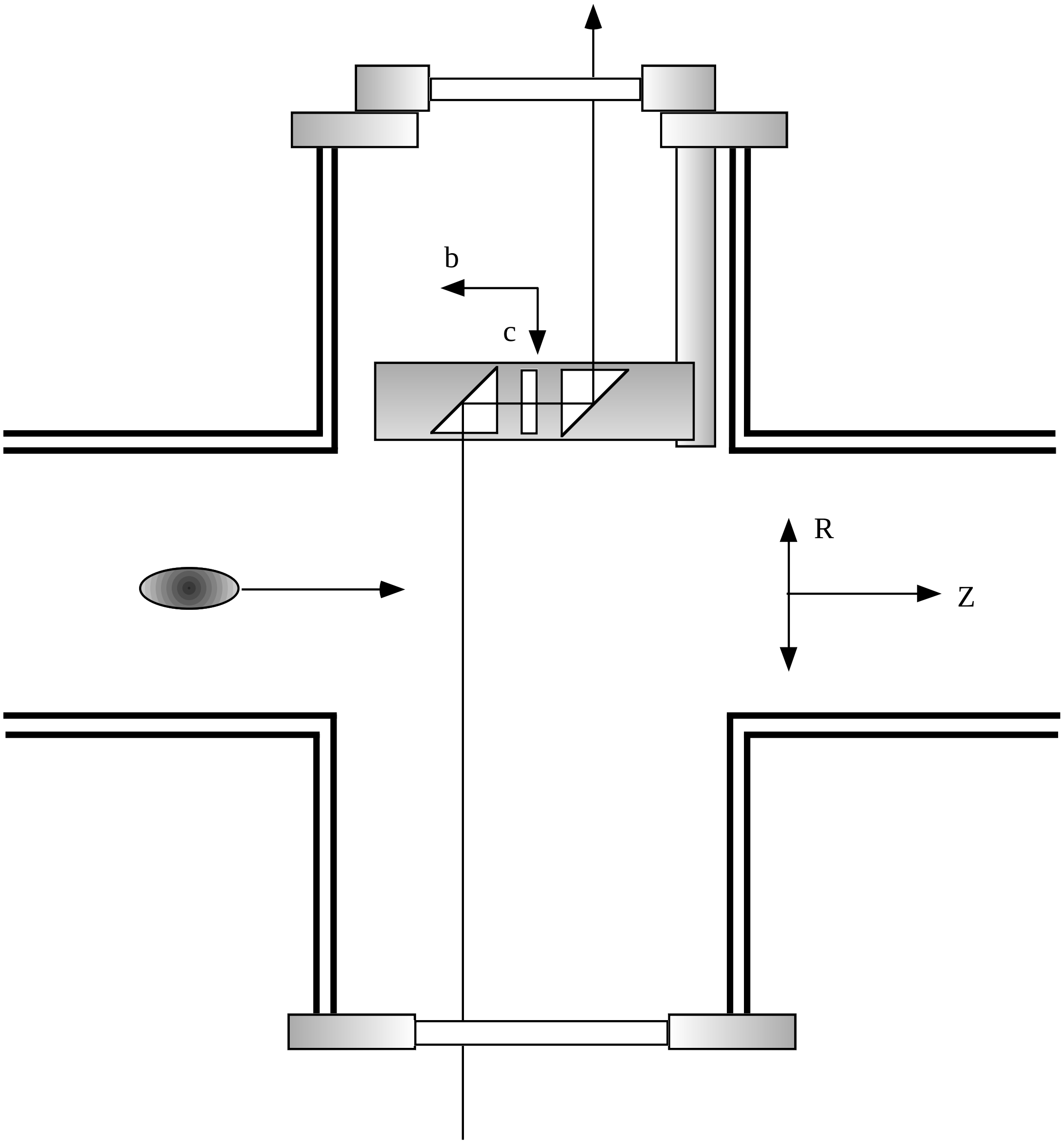

Figure 5.6: Crystal holder in cross X5: Geometry B.

5.5 Jones Matrix Analysis

The Jones vector for arbitrarily polarized light is

$$\begin{bmatrix} a \\ be^{i\delta} \end{bmatrix} \qquad a, b \quad \text{real} \quad a^2 + b^2 = 1 \tag{5.18}$$

where a and b are the E_x and E_y components of the electric field along a given x, y coordinate system. The light propagates along z.

In a new system rotated by angle θ the components $E_{x'}, E_{y'}$ are given by the rotation matrix

$$\vec{E}' = \hat{R}(\theta)\vec{E} = \begin{bmatrix} \cos\theta & \sin\theta \\ -\sin\theta & \cos\theta \end{bmatrix} \begin{bmatrix} a \\ b \end{bmatrix}, \qquad \det|R| = 1. \tag{5.19}$$

The rotation matrix also has the property $R^T(\theta)\, R(\theta) = R(-\theta)\, R(\theta) = \hat{1}$. A (perfect) polarizer is a projection operator.

$$\hat{P}_x = \begin{bmatrix} 1 & 0 \\ 0 & 0 \end{bmatrix} \qquad \hat{P}_y = \begin{bmatrix} 0 & 0 \\ 0 & 1 \end{bmatrix} \qquad \hat{P}_x + \hat{P}_y = \hat{1}, \qquad \det|P_x| = 0 = \det|P_y|$$

A retarding plate that introduces a phase shift $\delta \left(\delta = \dfrac{2\pi}{\lambda} \ell_R \right)$ along the y-axis is of the form

$$M(\delta) = \begin{bmatrix} 1 & 0 \\ 0 & e^{i\delta} \end{bmatrix} \qquad MM^\dagger = \hat{1} \tag{5.20}$$

The components E_x and E_y have the time dependence given by the convention $E = E_0 e^{-i\omega t}$ so the above matrix *retards* the y-component, and the y-axis of the retarding plate is said to be the slow axis. The common special cases are the half wave plate and quarter wave plate:

$$\lambda/2 \text{ plate}: \qquad M(\pi) = \begin{bmatrix} 1 & 0 \\ 0 & -1 \end{bmatrix} \tag{5.21}$$

$$\lambda/4 \text{ plate}: \qquad M\left(\frac{\pi}{2}\right) = \begin{bmatrix} 1 & 0 \\ 0 & i \end{bmatrix} \tag{5.22}$$

Now consider a $\lambda/4$ plate with its slow axis at an angle θ with respect to the coordinate axis x. To find its effect we rotate and rotate back,

$$R(-\theta)M\left(\frac{\pi}{2}\right)R(\theta) = \begin{bmatrix} \cos^2\theta + i\sin^2\theta & \cos\theta\sin\theta(1-i) \\ \cos\theta\sin\theta(1-i) & i\cos^2\theta + \sin^2\theta \end{bmatrix} \tag{5.23}$$

$$= \left(\frac{1-i}{2}\right)\begin{bmatrix} i+\cos 2\theta & \sin 2\theta \\ \sin 2\theta & i-\cos 2\theta \end{bmatrix} \tag{5.24}$$

Consider an arbitrary polarization state incident on the $\lambda/4$ waveplate at some at some angle θ followed by a polarizing beam splitter (the analyzer) and two detectors. Letting the coordinate system coincide with the analyzer, we have:

$$R(-\theta)M\left(\frac{\pi}{2}\right)R(\theta)\begin{bmatrix} a \\ be^{i\delta} \end{bmatrix} = \begin{bmatrix} \alpha \\ \beta \end{bmatrix} \tag{5.25}$$

Making use of the double angle formulas, after some algebra we obtain for the *intensities*

$$I_x = |\alpha|^2 = \frac{1}{2}\left[a^2(1+\cos^2 2\theta) + b^2(\sin^2 2\theta) + 2ab\sin 2\theta(\cos 2\theta\cos\delta + \sin\delta)\right] \tag{5.26}$$

$$I_y = |\beta|^2 = \frac{1}{2}\left[b^2(1+\cos^2 2\theta) + a^2(\sin^2 2\theta) - 2ab\sin 2\theta(\cos 2\theta\cos\delta + \sin\delta)\right] \tag{5.27}$$

The total intensity is seen to be conserved: $I_x + I_y = a^2 + b^2$, and the difference over sum of the two detectors is:

$$\frac{I_x - I_y}{I_x + I_y} = \frac{(a^2 - b^2)}{a^2 + b^2}(\cos 2\theta)^2 + \frac{2ab}{a^2 + b^2}(\sin 2\theta \sin \delta + \frac{1}{2} \sin 4\theta \cos \delta) \tag{5.28}$$

The arbitrary polarization vector we started with, $(\alpha, \beta e^{i\delta})$, represents the polarization after the electro-optic crystal. If δ is composed of a static term Δ and an electro-optic term Γ which is assumed to be small, then we can simplify:

$$\delta = \Delta + \Gamma, \quad \text{for } \Gamma \ll 1 \tag{5.29}$$

$$\cos \delta = \cos \Delta \cos \Gamma - \Gamma \sin \Delta \tag{5.30}$$

$$\sin \delta = \Gamma \cos \Delta + \cos \Gamma \sin \Delta \tag{5.31}$$

If a background subtraction is made, that is, the difference over sum with $\Gamma = 0$ (the background) is subtracted from the same expression including the electro-optic term, we have left only

$$\frac{2ab}{a^2 + b^2}\Gamma(\sin 2\theta \cos \Delta - \frac{1}{2} \sin 4\theta \sin \Delta) \tag{5.32}$$

If the two detectors are balanced, $a = b$ and the static birefringence vanishes, $\Delta = 0$, then the term reaches the maximum value for $\theta = \pi/4$ and is simply Γ. When $\Delta \neq 0$, however, it is not possible in general to find a $\lambda/4$ waveplate angle that fully compensates. We have plotted this function for several different values of Δ in Figure 5.7. The peak value varies from 1 to 1/2, and the minimum value varies from -1 to $-1/2$.

We expect Δ to be given by

$$\Delta = \frac{2\pi}{\lambda}(n_o - n_e)\ell = 11.4\,\pi \tag{5.33}$$

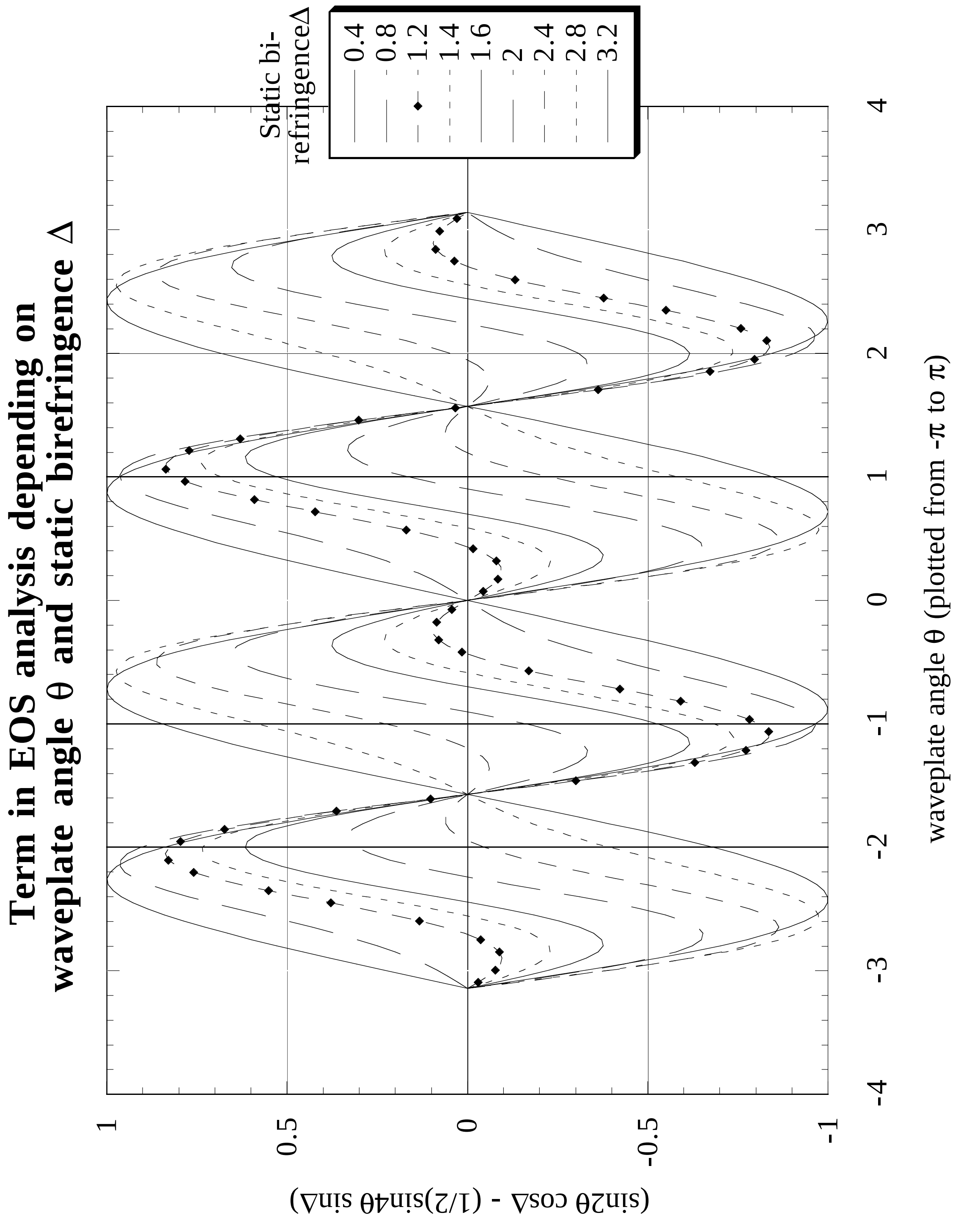

Figure 5.7: The effect of static birefringence on the EOS signal. Plot of $(\sin 2\theta \cos\Delta - \frac{1}{2}\sin 4\theta \sin\Delta)$ versus the quarter waveplate angle θ for several different values of the static birefringence Δ. The calculated value of $\Delta = 1.24$, (black diamonds).

for the thin $\ell = 1.5$ mm LiTaO$_3$ crystal. Because it is many waves, it is sensitive to temperature and to the angle of the laser. The non-integral part of Δ is $0.4\pi \sim 1.24$ rad (black diamond points in Figure 5.7), for which the peak value is $\sim$0.8 and is slightly shifted from the peak θ value for $\Delta = 0$.

In order to fully compensate the static birefringence, one could use a Soleil-Babinet compensator instead of a the $\lambda/4$ wave plate. The Soleil-Babinet is a continuously adjustable retardation plate capable of an arbitrary polarization delay between 0 and λ on an arbitrary axis with a resolution of 0.001λ. Though we considered purchasing one, we decided against it because it is expensive (> 7k$) and bulky. It also must be motorized for remote control in the high-radiation environment of the beamline enclosure.

5.6 Fast Fourier Transform (FFT)

In our analysis in the next Chapter, we often use the Fast Fourier Transform (FFT) to identify frequencies in the time-domain data. We review a few properties of the FFT with an interest in the frequency calibration and resolution, as well as amplitude recovery. More information can be found in Arfken [159].

Divide the finite interval $(0, T)$ into a set of $2N$ time values:

$$t_k = 0,\ \frac{T}{2N},\ \frac{2T}{2N},\ \frac{3T}{2N},\ \ldots,\ \frac{(2N-1)T}{2N} \tag{5.34}$$

$$t_k = \frac{kT}{2N}, \qquad \text{for } k \in \{0, 1, 2, \ldots, 2N-1\}. \tag{5.35}$$

For integers n, p, q there is the orthogonality condition:

$$\sum_{k=0}^{2N-1} [\exp(2\pi i p t_k/T)]^* \exp(2\pi i q t_k/T) = 2N\delta_{p,q\pm 2nN}. \tag{5.36}$$

This is proved by letting $s = q - p$, then the left hand side is a geometric series with $r = exp(\pi i s/N)$.

It is useful to define

$$\omega_p = 2\pi p/T, \qquad \text{for } p \in \{0, 1, 2, \ldots, 2N-1\} \tag{5.37}$$

then $\exp(\pm 2\pi i p t_k/T) = \exp(\pm i\omega_p t_k)$. The orthogonality condition now resembles the continuous Fourier case:

$$\frac{1}{2N}\sum_{p=0}^{2N-1}(\exp i\omega_p t_m)^*(\exp i\omega_p t_k) = \delta_{mk} \tag{5.38}$$

Using these orthogonal functions, the discrete Fourier transform can be defined. Consider a function $f(t_k)$ measured at each of the discrete time values t_k. The discrete Fourier transform of this function is:

$$F(\omega_p) = \sum_{k=0}^{2N-1} f(t_k)\exp(i\omega_p t_k). \tag{5.39}$$

The inverse is

$$f(t_k) = \frac{1}{2N}\sum_{p=0}^{2N-1} F(\omega_p)\exp(-i\omega_p t_k). \tag{5.40}$$

Definitions vary as to the placement of the prefactor $(2N)^{-1}$.

The Fast Fourier Transform (FFT) is a particular algorithm that greatly speeds the numerical evaluation of the discrete Fourier transform, especially if N is a power of 2. The FFT routine we used (packaged with Kaleidagraph) forces the frequency spectrum onto a number of bins which is a power of 2. This will spread the low frequency power into a number of frequency bins. The highest frequency is correctly given as the reciprocal of the time step $(T/2N)$, and the scale is in frequency units which are the inverse of the time units. So if the time-domain data is in units of picoseconds, the frequency scale is in THz. The FFT spectrum is symmetric about the midpoint; the upper half is from aliasing.

The FFT gives a good estimate of the strength (volts per meter) of frequency modes. From the peak of the time-domain waveform, one can also get a field strength estimate, but when multiple frequencies are present, the FFT can separate the contributions from different modes. The height of the frequency peak is multiplied by two (because of the aliasing at high frequencies) and divided by the total number of time measurements (the amplitude normalization to the number of measurements ($2N$) is preserved). We use the area of the peak instead of just the height. We checked the routine with waveforms composed of sines of different frequencies and known amplitudes. We found that taking the area of the peak by summing the highest bin with two or three bins on either side was sufficient to recover the original amplitude A within ±4%:

$$A = \frac{2}{(2N)} \sum_{\text{peak}} F(\nu_i) \tag{5.41}$$

where the sum is over the ν_i bins at the frequency peak. (The original time record had $2N$ measurements on the interval T.) We see that A recovered from Eq. 5.41 has the same units as the original time record $f(t_k)$.

Chapter 6

EO Sampling Results and Discussion

6.1 First results

Data with unambiguous detection of the wakefields were first obtained in August 1999, and are shown in Figure 6.1. An inset to this figure shows the Fourier components [from the fast Fourier transform, or FFT]. The time-domain waveform shows a modulated "ringing" pattern, and the frequency components at 12.6 GHz and 2.7 GHz are discernible by eye. This data is measured with the thin (1.5 mm) $\mathrm{LiTaO_3}$ crystal in geometry A, so as discussed in Section 5.4, it is sensitive primarily to $(1/\sqrt{2})(E_z + E_\theta)$.

Note that there is a baseline drift, from (thermal) variation in the static birefringence. With a shutter on the UV beam, but not the IR probe beam, the signal with electrons can be measured as well as the background without.

The origin of the time axis is arbitrarily chosen and was placed at the best estimation of the electron bunch arrival time from measurements of optical path differences. In Figure 6.1 the signal begins at a delay around ~ 100 ps; increasing (positive) delay implies that the laser probe pulse arrives *after* the electron bunch. In this data set, the time step was 1 ps, and four points taken at each step were averaged. We estimate the electron bunch length was about 25 ps FWHM (uncompressed), with charge 8 nC. The early region of the waveform expanded is

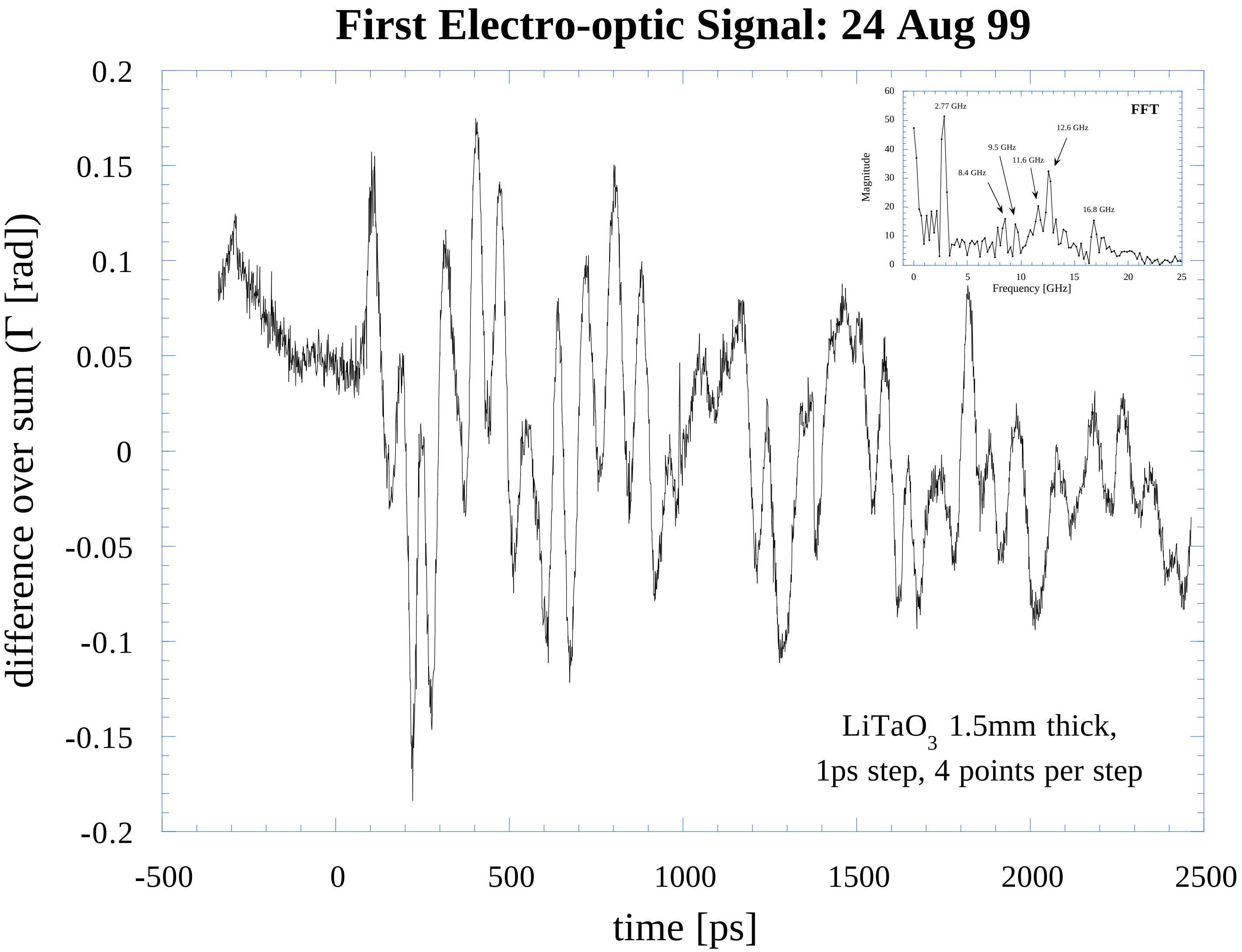

Figure 6.1: First unambiguous electro-optic detection of bunch fields. Inset: fast Fourier transform (FFT).

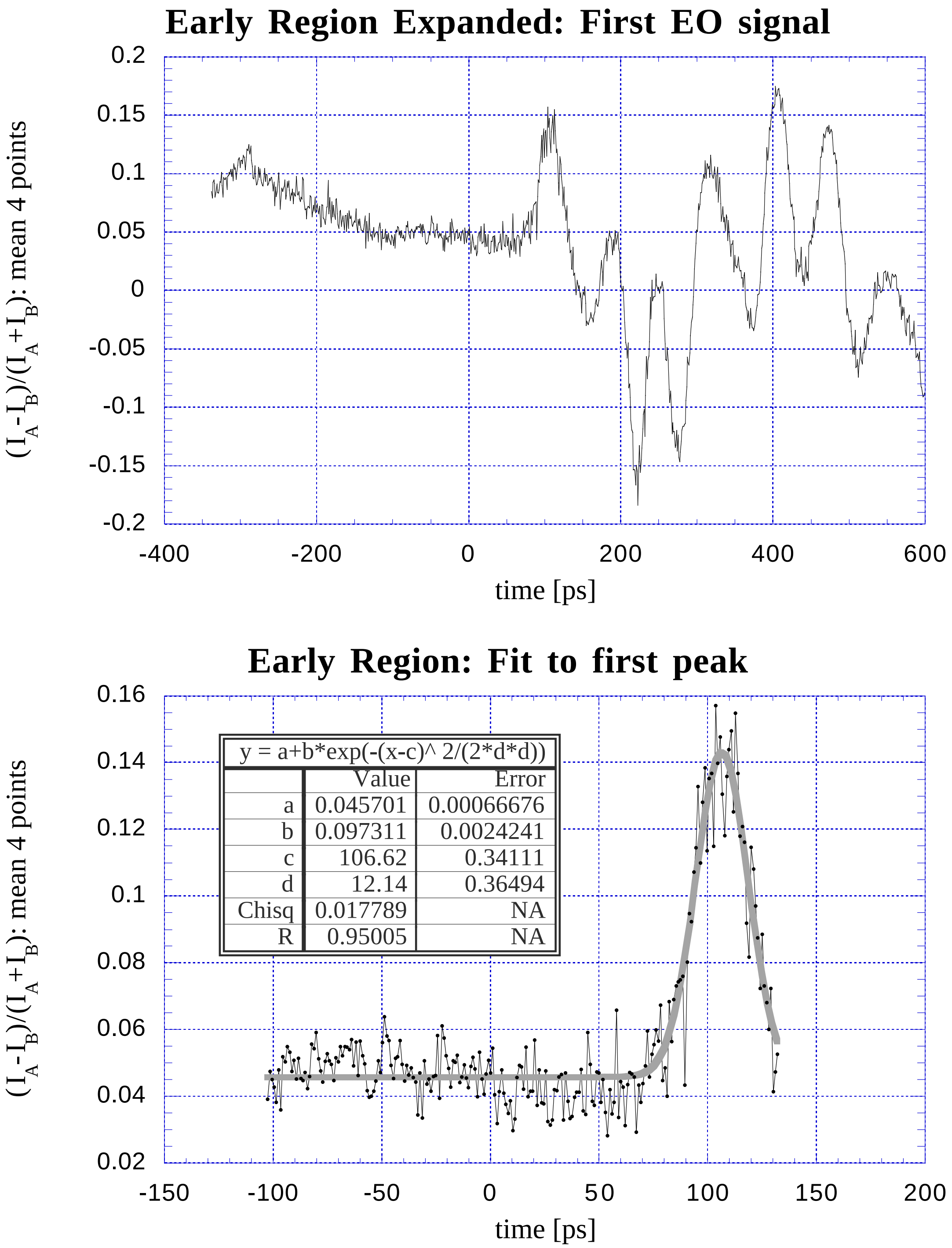

y = a+b*exp(-(x-c)^ 2/(2*d*d))

	Value	Error
a	0.045701	0.00066676
b	0.097311	0.0024241
c	106.62	0.34111
d	12.14	0.36494
Chisq	0.017789	NA
R	0.95005	NA

Figure 6.2: Early region of first EOS waveform (top) with fit to first peak (bottom). The Gaussian fit gives $\sigma = 12$ ps, or 28 ps FWHM.

shown in Figure 6.2 (top) with a Gaussian fit to the first peak (bottom). The fit gives $\sigma = 12.1$ ps, or 28.2 ps FWHM, but we note this is coincidental with the observed 12.6 GHz frequency component since the half-sine has a full-width at half maximum τ of

$$\frac{1}{3}\frac{1}{12.6\mathrm{GHz}} = 26.4 \text{ ps.} \tag{6.1}$$

There are a few remarks to be made that are generally valid for all the data. The fields are causal—there are no fields observed before the sudden onset. The fields are persistent, and remain well above noise at the end of our delay range, about 2.5 ns after the passage of the electron bunch. Generally, the higher frequency components have shorter damping times, giving the waveform the appearance of a frequency chirp. The magnitude of the fields is of the order of 100 kV/m, which is the correct order of magnitude (discussed below in Section 6.4). The observed frequency components are electro-magnetic modes in the structure (6-way cross, beampipe, *etc.*) which are impulse-excited by the transient passage of the beam.

6.2 Results in Geometry A

In Figure 6.3 we show data obtained with the compressed electron beam of charge 8 nC. The inset to this figure is the FFT of the waveform. In addition to the 2.7 GHz and 12.6 GHz frequencies are several new components at 7.0, 8.8, 9.6 GHz and a cluster around 16 GHz. The time step was 2 ps, so the physical high-frequency cutoff of the FFT is 250 GHz (Nyquist), but there is no significant power beyond the range plotted.

Again the same features of the time domain waveform are seen—a sudden onset of persistent ringing. The early part of the waveform shows the noise level of the system, typically 1–2%.

By replacing the 1.5 mm thick $LiTaO_3$ crystal with one 3 mm thick, we can

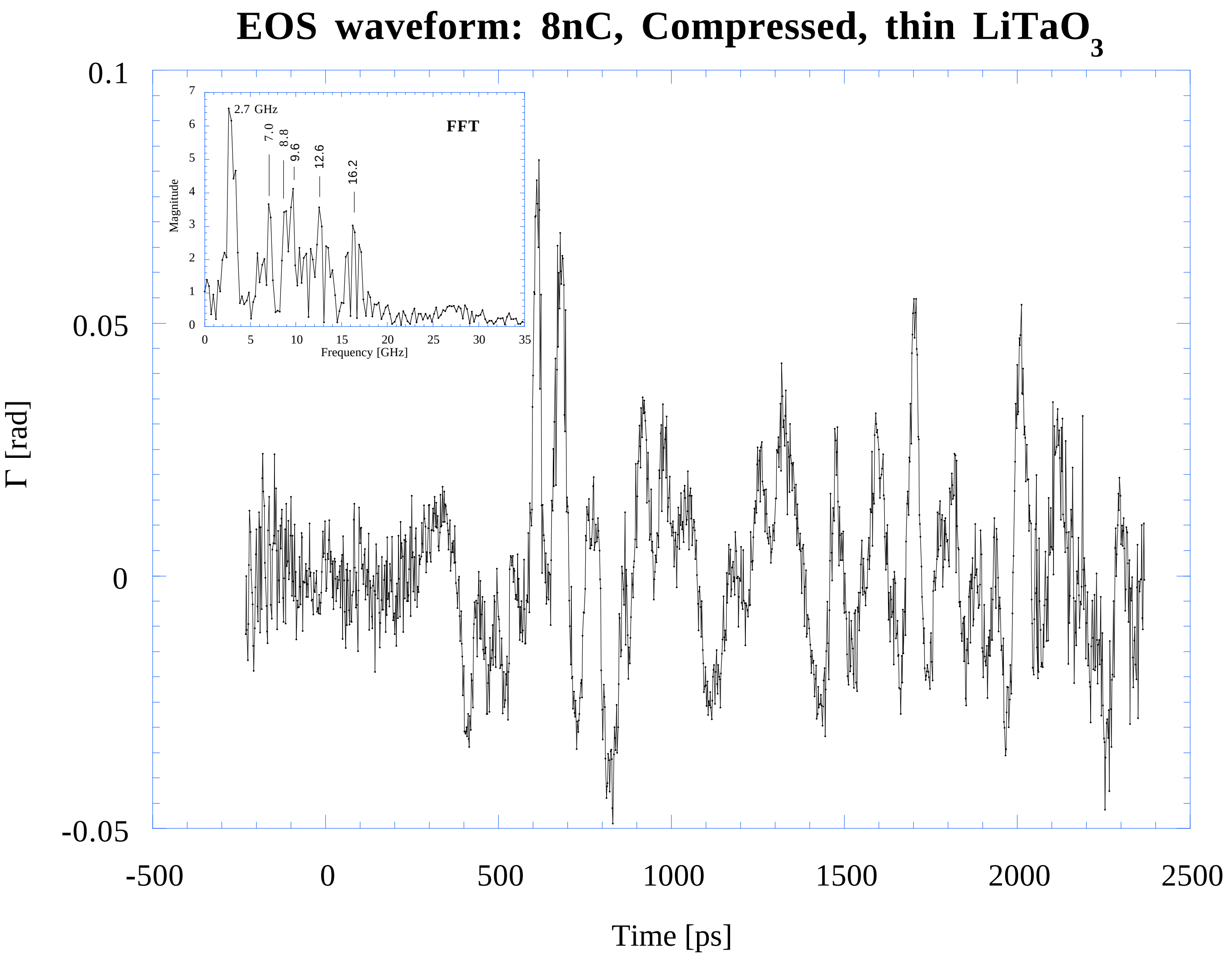

Figure 6.3: EOS waveform: 8 nC, compressed, thin LiTaO$_3$ crystal. Inset: fast Fourier transform (FFT).

test that the detected fields are not somehow trapped inside the crystal. The data are shown in Figure 6.4, with an inset plot of the FFT. Here, the charge is 7 nC, and the beam is not compressed. We can also note that the arrival time is earlier for the uncompressed beam, as it should be, since the bends in the chicane will delay the arrival of the electron beam. The observed difference, from ~100 ps to ~300–400 ps is consistent with the chicane geometry. The voltage sensitivity is increased with the thicker crystal, though the time resolution is degraded. In the FFT it can be seen that the broad peak at 2.7 GHz is resolved as two peaks at 2.77 and 3.3 GHz.

The peak Γ for the 3 mm thick crystal at 7 nC (Figure 6.4) is 0.125 and the peak Γ for the 1.5 mm thick crystal at 8nC (Figure 6.3) is 0.082 rad. Doubling the thickness of the crystal should double the rotation. Including proportionality to the charge, the predicted ratio is $2(\frac{7}{8}) = 1.75$, in reasonable agreement with the observed ratio of 1.52, since the beam conditions are not identical.

The EOS waveform is highly reproducible. By restoring machine settings from the previous day, and repeating the electro-optic sampling scan under the same conditions, the two waveforms shown in Figure 6.5 are nearly identical. The observed deviations are consistent with drifts in the gun phase and amplitude.

6.2.1 Impulse Excitation

The simplest model of the observed waveform is impulse excitation of electromagnetic modes in the structure. First consider a single frequency mode. Including causality and damping, we can write the response as

$$E(\zeta) = H(\zeta)\, e_o \exp(-\frac{\zeta\omega}{2Q})\, \sin(\omega\zeta) \tag{6.2}$$

with $\zeta = t - z/c$, for z the position along the linac, and $H(\zeta)$ is the Heaviside unit step function. We can extend this semi-empirical wake model to a superposition

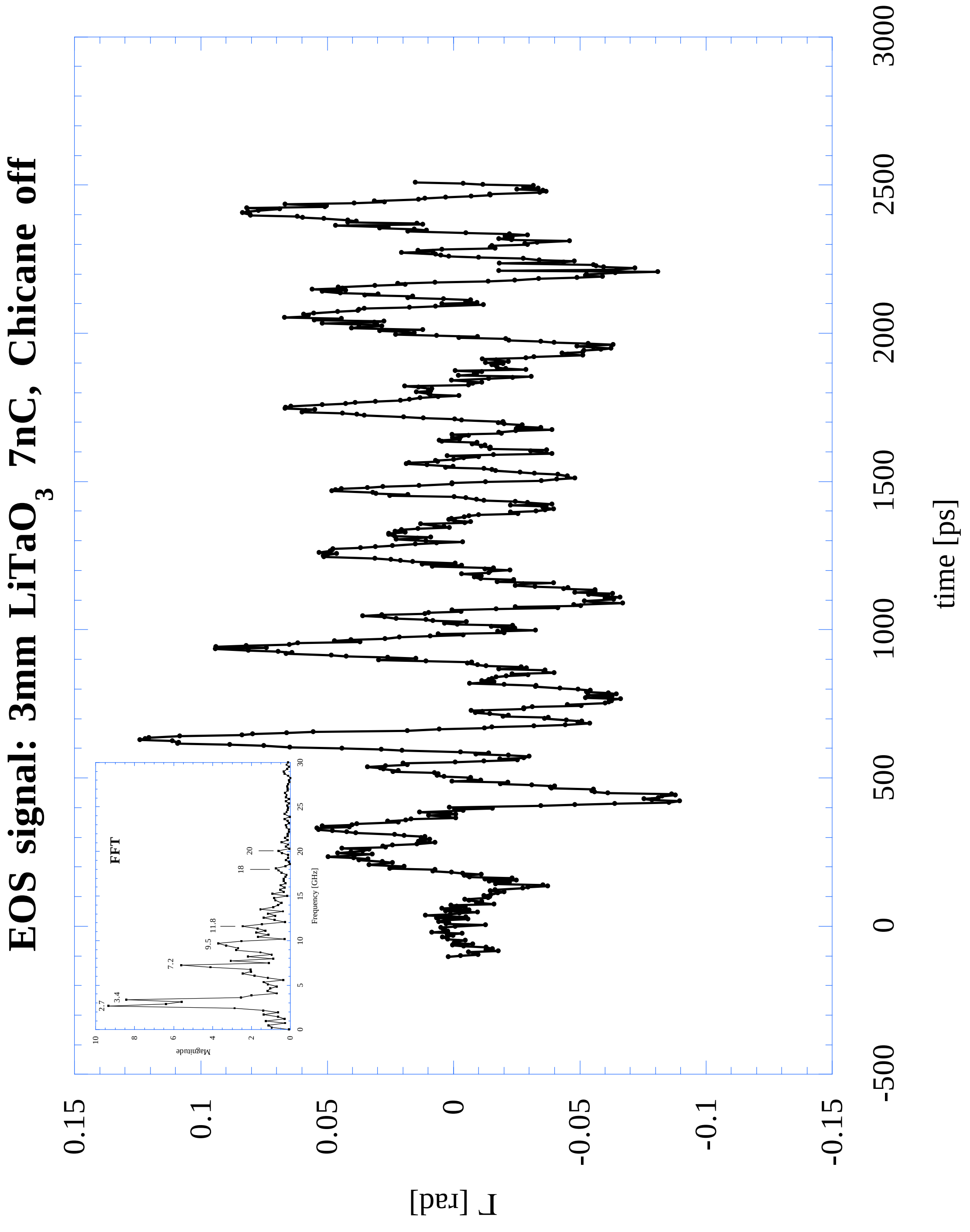

Figure 6.4: EOS waveform: 7 nC, uncompressed, thick LiTaO$_3$. Inset: fast Fourier transform (FFT).

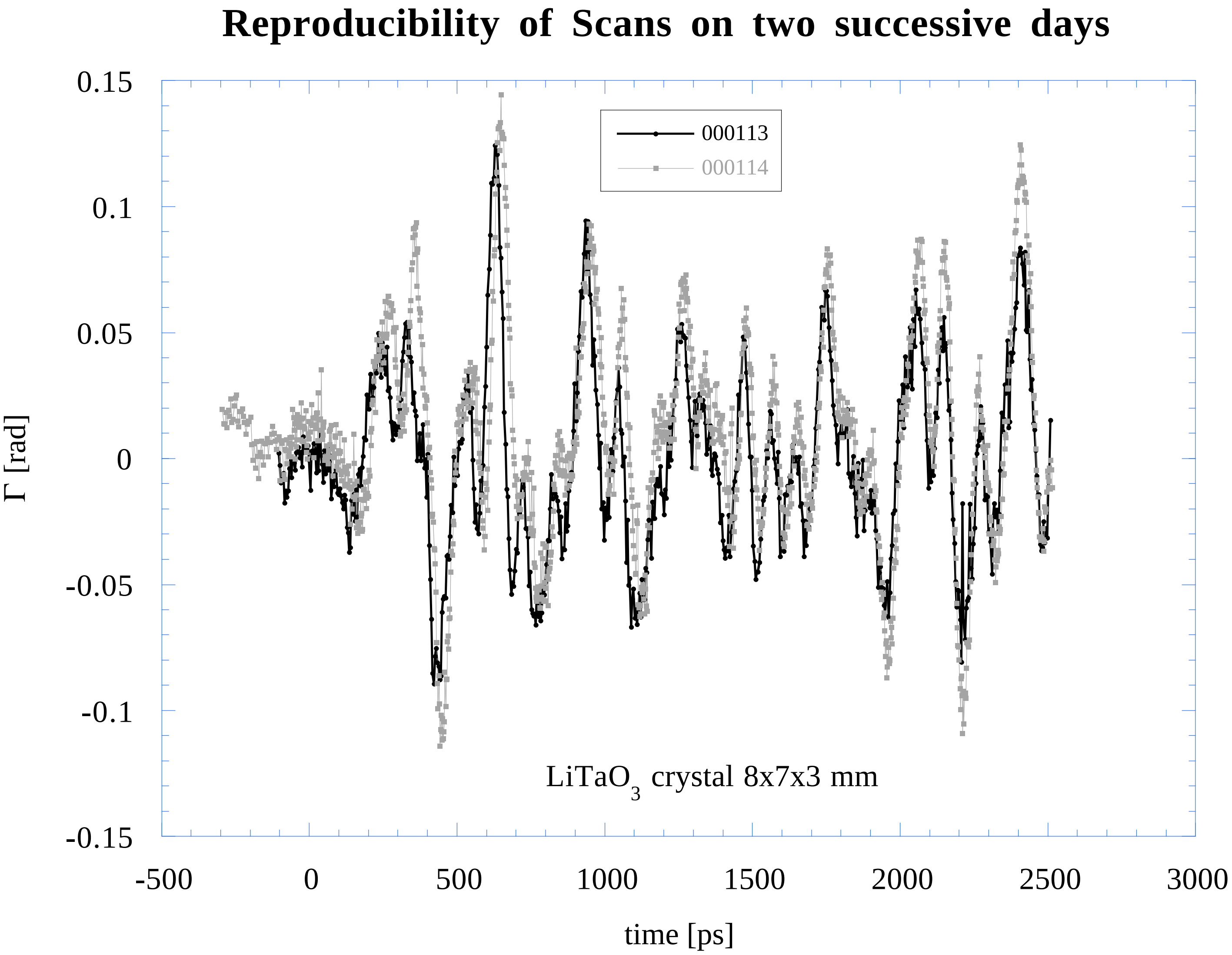

Figure 6.5: Reproducibility of scans on two successive days under identical conditions. Small drifts here are consistent with observed drifts in RF amplitude and phase in the gun.

of modes:

$$E(\zeta) = H(\zeta) \sum_i e_i \exp(-\frac{\zeta \omega_i}{2Q_i}) \sin(\omega_i \zeta + \phi_i) \tag{6.3}$$

This is a simplification because the modes have different spatial structure, but since we measure the E field at a fixed spatial point (small volume), we have carried along a possible phase (ϕ_i) difference.

The bunch is not an infinitely short impulse, so therefore it will not excite modes at infinitely high frequencies. For a longitudinal Gaussian bunch

$$f(t) = \frac{1}{\sqrt{2\pi}\sigma} \exp(-\frac{t^2}{2\sigma^2}), \tag{6.4}$$

the frequency content is

$$F(\omega) = \exp(-\omega^2 \frac{\sigma^2}{2}). \tag{6.5}$$

The rms frequency spread is

$$\nu_{\mathrm{rms}} = \frac{1}{2\pi\sigma} = 0.3748 \frac{10^{12}\mathrm{Hz}}{\tau[\mathrm{ps}]} \tag{6.6}$$

where τ is the full-width at half-maximum (FWHM) of the bunch. If we turn this relation around, and superimpose a Gaussian excitation spectrum on the observed FFT, as in Figure 6.6, the bunch length implied (53 ps FWHM) is several times longer than the actual measured bunch length. Clearly the density of modes and the mode strength are falling off more rapidly at high frequency than the bunch excitation spectrum. In Section 6.5.4 below, it will be shown that the observed frequency spectrum is the product of the bunch excitation spectrum and the structure impedance.

The fields persist for a long time. At the maximum delay of the stepper stage,

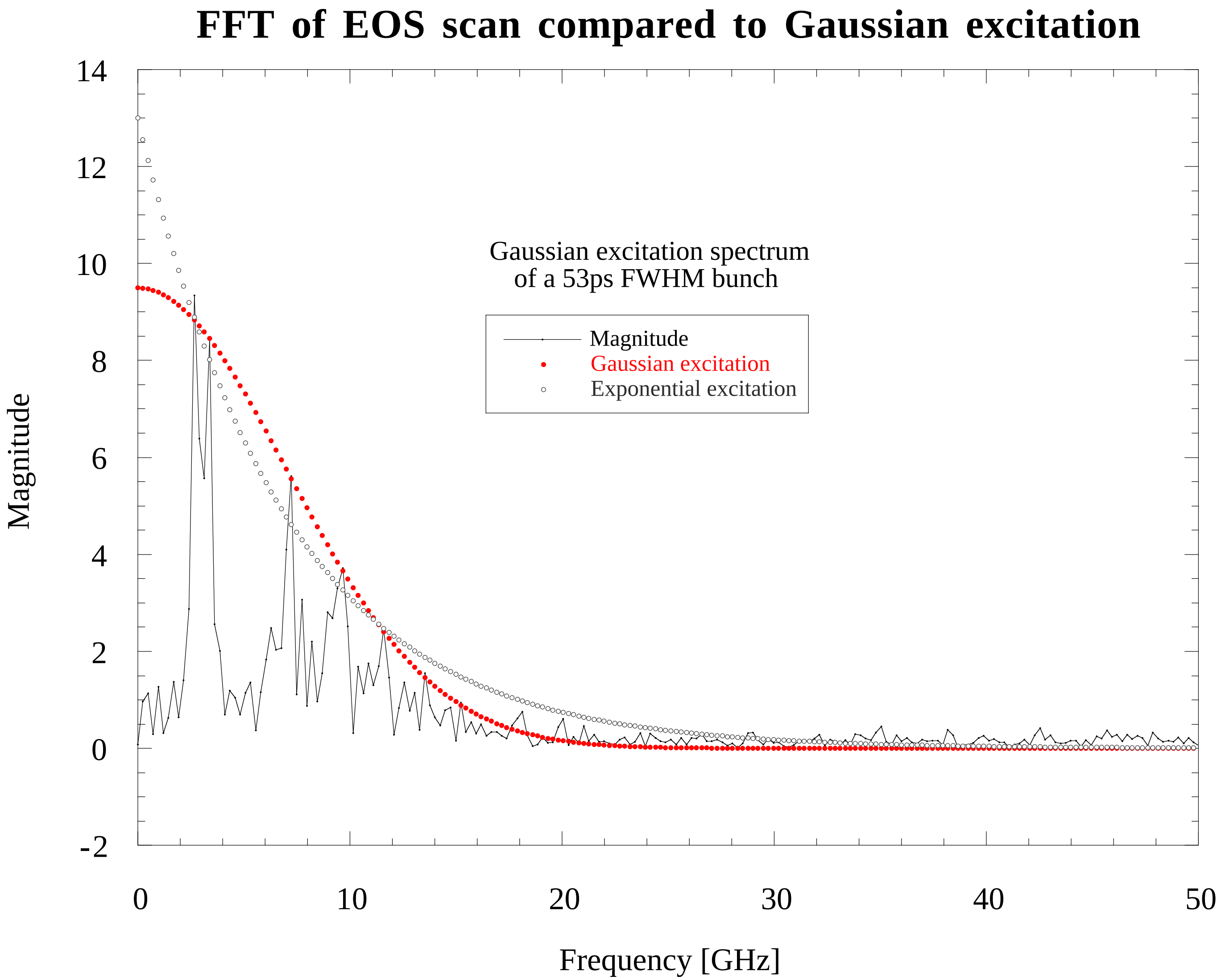

Figure 6.6: FFT of data in Figure 6.4 compared to Gaussian excitation.

more than 2 ns after the bunch passage, the amplitude of some oscillations has not decreased markedly enough for a good estimation of the damping time. To look for possible cumulative effects, we compared the EOS waveform from the first pulse to the 17th pulse in a pulse train of 20 pulses. Figure 6.7 shows the waveform triggered on the first pulse, and Figure 6.8 is triggered on the 17th, with other beam conditions held constant. For the 17th pulse, there is nothing observable above the noise from the preceding pulse(s), but a 1 μs damping time would be much longer than expected.

Using a capacitive RF pickup in the beam line, used for a beam position monitor (BPM), we looked for persistent fields with a digital sampling oscilloscope. The BPM signal has a negative spike of about 0.5 ns FWHM, followed by a slower-evolving positive discharge that has returned to ground by around 4.2–4.4 ns after the beginning. Since the pickup is capacitive, the signal must be bipolar and have zero integral, which it does. Smaller oscillations from 12 ns to 30 ns seen the with the BPM are probably cable reflections or other noise sources. We can therefore set rather weak limits on the damping times τ_i of the modes we observed:

$$3 \text{ ns} < \tau_i \ll 300 \text{ ns}. \tag{6.7}$$

As an experimental detail, the background (shutter closed) measured in Figure 6.8 was linear, and a fit to the background was subtracted from the signal to give the Γ values. For Figure 6.7, however, a point-by-point subtraction was used and there is more noise in Γ because the background data is of lower statistical quality than the signal (shutter open) data.

With a high-charge beam, also compressed to around 6 ps FWHM, the sample waveform is very similar. In Figure 6.9, we show the full waveform (top), the expanded early region (middle), and the FFT (bottom). The peak signal is about a factor of 2.5–3 higher than that in Figure 6.7, as the charge is higher by the same factor.

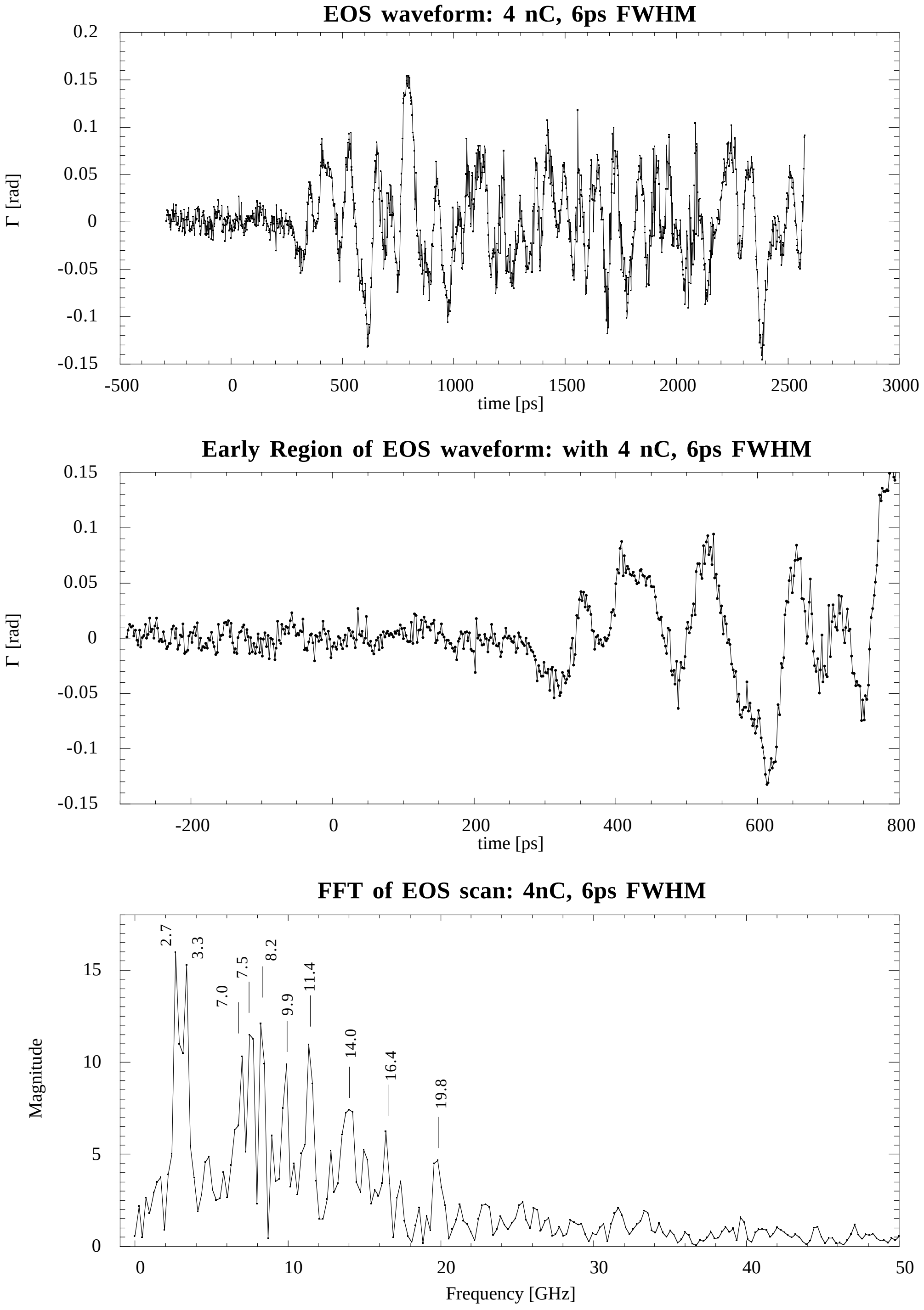

Figure 6.7: EOS waveform for $Q = 4$ nC and 6 ps FWHM. Trigger on the first pulse of 20.

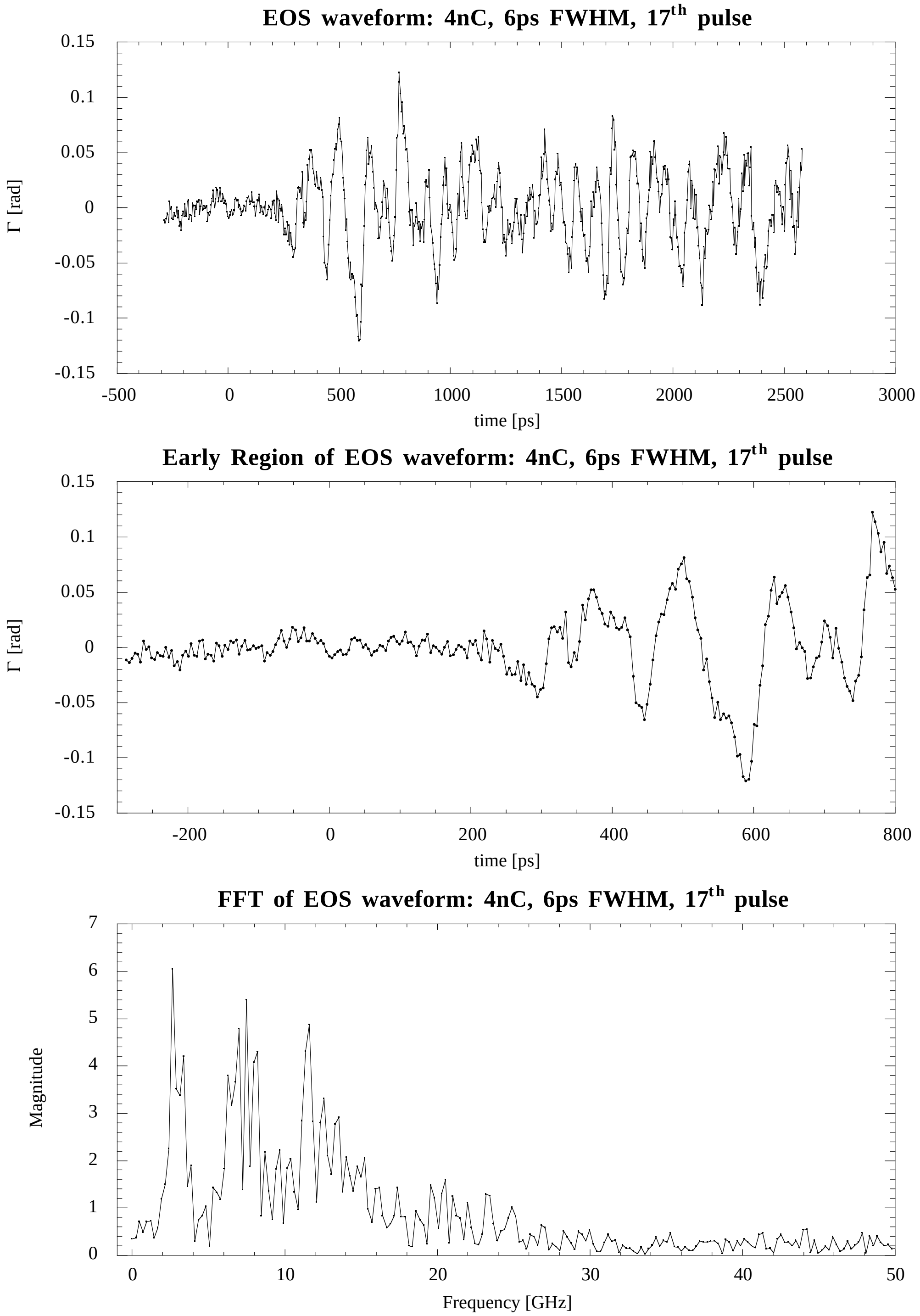

Figure 6.8: EOS waveform for $Q = 4$ nC and 6 ps FWHM. Trigger on the 17th pulse of 20.

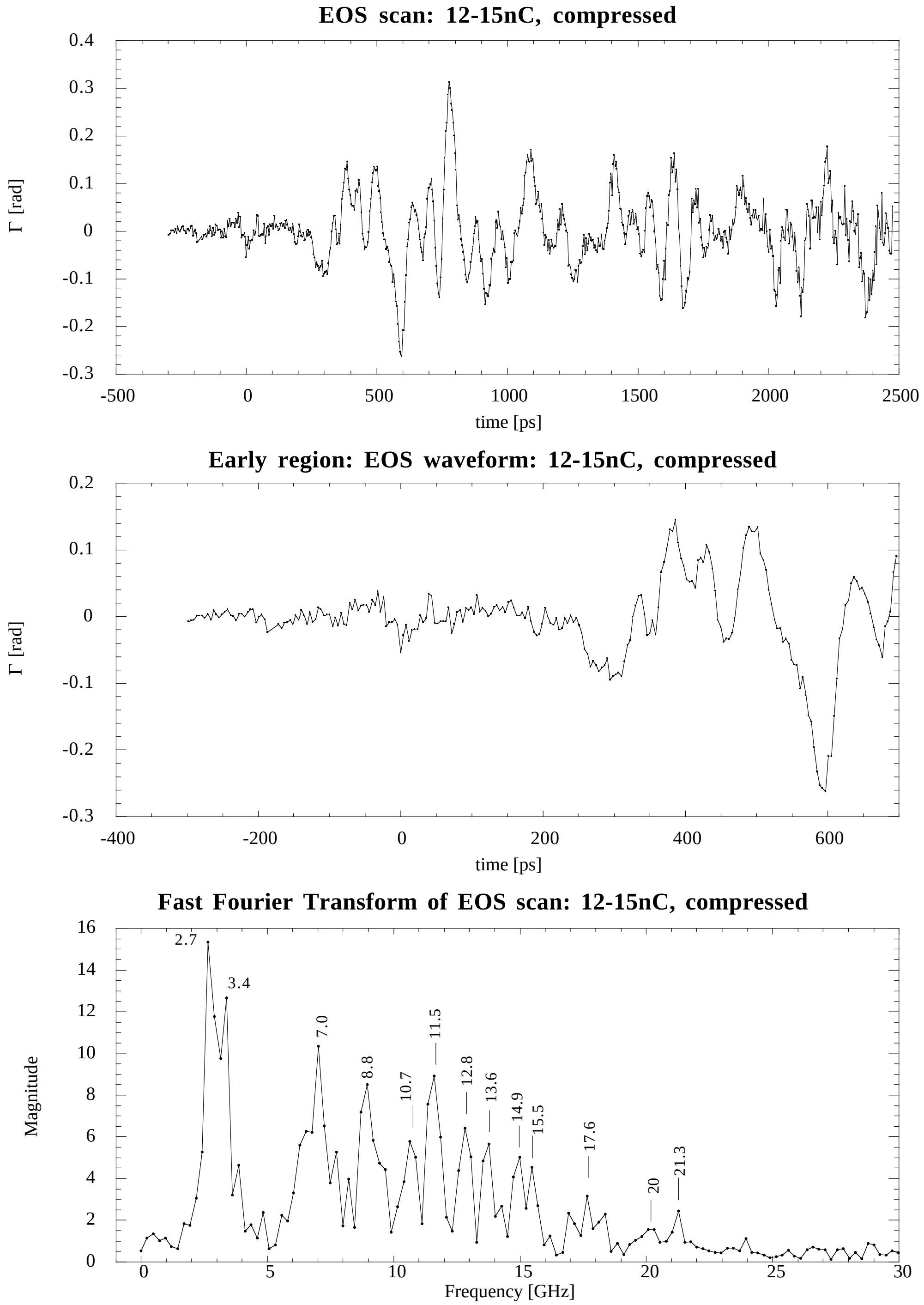

Figure 6.9: EOS waveform for Q = 12–15 nC and 6 ps FWHM. (top) Full waveform, (middle) expanded early region, and (bottom) FFT.

We have also varied the steering of the electron beam, and sampled the transient signal at different offsets from the symmetry axis. For brevity, we have not included the data.

6.3 Results in Geometry B

We changed the orientation of the 1.5 mm thick $LiTaO_3$ crystal so that the sensitive 3-axis (or c-axis) was now along the radial direction relative to the electron beam (see Figure 5.6 on 146). This configuration, which we call geometry B, includes two BK7 glass bending prisms mounted in a ceramic holder (MACOR, an high temperature, machinable, glass-mica ceramic). The probe laser is then traversing the crystal 2-axis, which is parallel to the electron velocity.

In order to observe an polarization ellipticity from an electric field applied on the 3-axis, the laser must be initially polarized at 45° between the 1- and 3-axes. We simply rotated a cube polarizing beamsplitter before the crystal, and used a waveplate before the polarizer to minimize the losses. The prisms have a null electro-optic coefficient, as do the glass vacuum windows, and the polarization is preserved up to the crystal.

The aim of taking data in geometry B, which is sensitive to E_r was to complement the previous data (geometry A), which is primarily sensitive to $\frac{1}{\sqrt{2}}(E_\theta + E_z)$, and might detect the direct Coulomb field of the bunch. From the first results in this configuration, Figure 6.10, it was clear that the EOS waveform was markedly different.

The FFT is dominated by a single peak at 8.8 GHz, with other smaller peaks visible. The time-domain waveform does not resemble a decaying exponential times a sine. However, the observed waveform could be produced by two closely spaced frequencies initially out of phase with each other. The appearance of a beat near 2000 ps suggests a frequency splitting of ~300 MHz. The FFT does

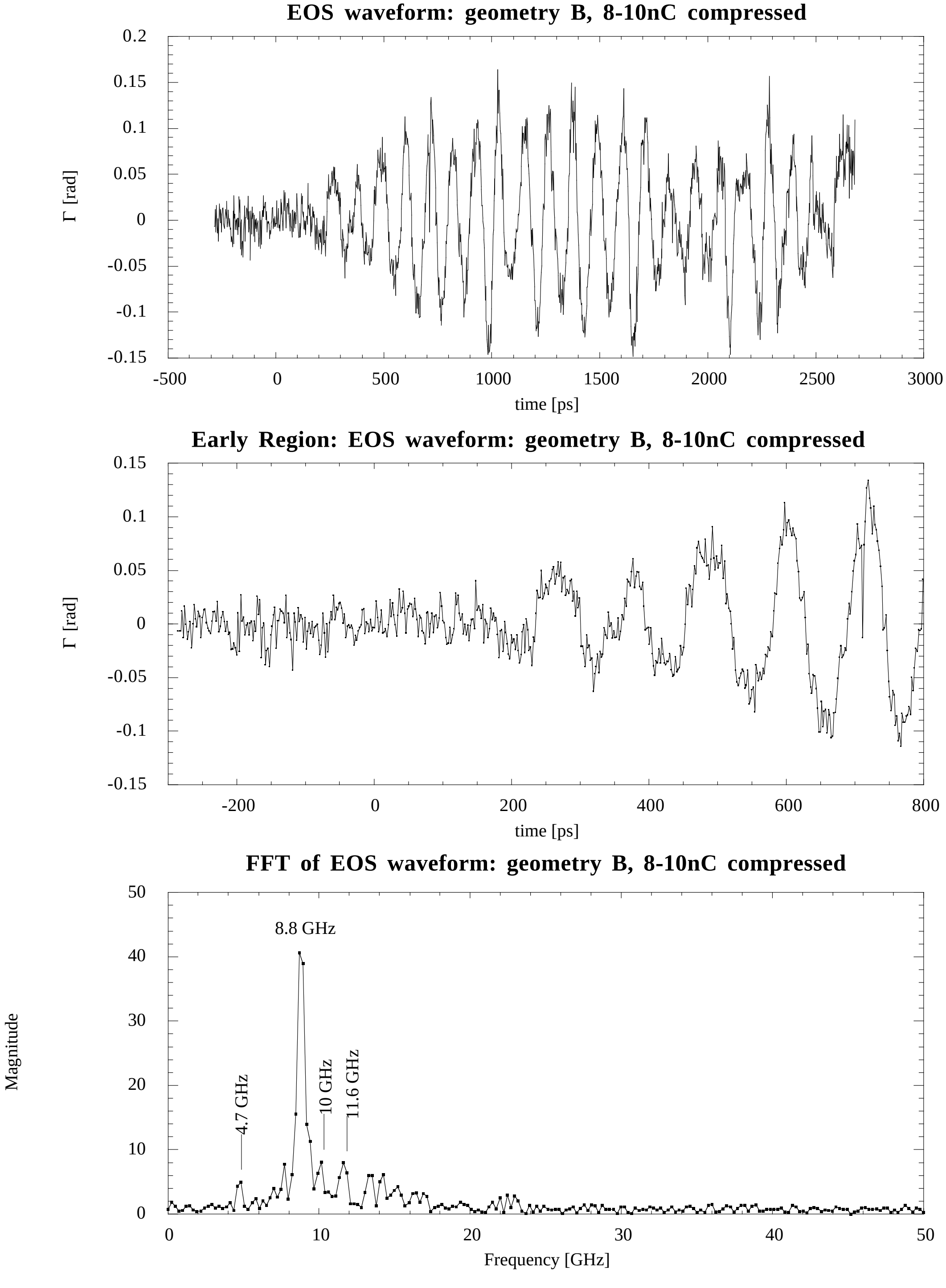
EOS waveform: geometry B, 8-10nC compressed

Early Region: EOS waveform: geometry B, 8-10nC compressed

FFT of EOS waveform: geometry B, 8-10nC compressed

Figure 6.10: EOS waveform in geometry B, 8–10 nC, compressed. (top) Full waveform, (middle) expanded early region, and (bottom) FFT. Sensitive to E_r.

not have enough resolution in this case to distinguish two separate peaks. With higher charge, 12 nC compressed to 6 ps FWHM, Figure 6.11, there is now the suggestion of a splitting in the FFT.

With the sampling experiment running parasitically to another experimental activity, we plot in Figure 6.12 the uncompressed beam at 4 nC (top) and at 8–10 nC (bottom). The waveform is again similar, but the amplitude Γ is lower.

Thick crystal regime

If the group velocity mismatch is large, and the crystal is thick, then the probe laser pulse sweeps over that portion of the transient field which is inside the crystal [160, 161], and the polarization rotation signal for $\mathrm{LiTaO_3}$ with E_z is:

$$\Delta\phi_s(T) = \frac{1}{2}\frac{\omega}{c}(n_o^3 r_{13} - n_e^3 r_{33}) \int_0^L E_s(\frac{z}{c}\Delta n + T)\, e^{-\alpha z} dz. \tag{6.8}$$

where the subscript s refers to the sampled electric field $E_s(T)$. Changing variables to an integration over time,

$$\Delta\phi_{THz}(T) = \frac{1}{2}\frac{\omega}{c}(n_o^3 r_{13} - n_e^3 r_{33})\frac{c}{\Delta n} \int_T^{T+\Delta nL/c} E_{THz}(t)\, e^{-\frac{\alpha c}{\Delta n}(t-T)} dt. \tag{6.9}$$

Assuming that the attenuation coefficient α is flat over the frequency range of interest, the transient pulse profile may be recovered by taking a numerical derivative:

$$E_{THz}(T) \propto \frac{d}{dT}\Delta\phi_{THz}(T) - \frac{\alpha c}{\Delta n}\,\Delta\phi_{THz}(T) \tag{6.10}$$

If the attenuation is negligible, $\alpha L \ll 1$, then the second term is a negligible correction.

In the last step, it was assumed that the sampled field E_s is short enough duration that at a late enough time, the entire waveform is embedded in the

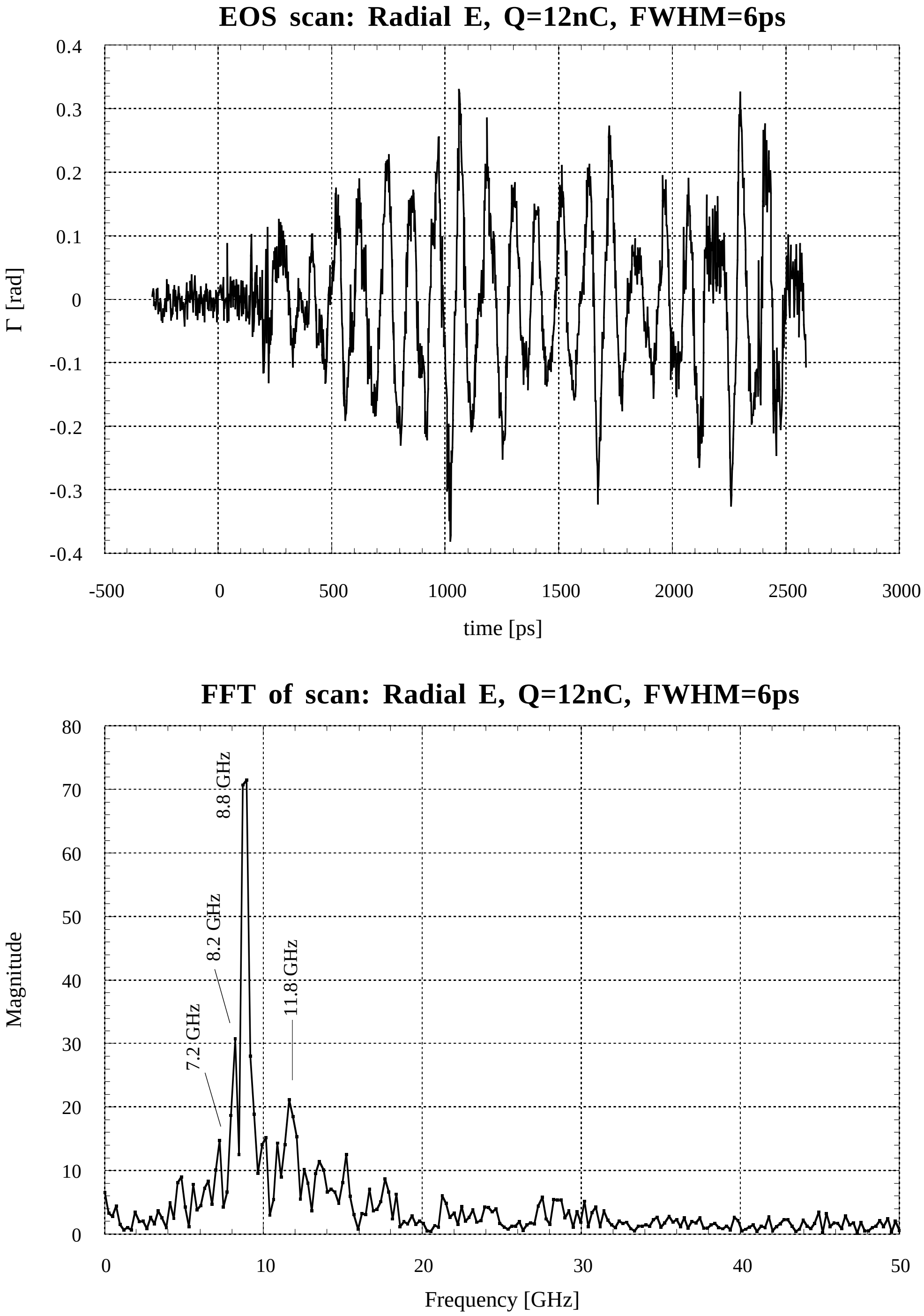

Figure 6.11: EOS waveform (top) in Geometry B sensitive to the radial electric field. Charge 12 nC, compressed to 6 ps FWHM. Fast Fourier transform (FFT) shown at bottom.

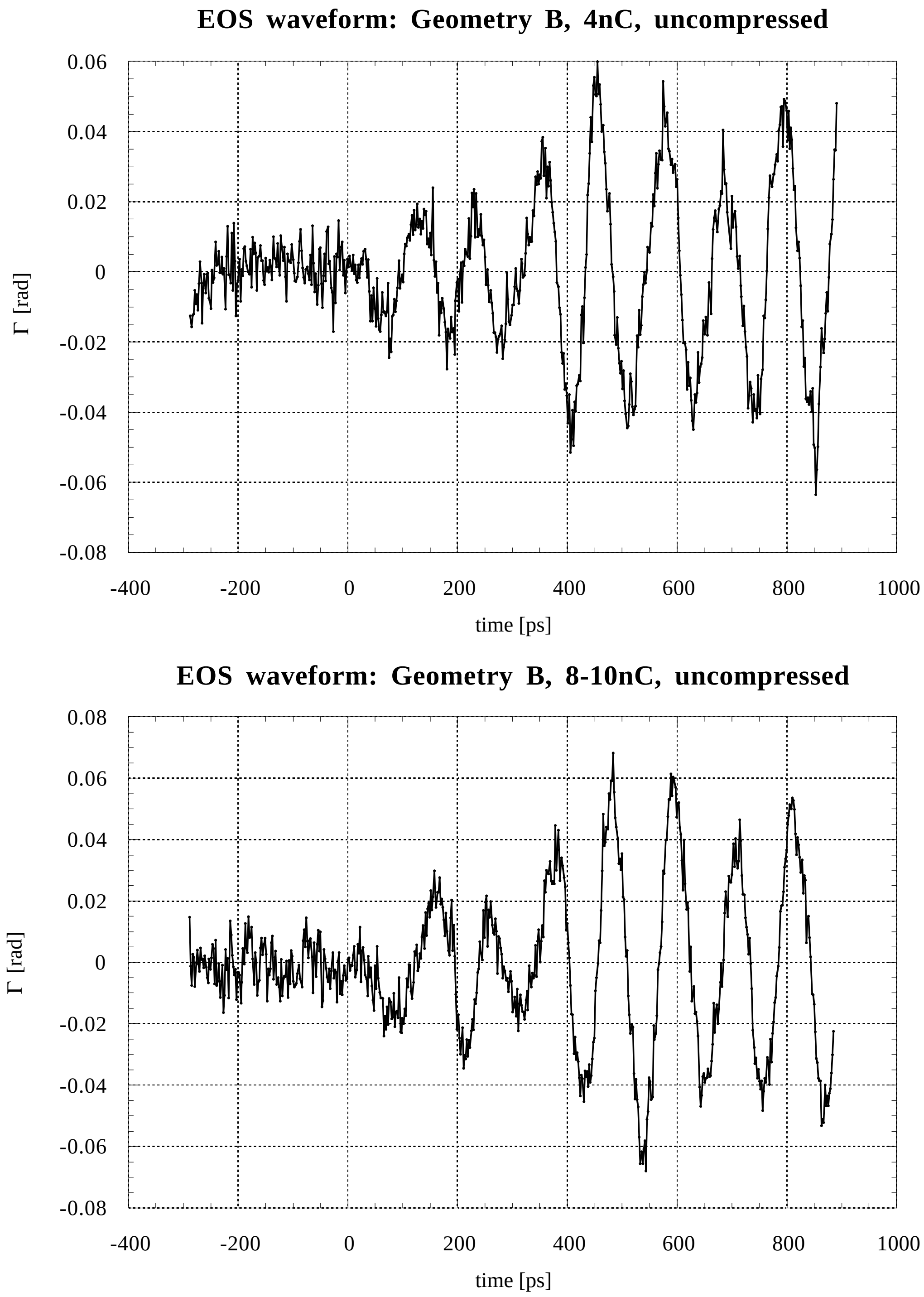
EOS waveform: Geometry B, 4nC, uncompressed

EOS waveform: Geometry B, 8-10nC, uncompressed

Figure 6.12: EOS waveform in Geometry B sensitive to the radial electric field, uncompressed beam. (top) Charge 4 nC, (bottom) 8–10 nC

crystal. When this in not the case, there will be another term representing the sampled field passing out the back of the crystal. However, for the early part of the waveform, Equation 6.10 remains valid.

A few of the time waveforms were of high enough statistical quality that it was worthwhile to try a numerical differentiation after some smoothing. In Figure 6.13, only the very beginning of the derivative waveform is plotted. The first peak was fitted to a Gaussian and was of width 16 ps FWHM. For comparison, the electron bunch length was ~6 ps FWHM.

6.4 Magnitude of the Electric Field

We have previously given our results in terms of Γ, the polarization rotation whose experimental value is given by

$$\Gamma \approx \sin\Gamma = \left(\frac{A-B}{A+B}\right)_{\text{signal}} - \left(\frac{A-B}{A+B}\right)_{\text{background}} \tag{6.11}$$

where A and B are shorthand for the intensity measured at the two detectors I_A and I_B. Even for the largest Γ in our dataset, $\Gamma \sim 0.4$, the approximation $\sin\Gamma \approx \Gamma$ has an error of only 0.01, so we do not use the arcsin correction.

From the tabulated electro-optic coefficients, the expected size of the rotation for a field $E = 100$ kV/m across a $d = 1.5$ mm thick LiTaO_3 crystal is:

$$\Gamma = \frac{1}{2}\frac{\omega}{c}(n_o^3 r_{13} - n_e^3 r_{33}) \int_0^d E\, dz \tag{6.12}$$

For the infrared probe laser, $\lambda = 1054$ nm, the electro-optic coefficients are $r_{13} = 8$ pm/V and $r_{33} = 30$ pm/V. The refractive indices are $n_o = 2.154$ and $n_e = 2.158$ and the expected polarization rotation is:

$$\Gamma_{\text{theory}} = \frac{1}{2}\frac{2\pi}{\lambda}(-2.215 \times 10^{-10}\ \text{m/V}) \cdot 100\ \text{kV/m} \cdot 1.5\ \text{mm} = 0.099\ \text{rad} \tag{6.13}$$

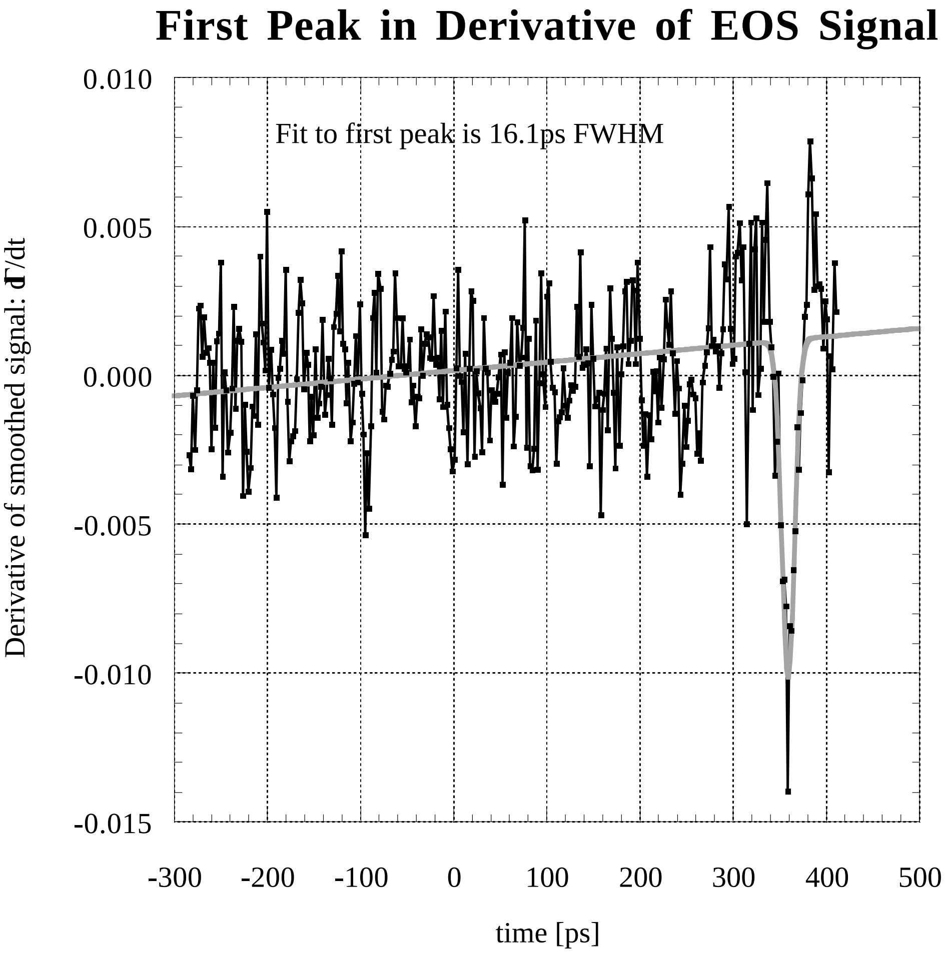

Figure 6.13: Numerical Derivative of EOS signal. The EOS signal was first smoothed, then differentiated. Only the earliest peak is shown, along with a Gaussian fit.

Using a duplicate crystal and a dedicated test station, we have checked the calibration by measuring the polarization rotation with a known field applied to the crystal. Using a high voltage DC source, it is possible to use an oscilloscope to see a change in the two photodiodes. However, because of the thermal drift in the birefringence of the crystal, we have had difficulties obtaining consistent and repeatable numbers with DC.

With an AC source, and using a lock-in amplifier for detection, the calibration measurement is made with much higher confidence.[1] The difference signal between the two photodiodes is measured (as a function of the waveplate angle) first with no applied field. It can be fit to an equation of the form of $(\sin 2\theta \cos \Delta - \frac{1}{2} \sin 4\theta \sin \Delta)$ as in Equation 5.32 on page 149. Then with a sinusoidal applied field of known amplitude applied, the waveplate is again scanned. From the fit coefficients of the two terms, the electro-optic contribution is unambiguously found. We have found a factor of 2 lower than the expected values from tabulated electro-optic coefficients. (This may be due to field penetration, or an underestimation of the dielectric constant ϵ, as discussed in Section 6.5.2.) For a 100 kV/m field applied along the most sensitive axis, the 3-axis, or c-axis, the measured rotation is:

$$\Gamma_{\text{calibration}} = 0.046 \text{ rad} \qquad \vec{E} \parallel \vec{c}, \qquad |E| = 100 \text{ kV/m} \tag{6.14}$$

which, compared with Equation 6.13 gave $\Gamma_{\text{theory}} = 0.099$ rad for the same field of 100 kV/m along the $\vec{c}$-axis. An example of the calibration data with fit is shown in Figure 6.14. We have collected the main results of calibration into Table 6.1. Note that there is sensitivity primarily only to fields parallel to the c-axis.

Using these calibration numbers, the largest polarization change observed in geometry B was 0.4 rad, which corresponds to an electric field strength of 870 kV/m in the radial direction. This is the correct order of magnitude.

---

[1] We acknowledge S. Seletskiy for his contributions to the calibration.

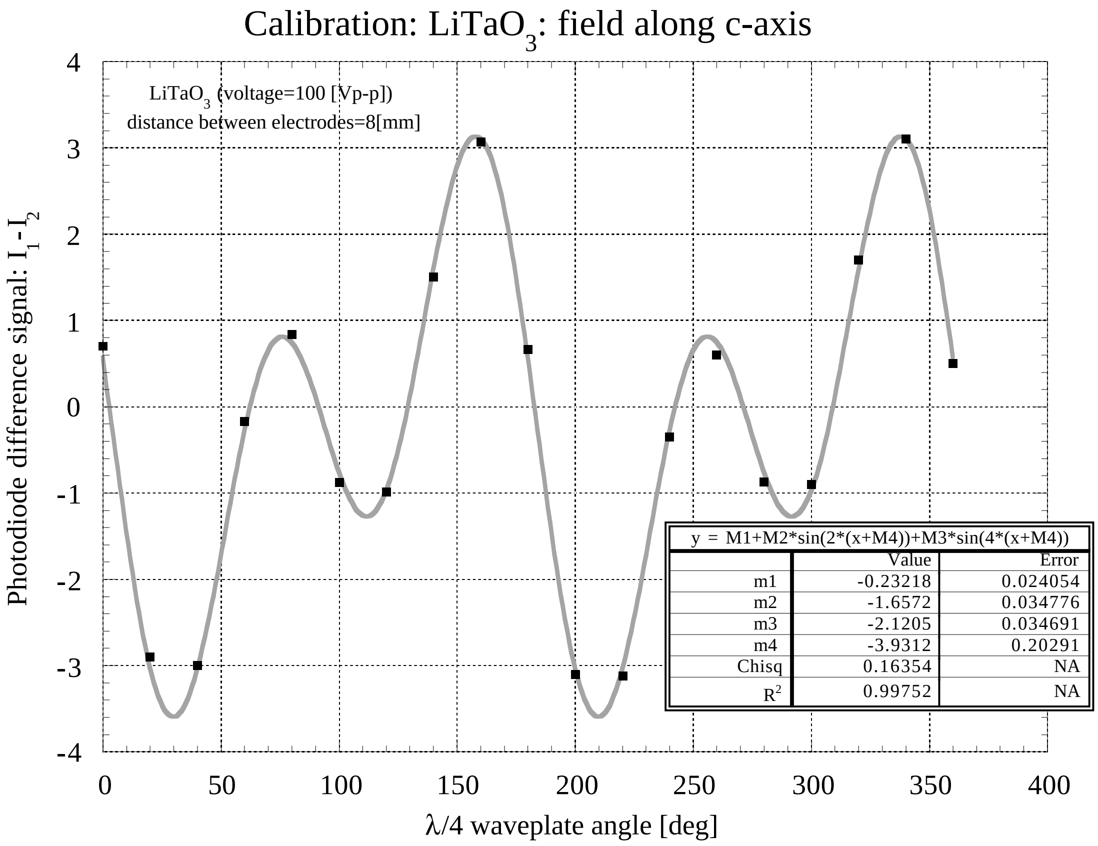

y = M1+M2*sin(2*(x+M4))+M3*sin(4*(x+M4))

	Value	Error
m1	-0.23218	0.024054
m2	-1.6572	0.034776
m3	-2.1205	0.034691
m4	-3.9312	0.20291
Chisq	0.16354	NA
R^2	0.99752	NA

Figure 6.14: Example Calibration: LiTaO3 for $E \parallel c$. The data are fitted to Eqn. 5.32.

It is not easy to determine the sign of the electric field because of the presence of static birefringence. It should be determined by the sign of the difference $A - B$. However, the term in Eqn. 5.32 (page 149) from static birefringence changes sign, and it is not easy in our case to unambiguously determine the sign of Γ and therefore the sign of E. The sign has remained consistent.

Scaling with Charge

To check the scaling with charge, we made a series of measurements of the EOS waveform with varying charges. The beam was compressed and its length mea-

Crystal axis	Γ_{cal} at 100 kV/m	Geometry A	Geometry B
c	0.046	$\frac{1}{\sqrt{2}}(E_z + E_\theta)$	E_r
b	0.003	E_r	E_z
a	0.0011	$\frac{1}{\sqrt{2}}(E_z - E_\theta)$	E_θ

Table 6.1: Calibration of EOS for $LiTaO_3$. The calibrated Γ is given in radians for an applied field of 100 kV/m.

sured with the streak camera. In Table 6.2 we give the peak rotation Γ [rad] from the time domain waveform. The integral of the peak in the FFT can be converted to a Γ value (from Eq. 5.41) and therefore to an electric field. We convert the electric field to V/pC, dividing by the measured charge and multiplying by the beampipe radius.

We also repeated this experiment with the compressor off, so the bunch length is both longer and dependent on the charge. The data are collected in Table 6.3. A plot of both groups of data is shown in Figure 6.15, and it is seen that the compressed data fall nicely along a line with zero origin, while the uncompressed data are too low for high charge. This is likely due to the much longer bunch length in this case. The electric field from Gauss' law (electro-static approximation) is $E = Q/(4\pi\epsilon_o b\ell)$ where ℓ is the bunch length, and b is the distance of observation (the beampipe radius, in this case). Plotting versus Q/ℓ instead of Q does not give a good fit, however.

6.5 Interpretation

6.5.1 Free Space

We first consider the electric fields from a point charge q moving relativistically in vacuum. Taking the z-axis to be the direction of the electron velocity $v = \beta c$,

Q [nC]	FWHM [ps]	max Γ [rad] time domain	Γ [rad] freq. domain	k [V/pC]
1.82±0.29	6.67±0.94	0.13	0.104	1.97
4.12±0.51	5.88±0.82	0.22	0.168	2.11
5.23±0.26	9.7±0.4	0.32	0.266	1.75
8.59±0.47	6.96±0.62	0.48	0.358	1.44

Table 6.2: EOS signal vs. Charge: Compressed.

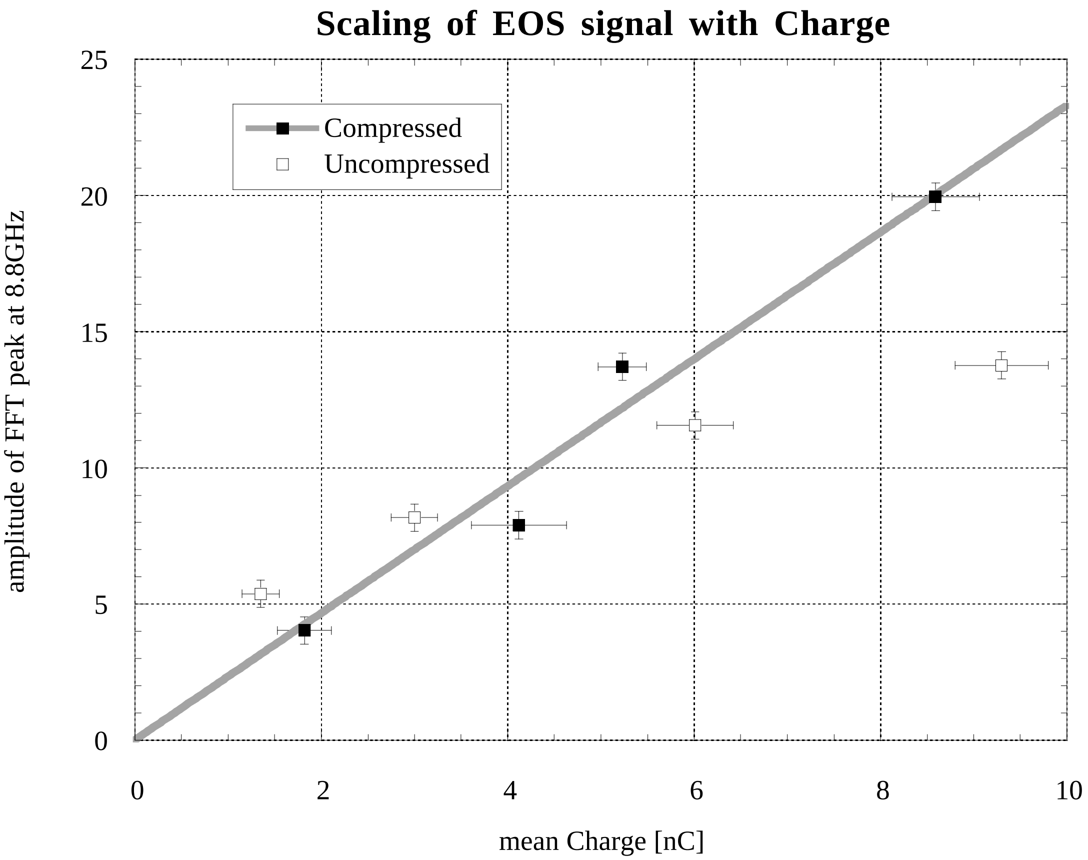

Figure 6.15: EOS signal vs. Charge. The data values are given in Tables 6.2 and 6.3.

Q [nC]	FWHM [ps]	max Γ [rad] time domain	Γ [rad] freq. domain	k [V/pC]
2.0±0.2	13.65±2.0	0.12	0.099	1.71
3.0±0.25	24.65±2.7	0.14	0.145	1.67
6.01±0.41	22.4±2.5	0.22	0.202	1.16
9.3±0.5	24.7±2.0	0.25	0.244	0.904

Table 6.3: EOS signal vs. Charge: Uncompressed.

and the observation point $P = (x = b, y = 0, z = 0)$. The time origin $t = 0$ is taken to be when the particle crosses $z = 0$. The vector $\vec{r}$ points from the particle to the observation point. The coordinate system is sketched in Figure 6.16.

The electric field is given by (see for example [90])

$$\vec{E} = \frac{q\vec{r}}{r^3\gamma^2(1-\beta^2\sin^2\psi)^{3/2}} = \frac{\gamma q\vec{r}}{(\gamma^2v^2t^2+b^2)^{3/2}} \tag{6.15}$$

where the relativistic factor γ is given by $\gamma = (1-\beta^2)^{-1/2}$. The electro-static Coulomb field is boosted to a thin pancake, and the observer P sees the width of this pancake as $\delta z \approx 1.5(b/\gamma)$. Note that because this is an electrostatic field, it is not a wavefield—the observer P at time $t = 0$ sees the summed contributions from all along the prior history of the particle, from $t = -\infty$ to $t = 0$, taking into account the proper retardation. The integral of E_x over all time is invariant:

$$\int E_x\,dt = \int_{\infty}^{\infty} \frac{\gamma q b}{(\gamma^2v^2t^2+b^2)^{3/2}}dt = \frac{2q}{vb} \rightarrow \frac{2q}{cb} \tag{6.16}$$

If instead of a point charge, we have a line charge of length ℓ, and take $t = 0$

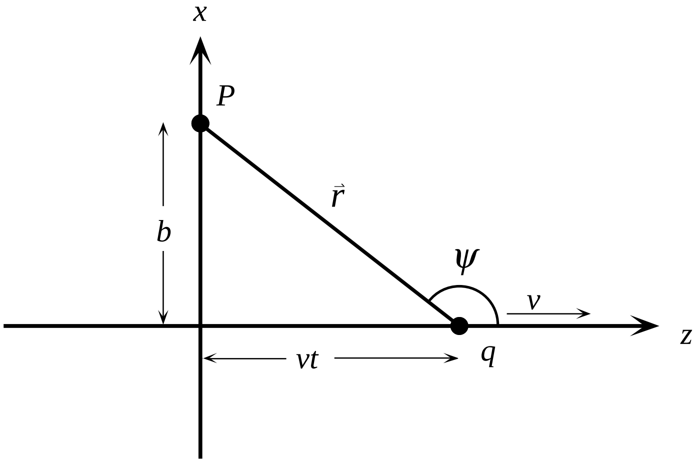

Figure 6.16: Coordinate system for a relativistic charged particle

to be when the center is at $z = 0$, then the field is:

$$E_x = \frac{Q}{\ell} \int_{-\ell/2}^{+\ell/2} \frac{\gamma b}{(\gamma^2 z^2 + b^2)^{3/2}} dz = \frac{2Q}{\ell b} \frac{\gamma \ell}{\sqrt{\gamma^2 \ell^2 + 4b^2}} \tag{6.17}$$

where the integral is elementary after the trig substitution $\gamma z = b \tan u$. Typical values for us are $\gamma = 36$, $b = 22$ mm, the charge $Q = 10$ nC, and bunch length $\ell \sim 1$ mm. The time resolution is of the order of $\tau \sim 2b/\gamma c$, which for the same typical values is 1.22 mm or 4 ps. This is comparable to the IR probe laser pulse length. The crystal thickness (1.5 mm or 3 mm) is also a factor in the time resolution. Clearly a thin crystal moved closer to the beam would give better resolution, as would sampling the beam at higher energy. The time resolution is also limited by the laser pulse length.

6.5.2 Dielectric boundaries

On the surface of the crystal, the dielectric boundary conditions must apply [90]:

$$(\mathbf{D}_2 - \mathbf{D}_1) \cdot \mathbf{n} = 4\pi\sigma \qquad (\mathbf{E}_2 - \mathbf{E}_1) \times \mathbf{n} = 0 \tag{6.18}$$

which means the normal field inside the crystal is reduced by a factor of ϵ/ϵ_o. The dielectric constant of $\mathrm{LiTaO_3}$ is high in the microwave region, $\epsilon \sim 40\epsilon_o$.

The largest signal observed in the EOS experiment was about 0.4, and the noise level (for typical averaging) is about 0.01, so the signal-to-noise ratio seems insufficient to detect the normal field components. We avoided this situation by sampling fields tangential to the crystal surface.

However, when sampling the radial field by orienting the crystal (geometry B), the bending prisms may be attenuating or scattering the direct Coulomb field. Probably a larger distance between the bending optics and the crystal is preferred.

6.5.3 Conducting Boundaries

In our experiment, the electron beam does not propagate in an infinite vacuum in the absence of any conducting boundaries. Rather, it is inside a vacuum pipe of *finite conductivity.* The boundary conditions at the metal interface require that image currents flow on the walls of the structure. In this way the beam interacts with the structure, coupling energy into wakefields. The wakefields in turn interact with the beam, and give rise to instabilities in accelerators. The calculation of wakes and wakefield effects is an active field of research, and an excellent text has been written by A. Chao [162]. A broader text which introduces the material of Chao, is Edwards and Syphers [111]. Lecture notes from accelerator schools [163–165] are also useful sources.

Because the conductivity σ of the walls is finite, there is a characteristic length scale z_o for the lag of the image currents behind the bunch.

$$z_o = \left(\frac{\epsilon_o c}{\sigma b}\right)^{1/3} b \tag{6.19}$$

Using $\sigma = 2 \times 10^7\,(\mathrm{m} \cdot \Omega)^{-1}$ and noting that the axially symmetric structure has a radius $b = 2.4$ cm, the characteristic length $z_o \lesssim 0.1$ mm is shorter than the bunch length.

From Maxwell's equations in cylindrical polar coordinates (r, θ, z), there are only three non-vanishing field components, E_r, E_z, and B_θ inside the cylindrical pipe. These fields generated by the beam current can act back on the beam, or on the next bunch.

6.5.4 Wake Functions

Rather than calculating the field components in great detail, it is sufficient to find the *average* forces acting on the bunch. Average forces are the basis for the wake functions defined in the literature [111, 162, 165–168]. In this section we make the basic connections to these wake functions [163, 164] without developing the theory in depth.

A relativistic point charge q traveling through a structure will be accompanied by electromagnetic fields that, by causality, are non-zero only behind it. For this reason, the fields are called "wakes". The Lorentz force does work on a test charge following a distance s after the exciting charge q. Integrating the work along the whole structure gives:

$$\mathbf{W}_\delta(x, y, s) = -\frac{1}{q}\int_{-\infty}^{+\infty} dz \cdot \left[\mathbf{E}(x, y, z, t) + \frac{\mathbf{v}}{c} \times \mathbf{B}(x, y, z, t)\right]\Big|_{t=(s+z)/c} \tag{6.20}$$

which is called the delta wake (or point wake) potential, and has units of [Volts/Coulomb]. Generalizing from a point charge to the bunch charge distribution $\lambda(s)$ (chosen with normalization $\int_{-\infty}^{+\infty} \lambda(s)\, ds = 1$) gives the wake potential as a convolution:

$$\mathbf{W}(s) = \frac{1}{q}\int_0^\infty ds'\, \lambda(s - s')\, \mathbf{W}_\delta(s'). \tag{6.21}$$

The longitudinal (z) component of the force causes an energy loss, and it is conventional to separate this component out from the transverse part, $\mathbf{W} = \hat{\mathbf{z}} W_{||} + \mathbf{W}_{\perp}$. Then the longitudinal loss factor $k_{||}$ is defined:

$$k_{||}\ [\mathrm{V/C}] = \frac{1}{q} \int_{-\infty}^{+\infty} ds\, W_{||}(x, y, s)\, \lambda(s) \tag{6.22}$$

and the transverse impulse factor is defined:

$$\mathbf{k}_{\perp}\ [\mathrm{V/C}] = \frac{1}{q} \int_{-\infty}^{+\infty} ds\, \mathbf{W}_{\perp}(x, y, s)\, \lambda(s). \tag{6.23}$$

The test charge following the bunch by a distance $s = ct - z$ sees the fields fluctuate about some average value. Since the loss factors $k_{||}$ and $\mathbf{k}_{\perp}$ are integrated over the whole structure, a great computational simplification can be made by replacing the fields by their average value. In this impulse approximation, the instabilities (beam disruption) are assumed to develop slowly, and it is also assumed that the bunch itself has no resonant modes.

In terms of the average fields, the time derivatives in Maxwell equations can be recast as z derivatives [111]. If f is the average value of any field component,

$$\frac{df}{dt} = \left(\frac{\partial f}{\partial t}\right)_z + \left(\frac{\partial f}{\partial z}\right)_t \frac{dz}{dt} = 0 \tag{6.24}$$

$$\Longrightarrow \quad \frac{\partial f}{\partial t} = -c \frac{\partial f}{\partial z} \tag{6.25}$$

The Fourier transform of the point wake potential is called the impedance $Z(\omega)$.

$$Z_{||}(x, y, \omega) = \frac{1}{c} \int_{-\infty}^{+\infty} ds\ W_{\delta,||}(x, y, s) \exp(-i\omega s/c) \tag{6.26}$$

6.5.5 Experimental Loss Factor

In this section, we develop a connection between our experimental data and loss factor calculations from MAFIA. The electro-optic sampling (EOS) waveforms we measured in the time domain at a fixed crystal location $(x_c\,, y_c\,, z_c)$ is $E_{\text{eos}}(x_c\,, y_c\,, t)$. Since the origin of the time is arbitrary, it is equivalent to $E(x_c\,, y_c\,, s)$. Now for the case that E_z is measured (as in Geometry A), the Lorentz force term $\mathbf{v} \times \mathbf{B}$ has a vanishing z-component, so $q\,W_{||} = -\int E_z(s)\,ds$. From Equation 6.21, the Fourier transform of $W(s)$ is, by the convolution theorem,

$$\int_{-\infty}^{+\infty} ds\, W(s) e^{-i\omega s/c} = \widetilde{\lambda}(\omega) Z(\omega) \tag{6.27}$$

where the Fourier transform of the longitudinal charge distribution $\lambda(s) \to \widetilde{\lambda}(\omega)$. The inverse of this relation,

$$W(s) = \int_{-\infty}^{+\infty} d\omega\, e^{+i\omega s/c} \widetilde{\lambda}(\omega) Z(\omega), \tag{6.28}$$

can be put into Eq. 6.22 which defines the loss factor.

$$\begin{aligned} k_{||} &= \frac{1}{q} \int_{-\infty}^{+\infty} ds\, W_{||}(x, y, s)\, \lambda(s) \\ &= \frac{1}{q} \int_{-\infty}^{+\infty} ds \int_{-\infty}^{+\infty} d\omega e^{+i\omega s/c} \widetilde{\lambda}(\omega) Z(\omega) \lambda(s) \end{aligned} \tag{6.29}$$

The integration over s can be performed, and gives $\widetilde{\lambda}^*(\omega)$. Then the loss factor is obtained in the frequency domain:

$$k = \int_{-\infty}^{+\infty} \widetilde{\lambda}^*(\omega) \widetilde{\lambda}(\omega) Z(\omega)\, d\omega = \int_{-\infty}^{+\infty} \left| \widetilde{\lambda}(\omega) \right|^2 Z(\omega)\, d\omega. \tag{6.30}$$

For the case where $\lambda(s)$ is a Gaussian distribution, the Fourier transform is purely real, and is also a Gaussian in frequency,

$$\lambda(s) = \frac{1}{\sqrt{2\pi}\,\sigma}\, e^{-s^2/2\sigma^2} \quad \Rightarrow \quad \widetilde{\lambda}(\omega) = e^{-\omega^2\sigma^2/2c^2} \tag{6.31}$$

The FFT of the EOS waveforms gives the product $\widetilde{\lambda}(\omega)\, Z(\omega)$, as in Eq. 6.27. The experimental loss factor is obtained from Equation 6.30, simply by multiplying the experimental spectrum by a weighting function and integrating. The weighting function is just the Gaussian frequency spectrum of the bunch from the measured (streak camera) bunch length. The integration over frequency is performed by taking the area of the peaks to suppress the noise power in the FFT (as explained in Section 5.6, Equation 5.41). We then use the calibration factor from Equation 6.14 (0.046 rad per 100 kV/m field for a 1.5 mm thick crystal) to convert to field strength (V/m). Then the measured charge is divided out (V/m·pC).

Now an assumption must be made as to how this field does work on a test charge trailing a distance s behind the beam and on-axis. The calculated k loss factor integrates the average work through the 6-port cross structure. Since the beampipe portion of the cross has very low loss, the gap at the cross is the dominant contribution to the work integral on ds. We assume that the average integrated field acts over a distance equal to the radius of the cross arms.

To illustrate, we show the data reduction for an example point. An EOS waveform was taken for a 12 nC beam compressed to 6 ps FWHM, or 0.76 mm σ_t, and is shown in Figure 6.9. After performing the FFT and multiplying by the gaussian weighting factor, the spectrum bin values are summed from 0 to 48 GHz with result 330. Noise power in the FFT is estimated by summing an equal-width (unweighted) region at high frequency with result 52. However, we do not know how much of this "background" is true background and how much could be real signal. So we subtract half the background, and assign an error bar as ± half the background, yielding 304 ± 26. The FFT normalization factor is $2/2N$, where $2N$ is the number of time-domain measurements, and in this case is 693. So we now have

$$\frac{2}{693} \times 304 = 0.877 \text{ rad.} \tag{6.32}$$

This particular data set used the 3 mm thick crystal, so we must double the calibration for a 1.5 mm crystal. We have

$$0.877 \text{ rad} \times \frac{100 \text{ kV/m}}{2 \cdot (0.046 \text{ rad})} = 953\text{kV/m}. \tag{6.33}$$

We now divide by the measured charge of 12 nC to get 79.4 V/m·pC. Finally, using the assumption that the average integrated field acts over an effective distance equal to the pipe radius, we multiply 79.4 V/m·pC × 0.024 m=1.9 V/pC, which is the experimental $k_{||}$ loss factor. We have also made the reasonable assumption that E_z is the same at the crystal location as on-axis since it is a monopole.

The same method can be applied to the EOS data which measure the radial electric field (Geometry B). However, there are two complications. Firstly, the magnetic term of the Lorentz force ($\mathbf{v} \times \mathbf{B}$) has a radial component, and is not measured at all. Secondly, the field is measured at the crystal location 32 mm off-axis, and we assume the field is a radial dipole that depends linearly on the radial displacement. So we simply divide by the crystal-to-beam distance to arrive at a quantity with units [V/(m pC)] which we call the "experimental transverse kick". This can be compared with the MAFIA calculations of the transverse loss factor $k_\perp$.

In Figure 6.17, we show the comparison of our experimental results with the MAFIA numbers. The top plot is the longitudinal loss factor from three data sets in Geometry A, one of which was our example above. The sc mafia points are scaled to a 48 mm conflat 6-port cross using a scaling law given by Tang and Ng [167] to interpolate their calculations for 35 mm and 63 mm conflat 6-port crosses. The bottom plot of Figure 6.17 is the experimental transverse kick compared with the transverse loss factor. The data points are extracted from data using $LiTaO_3$ in geometry B taken 6 March 2000. We chose this data set, labeled "Exp B" because eight different runs were made as a function of charge and bunch length on that date so trends can be seen.

The horizontal error bar is from the error in the streak camera bunch length, and the vertical error bar is an estimation of the background in the frequency integration as discussed above. The vertical scatter in the points around 1 and 3.5 mm σ correspond to different electro-optic sampling runs at different charges for the compressed and uncompressed beam. We note that the error bars of these points do not overlap. This may be due to a different bunch *shape* at higher charges, since the loss factor is sensitive to the shape. We feel the longitudinal data shows reasonably good agreement with MAFIA. The transverse data, however, is too large in comparison with MAFIA. Since the magnetic force term is not measured, we cannot expect good agreement here.

To our knowledge, this result is the first direct measurement of the $k_{||}$ loss factor at these very short bunch lengths. The use of electro-optic sampling is a new technique for experimentally obtaining the longitudinal loss factor $k_{||}$ from the wakefields. We feel this is reasonably good agreement with MAFIA. It is also possible to report our data in terms of beam impedance.

6.5.6 Mode Labeling

The arms of the 6-way cross are sufficiently long that we may treat them as a cylindrical waveguide with $\rho = 23.8$ mm radius. The transverse magnetic (TM) modes have $B_z = 0$ everywhere and satisfy the boundary condition $E_z\big|_s = 0$ on the surface S. The transverse electric (TE) modes have $E_z = 0$ everywhere and the normal derivative $\frac{\partial}{\partial n} B_z\big|_s = 0$ vanishes on S. The wavelengths are given by:

$$\lambda(\mathrm{TE}_{nm}) = \frac{2\pi\rho}{x'_{nm}} \tag{6.34}$$

$$\lambda(\mathrm{TM}_{nm}) = \frac{2\pi\rho}{x_{nm}} \tag{6.35}$$

where x_{nm} is the m-th zero of the Bessel function of order n, $J_n(x_{nm}) = 0$, and x'_{nm} is the m-th zero of the derivative, $J'_n(x'_{nm}) = \frac{d}{dx} J_n(x'_{nm}) = 0$. Using this formula

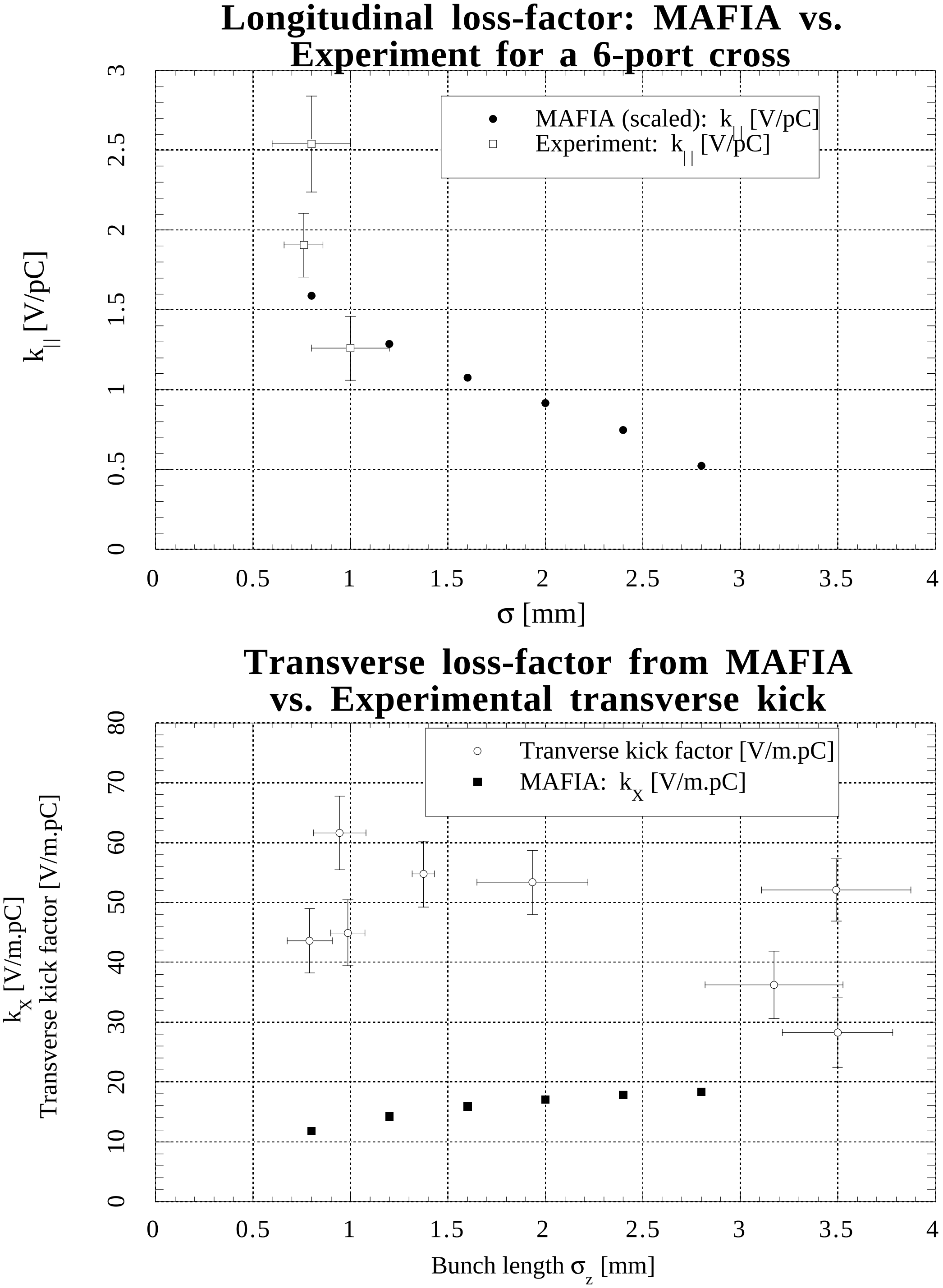

Figure 6.17: (top) Experimental longitudinal loss factor $k_{\|}$ vs. MAFIA calculations [167] scaled to a 48 mm conflat 6-port cross. (bottom) Experimental transverse kick vs. MAFIA transverse loss factor k_x

TE_{nm}	ν [GHz]	TM_{nm}	ν [GHz]
TE_{01}	7.68	TM_{01}	4.82
TE_{11}	3.69	TM_{11}	7.71
TE_{21}	6.12	TM_{21}	10.34
TE_{02}	14.07	TM_{02}	11.11
TE_{12}	10.69	TM_{12}	14.08
TE_{22}	13.45	TM_{22}	16.95

Table 6.4: Mode frequencies of a cylindrical waveguide, taking the beampipe radius $\rho = 23.8$ mm.

we give the frequencies in GHz for several of the low order modes in Table 6.4. Note that the lowest frequency is the TE_{11} mode at 3.7 GHz.

Exact agreement should not be expected between the frequencies in Table 6.4 and those observed, because clearly the cross arms are *not* infinitely long cylindrical waveguides. In geometry A, the sensitivity is $2^{-1/2}(E_z + E_\theta)$, but the E_θ component vanishes from symmetry. The TM modes have $E_z = 0$ at the wall, so we expect the observed modes to be primarily TE modes. In Table 6.5, we list observed mode frequencies taken from the data shown in Figure 6.9 (on page 167) together with the predicted frequencies and mode identification.

In geometry B, the sensitivity is highest for the TM_{nm} modes, and we list predicted and observed frequencies for these modes in Table 6.6. The effect of boundary conditions at the cross ends on these modes is discussed in Section 6.5.8 below.

Taking into account the finite length of the cross arms, we can treat the (horizontal) arm as a cylindrical cavity of length $d \approx 20$ cm. From [90], the TM resonant frequencies are given by

$$(\mathrm{TM}) \qquad \nu_{nmp} = \frac{c}{2\pi\sqrt{\mu\epsilon}}\sqrt{\frac{x_{nm}^2}{\rho^2} + \frac{p^2\pi^2}{d^2}} \tag{6.36}$$

TE_{nm}	ν [GHz] predicted	ν [GHz] observed
TE_{11}	3.69	3.4
TE_{01}	7.68	7.0
TE_{31}	8.42	8.8
TE_{12}	10.69	10.7
TE_{22}	13.45	13.6
TE_{02}	14.07	14.9
TE_{32}	16.07	15.5
TE_{13}	17.12	17.6
TE_{03}	20.39	21.3

Table 6.5: Observed and Predicted frequencies: $LiTaO_3$ in Geometry A, sensitive to E_z. Data taken from Figure 6.9 is high charge 12-15 nC, Compressed.

TM_{nm}	ν [GHz] predicted	ν [GHz] observed
TM_{11}	7.71	8.8
TM_{01}	4.82	4.7
TM_{21}	10.34	10.14
TM_{02}	11.11	11.5
TM_{31}	12.79	12.4

Table 6.6: Observed and Predicted frequencies: $LiTaO_3$ in Geometry B, sensitive to E_r.

and for the TE modes, replace x_{nm} by x'_{nm} as before. Since the cavity is *in vacuo*, we take $\sqrt{\mu\epsilon} = 1$. For $p = 0$, this reduces to the waveguide modes listed in Table 6.4. For the TM_{01p} modes, the splittings are small, $\mathrm{TM}_{010} \rightarrow 4.82$ GHz, $\mathrm{TM}_{011} \rightarrow 4.88$ GHz, and the $\mathrm{TM}_{022} \rightarrow 5.05$ GHz.

Finding the true eigenmode frequencies in a structure such as the six-way cross of our experiment with the crystal holders and other perturbations is a problem amenable to numerical methods.

6.5.7 Numerical Modeling

Maxwell's equations can be solved discretely on a mesh. The code MAFIA has an eigenmode solver and a time-dependent package. Calculations of the eigenmodes in a 6-port cross using MAFIA have been given by Tang [169], and by Tang and Ng [167]. Since our cross is a different size, it is necessary to scale the frequencies (cross X5 is a 48 mm conflat CF48, while the CF35 and CF63 were modeled).

A least-squares parametrization of the frequency scaling of resonant modes is given in Ref. [167]:

$$f[\mathrm{GHz}] = 4.618 - 0.032D - 48.54/D + 2276/D^2 \tag{6.37}$$

with the cross diameter D in mm. Equation 6.37 predicts a frequency ratio of 1.288, while simple scaling by the ratio of diameters is a factor $(47.6)/(35) = 1.36$ and we use the former value.

To reduce the number of mesh points, which reduces the computation time, one quarter of the cross was modeled in Ref. [167]. The mode frequencies identified include 3.09, 3.10, 3.7, 3.93, 4.21, 4.23, 4.4, 4.54, 4.55, and 4.88 GHz. Since the cutoff frequency for propagation down the beampipe is 3.7 GHz (the TE_{11} waveguide mode), those frequencies close to and above this cutoff might not be well modeled. The crystal holder and other minor differences in exact structure used in our experiment can be treated as perturbations from the idealized structure of Ng and Tang. Nevertheless, the observed frequencies at 2.7 and 3.3 GHz are identified with confidence as trapped modes in the cross.

6.5.8 Boundary conditions at ends of cross

The MAFIA simulations of Tang and Ng [167] and Tang [169] of a 6-way cross are made for transverse electric and transverse magnetic boundary conditions at the ends of the cross arms. The electro-optic crystal is mounted in cross X5 (see the beamline drawing, Figure 1.1 on page 5), the first cross downstream of the chicane. The vertical arm has an actuator with an OTR screen. The bottom opens into a titanium sublimation pump (TSP). The two horizontal arms have glass vacuum viewports, and one side also has the crystal holder. Consequently, none of these cross ends is terminated with boundary conditions like those simulated.

We decided to do a simple experiment to see how sensitive the observed EOS waveforms are to the cross ends by placing copper caps (with a small hole for the laser) over one or both windows. Of course, it would be better to place the shield on the vacuum side of the dielectric window. However, with a superconducting RF cavity that must be protected from contamination, the facility is not very nimble at making vacuum breaks. The effect of the copper caps, as seen in the time domain, was mainly a phase shift at late times. In the FFT, Figure 6.18, it can be seen that some of the minor peaks in the FFT were affected. In Table 6.7 we give the frequencies observed in the FFT (±0.1 GHz) along with the peak FFT magnitude. Then, for better comparison across the data sets, we normalize the peak magnitudes to the magnitude of the strong peak at 8.8 GHz.

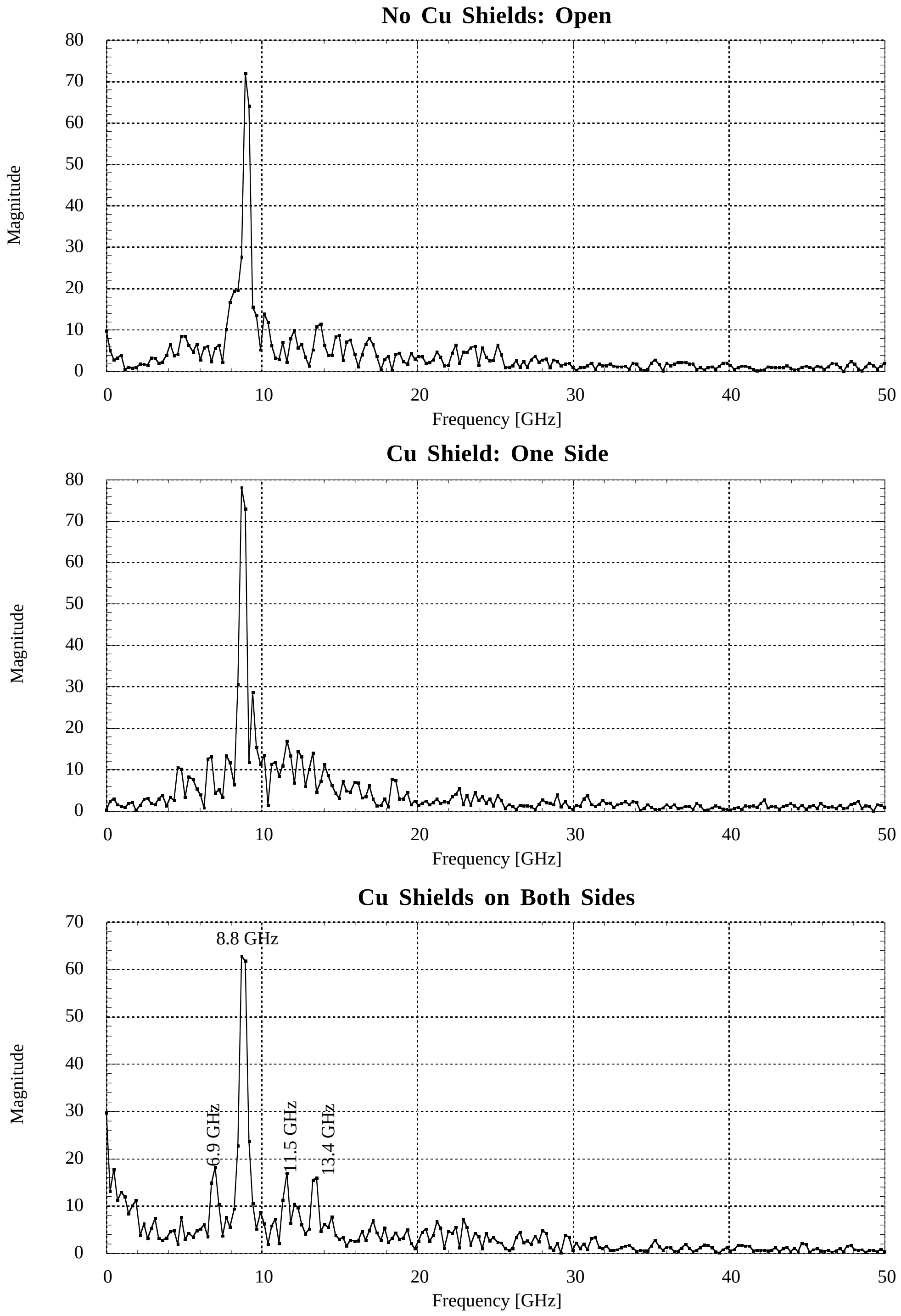

Figure 6.18: FFT of EOS waveform in geometry B, 10–12 nC, compressed to 6 ps FWHM. (top) Open–no Cu shields, (middle) Cu shield on one side, and (bottom) Cu shields on both sides.

6.6 Results in Geometry C

One of the main complications in understanding our dataset is the sub-optimal geometry of the 6-way cross. It is highly desirable to repeat the experiment in a simpler structure.

The smooth beampipe is a good case, as a detailed analytic theory exists [162]. A small hole in the beampipe is a necessary perturbation to mount the crystal and to admit the laser light. A second port for the laser exit is used. The existing beampipe already has small circular ports machined into it at various locations for capacitive beam position monitors (BPM's). We designed a small crystal holder to fit into a BPM port and modified two glass vacuum viewports to mate to the housing with a compression seal (Helicoflex). A sketch is shown in Figure 6.19. The electron beam velocity is out of the page. The crystal c-axis is also directed out of the page, so it is sensitive to E_z. In the cylindrical waveguide, the TE modes have $E_z = 0$, so we expect to see only TM modes in this case.

Because the crystal is now weakly coupled to the beampipe through a small hole, the observed signals in the time domain are small. The FFT is in this case very powerful for identifying weak signals. Several peaks are found in the FFT, shown in Figure 6.20. The observed frequencies are listed in Table 6.8 along with the probable mode identification and predicted mode frequency. The BPM housing is 4-fold symmetric, and with the windows on either side it is 2-fold symmetric (broken of course by the crystal holder). Since the field pattern inside the pipe (radius $\rho = 23.8$ mm) for TM modes is a linear combination of terms with the potential [90]

$$\psi(\rho, \phi) = A_{mn}\, J_m(x_{mn} r/\rho)\, \exp(\pm i m \phi), \tag{6.38}$$

we expect from the symmetry to see modes with $m = 2$ and $m = 4$, which are

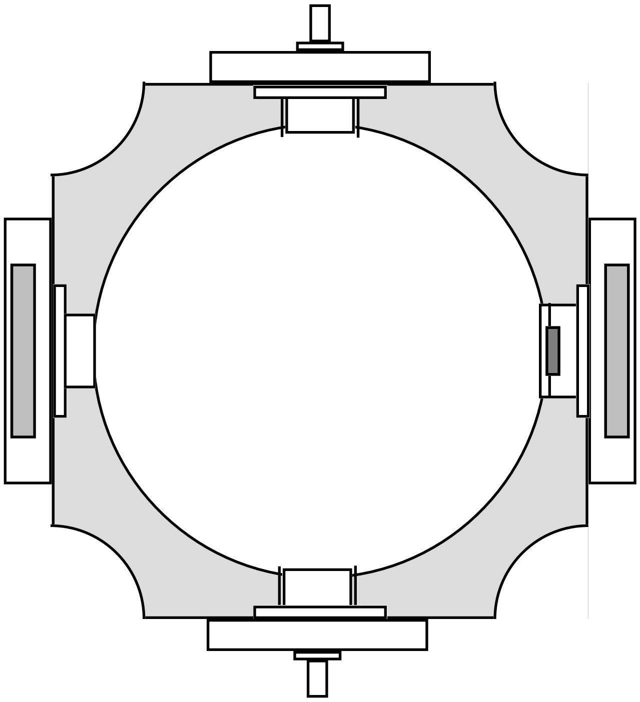

Figure 6.19: Crystal mount in a BPM housing: geometry C. The crystal and holder are on the right. Glass viewports for the laser entry and exit are on the right and left. Capacitive BPM's are at top and bottom. The electron beam motion is out of the page.

indeed present. The predicted TM mode frequency is $\nu_{mn} = cx_{mn}/(2\pi\rho)$ where x_{mn} is the nth zero of the Bessel function $J_m(x_{mn}) = 0$.

The peaks in the FFT are much weaker than previous data. This is expected since the wakefields in a smooth round pipe couple energy away from the beam only because of the finite conductivity of the walls.

6.7 Results for KD*P in geometry A

By using a crystal with a different electro-optic tensor, it is possible to probe other electric field components with the same geometry holder. For example, the electro-optic crystal potassium dihydrogen phosphate (KH_2PO_4, or KDP)

Open	freq. [GHz]	4.8	6.9	8.8	10.14	11.8	12.1	13.5
	norm. mag.	0.119	0.077	1	0.193	0.109	0.138	0.150
Cu one side	freq. [GHz]	4.7	6.8	8.8	10.14	11.5	12.4	13.3
	norm. mag.	0.135	0.167	1	0.173	0.217	0.183	0.180
Cu both sides	freq. [GHz]	4.8	6.9	8.8	9.9	11.5	12.3	13.4
	norm. mag.	0.121	0.289	1	0.138	0.270	0.152	0.253
	trend	≈	⇑		⇓	⇑	≈	⇑

Table 6.7: Effect of Cu shielding on frequency components. The normalized magnitude is the ratio to the strong peak at 8.8 GHz. The data are shown in Figure 6.18.

Observed ν [GHz]	TM_{mn} mode	Predicted ν [GHz]
7.4	TM_{11}	7.68
18.3	TM_{22}	16.88
	TM_{51}	17.59
29.0	TM_{43}	28.82
35.8	TM_{44}	35.32
38.1	TM_{54}	38.06
44.43	TM_{55}	44.55

Table 6.8: Observed and Predicted frequencies for the $LiTaO_3$ crystal in a small hole in the cylindrical beampipe (geometry C)

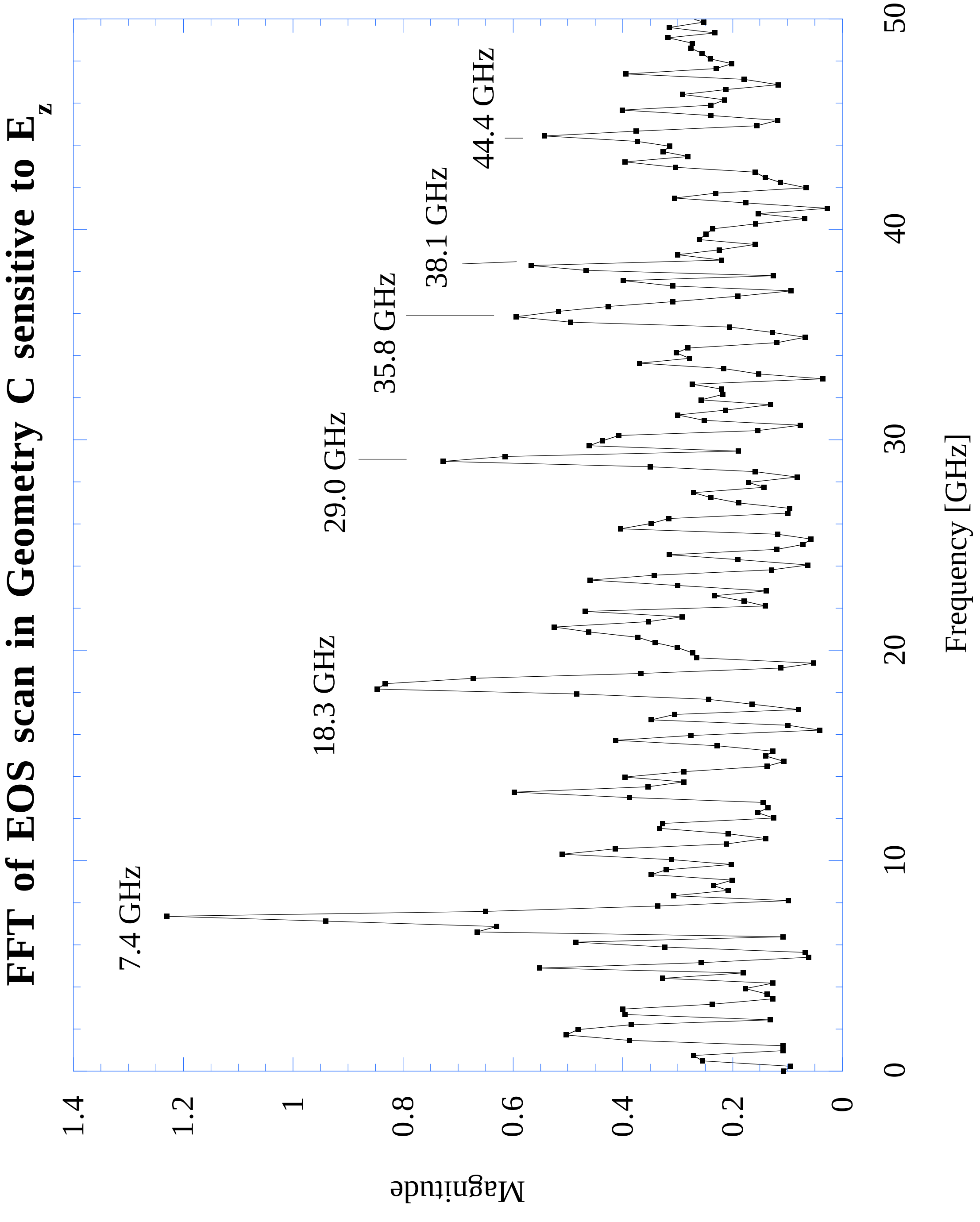

Figure 6.20: The FFT of the longitudinal field E_z is measured by a crystal mounted in a small hole in the cylindrical beampipe (geometry C). 4 nC, compressed.

has a transverse electro-optic effect. By replacing hydrogen with deuterium, the electro-optic coefficient is enhanced more than a factor of two. Deuterated KDP is abbreviated KD*P.

The EOS waveforms with KD*P in geometry A are sensitive to E_r. However, because E_r is normal to the crystal face, the boundary conditions reduce the field inside by the dielectric constant. The time domain data did not clearly show any signal above noise. Including the reduction from the dielectric constant, the expected signal is at most $\Gamma \sim 0.01$ which is marginally detectable.

The presence of frequency modes above noise could be seen by applying the FFT. As in geometry C, the four-fold symmetry of the structure explains the many TM_{4n} modes. The frequency-domain data is shown in Figure 6.21, and the observed frequencies together with mode labeling and predicted frequencies are collected into Table 6.9.

6.8 Summary

Since our first observation of the wakefields using electro-optic sampling, we have completed a number of experiments using the technique.

With different crystal orientations, the vector components of the electric field can be measured. The observed frequencies are identified as modes in the structure, and the frequencies predicted for the cylindrical cavity (waveguide) of the beampipe are in good agreement with those observed.

The magnitude of the electric fields is obtained from a calibration. The wakefield k loss factor can then be found, and is in good agreement with the predictions of MAFIA. More discussion of conclusions is given in the next chapter.

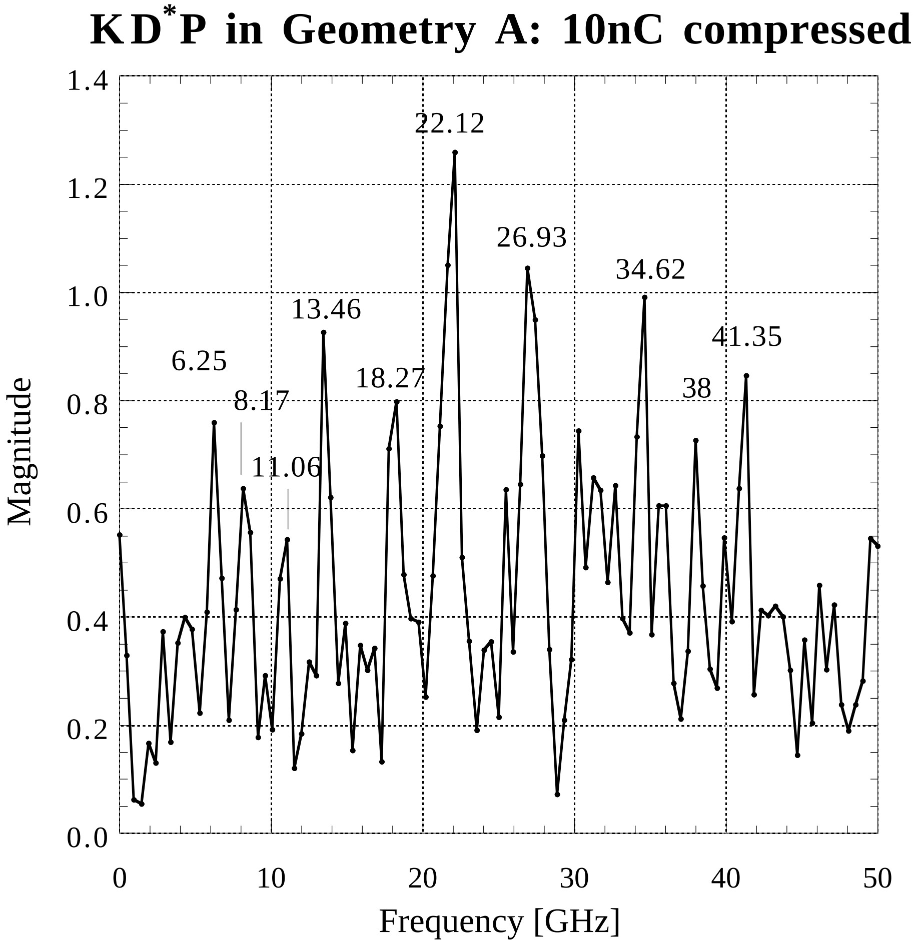

Figure 6.21: KD*P in geometry A: FFT, sensitive to E_r.

TM_{nm}	ν [GHz] predicted	ν [GHz] observed
TM_{42}	22.18	22.1
TM_{43}	28.82	26.9
TM_{44}	35.32	34.6
TM_{45}	41.76	41.4
TM_{31}? TM_{41}?	12.79 15.21	13.5
TM_{51}	17.59	18.3
TM_{54}	38.06	38.0
TE_{21}?	6.12	6.3
TM_{11}? TE_{01}? TE_{31}?	7.68 7.68 8.42	8.2
TM_{02}	11.07	11.06

Table 6.9: Observed and Predicted frequencies: KD*P in Geometry A, sensitive to E_r. Data taken from Figure 6.21. High charge 10 nC, compressed.

Chapter 7

Conclusions

7.1 Electro-Optic Sampling

We have shown that the electric fields from the passage of a relativistic electron beam can be measured with a time resolution of $\lesssim$5 ps. As the electro-optic effect has a fundamental response time at the femtosecond level, the limiting resolution of the technique is tens of femtoseconds.

The results we presented in Chapter 6 on electro-optic sampling (EOS) of the transient electric fields from the passage of a relativistic electron bunch are among the first successful applications of EOS to beams, with applications to bunch length measurement. From the EOS signal, we have obtained an experimental wakefield k loss factor, which is to our knowledge the first direct measurement of the k loss factor at these short (submillimeter) bunch lengths. Reasonably good agreement is found with calculations [167] using the code MAFIA, which solves the Maxwell equations on a 3-dimensional mesh.

The use of electro-optic sampling to measure the k loss factor is a new technique of beam measurement. The loss factors can be indirectly measured by inference from beam energy loss, or from disruption of the beam itself. The experimental waveform is Fourier transformed, weighted by a Gaussian function of the measured bunch length, and the result is integrated to obtain the $k_{||}$ loss factor. Because

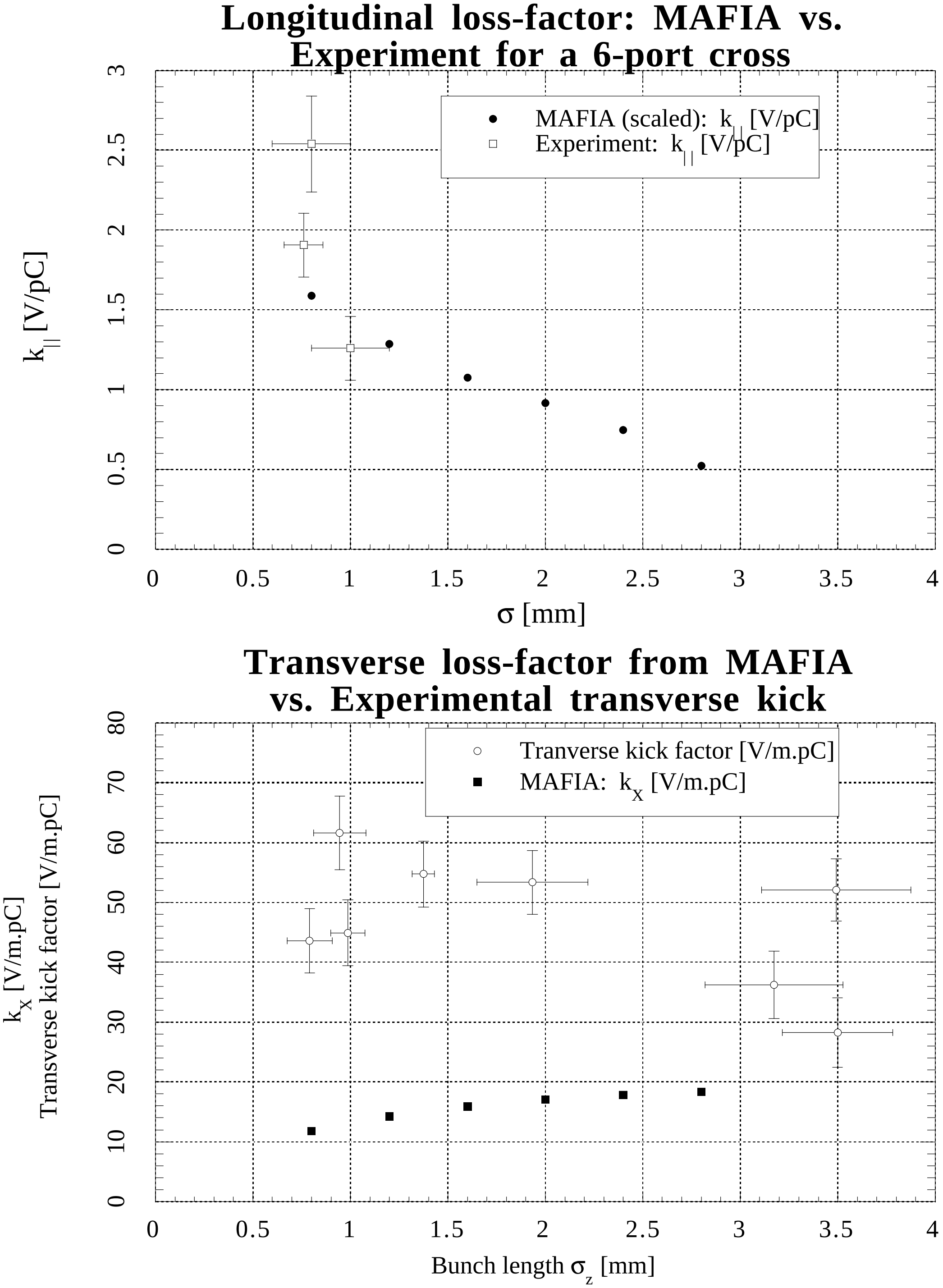

Figure 7.1: (top) Experimental longitudinal loss factor $k_{\|}$ vs. MAFIA calculations [167] scaled to a 48 mm conflat 6-port cross. (bottom) Experimental transverse kick vs. MAFIA transverse loss factor k_x

the magnetic force also contributes to $k_\perp$ but is not measured, we report the electric force "transverse kick factor". Figure 6.17 is repeated here as Figure 7.1 to emphasize this result. Note that the assumptions necessary to extract an experimental k loss factor from the electro-optic sampling data are discussed in Section 6.5.5.

A considerable effort within the accelerator community is devoted to analytical and numerical calculations of wakefield effects. Experimental numbers are also needed. Electro-optic sampling may have applications to wakefield characterization of structures. This may be very important to next-generation linear colliders, where wakefield effects lead to instabilities such as the beam break-up instability and the head-tail instability that limit the achievable luminosity [111, 162, 170].

The electric fields we measure are excitations in the beampipe structure. Some of the low frequencies can be identified with low-order cavity modes of the cylindrical cross arms. Many of the higher frequencies match predicted frequencies for (traveling) waveguide modes in the beampipe. The decay times of the modes are likely to be 10–100 ns since there is little decay at the longest delay of our stage (~3 ns), and no signal above noise by the next trigger (1 μs later).

The amplitude of the signal scales with the charge, and is the correct order of magnitude expected for the Coulomb field of the bunch, being ~0.8 MV/m. The signal is reproducible, and the jitter vanishes to first order since the infrared probe pulse and the UV pulse on the cathode that drives the electron beam are derived from the same pulse. The electron arrival time will drift with changes in the RF amplitude and phase, which is a "second order" jitter.

By orienting the crystal appropriately, one can selectively measure the three vector components E_z, E_r, and E_θ at the location of the crystal.

Another application of electro-optic sampling of charged particle beams is the measurement of very short bunch lengths. The ability to resolve the longitudinal charge distribution with a resolution of tens of femtoseconds is very attractive for x-ray free electron lasers and future linear colliders for high energy physics. Electro-optic sampling is, at present, the only time-domain method capable in principle of such time resolution.

7.2 Possible Improvements to EOS

Improvements to the time resolution of the electro-optic sampling experiment can be achieved on three fronts: reducing the laser pulse length, using a thinner crystal, and moving the crystal closer to the beam. Our main limitation at present is the laser pulse length, being in the regime of 2–4 ps σ. With minimal impact to the rest of the laser system, the IR probe beam could be passed through a saturable absorber, resulting in a modest improvement in the pulse duration, perhaps a factor of 2. The losses in the saturable absorber are not a problem for the probe beam since neutral density filters are already in use to keep the photodiodes in the linear regime.

The laser pulse length could also be shortened by upgrading to an Nd:glass oscillator. Of course, changing to a ultrafast system based on Ti:sapphire would be a major effort and expense.

With a thinner crystal, the sampling volume is reduced. Our choice of 1.5 mm thick was a practical decision based on the need for rigorous cleaning procedures and cleanroom assembly to protect the superconducting cavity from particulate contamination. The ZnTe crystals were the most fragile that we tested, and one of the 1.5 mm thick ZnTe crystals was broken during clean room handling. With $LiTaO_3$, reducing the thickness to 0.5 mm should not be a problem, since it is not as fragile as ZnTe.

Moving the crystal closer to the beam should also reduce the time resolution, which is of the order of $\tau \sim 2b/\gamma c$ with b the distance from the beam. Moving the crystal closer would likely require (in our beamline) mounting it on a vacuum actuator. Reproducibility of alignment is an issue.

Detecting all three vector components of the electric field can be done with only two crystals [171]. This technique may be useful for field mapping of RF cavities.

It is also desirable to decrease the noise level of the experiment, which is currently about 1%. The contrast of the polarizers is probably not the cause, as the polarizing beam splitters (cubes) have a polarization contrast of 500:1. An upgrade to Wollaston prism polarizers, or Glan polarizers would give a contrast of 10^5:1. A Soleil-Babinet compensator (Section 5.5) would allow cancellation of the static birefringence of the crystal.

The noise level is mainly determined by the amount of averaging. Orders of magnitude improvement in integration time are possible by utilizing the pulse trains of the facility. Reading measurements from a digital oscilloscope, as done here, limits the data acquisition to only one pulse in each pulse train.

One possible improvement using charge integrators and a synchronized digitizer card was tested. The accuracy of the charge integrator was at best 1%, which means that the difference over sum of two channels is much noisier than with a digital oscilloscope. Building a data acquisition system for the 1 MHz pulse trains should be a high priority of future improvements to the EOS experiment, as it would give lower noise with shorter averaging times.

There are many crystals which have an electro-optic effect. Another good choice is zinc telluride (ZnTe) in the $\langle 110 \rangle$ orientation.

7.3 Bunch Compression

In Chapter 4, we presented results from studies of magnetic bunch compression with the dipole chicane. Even at high charge, the bunch could be compressed to less than 1 mm σ_z. At the point of best compression, the peak current over an ensemble of shots was 2.8±0.1 kA. The highest peak current in a single shot was 3.02 kA.

We have shown that a magnetic compressor at low energy (16 MeV) can produce short bunches at high charge. The emittance growth in the compressor may be an issue. Both the emittance after compression and the energy spread after compression are topics of interest for future experiments. Preliminary results indicate that the emittance increases by a factor of ~2 after compression.

The compression experiments were repeated with two different UV laser pulse lengths on the cathode. The short laser pulse was Gaussian with 2 ps σ_t, and the long laser pulse was an approximate flat-top distribution with 10.7 ps FWHM. The uncompressed bunch length was measured versus the charge; again, this was repeated for both laser pulse lengths. The effects of space charge expansion are evident for the 2 ps laser pulse, even at low charge.

Characterizing the performance of the photoinjector as a function of the UV laser pulse length is an important step to optimizing current and future designs.

7.4 Photoemission

We have included in Chapter 3 some results on photoemission with high quantum efficiency Cs_2Te photocathodes. The same cathode has been used for more than one year in the RF gun, which demonstrates that Cs_2Te has sufficient durability and lifetime. We have measured the charge saturation with increasing laser energy from space charge. For a fixed laser energy as the accelerating gradient is varied, the charge extraction is shown to obey the Child-Langmuir limit. Once the gradient is sufficient to extract the full charge, the current does not plateau with further increases in gradient, but slowly increases from the Schottky field enhancement of the quantum efficiency.

7.5 Excitation Laser

The same laser system was used for photocathode excitation and electro-optic sampling. It is capable of long pulse train operation with 1 μsec micropulse spacing. We have demonstrated UV pulse trains 200 μsec long with a flat (rectangular) envelope at the design energy. Longer pulse trains 800 μsec long have also been demonstrated, but at lower energy because of the losses in the active envelope-shaping system.

We have used a "pulse stacker" for temporal pulse shaping of the UV pulses. A good approximation to a flat-top distribution with a 10.7 ps FWHM is shown. The photoinjector performance was characterized for both the short (unstacked) laser pulse and the long (stacked) laser pulse. Our studies of bunch compression for different laser pulse lengths illustrate the sensitivity of the photoinjector to the laser pulse length.

A simple scheme of spatial profile control gave good a truncated Gaussian laser spot. With a small truncation radius a good approximation to a uniform disc spot profile could be made.

Bibliography

[1] L. K. Spentzouris, J.-F. Ostiguy, and P. L. Colestock. Direct Measurement of Diffusion Rates in High Energy Synchrotrons Using Longitudinal Beam Echoes. *Physical Review Letters*, 76(4):620–623, 1996.

[2] Linda Klamp Spentzouris. *Coherent Nonlinear Longitudinal Phenomena in Unbunched Synchrotron Beams.* PhD thesis, Northwestern University, 1996.

[3] J. S. Hangst, J. S. Nielsen, O. Poulsen, P. Shi, and J. P. Schiffer. Laser Cooling of a Bunched Beam in a Synchrotron Storage Ring. *Physical Review Letters*, 74(22):4432–4435, 1995.

[4] E. G. Bessonov and K.-J. Kim. Radiative Cooling of Ion Beams in Storage Rings by Broad-Band Lasers. *Physical Review Letters*, 76(3):431–434, 1996.

[5] Valery Telnov. Laser Cooling of Electron Beams for Linear Colliders. *Physical Review Letters*, 78(25):4757–4760, 1997.

[6] A. A. Mikhailichenko and M. S. Zolotorev. Optical Stochastic Cooling. *Physical Review Letters*, 71(25):4146–4149, 1993.

[7] M. S. Zolotorev and A. A. Zholents. Transit-time method of optical stochastic cooling. *Physical Review E*, 50(4):3087–3091, 1994.

[8] Tsumoru Shintake. Proposal of a nanometer beam size monitor for e^+e^- linear colliders. *Nuclear Instruments & Methods in Physics Research A*, 312:453–464, 1992.

[9] W.P. Leemans, R.W. Schoenlein, P. Volbeyn, A. H. Chin, T.E. Glover, P. Balling, M. Zolotorev, K.J. Kim, S. Chattopadhyay, and C.V. Shank. X-Ray Based Subpicosecond Electron Bunch Characterization Using 90° Thomson Scattering. *Physical Review Letters*, 77(20):4182–4185, 1996.

[10] R. W. Schoenlein, W. P. Leemans, A. H. Chin, P. Volfbeyn, T.E. Glover, P. Balling, M. Zolotorev, K.-J. Kim, S. Chattopadhyay, and C.V. Shank. Femtosecond X-ray Pulses at 0.4 Å Generated by 90° Thomson Scattering:

A Tool for Probing the Structural Dynamics of Materials. *Science*, 274:236–238, 1996.

[11] Cha-Mei Tang, B. Hafizi, and Sally K. Ride. Thomson backscattered X-rays from an intense laser beam. *Nuclear Instruments & Methods in Physics Research A*, 331:371–378, 1993.

[12] E. Esarey, P. Sprangle, A. Ting, and S. K. Ride. Laser synchrotron radiation as a compact source of tunable short pulse hard X-rays. *Nuclear Instruments & Methods in Physics Research A*, 331:545–549, 1993.

[13] J. Chen, K. Imasaki, M. Fujita, C. Yamanaka, M. Asakawa, S. Nakai, and T. Asakuma. Development of a compact high brightness X-ray source. *Nuclear Instruments & Methods in Physics Research A*, 341:346–350, 1994.

[14] Kwang-Je Kim, S. Chattopadhyay, and C. V. Shank. Generation of femtosecond X-rays by 90° Thomson scattering. *Nuclear Instruments & Methods in Physics Research A*, 341:351–354, 1994.

[15] V. N. Litvinenko, B. Burnham, M. Emamian, N. Hower, J. M. J. Madey, P. Morcombe, P. G. O'Shea, S. H. Park, R. Sachtschale, K. D. Straub, G. Swift, P. Wang, Y. Wu, R. S. Canon, C. R. Howell, N. R. Roberson, E. C. Schreiber, M. Spraker, W. Tornow, H. R. Weller, I. V. Pinayev, N. G. Gavrilov, M. G. Fedotov, G. N. Kulipanov, G. Y. Kurkin, S. F. Mikhailov, V. M. Popik, A. N. Skrinsky, N. A. Vinokurov, B. E. Norum, A. Lumpkin, and B. Yang. Gamma-Ray Production in a Storage Ring Free-Electron Laser. *Physical Review Letters*, 78(24):4569–4572, 1997.

[16] C. E. Clayton, N. A. Kurnit, and D. D. Meyerhofer. Application of conventional laser technology to gamma–gamma colliders. *Nuclear Instruments and Methods in Physics Research A*, 355:121–129, 1995.

[17] D. D. Meyerhofer. High intensity lasers for gamma–gamma colliders. *Nuclear Instruments and Methods in Physics Research A*, 355:113–120, 1995.

[18] Steven John Boege. *Evidence of Light-by-Light Scattering with Real Photons.* PhD thesis, University of Rochester, 1996.

[19] Theofilos Kotseroglou. *Observation of Nonlinear Compton Scattering.* PhD thesis, University of Rochester, 1996.

[20] C. Bula, K. T. McDonald, E. J. Prebys, C. Bamber, S. Boege, T. Kotseroglou, A.C. Melissinos, D.D. Meyerhofer, W. Ragg, D.L. Burke, R.C. Field, G. Horton-Smith, A.C. Odian, J.E. Spencer, D. Walz, S.C. Berridge,

W.M. Bugg, K. Shmakov, and A.W. Weidemann. Observation of Nonlinear Effects in Compton Scattering. *Physical Review Letters*, 76(17):3116–3119, 1996.

[21] C. Bamber, T. Blalock, S. Boege, T. Kotseroglou, A. C. Melissinos, W. Ragg, D. Reis, D. D. Meyerhofer, J. Kelly, and M. Shoup III. 0.5-Hz, Phase-Stabilized Terawatt Laser System with a Nd:Glass Slab Amplifier for Nonlinear QED Experiments. *Laser Physics*, 7:135, 1997.

[22] D.L. Burke, R.C. Field, G. Horton-Smith, J.E. Spencer, D. Walz, S.C. Berridge, W.M. Bugg, K. Shmakov, A.W. Weidemann, C. Bula, K. T. McDonald, E. J. Prebys, C. Bamber, S. Boege, T. Kotseroglou, A.C. Melissinos, D.D. Meyerhofer, and W. Ragg. Positron Production in Multiphoton Light-by-Light Scattering. *Physical Review Letters*, 79(9):1626–1629, 1997.

[23] Mitsuru Uesaka, Toru Ueda, Takahiro Kozawa, and Toshiaki Kobayashi. Precise measurement of a subpicosecond electron single bunch by the femtosecond streak camera. *Nuclear Instruments and Methods in Physics Research A*, 406:371–379, 1998.

[24] Yukio Shibata, Toshiharu Takahashi, Toshinobu Kanai, Kimihiro Ishi, Mikihiko Ikezawa, Juzo Ohkuma, Shuichi Okuda, and Toichi Okada. Diagnostics of an electron beam of a linear accelerator using coherent transition radiation. *Physical Review E*, 50(2):1479–1484, 1994.

[25] B. I. Greene, J. F. Federici, D. R. Dykaar, R. R. Jones, and P. H. Bucksbaum. Interferometric characterization of 160 fs far-infrared light pulses. *Applied Physics Letters*, 59:893–895, 1991.

[26] Pamela Kung, Hung chi Lihn, Helmut Wiedemann, and David Bocek. Generation and Measurement of 50-fs (rms) Electron Pulses. *Physical Review Letters*, 73:967–970, 1994.

[27] Hung-chi Lihn, Pamela Kung, Chitrlada Settakorn, Helmut Wiedemann, and David Bocek. Measurement of subpicosecond electron pulses. *Physical Review E*, 53:6413–6418, 1996.

[28] R. Lai, U. Happek, and A. J. Sievers. Measurement of the longitudinal asymmetry of a charged particle bunch from the coherent synchrotron or transition radiation spectrum. *Physical Review E*, 50:R4294–R4297, 1994.

[29] TTF Conceptual Design Report. Technical Report TESLA 95-01, DESY, 1995.

[30] J. Rossbach. A VUV free electron laser at the TESLA test facility at DESY. *Nuclear Instruments and Methods in Physics Research A*, 375:269–273, 1996.

[31] R. Tatchyn et al. Research and development toward a 4.5–1.5 Å linac coherent light source (LCLS) at SLAC. *Nuclear Instruments and Methods in Physics Research A*, 375:274–283, 1996.

[32] R. Alley, V. Bharadwaj, J. Clendenin, P. Emma, A. Fisher, J. Frisch, T. Kotseroglou, R. Miller, D. T. Palmer, J. Schmerge, J. C. Sheppard, M. Woodley, A. D. Yeremian, J. Rosenzweig, D. D. Meyerhofer, and L. Serafini. The design for the LCLS rf photo-injector. *Proceedings of the 20th International Free Electron Laser and 5th Free Electron Laser Users' Workshop (FEL98)*, 1998. SLAC-PUB-8054, January 1999.

[33] J. M. J. Madey. Stimulated Emission of Bremsstrahlung in a Periodic Magnetic Field. *Journal of Applied Physics*, 42:1906, 1971.

[34] B. Faatz, J. Feldhaus, J. Krzywinski, E. L. Saldin, E. A. Schneidmiller, and M. V. Yurkov. Regenerative FEL Amplifier at the DESY TESLA Test Facility as a Fully Coherent VUV Laser. Technical report, TESLA-FEL 97-07, November 1997.

[35] C. W. Roberson and P. Sprangle. A review of free-electron lasers. *Phys. Fluids B*, 1(1):3, 1989.

[36] J. Andruszkow et al. First Observation of Self-Amplified Spontaneous Emission in a Free-Electron Laser at 109 nm Wavelength. *Physical Review Letters*, 85(18):3825–3829, 2000.

[37] Eric Ralph Colby. *Design, Construction, and Testing of a Radiofrequency Electron Photoinjector for the Next Generation Linear Collider*. PhD thesis, University of California Los Angeles, 1997.

[38] J. Early, J. Barton, R. Wenzel, D. Remelius, and G. Busch. The Los Alamos FEL Photoinjector Drive Laser. *IEEE Journal of Quantum Electronics*, 27(12):2644–2649, 1991.

[39] Triveni Srinivasan-Rao, editor. *Proceedings of the Workshop on "Lasers for RF Guns", Anaheim, CA*, 1994. BNL-52435.

[40] R. F. X. A. M. Mols and G. J. Ernst. Performance of a MOPA laser system for photocathode research. *Nuclear Instruments & Methods in Physics Research A*, 341:481–483, 1994.

[41] Vincent Le Flanchec, Jean-Paul Bléśes, Serge Striby, and Jean-Paul Laget. Stabilization system of a photoinjector drive laser. *Applied Optics*, 36(33):8541–8546, 1997.

[42] Ingo Will, Armin Liero, Dieter Mertins, and Wolfgang Sandner. Feedback-Stabilized Nd:YLF Amplifier System for Generation of Picosecond Pulse Trains of an Exactly Rectangular Envelope. *IEEE Journal of Quantum Electronics*, 34:2020–2028, 1998.

[43] A.R. Fry, M.J. Fitch, A.C. Melissinos, and B.D. Taylor. Laser system for a high duty cycle photoinjector. *Nuclear Instruments & Methods in Physics Research A*, 430:180–188, 1999.

[44] S. Schreiber, I. Will, D. Sertore, A. Liero, and W. Sandner. Running experience with the laser system for the RF gun based injector at the TESLA Test Facility linac. *Nuclear Instruments and Methods in Physics Research A*, 445:427–431, 2000.

[45] N. Barov. Private communication. On laser-plasma based experiments at the AØ Photoinjector, 2000.

[46] Milton J. Shoup III, John H. Kelly, and David L. Smith. Design and testing of a large-aperture, high-gain, Brewster's angle zigzag Nd:glass slab amplifier. *Applied Optics*, 36(24):5827–5838, 1997.

[47] Alan R. Fry. *Novel Pulse Train Glass Laser for RF Photoinjectors.* PhD thesis, University of Rochester, 1996.

[48] R. L. Fork, B. I. Greene, and C. V. Shank. Generation of optical pulses shorter than 0.1 psec by colliding pulse mode-locking. *Applied Physics Letters*, 38(9):671–672, 1981.

[49] Walter Koechner. *Solid-State Laser Engineering.* Springer-Verlag, third edition, 1992.

[50] P. Bado, M. Bouvier, and J. Scott Coe. Nd:YLF mode-locked oscillator and regenerative amplifier. *Optics Letters*, 12(5):319–321, 1987.

[51] Claude Rullière, editor. *Femtosecond Laser Pulses: Principles and Experiments.* Springer-Verlag, 1998.

[52] M. J. W. Rodwell, K. J. Weingarten, T. Baer D. M. Bloom, and B. H. Kolner. Reduction of timing fluctuations in a mode-locked Nd:YAG laser by electronic feedback. *Optics Letters*, 11:638–640, 1986.

[53] Lightwave Electronics, Mountain View CA. *Series 1000 Timing Stabilizer for Nd:YAG mode-locked laser*, 1989.

[54] Mark J. W. Rodwell, David M. Bloom, and Kurt J. Weingarten. Subpicosecond Laser Timing Stabilization. *IEEE Journal of Quantum Electronics*, 25:817–827, 1989.

[55] Donna Strickland and Gerard Mourou. Compression of Amplified Chirped Optical Pulses. *Optics Communications*, 56(3):219–221, 1985.

[56] M. Pessot, P. Maine, and G. Mourou. 1000 times Expansion/Compression of Optical Pulses for Chirped Pulse Amplification. *Optics Communications*, 62(6):419–421, 1987.

[57] P. Maine, D. Strickland, P. Bado, M. Pessot, and G. Mourou. Generation of Ultrahigh Peak Power Pulses by Chirped Pulse Amplification. *IEEE Journal of Quantum Electronics*, 24(2):398–403, 1988.

[58] D. Grischkowsky and A. C. Balant. Optical pulse compression based on enhanced frequency chirping. *Applied Physics Letters*, 41(1):1–3, 1982.

[59] Govind P. Agrawal. Optical solitons. In *Contemporary Nonlinear Optics*, chapter 2, page 41. Academic Press, Inc., 1992.

[60] Oscar Eduardo Martinez. 3000 Times Grating Compressor with Positive Group Velocity Dispersion: Application to Fiber Compensation in 1.3–1.6 μm Region. *IEEE Journal of Quantum Electronics*, QE-23(1):59–64, 1987.

[61] Steve Kane and Jeff Squier. Grating Compensation of Third-Order Material Dispersion in the Normal Dispersion Regime: Sub-100-fs Chirped-Pulse Amplification Using a Fiber Stretcher and Grating-Pair Compressor. *IEEE Journal of Quantum Electronics*, 31(11):2052–2057, 1995.

[62] EG&G Optoelectronics. *Silicon Photodiode - Application Note*, 1999. Typical photodiodes used are model FND-100 or FND-100Q.

[63] Laboratory for Laser Energetics, drawings 1Ω08-180, -181, -182.

[64] P. Laporta, V. Magni, and L. Pallaro. Optimization Study of a Picosecond Rotating-Mirror Autocorrelator. *Optics Communications*, 51(2):95–99, 1984.

[65] J. E. Murray and W. H. Lowdermilk. Nd:YAG regenerative amplifier. *Journal of Applied Physics*, 51(7):3548–3555, 1980.

[66] Daniel J. Gauthier, Paul Narum, and Robert W. Boyd. Simple, compact, high-performance permanent-magnet Faraday isolator. *Optics Letters*, 11:623–625, 1986.

[67] J. A. Glaze, S. Guch, and J. B. Trenholme. Parasitic Suppression in Large Aperture Nd:glass Disk Laser Amplifiers. *Applied Optics*, 13(12):2808–2811, 1974.

[68] Lee M. Frantz and John S. Nodvick. Theory of Pulse Propagation in a Laser Amplifier. *Journal of Applied Physics*, 34(8):2346–2349, 1963.

[69] Jonathan D. Zuegel and Wolf Seka. Direct Measurements of $^4I_{11/2}$ Terminal-Level Lifetime in Nd:YLF. *IEEE Journal of Quantum Electronics*, 31(10):1742–1746, 1995.

[70] Mark D. Skeldon, Andrei Babushkin, Wade Bittle, Andrey V. Okishev, and Wolf Seka. Modeling the Temporal-Pulse-Shape Dynamics of an Actively Stabilized Regenerative Amplifier. *IEEE Journal of Quantum Electronics*, 34(2):286–291, 1998.

[71] Incropera and DeWitt. *Fundamentals of Heat and Mass Transfer*. Wiley, third edition, 1990.

[72] Jasbir S. Uppal, Jagdish C. Monga, and Dilip D. Bhawalkar. Study of Thermal Effects in a Nd Doped Phosphate Glass Laser Rod. *IEEE Journal of Quantum Electronics*, QE-22(12):2259–2265, 1986.

[73] Max Born and Emil Wolf. *Principles of Optics*. Pergamon, 1965.

[74] Edmond B. Treacy. Optical Pulse Compression with Diffraction Gratings. *IEEE Journal of Quantum Electronics*, QE-5(9):454–458, 1969.

[75] P. S. Banks, M. D. Perry, V. Yanovsky, S. N. Fochs, B. C. Stuart, and J. Zweiback. Novel All-Reflective Stretcher for Chirped-Pulse Amplification of Ultrashort Pulses. *IEEE Journal of Quantum Electronics*, 36(3):268–274, 2000.

[76] J. A. Armstrong. Measurement of Picosecond Laser Pulse Widths. *Applied Physics Letters*, 10(1):16–18, 1967.

[77] Leon Cohen. Time-Frequency Distributions—A Review. *Proceedings of the IEEE*, 77(7):941–981, 1989.

[78] Leon Cohen. *Time-Frequency Analysis*. Prentice Hall, 1995.

[79] Daniel J. Kane and Rick Trebino. Characterization of Arbitrary Femtosecond Pulses Using Frequency-Resolved Optical Gating. *IEEE Journal of Quantum Electronics*, 29(2):571–579, 1993.

[80] C. Iaconis and I. A. Walmsley. Spectral phase interferometry for direct electric-field reconstruction of ultrashort optical pulses. *Optics Letters*, 23(10):792–794, 1998.

[81] L. Gallmann, D. H. Sutter, N. Matuschek, G. Steinmeyer, U. Keller, C. Iaconis, and I. A. Walmsley. Characterization of sub-6-fs optical pulses with spectral phase interferometry for direct electric-field reconstruction. *Optics Letters*, 24(18):1314–1316, 1999.

[82] Amnon Yariv. *Optical Electronics*. Holt, Rinehart & Winston, Inc., 3rd edition, 1985.

[83] David A. Reis. *Emittance Measurements from a Laser Driven Electron Injector*. PhD thesis, University of Rochester, 1999. UR-1573 and SLAC pub R-539.

[84] Craig W. Siders, Jennifer L. W. Siders, Antoinette J. Taylor, Sang-Gyu Park, and Andrew M. Weiner. Efficient high-energy pulse-train generation using a 2^n-pulse Michelson interferometer. *Applied Optics*, 37(22):5302–5305, 1998.

[85] Sang-Gyu Park, A. M. Weiner, Michael R. Melloch, Craig W. Siders, Jennifer L. W. Siders, and Antoinette J. Taylor. High-Power Narrow-Band Terahertz Generation Using Large-Aperture Photoconductors. *IEEE Journal of Quantum Electronics*, 35(8):1257–1268, 1999.

[86] Edward A. Kurz. Channel electron multipliers. *American Laboratory*, 1979.

[87] Toshio Sakurai and T. Hashizume. Determination of the detection efficiency of a channelplate electron multiplier. *Rev. Sci. Instrum.*, 57(2):236–239, 1986.

[88] G. W. Fraser and J. F. Pearson. Soft x-ray energy resolution with microchannel plate detectors of high quantum detection efficiency. *Nuclear Instruments and Methods in Physics Research A*, 219:199–212, 1984.

[89] *Instruction manual for universal streak camera C5680, Hamamatsu Photonics K.K.*

[90] John David Jackson. *Classical Electrodynamics*. John Wiley & Sons, second edition, 1975.

[91] Eric R. Colby. A High Charge, High Duty Factor RF Photoinjector for the Next Generation Linear Collider. *Proceedings of the 19th International Linear Accelerator Conference (LINAC 98)*, 1998. SLAC-PUB-7946.

[92] J.-P. Carneiro et al. Beam Transport, Acceleration and Compression Studies in the Fermilab High-Brightness Photoinjector. *Proceedings of the 19th International Linear Acclerator Conference (LINAC 98)*, 1998. Fermilab-Conf-98/329.

[93] J.-P. Carneiro et al. First Results of the Fermilab High-Brightness RF Photoinjector. In A. Luccio and W. MacKay, editors, *Proceedings of the 1999 Particle Accelerator Conference*, pages 2027–2029. IEEE, 1999.

[94] A. Fry, E. Hahn, W. Hartung, and M. Kuchnir. Experience at Fermilab with High Quantum Efficiency Photo-Cathodes for RF Electron Guns. *Proceedings of the 19th International Linear Accelerator Conference (LINAC 98)*, 1998.

[95] W. Hartung et al. Beam Test of a Superconducting Cavity for the Fermilab High-Brightness Electron Photo-Injector. In A. Luccio and W. MacKay, editors, *Proceedings of the 1999 Particle Accelerator Conference*, pages 992–994. IEEE, 1999.

[96] J. B. Rosenzweig, N. Barov, and E. Colby. Pulse Compression in Radio Frequency Photoinjectors—Applications to Advanced Accelerators. *IEEE Transactions on Plasma Science*, 24(2):409–420, 1996.

[97] Patrick L. Colestock. Private communication. On beam dynamics in the chicane.

[98] Jean-Paul Carneiro. *Etude experimentale du photo-injecteur de Fermilab*. PhD thesis, l'Universite Paris XI, 2000. (Expected completion 2000.).

[99] S. H. Kong, J. Kinross-Wright, D. C. Nguyen, and R. L. Sheffield. Photocathodes for free electron lasers. *Nuclear Instruments and Methods in Physics Research A*, 358:272–275, 1995.

[100] T. Srinivasan-Rao, J. Fischer, and T. Tsang. Photoemission studies on metals using picosecond ultraviolet laser pulses. *Journal of Applied Physics*, 69:3291–3296, 1991.

[101] T. Srinivasan-Rao, J. Schill, I. Ben-Zvi, and M. Woodle. Sputtered magnesium as a photocathode material for rf photoinjectors. *Review of Scientific Instruments*, 69(6):2292–2296, 1998.

[102] S. H. Kong, D. C. Nguyen, R. L. Sheffield, and B. A. Sherwood. Fabrication and characterization of cesium telluride photocathodes: A promising electron source for the Los Alamos Advanced FEL. *Nuclear Instruments and Methods in Physics Research A*, 358:276–279, 1995.

[103] S. H. Kong, J. Kinross-Wright, D. C. Nguyen, R. L. Sheffield, and M. E. Weber. Performance of cesium telluride photocathodes as an electron source for the Los Alamos Advanced FEL. *Nuclear Instruments and Methods in Physics Research A*, 358:284–286, 1995.

[104] D. Sertore, S. Schreiber, K. Floettmann, F. Stephan, K. Zapfe, and P. Michelato. First operation of the cesium telluride photocathodes in the TTF injector RF gun. *Nuclear Instruments and Methods in Physics Research A*, 445:422–426, 2000.

[105] A. di Bona, F. Sabary, S. Valeri, P. Michelato, D. Sertore, and G. Suberlucq. Auger and x-ray photoemission spectroscopy study on Cs_2Te photocathodes. *Journal of Applied Physics*, 80(5):3024–3030, 1996.

[106] S. C. Harman, N. Barov, C. Pellegrini, S. Park, J. Rosenzweig, G. Travish, R. Zhang, C. Clayton, P. Davis, M. Everett, C. Joshi, and G. Hairapetian. Initial measurements of the UCLA rf photoinjector. *Nuclear Instruments and Methods in Physics Research A*, 340:219–230, 1994.

[107] Langmuir and Blodgett. Currents Limited by Space Charge Between Coaxial Cylinders. *Physical Review*, 22:347, 1923.

[108] Christian Travier. An introduction to photo-injector design. *Nuclear Instruments and Methods in Physics Research A*, 340:26–39, 1994.

[109] W. Schottky. Über kalte und warme Elektronenentladungen. *Zeitschrift für Physik*, 14:63–106, 1923.

[110] M. Cardona and L. Ley, editors. *Photoemission in Solids I*. Springer-Verlag, 1978.

[111] D. A. Edwards and M. J. Syphers. *An introduction to the physics of high energy accelerators*. Wiley, 1993.

[112] Lev Davidovich Landau and Evgenii Mikhailovich Lifshitz. *Statistical Physics, Part 1*. Pergamon Press, third edition edition, 1980.

[113] X. Qiu, K. Batchelor, I. Ben-Zvi, and X.-J. Wang. Demonstration of Emit-

tance Compensation through the Measurement of the Slice Emittance of a 10-ps Electron Bunch. *Physical Review Letters*, 76(20):3723–3726, 1996.

[114] Bruce E. Carlsten. New Photoelectric Injector Design of the Los Alamos National Laboratory XUV FEL Accelerator. *Nuclear Instruments and Methods in Physics Research A*, 285:313–319, 1989.

[115] Helmut Wiedemann. Breaking the Picosecond Barrier. *SLAC Beam Line*, 27(2):25–30, 1997.

[116] Bruce E. Carlsten and Tor O. Raubenheimer. Emittance growth of bunched beams in bends. *Physical Review E*, 51(2):1453–1470, 1995.

[117] Bruce E. Carlsten. Calculation of the noninertial space-charge force and the coherent synchrotron radiation force for short electron bunches in circular motion using the retarded Green's function technique. *Physical Review E*, 54(1):838–845, 1996.

[118] Bruce E. Carlsten and Steven J. Russell. Subpicosecond compression of 0.1–1nC electron bunches with a magnetic chicane at 8 MeV. *Physical Review E*, 53(3):R2072–R2075, 1996.

[119] M. Dohlus and T. Limberg. Emittance Growth due to Wake Fields on Curved Bunch Trajectories. *Proceedings of the 1996 Free Electron Laser Conference (FEL96)*, 1996. TESLA-FEL 96-13.

[120] H. Braun, F. Chautard, R. Corsini, T. O. Raubenheimer, and P. Tenenbaum. Emittance Growth during Bunch Compression in the CTF-II. *Physical Review Letters*, 84(4):658–661, 2000.

[121] Jean-Paul Carneiro, 2000. Private communication.

[122] D. X. Wang, G. A. Krafft, and C. K. Sinclair. Measurement of femtosecond electron bunches using a rf zero-phasing method. *Physical Review E*, 57:2283–2286, 1998.

[123] M. Uesaka, K. Kinoshita, T. Watanabe, T. Ueda, K. Yoshii, H. Harano, J. Sugahara, K. Nakajima, A. Ogata, F. Sakai, H. Dewa, M. Kando, H. Kotaki, and S. Kondo. Femtosecond Electron Beam Generation by S-band Laser Photocathode RF Gun and Linac. *Advanced Accelerator Workshop: Eighth Workshop*, pages 908–917, 1999. AIP conference proceedings 472, Woodbury NY, Wes Lawson, Ed.

[124] M. E. Conde, W. Gai, R. Konecny, X. Li, J. Power, P. Schoessow, and

N. Barov. Generation and acceleration of high-charge short-electron bunches. *Physical Review Special Topics - Accelerators and Beams*, 1:041302, 1998.

[125] Guillaume Devanz. *Etude numérique et expérimentale de la dynamique du faisceau du photo-injecteur CANDELA et instrumentation associée.* PhD thesis, Université Pierre et Marie Curie, Paris VI, 1999.

[126] A. Loulergue, D. H. Dowell, S. Joly, J. P. de Brion, G. Haouat, and F. Schumann. Transverse and longitudinal emittance measurements in the ELSA linac. *Nuclear Instruments and Methods in Physics Research A*, 384:285–292, 1997.

[127] M. Babzien, I. Ben-Zvi, P. Catravas, J.-M. Fang, T. C. Marshall, X. J. Wang, J. S. Wurtele, V. Yakimento, and L. H. Yu. Observation of self-amplified spontaneous emission in the near-infrared and visible wavelengths. *Physical Review E*, 57(5):6093–6100, 1998.

[128] P. Catravas, W. P. Leemans, J. S. Wurtele, M. S. Zolotorev, M. Babzien, I. Ben-Zvi, Z. Segalov, X.-J. Wang, and V. Yakimento. Measurement of Electron-Beam Bunch Length and Emittance Using Shot-Noise-Driven Fluctuations in Incoherent Radiation. *Physical Review Letters*, 82(26):5261–5264, 1999.

[129] D. C. Nguyen, R. L. Sheffield, J. C. Goldstein C. M. Fortgang, J. M. Kinross-Wright, and N. A. Ebrahim. Self-Amplified Spontaneous Emission Driven by a High-Brightness Electron Beam. *Physical Review Letters*, 81(4):810–813, 1998.

[130] F. Zimmerman, G. Yocky, D. H. Whittum, K. A. Thompson, C. Ng, D. McCormick, T. Markiewicz, and K. L. F. Bane. First Bunch Length Studies in the SLC South Final Focus. *Proceedings of the 6th European Partical Accelerator Conference (EPAC-98)*, 1998. SLAC-PUB-7855.

[131] U. Happek, A. J. Sievers, and E. B. Blum. Observation of Coherent Transition Radiation. *Physical Review Letters*, 67(21):2962–2965, 1991.

[132] H. H. Braun, R. Corsini, L. Groening, F. Zhou, A. Kabel, T. Raubenheimer, R. Li, and T. Limberg. Coherent synchrotron radiation measurements in the CLIC Test Facility (CTF-II). In *Proceedings of the XX Linear Accelerator Conference (Linac 2000)*, 2000.

[133] D. H. Auston. Picosecond optoelectronic switching and gating in silicon. *Applied Physics Letters*, 26:101–103, 1975.

[134] David H. Auston and Martin C. Nuss. Electrooptic Generation and Detection of Femtosecond Electrical Transients. *IEEE Journal of Quantum Electronics*, 24(2):184–197, 1988.

[135] J. A. Valdmanis, G. Mourou, and C. W. Gabel. Picosecond electro-optic sampling system. *Applied Physics Letters*, 41:211–212, 1982.

[136] J. A. Valdmanis, G. Mourou, and C. W. Gabel. Subpicosecond Electrical Sampling. *IEEE Journal of Quantum Electronics*, QE-19:664–667, 1983.

[137] Q. Wu and X.-C. Zhang. Free-space electro-optics sampling of mid-infrared pulses. *Applied Physics Letters*, 71:1285–1286, 1997.

[138] A. Leitenstorfer, S. Hunsche, J. Shah, M. C. Nuss, and W. H. Knox. Detectors and sources for ultrabroadband electro-optic sampling: Experiment and theory. *Applied Physics Letters*, 74(11):1516–1518, 1999.

[139] Marc Currie, Roman Sobolewski, and Thomas Y. Hsiang. Subterahertz signal crosstalk in transmission line interconnects. *Applied Physics Letters*, 73(13), 1998.

[140] P. J. Channell. Use of Kerr cells to measure RF fields. Technical report, Los Alamos National Laboratory, 1982. Accelerator Theory Note AT-6:ATN-82-1.

[141] Yu. S. Pavlov and N. G. Solov'ev. Formirovanie i Izmerenie Pikosekundnykh Puchkov Zaryazhennykh Chastits (Formation and Measurement of Picosecond Beams of Charged Particles). In *Proc. VIII All-Union Charged Part. Accel. Conf.*, volume 2, pages 63–67, Protvino 1982. An English translation from the Russian may be obtained from MJF.

[142] M. Geitz, K. Hanke, and A. C. Melissinos. Bunch Length Measurements at TTFL using Optical Techniques. Technical report, DESY, 1997. Internal report TESLA collaboration.

[143] J. A. Riordan, F. G. Sun, Z. G. Lu, and X.-C. Zhang. Free-space transient magneto-optic sampling. *Applied Physics Letters*, 71:1452–1454, 1997.

[144] Y. K. Semertzidis, V. Castillo, R. C. Larsen, D. M. Lazarus, B. Magurno, T. Srinivasan-Rao, T. Tsang, V. Usack, L. Kowalski, and D.E. Kraus. Electro-Optical Detection of Charged Particle Beams. In A. Luccio and W. MacKay, editors, *Proceedings of the 1999 Particle Accelerator Conference*, pages 490–491. IEEE, 1999.

[145] K. P. Leung, L. H. Yu, and I. Ben-Zvi. RF Phase Stabilization of RF Photocathode Gun Through Electro-Optical Monitoring. *Proc. SPIE - Int. Soc. Opt. Eng.*, 2013:147–151, 1993. BNL-49276.

[146] M. J. Fitch, N. Barov, J.P. Carneiro, P. Colestock, H. T. Edwards, K. P. Koepke, A. C. Melissinos, and W. H. Hartung. Electro-optic Measurement of the Wake Fields of 16 MeV Electron Bunches. Technical report, University of Rochester, 1999. UR-1585 and FERMILAB-TM-2096.

[147] M. J. Fitch, A. C. Melissinos, and P. L. Colestock. Picosecond electron bunch length measurement by electro-optic detection of the wakefields. In A. Luccio and W. MacKay, editors, *Proceedings of the 1999 Particle Accelerator Conference*, pages 2181–2183. IEEE, 1999.

[148] G. M. H. Knippels, X. Yan, A. M. MacLeod, W. A. Gillespie, M. Yasumoto, D. Oepts, and A. F. G. van der Meer. Generation and Complete Electric-Field Characterization of Intense Ultrashort Tunable Far-Infrared Laser Pulses. *Physical Review Letters*, 83(8):1578–1581, 1999.

[149] D. Oepts, G. M. H. Knippels, X. Yan, A. M.MacLeod, W. A. Gillespie, and A. F. G. van der Meer. Picosecond electron-bunch length measurement using an electro-optic sensor. *Proceedings of the 21st International FEL Conference (FEL99)*, 1999. 23–28 August 1999, DESY.

[150] X. Yan, A. M. MacLeod, W. A. Gillespie, G. M. H. Knippels, D. Oepts, A. F. G. van der Meer, and W. Seidel. Sub-picosecond electro-optic measurement of relativistic electron pulses. *Physical Review Letters*, 85(16):3404–3407, 2000.

[151] Frits Zernike and John E. Midwinter. *Applied Nonlinear Optics*. John Wiley & Sons, 1973.

[152] Paul N. Butcher and David Cotter. *The elements of nonlinear optics*. Cambridge University Press, 1990. Includes several useful appendices.

[153] R. L. Byer. Parametric Oscillators and Nonlinear Materials. In *Nonlinear Optics*, chapter 2, pages 47–160. Academic Press, 1977. Proceedings of the Sixteenth Scottish Universities Summer School in Physics, 1975.

[154] Lev Davidovich Landau and Evgenii Mikhailovich Lifshitz. *Electrodynamics of Continuous Media*. Pergamon Press, 1984.

[155] Charles Kittel. *Introduction to Solid State Physics*. John Wiley & Sons, Inc., sixth edition, 1986.

[156] Neil W. Ashcroft and N. David Mermin. *Solid State Physics*. W. B. Saunders Company, 1976.

[157] D. A. Kleinman. Nonlinear Dielectric Polarization in Optical Media. *Physical Review*, 126(6):1977, 1962.

[158] Robert W. Boyd. Private communication. University of Rochester, Institute of Optics, 2000.

[159] George Arfken. *Mathematical Methods for Physicists*. Academic Press, Inc., third edition, 1985.

[160] P. Uhd Jepsen, C. Winnewisser, M. Schall, V. Schyja, S. R. Keiding, and H. Helm. Detection of THz pulses by phase retardation in lithium tantalate. *Physical Review E*, 53:R3052–R3054, 1996.

[161] C. Winnewisser, P. Uhd Jepsen, M. Schall, V. Schyja, and H. Helm. Electro-optic detection of THz radiation in $LiTaO_3$, $LiNbO_3$ and ZnTe. *Applied Physics Letters*, 70(23):3069–3071, 1997.

[162] Alexander W. Chao. *Physics of collective beam instabilities in high energy accelerators*. Wiley, 1993.

[163] T. Weiland and R. Wanzenberg. Wake fields and impedances. Technical report, Joint US-CERN Acclerator Course, 1990. DESY M-91-06 (May 1991).

[164] L. Palumbo, V. G. Vaccaro, and M. Zobov. Wake fields and impedance. Technical report, CAS Advanced School on Accelerator Physics, 1994. Laboratori Nazionali di Frascati LNF-94/041 (P).

[165] King-Yuen Ng. Physics of Collective Beam Instabilities. Technical report, FERMILAB-Conf-00/142-T, 2000. Lecture notes from USPAS, available online at `www-ap.fnal.gov/ng/uspas/`.

[166] S. A. Heifets and S. A. Kheifets. Coupling impedance in modern accelerators. *Reviews of Modern Physics*, 63(3):631–673, 1991.

[167] Ch. X. Tang and J. Ng. Wakefields in the Beamline of TTF Injector II. Technical report, DESY TESLA 97-11, 1997.

[168] E. Plawski. Wake-fields Induced by the Electron Beam Passing through the TESLA Accelerating System. Technical report, DESY TESLA 97-12, 1997.

[169] Ch. X. Tang. Longitudinal and Transverse Wakes for 6-port Cross CF35. Technical report, DESY TESLA, 1997.

[170] Courtlandt L. Bohn and King-Yuen Ng. Preserving High Multibunch Luminosity in Linear Colliders. *Physical Review Letters*, 85(5):984–987, 2000.

[171] K. Yang, L. P. B. Katehi, and J. F. Whitaker. Electro-optic field mapping system utilizing external gallium arsenide probes. *Applied Physics Letters*, 77(4):486–488, 2000.